Multi-scale Modelling for Materials Design in Additive Manufacturing

Weiling Wang

School of Engineering

Lancaster University

This dissertation is submitted for the degree of

Doctor of Philosophy

April 13, 2023

Declaration

I hereby declare that the contents of this thesis are entirely original and represent my own work, to the best of my knowledge and belief. Unless otherwise specified, this thesis is the culmination of my individual research efforts conducted within the School of Engineering at Lancaster University, spanning from October 2019 to April 2023. Additionally, this thesis adheres to the prescribed word limit of 60,000 words, inclusive of appendices and footnotes, but exclusive of the bibliography.

Abstract

Additively manufactured (AMed) austenitic stainless steels (SSs) possess exceptional properties like high strength and toughness. However, it is unclear how they perform under long-term exposure to high-temperature conditions, such as those found in nuclear reactors. These properties arise due to complex microstructures that develop during additive manufacturing (AM), including nanoscale dislocation cellular structures, microscale sub-grains with a high density of low-angle grain boundaries (LAGBs), and high dislocation density. Although the quasi-static mechanical properties of AM austenitic SSs, such as 316L SS, have been systematically investigated, the creep behaviour of such alloys is still a new area of research, with some experimental studies conducted in recent years. Additionally, the mechanical properties of most AMed alloys are anisotropic due to texture formation, and creep behaviour can be significantly influenced by microstructural differences in various building directions. Furthermore, the presence of AM-characterised microstructure is a notable feature of AM materials, and the size and shape of the pores can greatly influence stress concentration during loading. Thus, it is critical to quantify the effects of AM-characterised microstructure on the mechanical properties of materials.

As experimental methods have limitations for studying material properties, it is necessary to use computational modelling to extrapolate existing experimental data, especially for highly time-consuming experiments such as creep testing. This study

aims to provide a modelling framework for characterizing the evolution of microstructure and high-temperature creep behaviour in AM and wrought austenitic SSs, considering the impact of the initial microstructure. For AM materials, there are two types of samples: horizontally-built samples (loading direction parallel to the building direction) and vertically-built samples (loading direction vertical to the building direction). The choice of AM materials with different built directions is for studying the effect of the relative loading direction to the building direction on material creep behaviour. The materials strengthening mechanisms, including lattice friction, solid solution strengthening, dislocation hardening, and precipitation hardening, are quantified in detail. In addition to data from literature and experiments used to evaluate each strengthening mechanism, the precipitation evolution during the creep process is simulated through the thermokinetics calculation using Thermo-Calc software. Differently fabricated materials are originally simulated under the visco-plasticity self-consistent (VPSC) framework, using the materials' own characteristics as input. The creep mechanical responses of AM and wrought materials are compared, and the dominant deformation mechanisms are revealed and quantitatively compared. Due to the limitations of the VPSC, only the primary stage and secondary stage of creep behaviour are captured.

Based on this, the same physics-based model is employed under the crystal plasticity finite element method (CP-FEM) framework, which is full-field, and combined with the Gurson-Tvergaard-Needleman (GTN) damage model to capture the tertiary stage creep deformation. The original crystal plasticity model is highly microstructure-sensitive, and the detailed local structure can be analyzed through the finite element method. Therefore, the original electron backscatter diffraction (EBSD) information is pictured by MATLAB and used for materials input under the CP-FEM framework. In addition, DREAM3D software is used to extract microstructure information from raw EBSD data. The tertiary creep stages of horizontally-built and vertically-built AMed samples are simulated and compared, revealing that damage tends to accumulate on grain boundaries that are perpendicular to the loading direction. Additionally, the effects of AM-induced pores on creep deformation are evaluated by introducing them into the CP-FEM input. As selecting a specific region on the original EBSD data cannot summarize the overall AM materials characteristics, an artificial input is randomly generated

through a Voronoi diagram by MATLAB with assigned grain orientation. The artificial input is characterized by AM-induced elongated grain structure to study the effects of high angle grain boundaries (HAGBs) on materials creep behaviour, especially the damage evolution.

List of Publications

Journal publications:

- Microstructure-based modelling for creep behaviour: application to both additively manufactured and wrought SS316L- International Journal of Mechanical Sciences (under review)

Weiling Wang, Hossein Eskandari Sabzi, Richard J. Williams, Wei Wen, Pedro Eduardo Jose Rivera-Diaz-del-Castillo, 2023

- Modelling of creep and failure behaviour of additively manufactured SS316L using Crystal plasticity finite element method (CP-FEM)- (under review)

Weiling Wang, Wei Wen, Hossein Eskandari Sabzi, Pedro Eduardo Jose Rivera-Diaz-del-Castillo, 2023

Book chapter:

- Modelling in Crystal Plasticity: from theory to application- Encyclopedia of Materials: Metals and Alloys, Elsevier

Weiling Wang, Wei Wen, 2021

Acknowledgement

I wish to express my deep appreciation to Lancaster University for providing me with the opportunity to undertake my doctoral studies. I am especially grateful to the School of Engineering for awarding me the scholarship for international students. I would like to extend my gratitude to the individuals listed below, as I would not have been able to carry out my research without their invaluable contributions.

I am profoundly appreciative of my principal supervisor, Dr Wei Wen, for his unwavering inspiration and encouragement throughout the course of my doctoral research. His invaluable guidance and mentorship have not only aided me in the scientific inquiry but have also significantly contributed to my career trajectory. Moreover, under his tutelage, I have acquired a substantial amount of knowledge pertaining to the domain of computational materials science. I extend my gratitude towards Professor Pedro Rivera for his invaluable assistance, advice, and encouragement, which proved to be instrumental in guiding me through this research endeavour. His profound insights and extensive knowledge of the subject matter have been pivotal in my academic pursuits. Furthermore, I relished the time I spent with him during this research project.

I would like to express my gratitude to all those who extended their genuine friendship to me during this period. I am especially appreciative of my family, whose unwavering

support proved invaluable to me. Their unconditional love and positivity served as a source of inspiration and motivated me to persevere towards achieving my goal.

Contents

List of Figures

List of Tables

List of Symbols

k	Boltzmann constant
$\boldsymbol{b}$	magnitude of Burgers vector
μ	shear modulus
T	temperature
σ_0	yield strength
σ_i	friction stress
K	dislocation release factor,
τ_{bow}	the shear stress required for a dislocation to bow over the particle
σ_{cut}	the stress required to cut through the precipitate
r	the ratio of precipitation
f_P	precipitates volume fraction

ε'	lattice misfit strain
a_0	unstrained lattice parameter
a'_0	pseudomorphic lattice parameters
HV	Vickers hardness
Y	yield strength
$\mathbf{F}$	shape deformation gradient
$\mathbf{F}^P$	plastic deformation gradient
$\mathbf{F}^*$	elastic stretches and lattice rotation gradient
$\mathbf{L}$	microscopic velocity gradient
$\mathbf{L}^P$	plastic velocity gradient
$\mathbf{L}^*$	elastic velocity gradient
$\mathbf{D}^P$	plastic strain rate tensors
$\mathbf{D}^*$	elastic strain rate tensors
$\mathbf{\Omega}^P$	plastic spin
$\mathbf{\Omega}^*$	rigid lattice spin
s	slip system
$\mathbf{m}^s$	Schmid tensor of slip system s
$\mathbf{b}^s$	Burgers vector (slip direction) of the slip system s
$\mathbf{n}^s$	slip plane normal direction of the slip system s
$\mathbf{P}^s$	symmetric part of Schmid factor

$\mathbf{A}^s$	anti-symmetric part of Schmid factor
$\dot{\gamma}^s$	shear rate of the slip system s
$\bar{\dot{\gamma}}^s$	mean shear rate
$\dot{\gamma}_0$	reference shear rate
τ_c^s	critical resolved shear stress of the slip system s
τ^s	shear stress of the slip system s
$\bar{\tau}^s$	mean shear stress
ϕ_1, Φ, ϕ_2	rotation angles about Z, X and Z axis respectively (three Euler angles)
R	transformed orientation matrix
R^{rot}	incremental rotation matrix
α	rotation angle in each incremental step
Δt	incremental step
f_{tw}	the volume fraction of the twinning region
f_{tw}^s	the volume fraction of twinning accumulated by slip system s
$Ns - t$	the number of slip systems in the twined region
Ns	the number of slip systems in the untwined region
Ntw	the number of twinning systems in the untwined region
γ^{tw}	the shear strain of the twinning system
$\boldsymbol{S}$	the deviatoric Cauchy stress tensor

$\boldsymbol{S}^{tw}$	twined deviatoric Cauchy stress tensor
$\boldsymbol{S}^{untw}$	untwined deviatoric Cauchy stress tensor
Δf_{tw}^{s}	transferred volume fraction of twinning
$\mathbf{c}^{s}$	dislocation climb tensor
$\boldsymbol{\chi}^{s}$	dislocation gliding direction
$\mathbf{t}^{s}$	the direction along the dislocation line
ψ'	the angle between the dislocation coordinate system and the slip coordinate system
τ_{climb}^{s}	shear stress of dislocation climb
Q^{s}	the symmetric part of $\mathbf{c}^{s}$
$\dot{\beta}^{s}$	climb strain rate
$\bar{L}$	velocity gradient of the aggregate
R'	total number of relaxations
K^{r}	relaxation modes
$\dot{\gamma}_{r}^{rlx}$	a free variable
D	local plastic strain rate
$\bar{\mathrm{D}}$	macroscopic plastic strain rate of the aggregate
S	local deviatoric Cauchy stress
$\bar{\mathrm{S}}$	macroscopic deviatoric Cauchy stress of the aggregate
M	local fourth-order visco-plastic compliance tensors

$\bar{\mathrm{M}}$	macroscopic fourth-order visco-plastic compliance tensors
D_0	back-extrapolated terms for the single grain
$\bar{\mathrm{D}}_0$	back-extrapolated terms for the bulk
$\widetilde{\mathrm{M}}$	interaction tensor
$\bar{\mathrm{M}}^{\mathrm{secant}}$	macroscopic visco-plastic compliance tensor for the Secant case
$\mathrm{n}^{\mathrm{eff}}$	interaction parameter
$\dot{\varepsilon}^{p}$	plastic strain rate
$\dot{\varepsilon}^{d}$	strain rate contributions from dislocation glide
$\dot{\varepsilon}^{coble}$	strain rate contributions from Coble creep
P	Gaussian distribution function
$\boldsymbol{\sigma}$	deviatoric Cauchy stress tensor of one grain
V	distribution variance
v^{s}	average velocity of dislocations travelling between obstacles
λ^{s}	mean spacing for dislocations to travel between obstacles
t^{s}	mean time for dislocations to travel between obstacles
t_{t}^{s}	the average time travelling within the free spacing
t_{w}^{s}	the average time a dislocation spends waiting at an obstacle before the bypass

$\lambda_{p,cell}^{s}$	mean free path for dislocation-dislocation interaction
$\lambda_{\rho,cell}^{s}$	mean free path for dislocation-obstacle interaction
N_p^{cell}	number density of the precipitates inside the cell
N_p^{cw}	number density of the precipitates on the cell wall
D_p^{cell}	mean size of the precipitates inside the cell
D_p^{cw}	mean size of the precipitates on the cell wall
C_s	shear wave velocity
P_ρ	probability for a moving dislocation encounter the other dislocations
$t_{w,\rho}^{s}$	waiting time for a moving dislocation encounter the other dislocations
$t_{w,p}^{s}$	waiting time for a moving dislocation encounter the the precipitates
ΔG_i^s	activation energy for the dislocation ($i = \rho$) and precipitate ($i = p$) unpinning process
ρ_0	mass density
h_p	trapping coefficient for $M_{23}C_6$ precipitate
ρ_{cell}^{s}	initial cell dislocation density for each slip system
ρ_{cw}^{s}	initial cell wall dislocation density for each slip system
$\alpha^{ss'}$	latent hardening matrix
$\Delta G_{0,\rho}$	zero stress activation energy for dislocations

$\Delta G_{0,p}$	zero stress activation energy for precipitates
p	exponent parameter
q	exponent parameter
T	temperature
τ_0	lattice frictional stress
τ_ρ^s	dislocation hardening on slip system s
τ_p	precipitation hardening on slip system s
τ_{ss}	solid solution hardening
υ_p	attack frequency for precipitation obstacles
χ	entropy factor
$\dot{\rho}_{cell,gen}^s$	generation of dislocation density
$\dot{\rho}_{cell,ann}^s$	annihilation of dislocation density
$\rho_{cell,trap}^s$	dislocation density trapped in cell wall
k_1	material constant
k_2	material constant
n_0	annihilation strain rate sensitivity
$\dot{\varepsilon}^0$	reference strain rate
f_{re}	dynamic recovery parameter
D	grain size
D_{sub}	sub-grain size

α_{gb}	constant
δ_{gb}	grain boundary thickness
Ω	atomic volume
D_{gb}	grain boundary diffusion coefficient
$D_{gb,0}$	pre-exponential factor
Q_{gb}^{f}	vacancy formation energy on the grain boundary
Q_{gb}^{m}	vacancy migration energy on the grain boundary
A_{Coble}	Coble creep parameter
Q_{gb}	activation energy for grain boundary diffusion
β	constant
$\dot{\varepsilon}_{GBS}$	creep rate caused by grain boundary sliding
$\mathbf{\Gamma}$, $\mathbf{\Gamma}^{s}$	fourth order interaction tensor
$\mathbf{A}^{\mathrm{t}}$, $\mathbf{A}^{\mathrm{s}}$	fourth order tensor represents tangent/secant modulus of the polycrystals
$M^{(r)}$	visco-plastic compliance
$\dot{\varepsilon}^{0(r)}$	back-extrapolated term of grain r
$\dot{E}^{0}$	macroscopic back-extrapolated term
$\dot{\varepsilon}^{*}(\bar{x})$	eigen-strain-rate field
$\tilde{u}(\bar{x})$	velocity gradient vector
$\mathrm{f}_i(\bar{x})$	fictitious volume force

$B^{(r)}, b^{(r)}$	localization tensors
u_x	displacement along x axis
u_{disp}	displacement input
u_y	displacement along y axis
u_z	displacement along z axis
$\boldsymbol{C}$	stiffness tensor
n_{HAGB}	pixel numbers for high angle grain boundaries
n_{LAGB}	pixel numbers for low angle grain boundaries
η	scaling coefficient
ϕ	plastic potential
σ_{eq}	equivalent stress
$\bar{\sigma}$	updated flow stress
σ_{kk}	hydrostatic stress
f^*	porosity
q_1, q_2	constants
$\overline{D}$	damage factor
f	porosity term
$h(\psi)$	geometry factor for relating void radius to volume
ψ	the angle of the void surface with respect to the grain boundary at their intersection

$\tilde{n}_i$	void population number density
a_i	voids population's collective void radius
a_c	critical void size
$\tilde{n}_0$	number density of newly nucleated voids
$\tilde{n}_{0\to a_c}$	number density of newly nucleated voids
$\tilde{n}_{a\to a^*}$	the number density of voids have grown
$\tilde{n}_i^{\varepsilon}$	number densities of voids nucleated from strain
$\tilde{n}_i^{\sigma}$	number densities of voids nucleated from stress
F_i	cumulative distribution functions of the number densities of voids which induced by strain
K_i	cumulative distribution functions of the number densities of voids which induced by stress
R_{ε}	proportion of the nucleation of voids which induced by strain
$\tilde{n}_{sat}$	total number density of latent nucleation sites
ε_c	critical nucleation strain of void nucleation
σ_c	critical nucleation stress of void nucleation
σ_y	yield stress
V_{ε}	statistical variance in nucleation strain
V_{σ}	statistical variance in nucleation stress
$\dot{a}_i^{vp}$	visco-plasticity induced void growth

a_i^d	diffusion induced void growth
α_n	creep expansion constants
β_n	creep expansion constants
n_h	hardening exponent
D_d	diffusivity term along the grain boundary
σ_n	local stress resolved in the direction vertical to the grain boundary
f_{adj}	adjusted porosity term
σ_s	sintering stress
γ_s	free surface energy
L	characteristic material length scale term
K	constant
L_0	constant
n_L	exponent factor
T_m	melting temperature
f_c	critical porosity magnitude
κ	coalescence effect factor
f_f	magnitude of porosity when the material is at failure
$\bar{\tau}_D^s$	resolved shear stress with damage effect
$\dot{\varepsilon}_D^p$	plastic strain rate with damage effect

Abbreviations

The ensuing table elucidates the explications of abbreviations and acronyms employed throughout the dissertation. Additionally, the corresponding chapter number in which each abbreviation or acronym is initially introduced or defined is presented. Notably, any atypical acronyms utilized to abbreviate the names of specific terminologies in certain sections are not included in this tabulation.

AM	additive manufacturing	Chapter 1
AMed	additive manufactured	Chapter 1
AM-H	additive manufacturing horizontally built	Chapter 3
AM-V	additive manufacturing vertically built	Chapter 3
BCC	body centred cubic	Chapter 2
CP	crystal plasticity	Chapter 1
CP-FEM	crystal plasticity finite element method	Chapter 1
CP-FFT	crystal plasticity fast Fourier transform	Chapter 2
CRSS	critical resolved shear stress	Chapter 2

DED	direct energy deposition	Chapter 2
EBSD	electron backscatter diffraction	Chapter 1
EBM	electron beam melting	Chapter 2
FCC	face centred cubic	Chapter 2
FE	finite element	Chapter 2
GBS	grain boundary sliding	Chapter 2
GTN	Gurson-Tvergaard-Needleman	Chapter 3
HAGBs	high angle grain boundaries	Chapter 1
HCP	hexagonal close packed	Chapter 2
HEM	homogeneous effective medium	Chapter 1
HMS	hierarchical multi-scale	Chapter 1
LAGBs	low angle grain boundaries	Chapter 1
LMD	lase metal deposition	Chapter 2
LPBF	laser-sourced powder bed fusion	Chapter 2
MD	molecular dynamics	Chapter 3
PBF	powder bed fusion	Chapter 2
PTR	predominant twin reorientation	Chapter 2
RVE	representative volume element	Chapter 3
SFE	stacking fault energy	Chapter 2
SLM	selective laser melting	Chapter 2

SLS	selective laser sintering	Chapter 2
SS	stainless steel	Chapter 1
VPSC	visco-plasticity self-consistent	Chapter 1

Chapter 1 Introduction

1.1 Motivation

1.1.1 Hierarchical multi-scale (HMS) modelling

Numerical experimental observations have proven that, apart from the effects of service environment or loading conditions, the behaviour of materials is greatly dependent on their own characteristic microstructure. According to the microstructural features, the existence of corresponding micro-mechanisms is crucial to define the mechanical behaviour of materials. Hence, there is a need to quantify and describe the detailed deformation mechanisms to understand the mechanical properties, and eventually, offering feedback to materials design and fabrication strategies.

Hierarchical multi-scale (HMS) modelling is a computational technique, which can break down the whole system into multiple scales of interactions. In materials science studies, by modelling each scale and linking them together, researchers can describe the mechanical behaviour of the complex comprehensively. Through this approach, the information from multiple scales, e.g. atomic scale, micro-scale, meso-scale and macro-scale, are incorporated into a single model. In addition, the mechanisms underlying the emergence of these material properties through multi-scale interactions will be unveiled.

1.1.2 Additive manufacturing of metallic

Metallic powder bed fusion additive manufacturing (AM) techniques are capable of fabricating components with complex geometries while preserving the material properties. Such advantage makes it attract increasing attention from several manufacturing industries, i.e. aerospace, automotive, nuclear energy and medical devices. AM products usually serve as key components in the above industries, which are required to possess advanced mechanical properties such as high toughness, long fatigue life, and the capability to withstand extreme service conditions. As such, there is a worldwide need for material and process design methods to improve the quality of AM products.

AM is a complex process - many factors need to be considered in the material design and processing strategies. Due to a lot of uncertainties during the additive manufacturing (AM) processes, there is a requirement for both process and materials design to stabilize and optimize the AM products quality. Therefore, trial-and-error approaches cannot be employed. Moreover, AM materials are well-known for their unique heterogeneous microstructure. Therefore, addressing the detailed processing-structure-property-performance (PSPP) relationships is critical to understand the coupled effects of the chemistry and AM processing factors on the material properties, which is deemed to be the pathway to achieve the desired product. In this case, HMS crystal plasticity modelling is an ideal method to link the AM-induced sophisticated microstructure and the corresponding mechanical properties.

1.2 Objectives

The development of a Hierarchical Multi-Scale (HMS) modelling framework is the main aim of this project. This framework is capable of capturing and evaluating the effects of deformation mechanisms effectively, as a function of microstructure, to guide future microstructure-tailoring for AM materials.

1.2.1 A unified model for wrought and additive manufactured materials

The first objective is to develop a mechanism-based unified model for both wrought and additive manufactured (AMed) materials.

AM-characterised microstructure and the resultant unusual mechanical properties benefits from the extremely high cooling rate and cyclic thermal history. Compared to the wrought material, the AM material is non-equilibrium. Even though, for the same chemical composition products, the deformation mechanisms and hardening principles are exactly the same. Therefore, the classic deformation formulations are still applicable to describe the creep behaviour of both wrought and AM materials. The difference between wrought and AM materials will be highlighted by microstructure parameters, e.g. dislocation densities (inside the cell and on the cell wall), grain size, sub-grain size, precipitation size and number density etc.

1.2.2 Visco-plasticity self-consistent framework

The proposed mechanism-based unified model for both wrought and AM materials is firstly embedded into the visco-plasticity self-consistent (VPSC) framework to capture the primary state and secondary state of creep behaviour.

VPSC is an intermediate approach which can consider each grain in the polycrystal as a visco-plastic inclusion embedded in a homogeneous effective medium (HEM) (Lebensohn et al., 2007; Lebensohn and Tomé, 1993). The properties of the entire aggregate are taken into account concurrently. According to the orientation of each grain, the local interaction between each grain and HEM are determined. In this way, the texture-related intergranular stress/strain response is included in this mean-field framework. Through the simulation under the VPSC framework, the primary and secondary states of creep behaviour are validated. More details will be introduced in Chapter 2.

1.2.3 Crystal plasticity finite element method framework

The developed mean-field framework is transferred into the crystal plasticity finite element method (CP-FEM) framework to solve the tertiary state creep deformation. The mechanistic damage model is embedded into the full-field framework. The grain boundaries of polycrystals are assumed to be the source of damage. Apart from the dislocation densities, precipitation evolution, and stress/strain distribution, the void evolution is also tracked at different length/time scales. Moreover, the time-dependent visualised outputs are generated through ParaView, which is is an open-source, cross-

platform data visualization and analysis software widely used in scientific and engineering domains.

Both of VPSC and CP-FEM are based on the crystal plasticity (CP) theory, which will be introduced in Chapter 2 in detail.

1.2.4 Additive manufacturing characterised microstructure study

Analysing the AM-induced unique microstructure with pores and elongated grains resultant effects on materials creep behaviour. By introducing a bias, the microstructures decorated with differently elongated grains are generated randomly through Voronoi diagram principle. Various types of AM-characterised pores are inserted via assigning different sizes, shapes and locations of pores manually inside the microstructure. This microstructure study is processed under CP-FEM framework, which is aiming to investigate the relationship between characterised structure and creep behaviour, especially the damage behaviour. The input parameters for artificially generated microstructure simulations are inherited from the real AM materials, through which can preserve the original AM materials features. In addition, the boundary condition for pores is the same as the boundary condition for the whole structure. The stress/strain concentration is analysed around the pore.

1.3 Approaches and tools

The numerical simulations are employed in this project to capture and predict the mechanical behaviour of materials under various conditions (temperature and external loading).

1.3.1 Generation of input

DREAM. 3D software is commonly used to extract the microstructure information from electron backscatter diffraction (EBSD) raw data. DREAM.3D encompasses a collection of data analysis tools referred to as "Filters," which facilitate the creation of tailored analytical processes known as "Pipelines" for data examination. Notably, DREAM.3D presents a versatile and expandable data framework that facilitates seamless data exchange among collaborators by employing a non-proprietary data

format for data storage. 3D Reconstruction of EBSD data from EDAX (.ang), Oxford (.ctf) and Bruker (.ctf) data files. The reconstructions can utilize an array of alignment, cleaning, segmentation algorithms and colouring algorithms.

MATLAB is a widely recognized software environment renowned for its powerful computational capabilities in academic and scientific research. It provides a comprehensive set of tools for numerical analysis, data visualization, and algorithm development. With its user-friendly interface and extensive library of functions, Its graphical capabilities also aid in data interpretation and communication. In this project, MATLAB is used to present the microstructure based on three Euler angles of each material point and generate the input file. The high angle grain boundaries (HAGBs) are classified if the misorientation is greater than 15^{o}, while low angle grain boundaries (LAGBs) are characterised by a misorientation between 2^{o} to 15^{o}.

In order to customise the microstructure with differently elongated grains and collect full information from the generated structure. A self-developed Voronoi diagram code is adapted for random microstructure generation.

A pore indicator for each node is employed under CP-FEM framework to assign the pore location. By minimising the stiffness, the nodes assigned as pores are distinguished.

1.3.2 Commercial software package

The VPSC 7D written in Fortran is conducted through MATLAB 2022a software. The VPSC framework is originally developed by Tome and Lebensohn (Tome and Lebensohn, 2023). The CP-FEM written in C++ has been conducted through FreeFem++ (4.6) open-source FE solver, which is originally developed by Bieberdorf et al. (Bieberdorf et al., 2021).

1.4 Outline of the thesis

The outline of this thesis is as follows:

Chapter 1 Introduction: a summary of this project, which includes the motivation of this research, the main aim, and the methods used to achieve the aim. Moreover, the importance of the development and application of the HMS modelling is addressed.

Chapter 2 Literature review: reviews the characteristics of AM-produced materials, especially 316L stainless steel (SS). The deformation mechanisms and hardening mechanisms in metallic materials are summarised. The single-crystal and polycrystal modelling techniques adopted to capture the mechanical behaviour of materials are reviewed.

Chapter 3 A physics-based model to study plasticity under the VPSC and CP-FEM frameworks: introduces the simulation-targeted materials and experimental data. The unified physics-based CP model for both AM and wrought materials is described in detail. The employed frameworks: mean-field VPSC and full-field CP-FEM are introduced, including their principles, formulations, numerical algorithms, and implementations.

Chapter 4 Application of physics-based model in comparison of AM and wrought 316L stainless steel high-temperature thermal behaviours: both the AMed and wrought materials creep behaviour are simulated and compared under the VPSC framework based on the physics-based crystal plasticity model proposed in Chapter 3. The dominant deformation mechanisms in wrought and AMed materials are illustrated and quantified. The different roles of grain and sub-grain sizes are revealed, which can give feedback to the material design.

Chapter 5 Microstructurally sensitive creep damage law for polycrystalline material systems: application of the physics-based crystal plasticity model combined with GTN damage model, capturing the tertiary stage creep of AM materials under CP-FEM framework. The horizontally-built and vertically-built AMed sample damage behaviour is compared. The relation between the grain boundary orientation and loading direction is clarified: the damage prefers to accumulate on the grain boundaries that are perpendicular to the loading directions.

Chapter 6 AM microstructural related creep behaviour study: the AM-induced unique microstructures: elongated grains are generated according to the principle of the Voronoi diagram, and pores with specific sizes and shapes are created manually and added into the EBSD input file. A bias is introduced to achieve the microstructure with differently elongated grains. While the investigation of grains morphology effects on

materials creep behaviour is based on the artificially generated microstructure, real EBSD data is used as an input with manually added pores for pores study.

Chapter 7: Summarises the key findings, discusses the findings of the research, and offers conclusions based on the work provided in the thesis. The primary research contributions of this thesis are then presented. Following that, it discusses the existing limits of the suggested methodologies and offers potential directions for further investigation.

Chapter 2 Literature Review: Polycrystal modelling and additive manufactured metal materials

In this chapter, a literature review of the main features of Additive Manufacturing (AM) of metal techniques, the AM-induced microstructural characters, especially the AM 316L SS, the mechanisms of metals deformation and the application of Crystal Plasticity Finite Element Method (CP-FEM) are provided.

2.1 Additive manufacturing technique

Since 1973, Pierre Ciraud (Ciraud, 1973) originally applied the patent for manufacturing any fusible materials by high-energy beams, the development of Additive Manufacturing (AM) has derived into a range of methods. According to the ASTM technical committee, there are seven kinds of AM processes, which include powder bed fusion (PBF), direct energy deposition (DED), binder jetting, material

jetting, Vat photopolymerization, material extrusion, and sheet lamination (Standard, 2012). The PBF, DED, binder jetting, material jetting, and sheet lamination processes are normally used for metal materials (Tapia and Elwany, 2014). Especially for PBF and DED are the most common metal-based AM techniques, which have been extensively studied. PBF is a powder bed-based AM process, and based on the different heat sources, it can be divided into Selective Laser Melting/Sintering (SLM/SLS) and Electron Beam Melting (EBM). According to their names, it can be told the former utilises the laser beam as heat input, while the latter employs the electron beam as an energy source (Kruth et al., 2007). As for powder-fed AM technology, the most used DED process is Laser Metal Deposition (LMD) (Herzog et al., 2016).

The schematic examples of SLM and DED processes are shown in Figure 2. 1. Both SLM and DED processes melt the powders layer by layer and print in cycles. Each layer is bounded by melting and remelting between a specific thickness of metal powder. The SLM is only able to process the printing in a single direction, while the DED can be equipped with 5+ axis systems to achieve multiple directions printing, which enables the printing process more flexible.

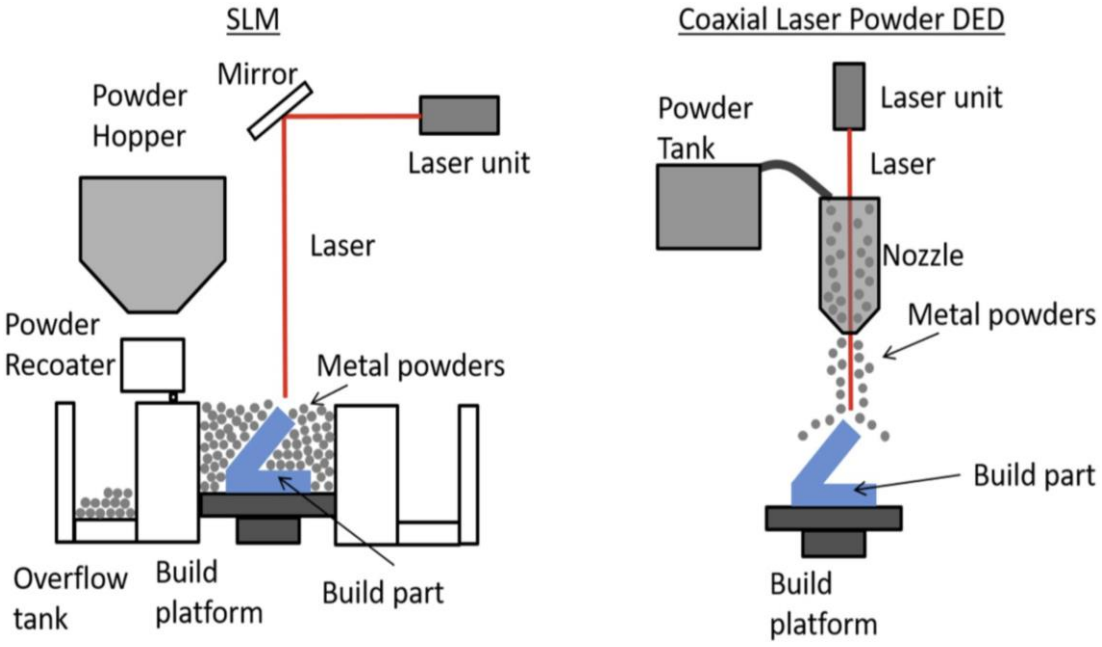

Figure 2. 1 Schematic of selective laser melting (SLM) and directed energy deposition (DED) processes (Tan et al., 2020).

Compared with laser-sourced PBF (LPBF), EBM can provide higher energy input and density, which means the EBM process is more efficient. Moreover, the high energy density and efficiency also result in a less obvious scanning track than LPBF products (Luo and Zhao, 2018). As the powder bed can be preheated up to 900 ℃ in the EBM process, the residual stress is greatly released under as-built conditions (Murr et al., 2012; Wang et al., 2018a). However, EBM is also more complex compared to LPBF, since more process parameters need to be adjusted (Ghaoui et al., 2020).

The AM-characterised metallic microstructure shows elongated columnar grains along the building direction, and the cross-section perpendicular to the building direction is decorated with equiaxed grains. The uneven grain distribution enables AM products great anisotropy. Moreover, by varying the printing parameters, the resulting as-built material microstructure and mechanical properties will vary as well. However, experimentation on different printing parameters for various materials is cost- and time-consuming, and the trial-and-error method is not applicable anymore. Therefore, numerical simulations with high fidelity are needed to acquire insight and understanding of AM-characterised microstructures, and predicted the corresponding mechanical behaviour.

2.1.1 Defects in the additive manufacturing process

Although the AM-characterised materials show advanced mechanical properties compared to traditionally fabricated materials. There are defects introduced by AM process, which are detrimental to the mechanical behaviour of materials. Lack of fusion, keyhole, balling, gas entrapment porosity, and cracks are the most common and discussed defects in AM materials (Cunningham et al., 2017; Khairallah et al., 2016a; King et al., 2014; Seifi et al., 2016; Snow et al., 2020; Zhang et al., 2017). Figure 2. 2 shows the different types of defects in AM products.

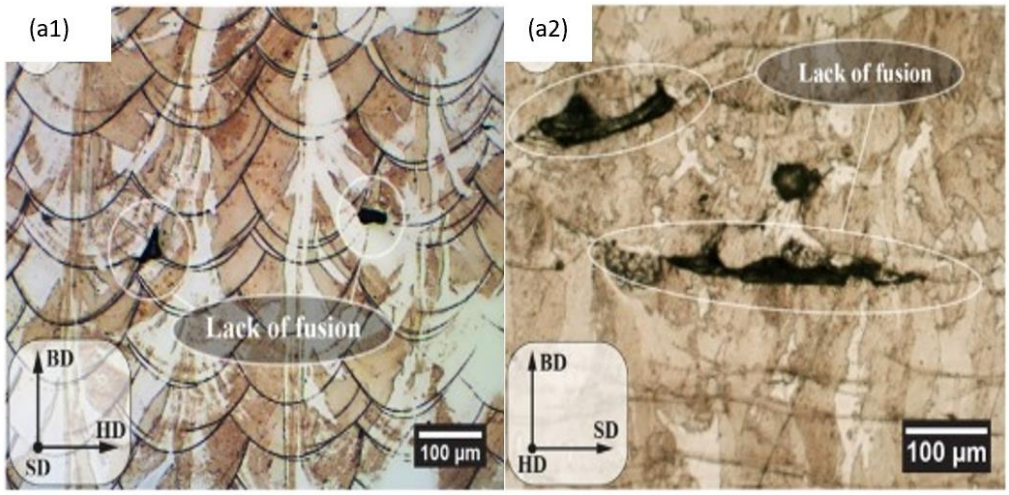
(a1)
Lack of fusion
BD
HD
SD
100 μm
(a2)
Lack of fusion
BD
SD
HD
100 μm

(a)

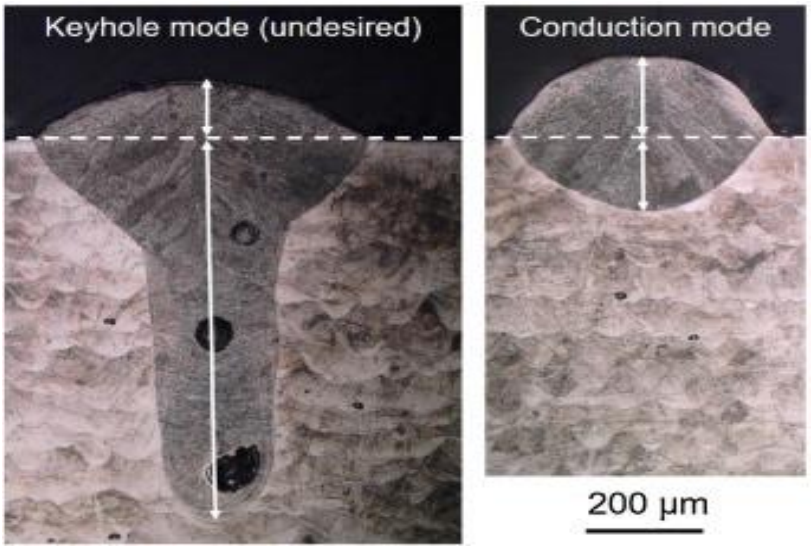
Keyhole mode (undesired)
Conduction mode
200 μm

(b)

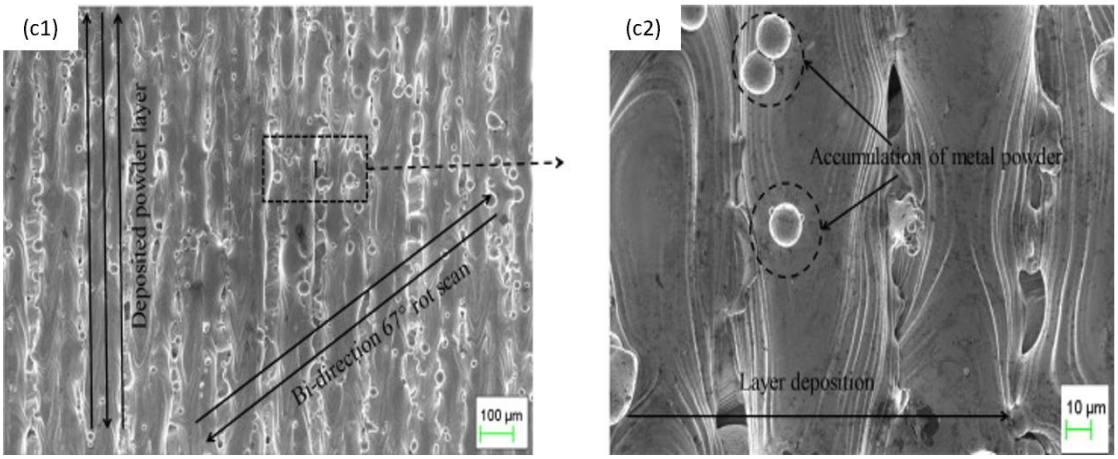
(c1)
Deposited powder layer
Bi-direction 67° rot scan
100 μm
(c2)
Accumulation of metal powder
Layer deposition
10 μm

(c)

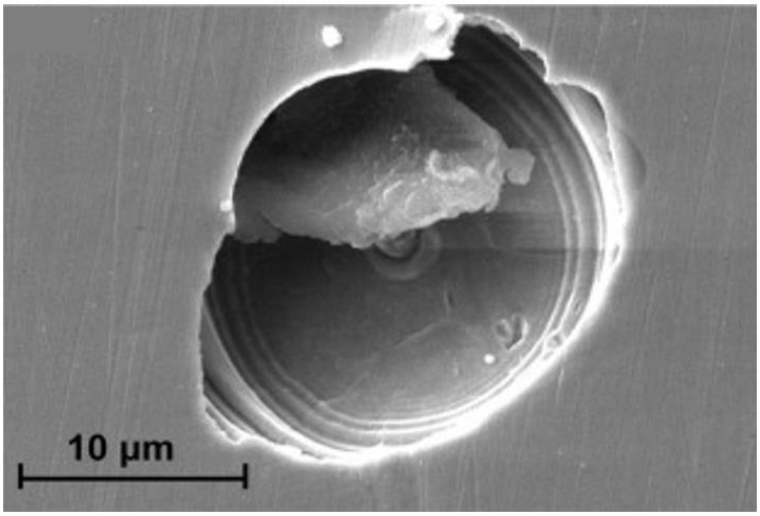

(d)

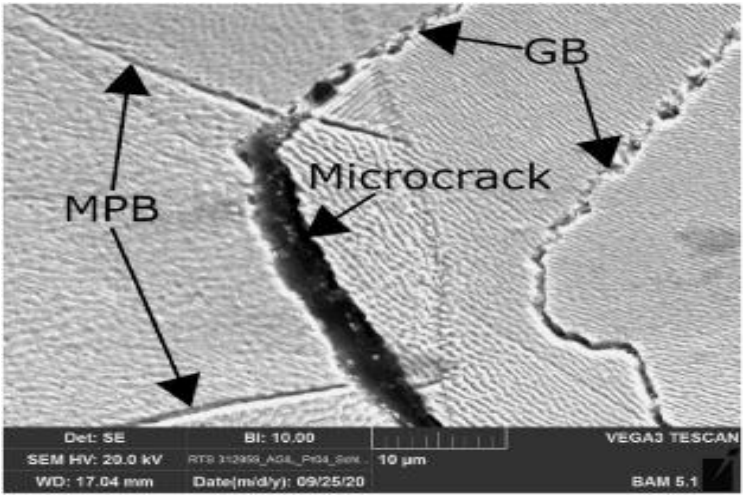

(e)

Figure 2. 2 (a) Lack of fusion defects (BD-building direction, SD-scan direction, and HD-hatch direction) (Ronneberg et al., 2020); (b) Keyhole defects (Metelkova et al., 2018); (c) Balling effects (Dwivedi et al., 2022); (d) Gas entrapment defect (Zhang et al., 2021b); (e) Hot cracking, GB-grain boundaries, and MPB-melt pool boundaries (Ávila Calderón et al., 2022).

The lack of fusion pores normally exist in non-sintered area or delamination, which can be observed both horizontally and vertically around the melting pool boundaries. Figure 2. 2 (a) shows the lack of fusion defects that appear at layer-layer melting pool boundaries and track-track junctions, and are elongated by the layer-layer pool boundaries. This phenomenon is because of insufficient overlap areas during the AM process, which are also accompanied by unmelted particles. The size of lack of fusion

type defect can range from 15-600 μm with irregular shape (Carlton et al., 2016; Mertens et al., 2014; Pham et al., 2017). This kind of sharp shape can result in stress and strain concentration, which is destructive to material properties. The anisotropic ductility and failure are found dominated by lack of fusion type defects (Ronneberg et al., 2020). In addition, the sharp area can also work as pre-cracks in dynamic loading (Wilson-Heid et al., 2019; Zhang et al., 2017). The occurrence of lack of fusion is attributed to insufficient energy input, which is related to the AM printing parameters. Adjusting hatching space, laser energy and scanning speed can effectively prevent it. Metelkova et al. studied in AMed SS316L by adjusting the hatch spacing to adjust the overlapping between two adjacent melting pools, the lack of fusion can also be avoided (Metelkova et al., 2018). In addition, the lack of fusion area is also companied by unmelted or partially melted powder particles (Sanaei and Fatemi, 2021).

Opposite to the lack of fusion, the keyhole is the defect resulting from excessive energy input. Originally, it is called “keyhole mode” in laser welding (Rai et al., 2007). It is characterised by a keyhole-like shape, and the depth can achieve to ~300 μm depending on the input energy (King et al., 2014; Metelkova et al., 2018; Trapp et al., 2017). Trapp et al. studied the influence of the combination of laser power and scanning speed on keyhole formation during the AM process of 316L SS (Trapp et al., 2017). Moreover, the over-heating can not only lead to keyhole pores, but the evaporation of alloying elements with lower boiling points such as Mn, Cr, and Ni, and even the formation of plasma in SS316L (King et al., 2014; Sabzi et al., 2020b). Figure 2. 2 (b) shows the classic keyhole shape with deep penetration, whose depth is also determined by the conduction of heat in the underlying solid materials (King et al., 2014).

As for balling-type interior pores, it is caused by a non-stabilised melting pool (spheroidization of the liquid melting pool), which is a result of both low- and high-energy inputs (Kruth et al., 2004). For capillarity caused non-stabilised melting pool, the powder particles lack proper wetting, which can lead to discontinuity in materials (Sanaei and Fatemi, 2021). The remelting of each layer can stimulate the microstructure evolution, therefore, reduce the balling effect (Bejan and Kraus, 2003; Frewin and Scott, 1999). The formation of discontinuous scanning tracks and poor inter-line bounding in as-built AM materials causes the degradation of mechanical properties. Moreover, the

subsequent layers of power are harder to spread uniformly. With different printing parameters, the balling-induced pores size in AM SS316L can range from 10-50 μm (Cherry et al., 2015; Gu and Shen, 2009). Field emission scanning electron microscopy (FESEM) of balling defects is shown in Figure 2. 2 (c) with magnified view.

Excessive energy can also lead to gas entrapment, as shown in Figure 2. 2 (d), whose size is normally around several microns in 316L SS. The effect of gas entrapment on the mechanical properties of materials is negligible compared to the other types of pores (Ávila Calderón et al., 2022; Sabzi et al., 2020b). The high energy input can dissolve the shielding gas or entrap it, as the vapour recoil in the melt pool does not have enough time to escape with rapid solidification rates (Yadollahi et al., 2015; Zheng et al., 2008). Moreover, the spherical shape makes entrapped gas pores have less strain/stress concentration. Ávila Calderón et al. suggested that the gas pores do not play a main role in the damage evolution of 316L SS creep behaviour (Ávila Calderón et al., 2022).

Due to the high cooling rate during the AM process, the resulting significant residual stress can lead to cracks in as-built products through solidification shrinkage and thermal contraction (Dwivedi et al., 2022; Hyer et al., 2021; Khairallah et al., 2016a; Laleh et al., 2019; Mirkoohi et al., 2020a). This kind of phenomenon is also called solidification cracking or hot cracking, which is shown in Figure 2. 2 (e). Hot cracking is the only crack type in AMed austenitic stainless steels (Sabzi et al., 2020b). Apart from the extremely high cooling rate, the solidification temperature range and solid fraction can also influence the formation of cracks, which are highly determined by the compositions of materials (Böttger et al., 2013; Eskandari Sabzi and Rivera-Díaz-del-Castillo, 2019; Hyer et al., 2021).

The value of residual stress can be measured by neutron diffraction (Grilli et al., 2020; Webster and Wimpory, 2001), X-ray diffraction (Hocine et al., 2020), contour method (Vrancken et al., 2014) and semi-destructive hole drilling method (Martínez-García et al., 2019; Sandmann et al., 2022). The excessive residual stresses can achieve the same magnitude of the material yield strength, which means not only the geometrical dimensions of the as-built AM product can be changed, but the material properties can be influenced (Gu et al., 2012; Williams et al., 2020). The accumulation of residual stress can concentrate on the sharp edge of defects or inclusions, which can be the pre-

crack source during the loading. Apart from optimising the scanning strategy and parameters, there are also additional processes have been used to reduce the residual stress in as-build samples.

As residual stress is highly influenced by the temperature gradient, preheating the powder bed or the substrate can effectively reduce the temperature gradient. Moreover, it has been proven that the preheating temperature is inverse to the residual stress (Ali et al., 2017; Lu et al., 2018; Vastola et al., 2016). Normally, the temperature gradient along the building direction is more significant than along the horizontal direction. This is because the metal powder constrains the heat conduction along the direction vertical to the melting pool. However, when the AM product has a larger size, the preheating is harder to be uniform, which requires localised preheating (Aggarangsi and Beuth, 2006). In addition, preheating is the most promising method for eliminating residual stress, when all the other factors are not considered (Chen et al., 2022). Originally, Hybrid Additive Manufacturing (Hybrid AM) is proposed to enhance the quality of AM products or improve production efficiency. It has been found that Hybrid-AM by remelting, Hybrid-AM by rolling and Hybrid-AM by peening can effectively reduce the residual stress and optimise its distribution (Sealy et al., 2018; Shiomi et al., 2004). Similar to traditionally fabricated materials, the residual stress in AM products can also be released by post-heat treatment. Accordingly, the post-heat treatment is commonly used for LPBF products to release high residual stress. It is reported that the AM-induced residual stress can be eliminated by about 90% by post-heat treatment (Syed et al., 2019). However, the reducing rate of residual stress is also related to the AM products' original state (Tong et al., 2019; Williams et al., 2020). In addition, the heat treatment regime can affect the initial AM-introduced microstructures. In order to preserve the AM characters, the heat treatment regime should be carefully considered for different materials.

2.1.2 Computational simulation of AM process

Respecting reducing the detrimental effects of these defects in the as-built AM products, a range of optimisation strategies have been proposed regarding the printing parameters to enhance printability. The purpose of adjusting printing parameters is to achieve scanning strategy optimisation. The scanning strategy is the heat input path, which does

not only include the single layer scanning, but also the interaction between each layer. Experimental studies can be found in the literature analysing the specific key printing parameters effects on AM products quality (Balit et al., 2020; Hassan et al., 2021; Johnson et al., 2019; Mukherjee et al., 2016; Pagac et al., 2017; Paul et al., 2014; Seede et al., 2020; Vukkum and Gupta, 2022; Wood et al., 2019; Yang et al., 2019). The fundamental strategy is stabilising the properties of the melting pool by adjusting the combination of a range of printing paraments. However, the choice of different printing parameters highly depends on the different alloys, which is aiming for a specific chemical composition. The experimental study can find a printing trend for different scanning strategies, however, which is not necessarily applicable to all the materials. The experiment method is time-consuming and high-cost. Furthermore, computational simulation is needed for a systematic method of validating the materials' printability under diverse printing conditions, which is accompanied by a thermo-mechanical-metallurgical imbalance (Chen et al., 2022; Eskandari Sabzi, 2022).

As shown in Figure 2. 3, based on numerical models, computational simulation is an efficient way to optimise the AM products' quality by considering both the materials' properties and scanning strategies. For instance, Sabizi et al. proposed the criteria of printing strategy to control the shape of the melting pool based on thermodynamic models, which can effectively prevent different types of defects in AM SS316L (Sabzi et al., 2020b). Gu et al. developed a framework modelling the development of a melting pool considering multiple materials upon multi-track and multi-layer (Gu et al., 2020).

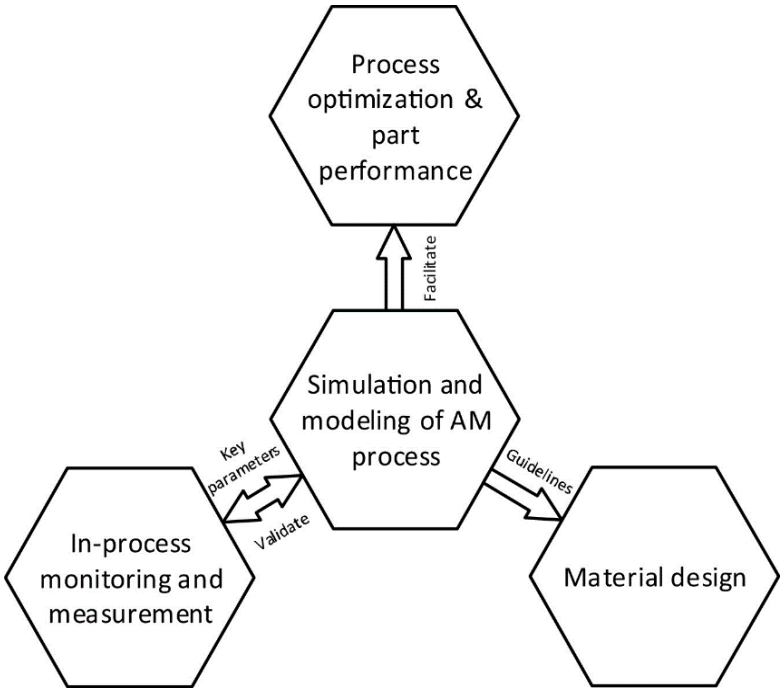

Figure 2. 3 Relationships between AM modelling, simulation and other AM aspects (Luo and Zhao, 2018).

The primary focus of simulating the AM process revolves around modeling the temperature and thermal stress fields (Luo and Zhao, 2018). Typically, the thermal-analysis and mechanical analysis are needed in residual stress simulation formed during the AM process. Length- and time-scale are also coupled in the modelling to enable the multi-scale simulation (Megahed et al., 2016). At the micro-scale, the heat source feedstock interaction, heat absorption and phase changes are considered to model the fluid flow in the melting pool (Ganeriwala and Zohdi, 2014). Meso-scale models are composition- and temperature-dependent, which can provide specific information to micro-scale and macro-scale simulations, e.g. grain and microstructure evolution. For macro-scale modelling, only the dimensions of the heat-affected zone and the thermal cycle are considered for residual stress calculation.

As Finite Element (FE) method is capable of qualitative and quantitative analysis, it is widely used for residual stress simulation induced by thermo-mechanical-metallurgical imbalance (Luo and Zhao, 2018). Meanwhile, it can be coupled with the thermo-mechanical model or crystal plasticity model to deliver more detailed physics meaning.

Apart from physics-based models in melting pool condition simulations, machine learning modelling is also employed to optimise the AM printing parameters. La Fé-Perdomo et al. used statistical modelling combined with machine learning algorithms, which can facilitate the selection of scanning strategies to achieve the expected AM products with specific features (La Fé-Perdomo et al., 2022). Jiang et al. proposed a machine learning integrated design under AM framework, with which, the property-structure relationship is given efficiently (Jiang et al., 2022). The modelling of machine learning is based on various databases, however, which requires numerous experiments. With the development of AM technology, the previous experimental results might be not worthy to reference. Moreover, for the newly designed materials, there might not be enough data to be considered. Therefore, machine learning simulation is not always as applicable as physics-based modelling. On the other hand, the detailed physics model can lead to high simulation costs, and the solution accuracy mainly depends on the computational cost. Furthermore, the tangled complicated physical phenomena cannot always be fully described by the physics model, and the according simplification can cause some discrepancies (Luo and Zhao, 2018).

2.2 Plastic deformation mechanisms in single crystal

2.2.1 Introduction

Polycrystals are the result of the aggregation from a range of single crystals. Similar to single crystal, the dominant plastic deformation mechanisms in polycrystals are slip and twinning. Compared to elastic deformation, plastic deformation is an irrecoverable and permanent distortion. When the materials are undergoing tension, compression, bending, or torsion, which are over the yield strength, plastic deformation will happen. This work targets the multi-scale modelling of materials' mechanical properties. It is crucial to understand the micro-scale deformation mechanisms, and then link them with macro-scale properties.

Figure 2. 4 shows four stages of the stress-strain curve of a single crystal during the elastic and plastic deformations. Notice that, if the external stress is below the critical resolved shear stress (CRSS) value, the material will only exhibit elastic deformation.

The elastic deformation will be shown as a linear relationship on the stress-strain curve, which is also referred to Hooke's law (Soutas-Little, 2012).

Stage 1 - single gliding, which is also called "easy glide", has only one slip system activated. The parallel dislocations of a single slip system all glide in one direction. Moreover, the dislocation can glide without being hindered by dislocations from other slip systems. Due to the accumulation of dislocation debris in the form of dipoles, there can be some work hardening in stage 1 (Alcalá et al., 2015).

The multiplication and interaction of dislocations happen in stage 2 - multiple gliding, which causes the most of work hardening. Apart from the primary slip system in stage 1, another slip system is also operative. Kinks, jogs, locks and pile-ups are formed and interacted by the movement of dislocations on both slip systems. The work hardening rate of this stage is approximately $G/200$. Here, G is the shear modulus, which is generally temperature-dependent (Anand, 2004; Cazacu et al., 2019; Karaman et al., 2001).

Stage 3 is the recovery stage, the crystal is "recovered" from the hampering of the dislocation movement. Due to diffusion, dislocations can spread on different slip planes. The multiple cross slip can be achieved by screw dislocations, while the deformation climbing can be achieved by edge dislocations. Therefore, less stress increment is required for further deformation (Karaman et al., 2001; Svoboda and Lukáš, 1997).

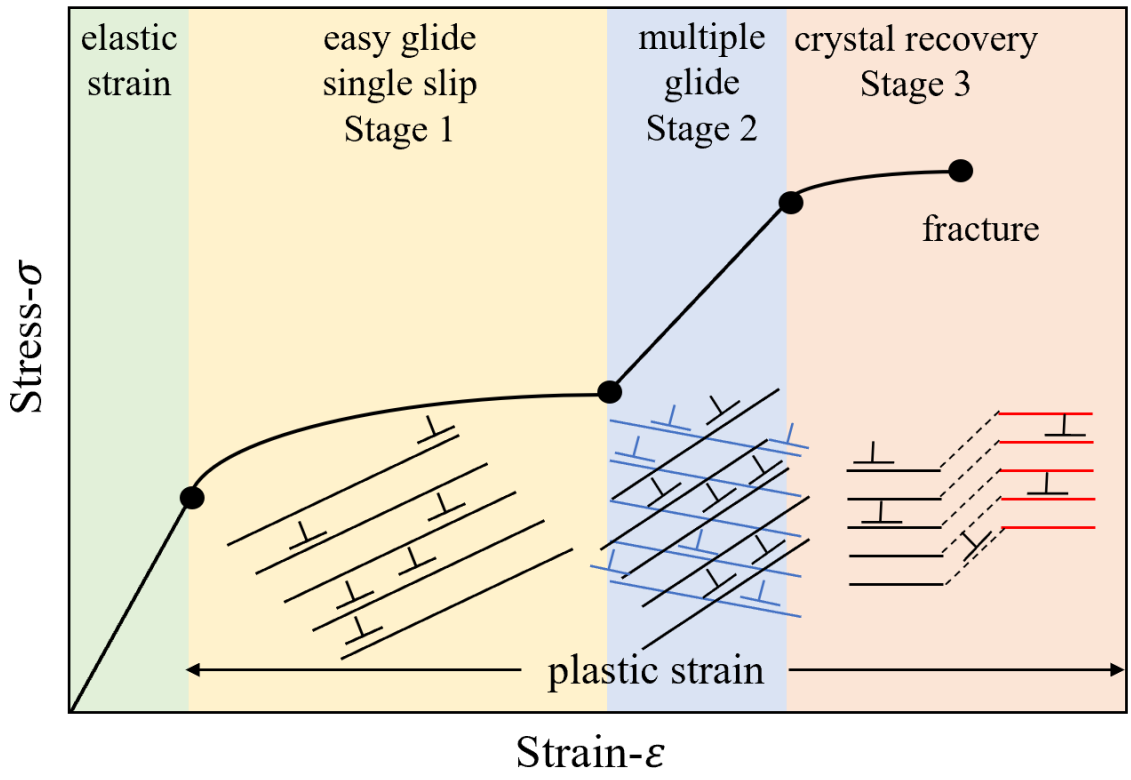

Figure 2. 4 Schematic stress-strain response of single crystal.

2.2.2 Slip

Figure 2. 4 shows the stylised movement of atoms under uniaxial external loading. The atom arrangement is depicted in two dimensions. Compared to Figure 2. 5 (a), the atom distance has changed in Figure 2. 5 (b), which is due to the elastic deformation. At this point, the lattice structure will be back to its original status with unloading. In Figure 2. 5 (c), the displacement of atoms on the specific slip plane along the specific direction is slip. Plastic deformation occurred due to the slip, which is irreversible (Anderson et al., 2017; Dieter and Bacon, 1976; Nabarro, 1979; Wert et al., 1970).

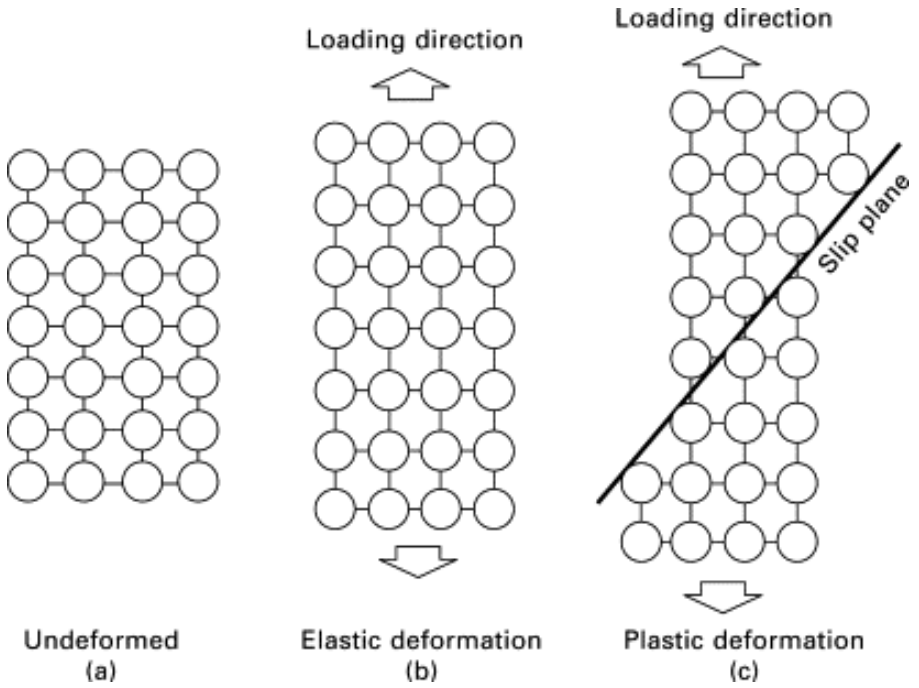

Figure 2. 5 Illustration of slip-caused deformation (Nakano, 2010).

2.2.2.1 Slip systems

Normally, the slip plane is the one that contains atoms most closely packed, while the slip direction is also the one in which the atoms are most closely arranged. As the energies required for the slip to occur on these planes and directions are relatively low, the stable crystal structure is less broken down (Nakano, 2010). For different lattice structures, the slip systems consisted of slip planes and slip directions are different.

As shown in Figure 2. 6, the face-centred cubic (FCC) crystals contain 12 slip systems, which occur on [111] planes along <110> directions. The body-centred cubic (BCC) crystals, which are shown in Figure 2. 7, can contain up to 48 slip systems. The slip in BCC structure occurs on: 1) [110] planes along <111> directions; 2) [123] planes along <111> directions; 3) [112] planes along <111> directions. The hexagonal close-packed (HCP) crystals has limited slip systems, which normally happens on [0001] planes along $<11\bar{2}0>$ directions. Figure 2. 8 shows the typical slip systems of the HCP structure.

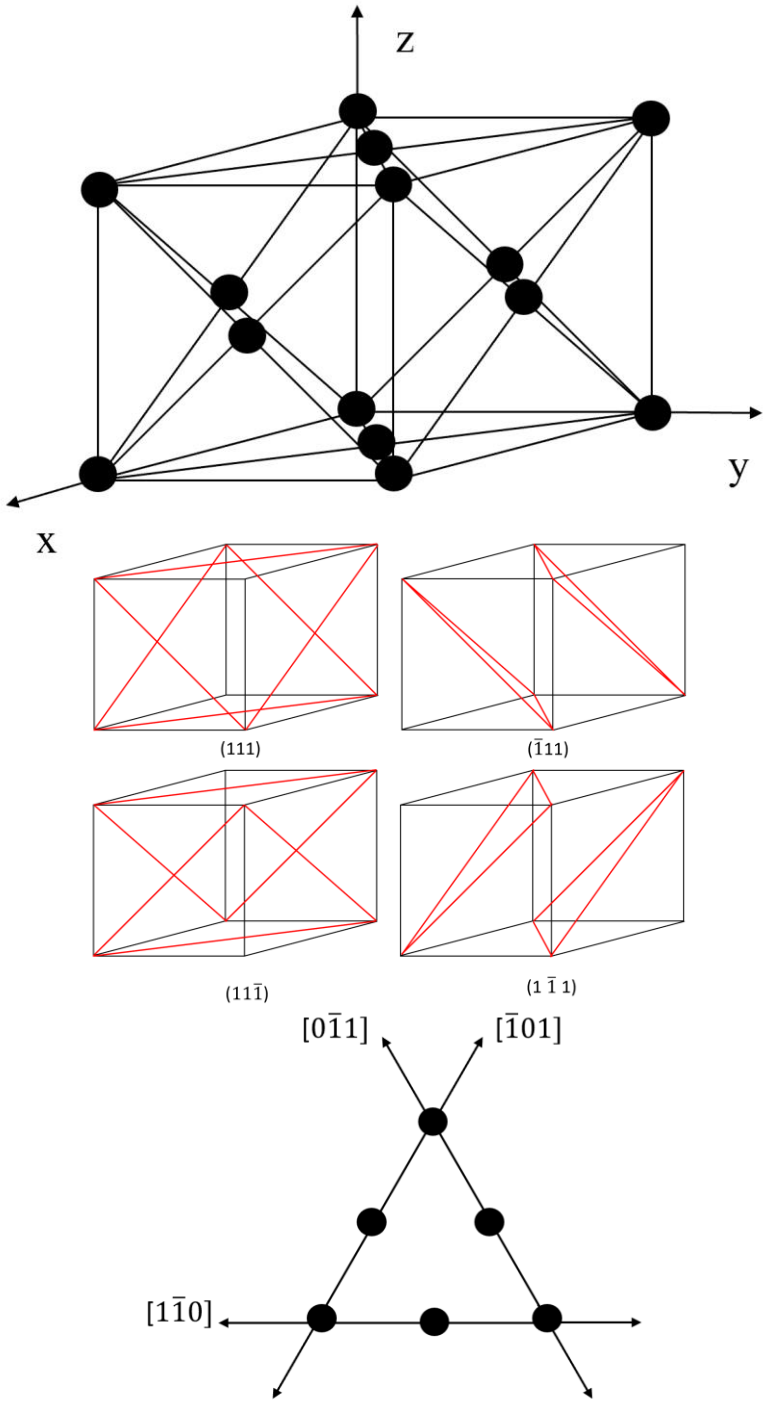

Figure 2. 6 FCC structure and slip planes in FCC structure.

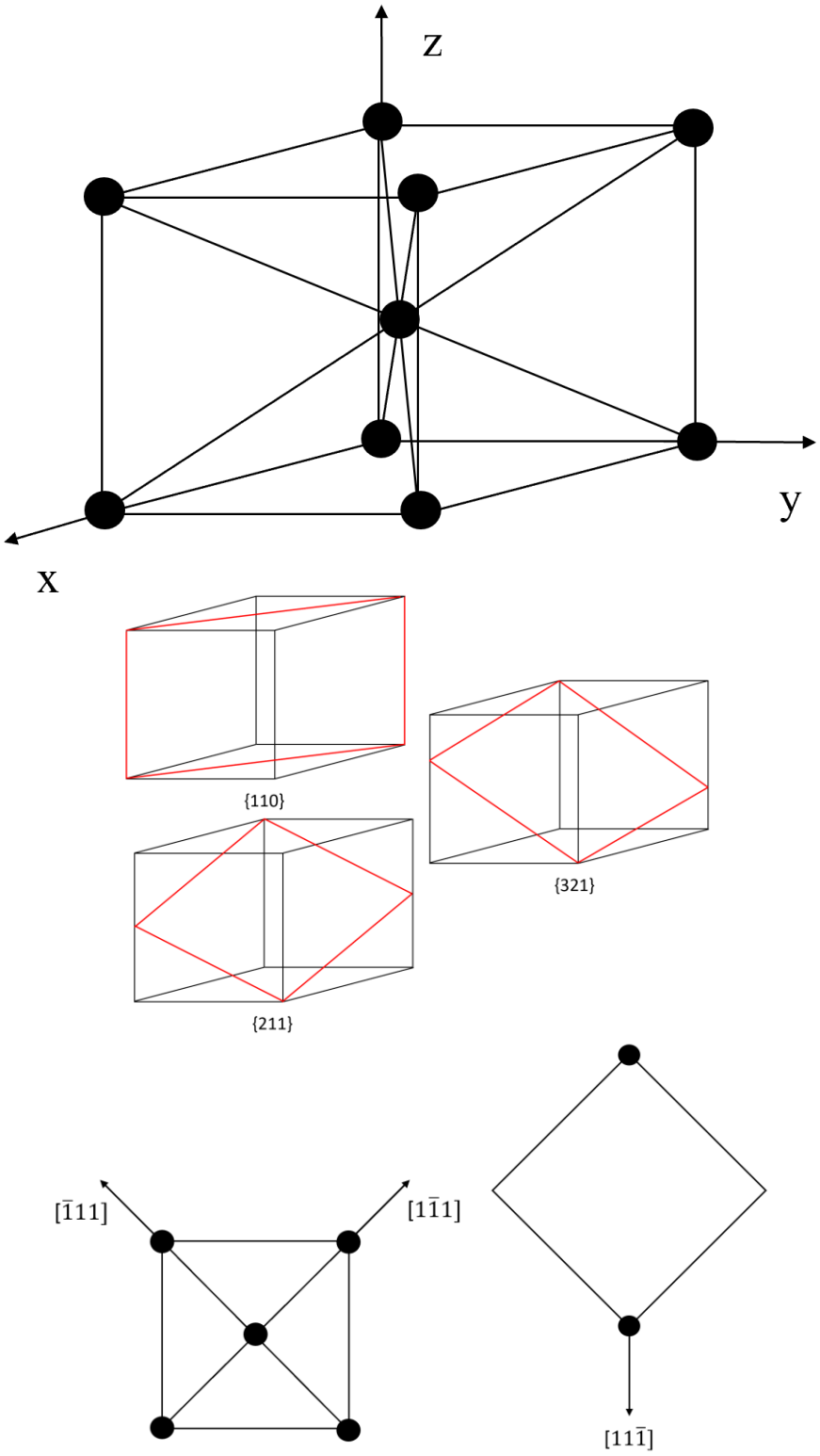

Figure 2. 7 BCC structure and slip planes in BCC structure.

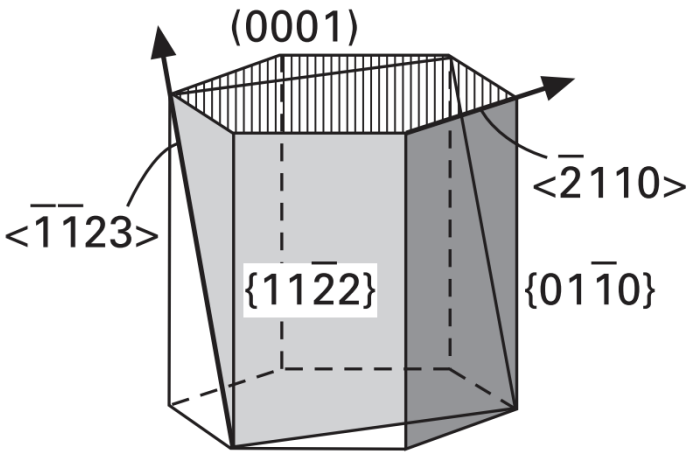

Figure 2. 8 Typical slip systems of HCP structure (Jackson, 1991; Nakano, 2010).

2.2.2.2 Dislocation glide

In a pristine crystal lattice, the application of external stress induces elastic deformation leading to atomic displacements and consequent dislocation formation. However, in practical scenarios, the emergence of fresh dislocations occurs via obstacles bypassed by pre-existing dislocations. The dislocation is a linear defect in crystal structures, which contains a boundary between the slipped plane and the un-slipped plane (Anderson et al., 2017). When there is an external loading, the dislocation will move to adjust its configuration to minimise the strain. Accordingly, the dislocation gliding is also called slip. The slip happens on the slip plane, activated by the shear stress along the slip direction exceeding a threshold value. Schmid defined the threshold shear stress as the critical resolved shear stress (CRSS) (Schmid, 1924). The shear stress required for the regularly arranged lattice structure to form a dislocation $\boldsymbol{b}$ is estimated to be around a sixth of the shear modulus of rigidity in metals ($\boldsymbol{b}$-Burgers vector, represents the magnitude and direction of lattice distortion, which is normally used to represent the dislocation). However, the real stress is normally less than this (Nakano, 2010).

There are two types of dislocations, edge dislocation and screw dislocation, which are illustrated in Figure 2. 9. When the dislocation line is perpendicular to the Burgers vector, the dislocation is called edge dislocation (Orowan, 1934a, b), and the relative slip is perpendicular to the dislocation line. When the dislocation line and the Burgers vector are parallel, it is called screw dislocation (Burgers, 1939), and the relative slip is

parallel to the dislocation line. Moreover, the combination of these two is the third type of dislocations - mixed dislocation.

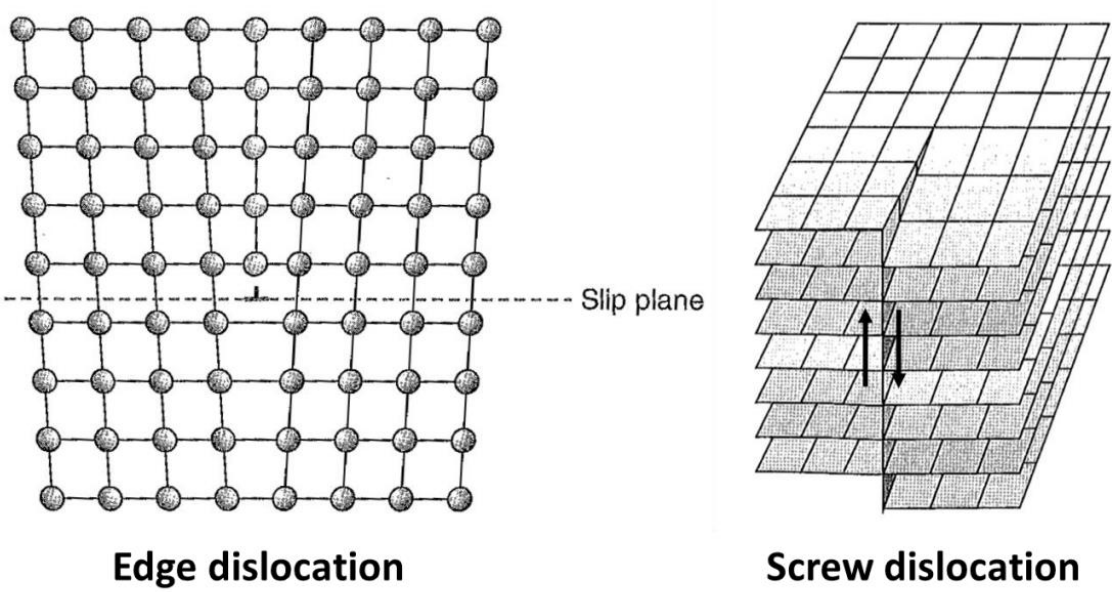

Figure 2. 9 Schematic of edge dislocation and screw dislocation (Tilley, 2004).

Different from edge dislocation, screw dislocation can change the slip plane to achieve cross slip to avoid obstacles during the deformation (Cai and Nix, 2016).

2.2.3 Dislocation climb

Different from slip, in which the dislocation moving direction is parallel to the slip plane, dislocation climb movement is perpendicular to its slip plane. As the climb is associated with the movement of vacancies, the diffusion of vacancies and interstitial under high temperature and/or radiation conditions can highly accelerate the dislocation climb. In addition, at low temperatures, the dislocation glid is the dominant deformation mechanism, while the dislocation climb is more active under high-temperature deformation. With the assistance of diffusion, dislocation climb is a non-conservative motion. Figure 2. 10 shows the edge dislocation climb process assisted by vacancy diffusion.

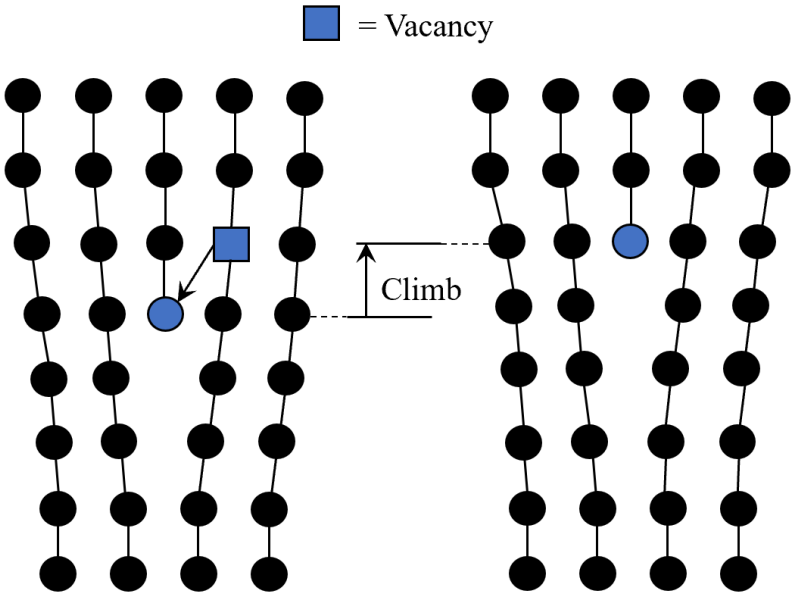

Figure 2. 10 Schematic edge dislocation climb.

Due to the character of the climb, only edge dislocation can climb, and controlled by the nucleation of jog-pairs. Moreover, edge dislocation avoids obstacles by climbing; while screw dislocation avoids obstacles by cross slip. The interstitial atom or vacancy added to the edge dislocation can form a jog-pair. Therefore, the climbing activity in different materials is determined by the self-diffusion energies. Moreover, the more alloy elements in the material can result in more complicated different climbs, especially for commercially used material like 316L SS. Apart from the vacancy and interstitial atom, the interaction between two dislocations can also create a jog-pair.

There are positive climb and negative climb. For the positive climb, the edge dislocation will act as a vacancy sink, which means it can absorb vacancy to transfer itself upwards; while for the negative climb, the edge dislocation will act as a vacancy source, which means the original vacancy at the bottom of the dislocation can be replaced by an atom and results in dislocation move downwards.

2.2.4 Deformation twinning

Deformation twinning is formed during plastic deformation to accommodate the strain, which requires certain loading conditions for different materials. Normally, when the dislocation slip is inhibited, the deformation twinning will appear. The activation of deformation twining is mainly influenced by stacking fault energy (SFE), temperature,

obstacles, strain rate etc. (Christian and Mahajan, 1995; González-Velázquez, 2020b). The deformation twinning can be easily identified by electron backscatter diffraction (EBSD) maps or metallographic microscope, as there is a part of reoriented crystal lattice (child region) mirrored to the original region (parent region), which is distinguished by a twin boundary (TB) (Beyerlein et al., 2014). The TBs can act as obstacles to dislocation movement. The specific mechanisms for deformation twinning can be various according to different crystal structures, e.g. FCC, BCC, and HCP. Figure 2. 11 illustrated the formation of deformation twinning.

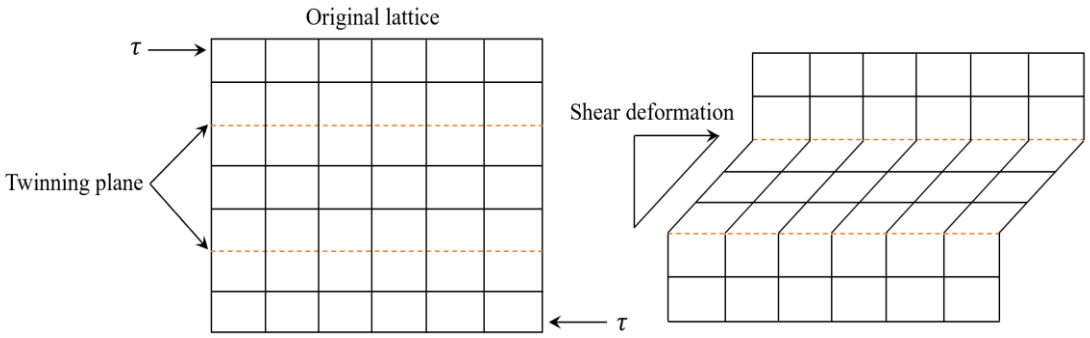

Figure 2. 11 Illustration of twinning caused deformation.

Although mechanical twinning is one of the deformation mechanisms in metallic materials, it is less important in FCC-type material under high temperatures, which only exhibits twinning at very low temperatures (Ashby, 1972)

2.3 Strengthening mechanisms in polycrystals

Strengthening is also known as “hardening”, which represents the ability of the material to resist external forces without failure. It is normally represented by toughness, which means the yield and tensile strength are increased without losing ductility. The strengthening of materials can improve mechanical properties.

Materials strengthening can be achieved by various mechanisms: grain boundary hardening, solid solution hardening, strain hardening, precipitation hardening, and second phase hardening. These strengthening mechanisms are related to either microstructure character or materials' elemental composition (Gasson, 2008). And the principle of strengthening mechanisms is inhabiting the movement of dislocation.

There is an individual strain field around each dislocation segment. The effect of which is overlapped on the matrix. The strength of the material mainly depends on the difficulty of dislocation movement. Moreover, the dislocation self-energy is proportional to the $\boldsymbol{b}^2$. As a result, the magnitude of the Burgers vector can significantly influence the evolution of dislocation (Nakano, 2010).

2.3.1 Grain boundary hardening

Grain boundary hardening is also called grain size reduction, as better mechanical strength can be achieved by reducing the grain size. It is not only because the smaller grain size limited dislocation movement, but the grain structure itself also provides strengthening. Therefore it is a mixture of strengthening mechanisms. Normally, the grain boundary hardening shows an inversely proportional relationship with temperature. Each grain has its own orientation, which is different from the neighbouring grains. When the material is deformed, each grain needs to adjust itself to accommodate the adjacent grains. Inside the grain, the movement of dislocation slip is active and restricted by grain boundaries. There are two types of grain boundaries: the boundaries characterised with misorientation between 2^o to 15^o are recognised as low angle grain boundaries (LAGBs); while the boundaries with misorientation greater than 15^o are defined as high angle grain boundaries (HAGBs). Typically, the grain size is related to HAGBs, while the sub-grain is formed by LAGBs. However, this is not always applicable (Zhao and Palmiere, 2018).

The grain size-related yield strength is given by the classic Hall-Petch Law (Hall, 1951; Petch, 1953):

$$\boldsymbol{\sigma_0 = \sigma_i + \frac{K}{\sqrt{D}}} \qquad \textbf{(2. 1)}$$

Where $\boldsymbol{\sigma_0}$ is the yield strength, $\boldsymbol{\sigma_i}$ denotes the friction stress, K is the dislocation release factor, and D denotes grain size (diameter).

Apart from the grain boundary hardening itself, the grain size is also related to the cell wall dislocation density. The relation is given as (Holt, 1970; Toriumi, 1979):

$$D \propto \frac{1}{\sqrt{\rho_{cw}}} \quad \textbf{(2. 2)}$$

Where ρ_{cw} is cell-wall dislocation density. Therefore, the grain boundary hardening can be represented by the cell-wall dislocation hardening.

A fine grain structure is always desirable for enhancing the mechanical properties of materials. Not only yield strength, but ductility, fracture toughness, and weldability can be improved with a finer grain structure. However, it is not applicable to nano-scale materials. The grain boundary hardening is not suitable for a grain size smaller than 10 nm, as grain boundary sliding will be the dominant deformation mechanism (González-Velázquez, 2020b).

2.3.2 Precipitation hardening

Precipitation hardening is also called fine particle hardening. Compared to the metallic matrix, it can be called the second phase as well. It was first reported by Wilm (Wilm, 1911) from the ageing of a supersaturated solid solution alloy. The nano-sized precipitation in the metal is normally formed during the subsequent heat treatment. According to the chemical compositions of the material and the heat treatment conditions, various precipitations exist in the metallic matrix. The exitance of precipitation can increase the hardness, strength, and wear resistance of the material. However, it is detrimental to the ductility and toughness of the material.

The mechanism of precipitation hardening depends on whether the dislocation can bypass the precipitate or the dislocation can cut the precipitate. The existence of precipitate can hinder the movement of dislocation by pinning. When the precipitate cannot be cut by the dislocation, it will be surrounded by a dislocation ring, as the dislocation bows around the un-shearable precipitate. This process is called Orowan's looping (dislocation bypass) (Orowan, 1940), which is shown in Figure 2. 12.

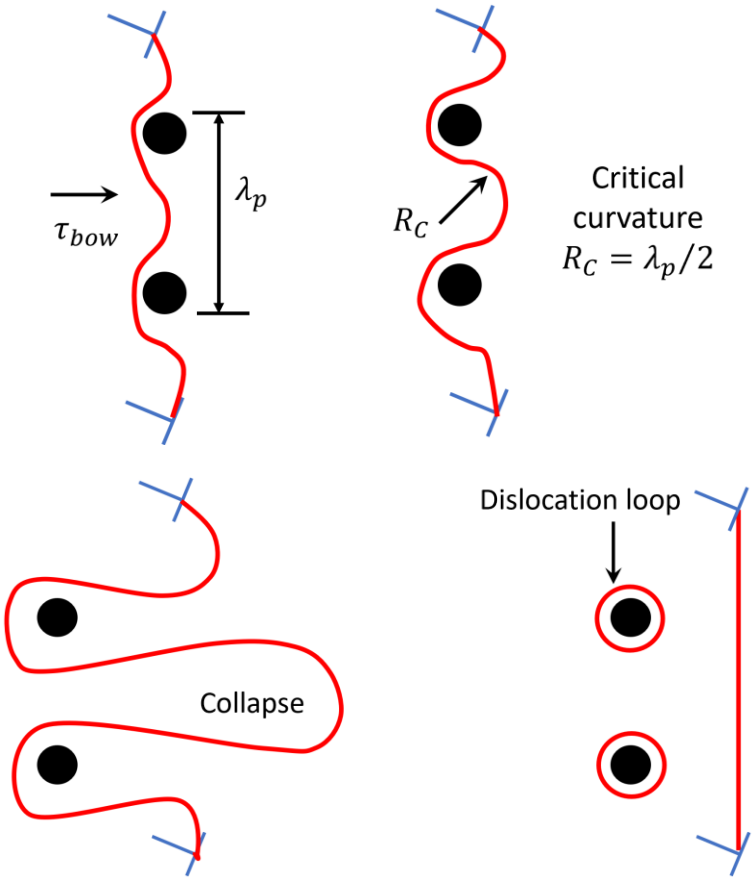

Figure 2. 12 Schematic of Orowan's strengthening mechanism: non-shearable particles.

The shear stress τ_{bow} required for a dislocation to bow over the particle is given as (González-Velázquez, 2020b; Orowan, 1940):

$$\tau_{bow} = \frac{\mu \boldsymbol{b}}{\lambda_p} \qquad \textbf{(2. 3)}$$

where μ is the matrix shear modulus, $\boldsymbol{b}$ is the Burgers vector, and λ is the spacing between two particles.

For the shearable precipitate, the dislocation can cut through it, which is illustrated in Figure 2. 13.

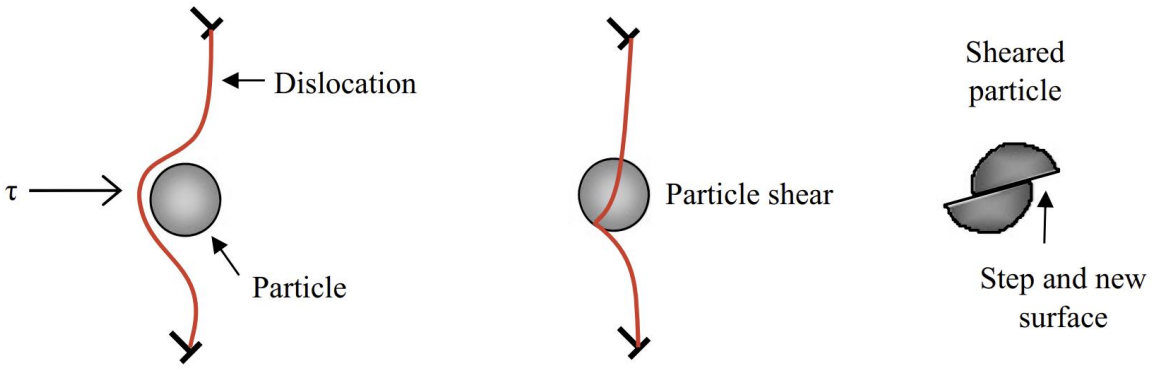

Figure 2. 13 Schematic of shearable particle cut by dislocation (González-Velázquez, 2020a).

The stress σ_{cut}required to cut through the precipitate is given as (Mott and Nabarro, 1940):

$$\sigma_{cut} = \mu\varepsilon'^{3/2}\sqrt{rf_p} \tag{2. 4}$$

$$\varepsilon' = \frac{\boldsymbol{a'_0} - \boldsymbol{a_0}}{\boldsymbol{a_0}} \tag{2. 5}$$

where r denotes the ratio of precipitation, f_p denotes the precipitate volume fraction and ε' is the lattice misfit strain. $\boldsymbol{a_0}$ is the unstrained lattice parameter, while $\boldsymbol{a'_0}$ is the pseudomorphic lattice parameters.

However, the justification of the shearable and non-shearable particles lies in the structures of both particle and matrix. A particle can easily be cut when it is characterised by the same structure of the lattice. Therefore, the classic criterions mentioned above are not always applicable. In addition, the $M_{23}C_6$ investigated in this project is non-shearable (Hidalgo et al., 2020). Ostwald ripening is also called coarsening for precipitation process, which is controlled by diffusion (Huo et al., 2011). By capturirng the size evolution of precipitates, the Ostwald ripening effect can be considered.

2.3.3 Dislocation hardening

Dislocation hardening is the result of the aggregation and interaction of dislocations during plastic deformation. Under quasi-static loading conditions, plastic deformation can usually lead to a higher dislocation density, which results in harder dislocation movement. Therefore, there is a requirement for higher stress to maintain the strain increasing, accordingly the dislocation hardening can also be called strain hardening. Moreover, the strain-stress curve is the result of strain hardening (dislocation hardening).

As shown in Figure 2. 4, there are two slip systems operative during stage 2 of the deformation in a single crystal. When the dislocations in the other slip system are immobile, those dislocations are referred to as forest dislocations. And the resultant dislocation strengthening mechanism is called forest hardening, which is the dominant dislocation-strengthening mechanism (Gromov et al., 2022; Karaman et al., 2001; Queyreau et al., 2010).

When dislocation interacts with the other dislocation, a kink or jog will be formed by dislocations intersection moving at different planes. The kink is a step in the dislocation line in the slip plane, while the jog is a step with the same length and direction as ***b*** of the other dislocation on a different slip plane. The formation of the kink and jog are shown in Figure 2. 14. Notice that the jog is also an edge dislocation, whose slip plane is perpendicular to the parent dislocation; while the kink is also a screw dislocation.

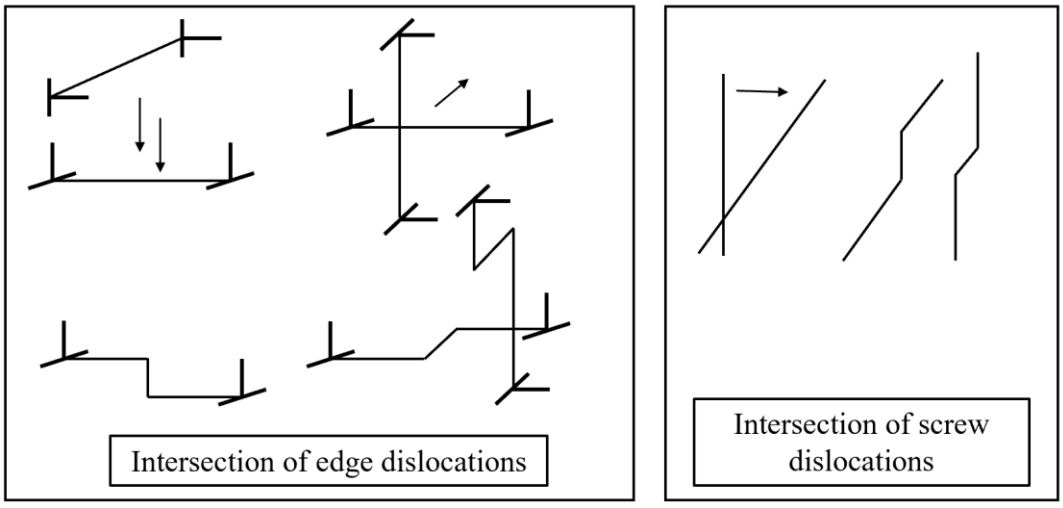

(a)

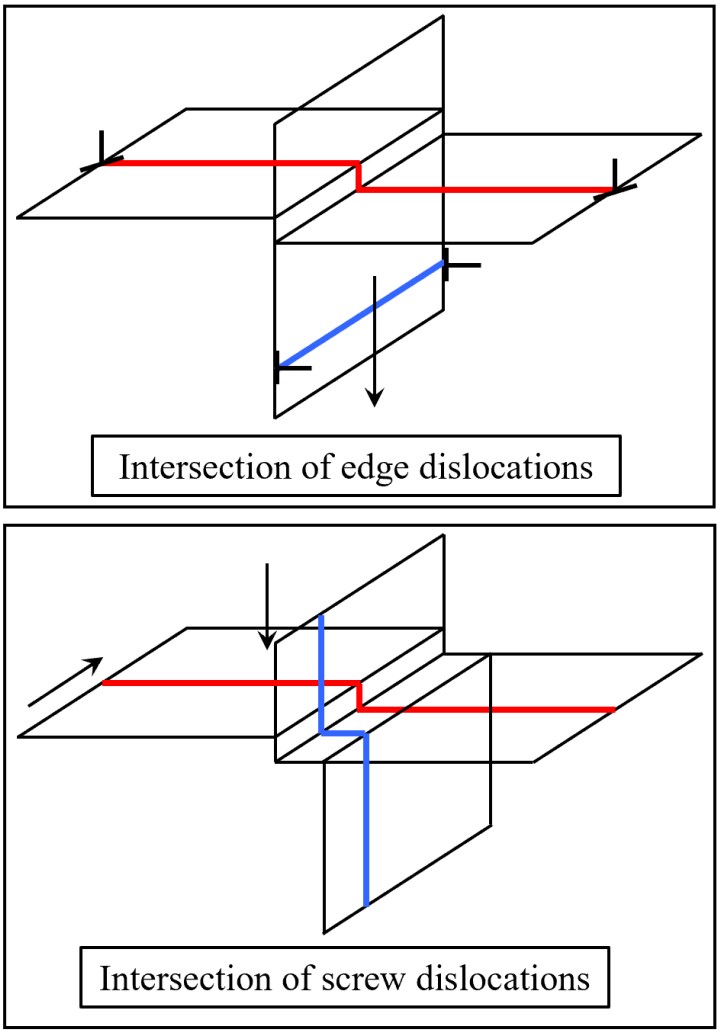

(b)

Figure 2. 14 Schematic intersection of dislocations, (a) the formation of kinks; (b) the formation of jogs.

The dislocation hardening includes not only the interactions between dislocation and dislocation, but also the interactions between dislocation and obstacles. When the obstacle is precipitate, the strengthening mechanism can also be called precipitation strengthening. When the obstacle is a foreign solute atom, the strengthening mechanism is also known as solid solution strengthening. Notice that, the exitance of the other types of obstacles can also accelerate the forest hardening by hampering the motion of the dislocations.

2.3.4 Solid solution strengthening

Solid solution strengthening is the main hardening mechanism used in alloying metals, which can increase the strength of materials by hindering the dislocation movement. The inhibited dislocation movement is not only caused by attraction or repulsion from solute atoms, but the solute atoms resultant lattice distortion (different atomic size and lattice parameters). The interaction between the lattice and solute atoms is controlled by a combination of atomic size, modulus misfit interactions and chemical effects (Mitchell, 2001). Due to the difference between the foreign atoms and the matrix, a high-stress field around the solute atom is created. Moreover, the energy around the dislocation is enhanced, which means higher external stress is required to move the dislocation (Tilley, 2004). Accordingly, the CRSS of the material is increased.

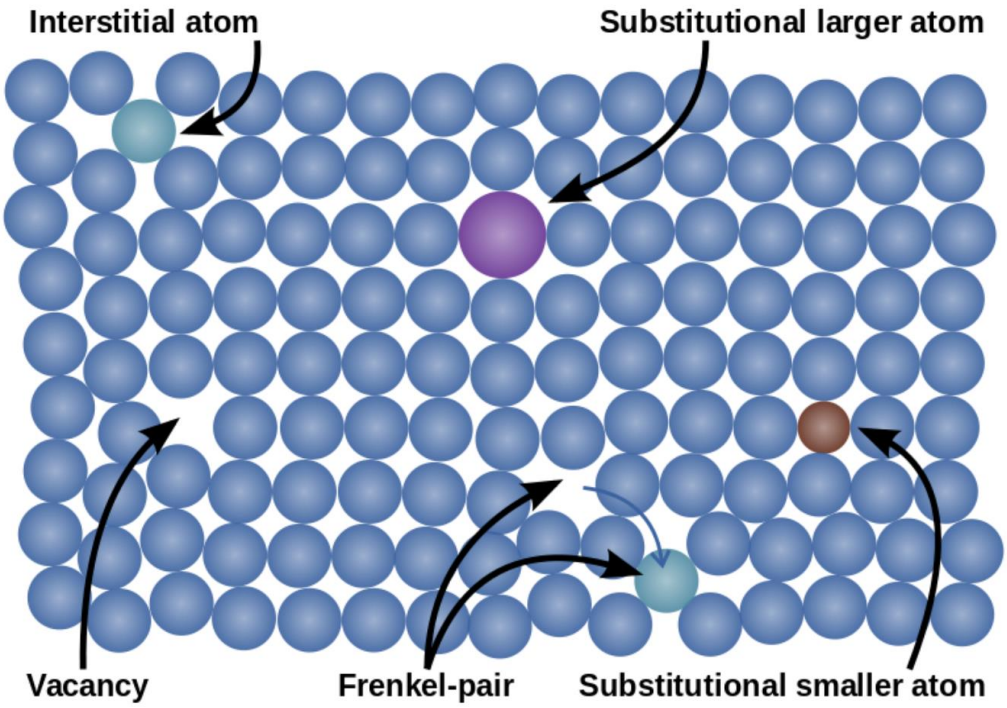

Figure 2. 15 Illustration of interstitial atoms, substitutional atoms and lattice distortion (Dani Feri, 2011).

As shown in Figure 2. 15, there are two types of solute atoms, interstitial atoms and substitutional atoms, which depend on the relative sizes of the foreign atoms. For the foreign atoms, which are differ by less than 15% of the main matrix atoms, they can be substitutional atoms by replacing a solvent atom. For the foreign atoms are similar/smaller in size compared to the main matrix atoms, they can occupy the

interstices of the lattice, therefore, forming the interstitial atoms (Tilley, 2004). Normally the interstitial atoms can generate a stronger elastic field than the substitutional atoms due to higher lattice distortion. The stress field around the substantial atom is spherical without shear stress components, which cannot interact with screw dislocations. The interstitial atom can generate tetragonal distortion with shear stress components, which can interact with both edge and screw dislocations.

Despite the spinning effect on the dislocation movement, the solute-induced lattice distortion can also hinder dislocation mobility. C and N are the most common interstitial atoms in steels, which are often incorporated into the surface layers to enhance their properties by carburizing (Scheuer et al., 2012), nitriding (Soleimani et al., 2012), or nitrocarburizing (Liu et al., 2012). In the classic work of Cottrell and Bilby, if the dislocation is located in high solubility region, the dislocation can collect a cluster of interstitial solute atoms around its core (Cottrell and Bilby, 1949). Therefore, the Cottrell atmosphere is formed, which is shown in Figure 2. 16. Additional stress is required to unpin the dislocation from the Cottrell atmosphere.

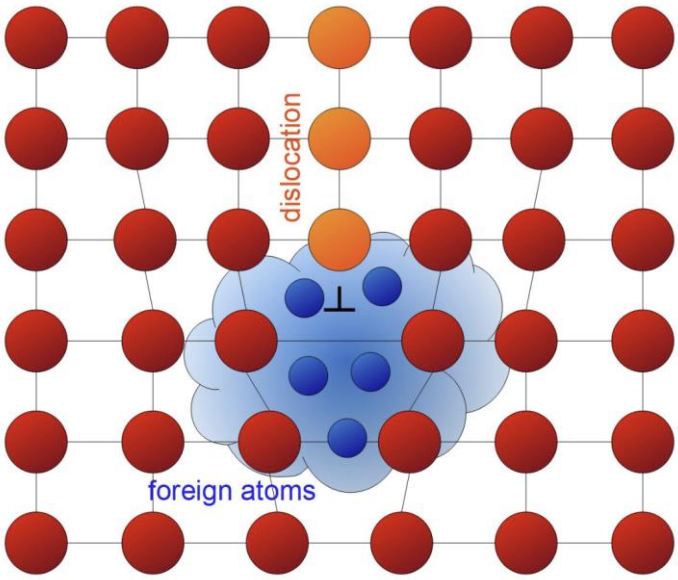

Figure 2. 16 Cottrell atmosphere (tec-science, 2023).

Compared with metal atoms, C and N show smaller sizes, lighter atomic mass and better mobility, which facilitate the formation of the Cottrell atmosphere and are carried by dislocations. Correspondingly, C and N have strong solid solution hardening in most

alloys. Meanwhile, the bigger-sized alloying elements like Cr, Ni, Mo, and Mn are performing as substitutional atoms (Liu et al., 2003). The solid solution strengthening from lattice distortion caused by these elements is defined as atom misfit. This atom misfit consists of the volume misfit and the chemical misfit. The latter is quantified by elastic interaction energy required by atomic-scale simulation (Leyson et al., 2010; Wakeda et al., 2017). The quantification of the lattice distortion has been determined by Friedel- and Labusch-type solute solution hardening models (Leyson and Curtin, 2013; Leyson et al., 2010; Wu et al., 2016). However, both Friedel and Labusch models have the precondition that the solute atoms are fixed. This is not applicable to the high-temperature creep environment where the diffusion of solute atoms is highly active. Leyson et al. (Leyson and Curtin, 2013) and Curtin et al. (Curtin et al., 2006) proposed a core-diffusion model to describe the diffusion of solutes around the dislocation core and the dislocation pinning effect. The implantation of this core diffusion model to creep behaviour has been reported by Wen et al. (Wen et al., 2018). However, further studies are required for materials with multicomponent phases; and reliable atomic-scale parameters for 316L SS are not complete in the literature. There is a need for an accurate expression for solid solution hardening, which should be a function of chemical composition and loading conditions.

In 316L SS material, the most interstitial alloying elements are Cr and Ni. However, there is little literature reported about the Cottrell atmosphere caused by these elements. In commercial materials, such as SS316L, the high concentration of solutes of more than 10 alloying elements tends to interfere with vacancy/interstitial diffusion. Such a process can be complex and, to the best knowledge of the author, has not been investigated through low-scale simulation or experimental methods. There are limited models that can describe the solid solution hardening in 316L SS with temperature dependence. Matijasevic et al. (Matijasevic and Almazouzi, 2008) investigated the hardening effect of Cr in the Fe-Cr binary alloy under various temperatures. Okazaki et al. (Okazaki, 1996) has summarised the hardening effects of a range of alloying elements below 500 K. Stephens et al. (Stephens and Witzke, 1976) did similar research but the results are reported in Vickers hardness. Although it is a universal assumption that $HV = 2.9Y \sim 3.0Y$ (HV, Vickers hardness; Y, yield strength) (Quarrell, 1952). There are a lot of uncertainties during the hardness tests, so it is not reliable to adjust

alloy hardening only based on hardness. Moreover, this kind of relationship only exists in isotropically hardening material, which is not applicable to AM case (Tekkaya and Lange, 2000). Furthermore, even the solute solution hardening is known in the binary Fe alloy. The strengthening effects vary in the different lattice structures. For the study mentioned above, the binary Fe alloys are ferritic alloys, which is not applicable to other materials (Cabanas et al., 2006; Stephens and Witzke, 1976). Moreover, the strong interactions between interstitial atoms and substitutional atoms require atomistic simulation techniques such as ab initio calculations, which is beyond the scope of this project (You and Yan, 2013).

The Frank-Read source is a mechanism that describes the creation and movement of dislocations in crystalline materials, based on dislocation multiplication in a slip plane under shear stress. (Frank and Read, 1950). The mechanism of Frank-Read source is illustrated in Figure 2. 17: within the realm of dislocation dynamics, a Frank-Read source configuration manifests as a dislocation pinned at two points. Under the influence of an applied shear stress, the immobile dislocation undergoes a distinctive phenomenon characterized by sequential expansion and repetitive looping. This intricate process entails the dislocation progressively elongating and recurrently curving, resulting in the emergence of successive dislocation loops.

The value of shear stress τ_{F-R} required to form the Frank-Read source is given as (Hosford, 2005):

$$\tau_{F-R} = \frac{2\mu \boldsymbol{b}}{x} \qquad \textbf{(2. 6)}$$

where μ is the shear modulus, $\boldsymbol{b}$ is the Burgers vector, and x is the distance between the two pinning sites.

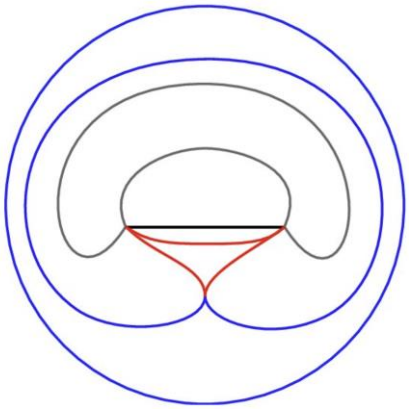

Figure 2. 17 Activation of a Frank-Read source (Khan and Huang, 1995).

The Frank-Read source mechanism provides an explanation for the preferential generation of dislocations on specific slip planes. According to this mechanism, dislocations are predominantly generated within those planes that possess Frank-Read sources (Khan and Huang, 1995).

2.4 Elevated-temperature creep behaviour

Creep behaviour is an important mechanical character for structural materials serving in an elevated-temperatures environment for a long duration. Similar to tensile behaviour, the initial elastic behaviour is followed by plastic deformation. Figure 2. 18 shows it is a typical creep curve for a constant load, which illustrates the creep strain versus time. In this schematic plot, there are three stages of creep deformation: transient, secondary steady state, and tertiary. Normally, the first stage can finish relatively faster than the other two stages. According to the different combinations of creep temperatures and stress, the contributions from different creep mechanisms will be different. As shown in Figure 2. 19, the creep mechanisms of fcc type stainless steel include dislocation creep, bulk diffusion creep, grain boundary diffusion creep and core diffusion creep (Jones and Ashby, 2019). The bulk diffusion creep is also called Nabarro-Herring creep controlled by diffusional mass transport (Ohring, 2014). At elevated temperatures, atoms have higher kinetic energy and can move through the lattice by diffusion, causing lattice planes to glide and resulting in material deformation. Additionally, smaller grain sizes can enhance the creep rate since there are more grain boundaries available for atom diffusion. This diffusion is driven by the concentration gradient of atoms within the crystal (Herring, 1950) (Cocks, 1996). The boundary

diffusion creep is also known as Coble creep, which is similar to Nabarro–Herring creep, dominant at lower stress and higher temperature regions (Courtney, 2005). In Coble creep, the primary mechanism of deformation is the migration of atoms through grain boundaries. Since the higher diffusivity on grain boundaries compared with grain interior (Gjostein, 1972; Shewmon, 2016), the occurrence of Coble creep requires lower temperature conditions than Nabarro-Herring creep, which is illustrated in Figure 2. 19 (Ashby, 1972).

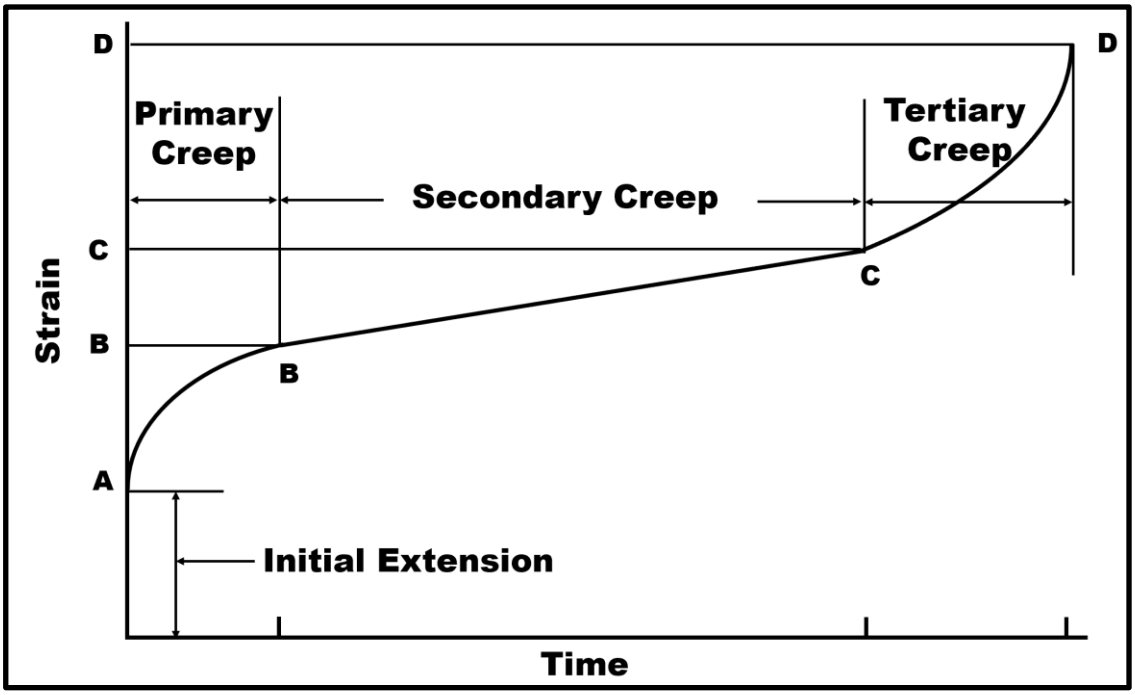

Figure 2. 18 Schematic creep behaviour, strain versus time (Jones and Ashby, 2019).

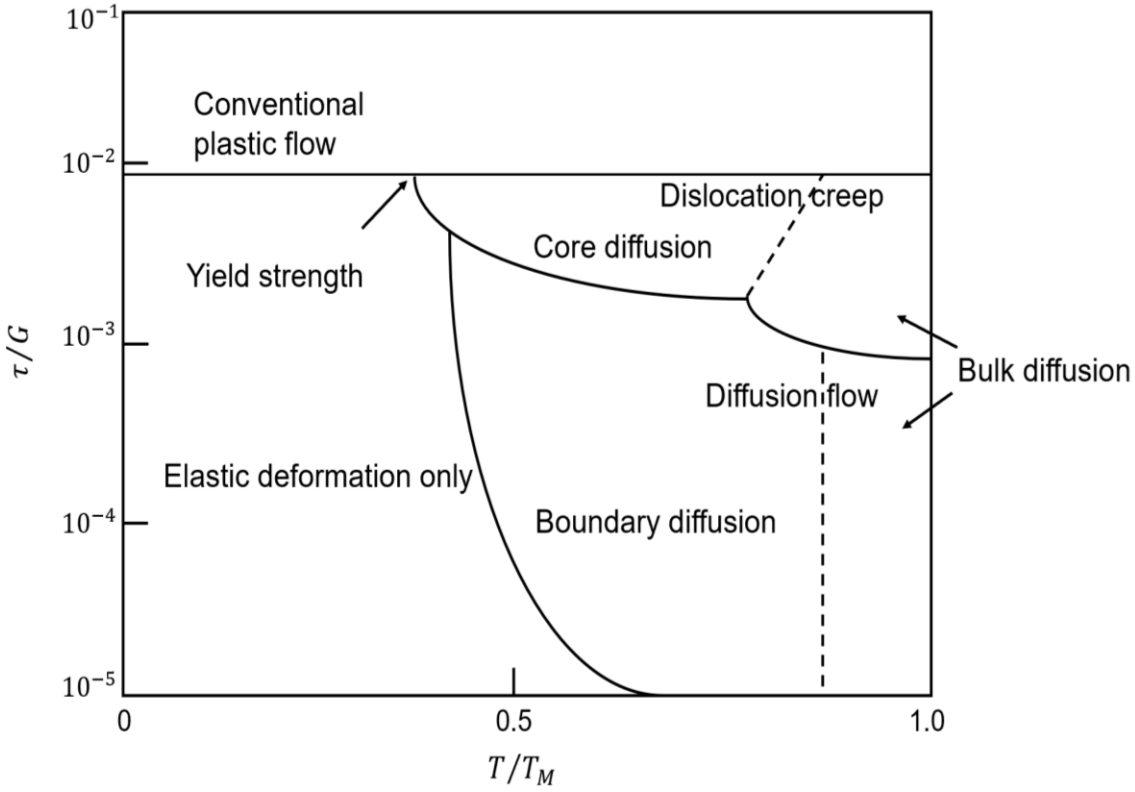

Figure 2. 19 Creep mechanisms with respect to stress and temperature for fcc type stainless steel (Jones and Ashby, 2019).

The steady-state creep is the most discussed and attracts the interest of engineering. The creep models are mainly built based on steady-state mechanisms and behaviour, where the creep rate is almost constant. Apart from the dislocation movement, atomic diffusion is another main mechanism in the steady state. The tertiary creep is the least predictable stage, as there is stress accumulation in the aged materials and dynamic recrystallization rendering the deformation tolerance of materials (Farhat, 2021). The understanding of the tertiary stage can promote the evaluation of component service life estimation. The damage development during the tertiary stage includes not only includes the cavitation process (void nucleation, void growth, and void coalesce), but the crack initiation and growth, and failure or stress rupture.

For room temperature tensile tests, the finer grain structure can result in higher tensile strength. However, during the creep deformation, the grain boundary sliding (GBS) is one of the deformation mechanisms. In this case, finer grain structure resulting in more grain boundaries can accelerate the creep via GBS. Moreover, grain boundaries are also the media of Coble creep. The existence of more grain boundaries can promote

diffusion-mediated creep by assisting Coble creep. Therefore, the deformation mechanism contributions to elevated-temperature creep behaviour are different from tensile behaviour. Accordingly, the materials system design for components employed under elevated-temperature environments should consider the contributions of all relevant mechanisms.

2.5 Materials and experimental data

Since 316L austenitic SS is one of the crucial structural alloys in the nuclear industry, the high-temperature creep behaviour of this alloy is of great significance. Hence, AMed and traditionally-fabricated 316L SSs were investigated as validating alloys for the developed mechanism-based model. The sophisticated microstructure in AM products leads to significant differences in mechanical properties compared to the traditionally fabricated wrought materials (Haghdadi et al., 2020; Hamza et al., 2021; Khairallah et al., 2016b). As a consequence of complex thermal history, various grain morphologies distribute hierarchically and anisotropically as evidenced by EBSD (Hamza et al., 2021; Mirkoohi et al., 2020b; Sabzi et al., 2020a). While experimental investigations have been conducted to establish correlations between microstructure and creep behavior in austenitic stainless steels (Calderón et al., 2022; Hong et al., 2021b; Li et al., 2021b; Yoon et al., 2020),there remains a dearth of systematic modeling research that can numerically elucidate the relationship between evolving microstructures and the creep behavior of AM austenitic SSs. Existing modeling approaches have demonstrated satisfactory agreement with creep experiments for conventionally wrought austenitic SSs (Lindvall, 2020; Shin et al., 2019; Sourmail et al., 2002; Yamamoto et al., 2022), but they cannot be directly applied to AMed materials as they fail to consider the unique microstructural characteristics associated with additive manufacturing. Moreover, thermokinetics techniques have been employed to gain insights into the evolution of precipitates during high-temperature creep (Andersson et al., 2002), but a direct connection with creep behavior has not been established.

Table 2. 1 shows the chemical composition and denomination of the materials studied in this project. The experimental results on the microstructure and creep behaviour have been obtained from the literature (Rieth et al., 2004b; Williams et al., 2021). In the work

of Reith et al. (Rieth et al., 2004b), the wrought 316L SS samples were received as hot rolled plates after solid solution treatment at 1373 K followed by water quenching. Moreover, the total creep experiment lasted almost 10 years under a range of loading conditions and temperatures, which are listed in Table 2. 3. The AMed 316L SS was produced by laser powder bed fusion (LPBF) with processing parameters that are presented in Table 2. 2 (Williams et al., 2021). In the work of (Williams et al., 2021), the creep experiments were conducted by loading parallel and perpendicular to the LPBF building direction under 923 K with various stresses on the AMed samples. The detailed loading information is shown in Table 2. 3**.** The stress increments between tests are around 10 MPa for AM materials and 20 MPa for wrought ones. Such dense experimental data are sufficient to support the modelling of the creep behaviour and the effects of deformation mechanisms within relevant stress and temperature intervals. The schematic relation between the loading and building directions of AMed samples is illustrated in Figure 2. 20. AM-H means the creep testing samples were built vertically to the horizontal baseplate with the creep testing loading direction parallel to it, while the AM-V denotes the creep testing samples were built orthogonal to the baseplate and the external loading is parallel the build direction. The EBSD IPF-γ maps of the AM-H and AM-V samples, which are used for microstrure information input are shown in Figure 2. 21.

Table 2. 1 Chemical composition (in wt%) of the steels tested in this work.

Steel	C	Si	Mn	P	S	Cr	Ni	Mo	Cu	N	O	Fe	Ref.
AMed	0.03	0.75	2.00	0.03	0.015	17.50	12.00	2.25	0.75	0.1	0.1	Bal.	(Williams et al., 2021)
Wrought	0.02	0.32	1.80	0.02	0.006	17.34	12.50	2.40	0.12	0.08	-	Bal.	(Rieth et al., 2004b)

Table 2. 2 LPBF processing parameters of AMed 316L SS samples (Williams et al., 2021).

Processing parameter	Value

Laser power (W)	200
Scan speed (m/s)	0.75
Hatch distance (μm)	110
Layer thickness (μm)	50
Spot size (μm)	65

Table 2. 3 Summary of the creep experiment conditions for both AMed and wrought materials investigated in this work.

Material	Temperature (K)	Creep stress (MPa)	Reference
AM horizontally built (AM-H)	923	97 111 119	(Williams et al., 2021)
AM vertically built (AM-V)	923	119 124 133 142 150	(Williams et al., 2021)
Wrought	823	135 150 180 210	(Rieth et al., 2004b)
Wrought	873	80	(Rieth et al., 2004b)

100

120

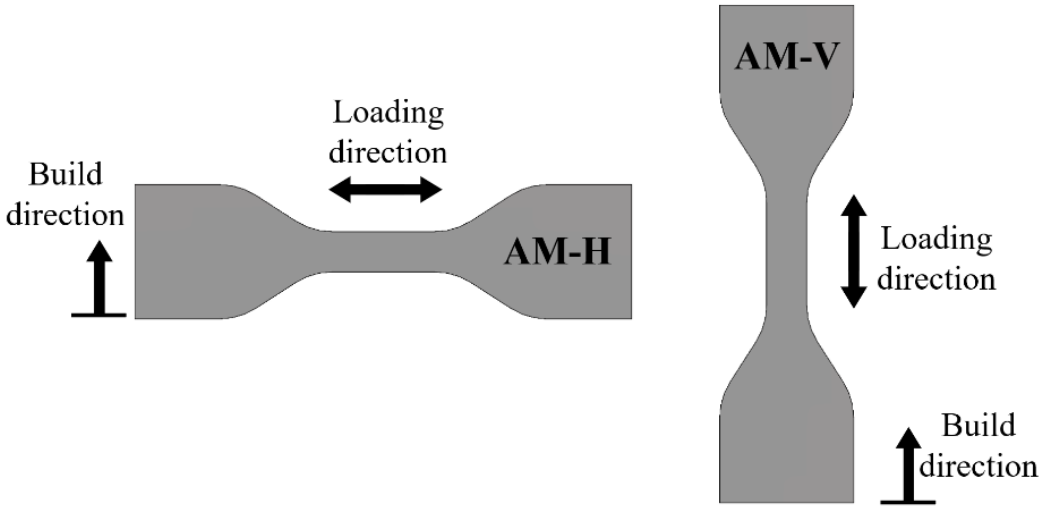

Figure 2. 20 Schematic illustration of the building and loading directions of AM-H and AM-V samples.

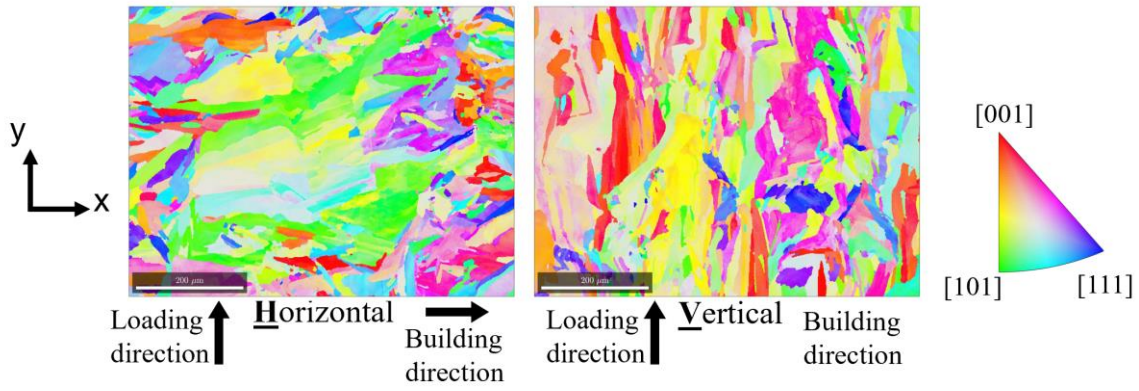

Figure 2. 21 EBSD IPF-γ maps of the AM-H and AM-V samples in the as-build condition and prior to testing (Williams et al., 2021).

Normally, slender columnar grains lie parallel to the build direction, since dendrites grow epitaxially along the solidification front (Hadadzadeh et al., 2018; Hamza et al., 2021; Kong et al., 2019; Laleh et al., 2019; Mishurova et al., 2021; Pradeep et al., 2020). As a result of microstructural anisotropy, several research efforts have been carried out to study the different mechanical responses in the directions parallel and perpendicular to the building direction (perpendicular to the baseplate). It was found that the materials have lower strength (under quasi-static loading) and stronger creep resistance along the

build direction in 316L SS (Yang et al., 2021b; Yoon et al., 2020). A similar phenomenon was reported in AISI 420, showing that the building direction effect causes anisotropic tensile mechanical properties (Shen et al., 2020). Furthermore, the building direction of AM-maraging steel can still influence the mechanical properties after ageing, especially on wear resistance (Podgornik et al., 2021). Therefore, it is worthy to capture the AM materials' creep behaviour when the loading is applied in different directions. As for wrought 316L SS, it is normally assumed that the material is characterised by equiaxed crystal (grain size depends on the thermo-mechanical processing). The microstructural characterisation of AM materials has been reported by Williams et al. (Williams et al., 2021). The electron backscatter diffraction (EBSD) maps were acquired with a step size of 1 μm. In this work, the EBSD post-processing was performed using DREAM.3D software (Groeber and Jackson, 2014). The microstructural features extracted from EBSD data, including grain and sub-grain sizes and the corresponding textures, will be used as the input information for the simulations (see Chapters 4, 5 and 6).

The steady-state creep rates (minimum creep rates) reported by Rieth et al. (Rieth et al., 2004a) and Williams et al. (Williams et al., 2021) are summarised in Figure 2. 22. Apart from the minimum creep rates for AMed materials straight reported in (Williams et al., 2021), the steady-state creep rates for wrought 316L SS are summarised from the graphed creep response (Rieth et al., 2004a). All of these creep testing results demonstrate a power-law creep behaviour. However, the AMed materials show a notably lower strain rate sensitivity, which is expressed by the power n in Figure 2. 22. The stress exponent n of the steady-state creep rate can represent the creep mechanisms type or transition during the material' deformation (Blum et al., 2002). However, the specific value of n can vary for different materials and different loading conditions (Athul et al., 2016; Hollenberg et al., 1971; Liu et al., 2007; Sandström, 2023).

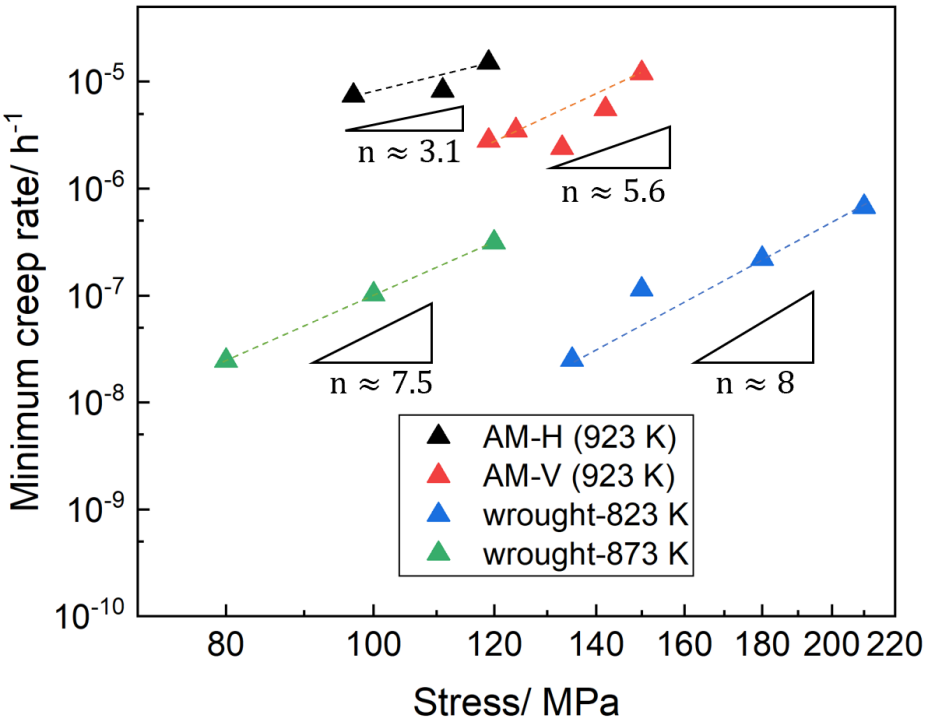

Figure 2. 22 Experimental minimum creep rates for (Rieth et al., 2004b) and AMed 316L SS (Williams et al., 2021), AM-H and AM-V are horizontally and vertically built, respectively.

It is worth mentioning that it is accustomed to use three to five experimental data points to determine the stress exponent n in the creep behaviour studies, e.g. (Carsí et al., 2004; Li et al., 2013; Liu et al., 2022a; Roodposhti et al., 2016; Singh et al., 2019; Sklenička et al., 2017; Su et al., 2013). Moreover, the stress increments between tests are around 10 MPa for AM materials and 20 MPa for wrought ones. Such narrowed steps of experimental data collection have assured the reliability of creep behaviour trends, and are adequate to support the modelling work for the creep response and the description of each relevant mechanism within relevant stress and temperature intervals. Apart from the minimum creep rate, the homologous creep curves reported by Williams et al. (Williams et al., 2021) and Rieth et al. (Rieth et al., 2004a) will also be simulated to demonstrate the prediction capability of the proposed model, which will be presented in Chapter 4 and Chapter 5.

2.6 Crystal Plasticity Formulation

2.6.1 Crystal Plasticity Theory

Different from macroscopic plasticity, crystal plasticity (CP) is a detailed physics-based theory, which can capture explicit microscopic information. Based on the deformation description on the single crystal level, the predictions of macroscopic behaviour are captured by incorporating Schmid's law at each integration point. Generally, CP models are expressed by phenomenological expressions, through which, the slip rates and the corresponding internal variables are conducted. Originally, CP is a classic theory to describe the stress-strain response of a single crystal. As mentioned before, the *constitutive* laws assume that plastic deformation is accommodated only by the dislocation gliding on certain planes (slip). This was extended to consider the contribution from twinning and dislocation climb later. Technically, CP theory is established based on the decomposition of the deformation gradient for a single crystal into the pure plastic part and the elastic part which includes the rigid rotation, written (Armstrong et al., 1962; Asaro and Needleman, 1985; Asaro and Rice, 1977; Kalidindi, 1998; Kröner, 1958, 1959, 1981; Lee and Liu, 1967):

$$\mathbf{F} = \mathbf{F}^{*}\mathbf{F}^{\mathrm{P}} \tag{2. 7}$$

here the shape deformation $\mathbf{F}$ can be multiplicatively decomposed into: $\mathbf{F}^{\mathrm{P}}$, the plastic deformation gradient (irreversible), representing the effects of shearing caused by dislocation slip, and $\mathbf{F}^{*}$, denotes the contribution of both elastic stretches (reversible) and lattice rotation. There is an intermediate, relaxed configuration introduced by $\mathbf{F}^{\mathrm{P}}$, which is considered to achieve a perfect lattice without external stress. However, it cannot be realised as the dislocation movement is not allowed. Practically, due to the dislocations, there is the existence of balanced internal stress. The decomposition of the deformation gradient is schematically illustrated in Figure 2. 23.

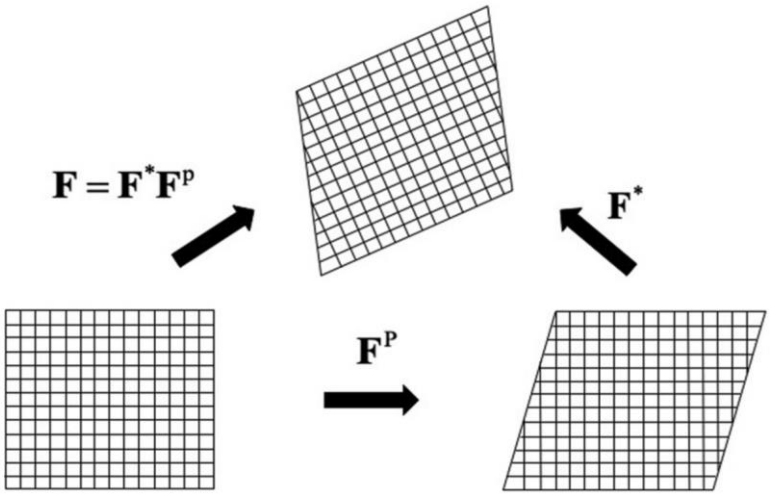

Figure 2. 23 Decomposition of deformation gradient, kinematic scheme proposed by (Asaro and Rice, 1977).

The total deformation can also be expressed in terms of the microscopic velocity gradient $\mathbf{L}$ with both elastic ($\mathbf{L}^{*}$) and plastic ($\mathbf{L}^{\mathrm{P}}$) parts (Alcalá et al., 2015; Asaro and Rice, 1977; Kuhlmann-Wilsdorf, 1999):

$$\mathbf{L} = \dot{\mathbf{F}}\mathbf{F}^{-1} = \mathbf{L}^{*} + \mathbf{L}^{\mathrm{p}} \tag{2. 8}$$

Meanwhile $\mathbf{L}^{*}$and $\mathbf{L}^{P}$ can also be divided as (Alcalá et al., 2015; Asaro and Rice, 1977; Kuhlmann-Wilsdorf, 1999):

$$\mathbf{L}^{*} = \dot{\mathbf{F}}^{*}\mathbf{F}^{*-1} = \mathbf{D}^{*} + \boldsymbol{\Omega}^{*} \tag{2. 9}$$

$$\mathbf{L}^{\mathrm{P}} = \dot{\mathbf{F}}^{\mathrm{P}}\mathbf{F}^{\mathrm{P}-1} = \mathbf{D}^{\mathrm{P}} + \boldsymbol{\Omega}^{\mathrm{P}} \tag{2. 10}$$

where $\mathbf{D}^{*}$ and $\mathbf{D}^{\mathrm{P}}$denotes the elastic and plastic strain rate tensors, respectively. $\boldsymbol{\Omega}^{\mathrm{P}}$ is the plastic spin induced by dislocation slip. $\boldsymbol{\Omega}^{*}$ represents the rigid lattice spin which is essential to determine the evolution of grain orientation. Notice that in some specific research topics, such as metal forming with large plastic deformation involved, the elastic deformation can be ignored. In such a case, equation. (2. 8) can be rewritten as $\mathbf{L} = \boldsymbol{\Omega}^{*} + \mathbf{L}^{\mathrm{p}}$.

The Schmid tensor is another important concept in CP theory to account for the directionality of each slip system, defined as (Alcalá et al., 2015; Asaro and Rice, 1977; Kuhlmann-Wilsdorf, 1999):

$$\mathbf{m}^s = \mathbf{b}^s \otimes \mathbf{n}^s \tag{2. 11}$$

with $\mathbf{b}^s$ and $\mathbf{n}^s$ vectors represent respectively the Burgers vector (slip direction) and slip plane normal of the slip system s. m^s can be decomposed into the symmetric part $\mathbf{P}^s$ and the anti-symmetric part $\mathbf{A}^s$ as (Alcalá et al., 2015; Asaro and Rice, 1977; Kuhlmann-Wilsdorf, 1999):

$$\mathbf{m}^s = \mathbf{P}^s + \mathbf{A}^s \tag{2. 12}$$

$\mathbf{P}^s$ and $\mathbf{A}^s$ are defined as follows:

$$\mathbf{P}^s = (\mathbf{b}^s \otimes \mathbf{n}^s + \mathbf{n}^s \otimes \mathbf{b}^s)/2 \tag{2. 13}$$

$$\mathbf{A}^\alpha = (\mathbf{b}^s \otimes \mathbf{n}^s - \mathbf{n}^s \otimes \mathbf{b}^s)/2 \tag{2. 14}$$

Through the decomposed Schmid tensor, the plastic velocity gradient L^p can be linked with the shear rate $\dot{\gamma}^s$ of all activated slip systems (Alcalá et al., 2015; Asaro and Rice, 1977; Kuhlmann-Wilsdorf, 1999):

$$\mathbf{L}^\mathrm{p} = \sum_s^n \dot{\gamma}^s \, (\mathbf{P}^s + \mathbf{A}^s) = \sum_s^n \dot{\gamma}^s (\mathbf{b}^s \otimes \mathbf{n}^s) \tag{2. 15}$$

with

$$\mathrm{D}^\mathrm{P} = \textstyle\sum_s^n \dot{\gamma}^s \mathrm{P}^s \text{ and } \Omega^s = \sum_s^n \dot{\gamma}^s \mathrm{A}^s \tag{2. 16}$$

2.6.1 Constitutive laws for slip

The kinematic equations mentioned in 2.5.1 demonstrate a connection between the strain rate for a single crystal and the shear rates of all slip systems. The expression of $\dot{\gamma}^s$ as a function of stress is essential to establish the single-crystal stress-strain

relationship. The driving stress for a dislocation to glide is commonly known as the resolved shear stress (RSS), given as $\tau^s = \mathbf{P}^s \cdot \mathbf{S}$, where **S** denotes the applied deviatoric Cauchy stress tensor as hydrostatic pressure does not contribute to slip. In general, two types of rate-sensitive laws are commonly used in CP modelling to address the relationship between $\dot{\gamma}^s$ and τ^s, namely the visco-plastic power law and the Arrhenius-type law. The former is a simplified empirical equation proposed by Hutchinson (Hutchinson, 1970), written as:

$$\dot{\gamma}^s = \dot{\gamma}_0 \cdot \left(\frac{|\tau^s|}{\tau_c^s}\right)^n \operatorname{sign}(\tau^s) \qquad \textbf{(2. 17)}$$

with $\dot{\gamma}_0$ represents the reference shear rate. τ_c^s is defined as the critical resolved shear stress (CRSS) which weighs the resistance of dislocation motion on slip system s. Here $\operatorname{sign}(\tau^s)$ indicates the direction of the shear rate is enforced to be the same as the driving stress.

2.6.2 Crystallographic Texture

Normally, the macroscopic mechanical properties are determined by the crystallographic texture (Klosek, 2017). Polycrystals are aggregates of single crystals, whose orientation is highly dependent on the manufacturing process. If the grains exhibit a completely random orientation distribution, the macro-scale material behaviour would be isotropic. Conversely, the anisotropic materials show a preferably orientated texture. Therefore, the anisotropic behaviour of crystallographic texture is indicated by the grain orientations via the individual tensorial character of each grain and orientation-dependent boundary conditions. In other words, the grain orientation built-up crystallographic texture is an essential parameter in materials property prediction, which means the macro-scale behaviour is indicated by micro-scale anisotropic texture.

By considering the crystallographic texture in modelling, the main anisotropic character of polycrystals is taken into account. Moreover, its evolution under deformation can be described through crystal plasticity, which is inherent via associated deformation mechanisms (dislocation, twins, phase transformation etc.). As the grains have preferred

rotate orientations under forming, the texture evolution is tracked in the deformation process during the simulation.

2.6.2.1 Euler angle notations

The grain orientation is normally described by three Euler angles, ϕ_1, Φ and ϕ_2. The single crystal rotation is shown in Figure 2. 24, which describes the transition from the reference coordinate system (XYZ) to the crystallographic coordinate system (xyz). By rotating ϕ_1 about Z axis, Φ about X axis, and ϕ_2 about Z axis, the orientation of the grain is defined. Notice that the magnitude of the rotation range is between 0^o to 45^o due to the symmetric character of the specimen. Moreover, by considering the individual grain orientation altogether, the texture of the composed polycrystals is also determined.

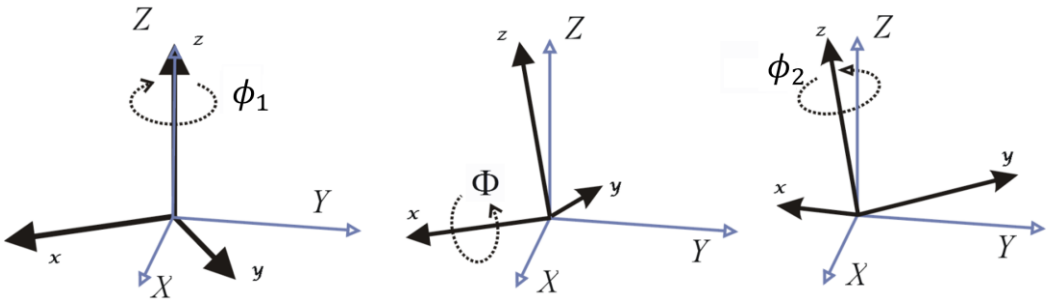

Figure 2. 24 Grain rotation with Euler angles ϕ_1, Φ and ϕ_2 (Wen, 2013).

2.6.2.2 Grain orientations evolution

Rotation angle ϕ_1 about the Z axis is described through the matrix (Landau and Lifshits, 1960; Rose, 1995):

$$Z_1 = \begin{pmatrix} \cos\phi_1 & \sin\phi_1 & 0 \\ -\sin\phi_1 & \cos\phi_1 & 0 \\ 0 & 0 & 1 \end{pmatrix} \quad \textbf{(2. 18)}$$

Rotation angle Φ about the X axis is described as (Landau and Lifshits, 1960; Rose, 1995):

$$X = \begin{pmatrix} 1 & 0 & 0 \\ 0 & \cos\Phi & \sin\Phi \\ 0 & -\sin\Phi & \cos\Phi \end{pmatrix} \quad \textbf{(2. 19)}$$

Rotation angle ϕ_2 about the Z axis is described by (Landau and Lifshits, 1960; Rose, 1995):

$$Z_2 = \begin{pmatrix} \cos\phi_2 & \sin\phi_2 & 0 \\ -\sin\phi_2 & \cos\phi_2 & 0 \\ 0 & 0 & 1 \end{pmatrix} \quad \textbf{(2. 20)}$$

Therefore, in the simulation, the corresponding transformed orientation matrix R is given as:

$$R = Z_1 \cdot X \cdot Z_2$$
$$= \begin{pmatrix} \cos\phi_1\cos\phi_2 - \sin\phi_1\sin\phi_2\cos\Phi & \sin\phi_1\cos\phi_2 + \cos\phi_1\sin\phi_2\cos\Phi & \sin\phi_2\sin\Phi \\ -\cos\phi_1\sin\phi_2 - \sin\phi_1\cos\phi_2\cos\Phi & -\sin\phi_1\sin\phi_2 + \cos\phi_1\cos\phi_2\cos\Phi & \cos\phi_2\sin\Phi \\ \sin\phi_1\sin\Phi & -\cos\phi_1\sin\Phi & \cos\Phi \end{pmatrix}$$

(2. 21)

The orientation matrix R is updated in each incremental step for each grain. The incremental rotation matrix R^{rot} is given by the rotation angle α, and lattice rotation $\mathbf{\Omega}^*$ as follows:

$$R^{rot} = I + \frac{\sin\alpha}{\alpha}\cdot\widehat{\Omega} + \frac{1-\cos\alpha}{\alpha^2}\cdot\widehat{\Omega}^2 \text{ with } \widehat{\Omega} = \mathbf{\Omega}^*\Delta t \quad \textbf{(2. 22)}$$

The rotation angle α is obtained from $\mathbf{\Omega}^*$ (Lee et al., 2001):

$$\alpha^2 = \frac{\mathrm{tr}(\widehat{\Omega})}{2} \quad \textbf{(2. 23)}$$

Thus, the updated orientation matrix $R_{t+\Delta t} = R^{rot}\cdot R_t$. At the first step, $R_t = R$.

2.6.3 Extension of crystal plasticity formulation to twinning and dislocation climb

As mentioned previously, the CP theory is originally introduced to describe the effects of dislocation slip accounting for the geometric configuration of the slip systems. The formulation introduced in section 2.5.1 is a mature method. However, it cannot fulfil the need for certain materials and loading conditions where slip may not be the only activated plastic deformation mechanism. With certain properties or under certain loading conditions, mechanical twinning and dislocation climb can be found and significantly affect the material properties. As for slip, the activation of these mechanisms is restricted to specific planes and directions depending on the lattice structure, and thus their effects can be accounted for in the CP framework owing to its tensional nature (expressed in tensors).

2.6.3.1 Crystal plasticity based mechanical twinning model

Mechanical twinning is considered as one of the fundamental plastic deformation mechanisms in metals. The corresponding effects on plastic deformation can be summarised in two kinds: the orientations of twinning and the slip associated with twinning formation. The occurrence of twinning is related to stacking fault energy (SFE), temperature, strain rate etc. (Christian and Mahajan, 1995). As activated by strong shear stress, part of the lattice matrix will be rearranged and the twinned region (layer) will be formed which is mirrored to the original region. The twinning mechanism is driven by the RSS and accumulates shear strain on the same twinning planes. Twinning is a variety of dislocation glide (Ashby, 1972). Therefore in CP modelling, twinning can be treated as a special slip (with different stress-strain relationships). Different from the slip, which can be activated in both positive and negative directions, mechanical twinning can only be activated in one direction.

Moreover, additional treatments on the reorientation of the twined region are accordingly necessary as well. In 1987, (Van Houtte, 1978) proposed a twinning model that divided one grain into a number of independent sub-grains with the same orientation. The sub-grains can be orientated according to a given twinning system. However, this is also the disadvantage of the Van Houtte model, as the given twinning system may not be the most active twinning system (Tomé et al., 1991).

Later in the Anand-Kalidindi twinning model (Kalidindi, 1998; Staroselsky and Anand, 1998), each grain is assigned a twined region with a volume fraction (initially zero) varying during the plastic deformation (see Figure 2. 25).

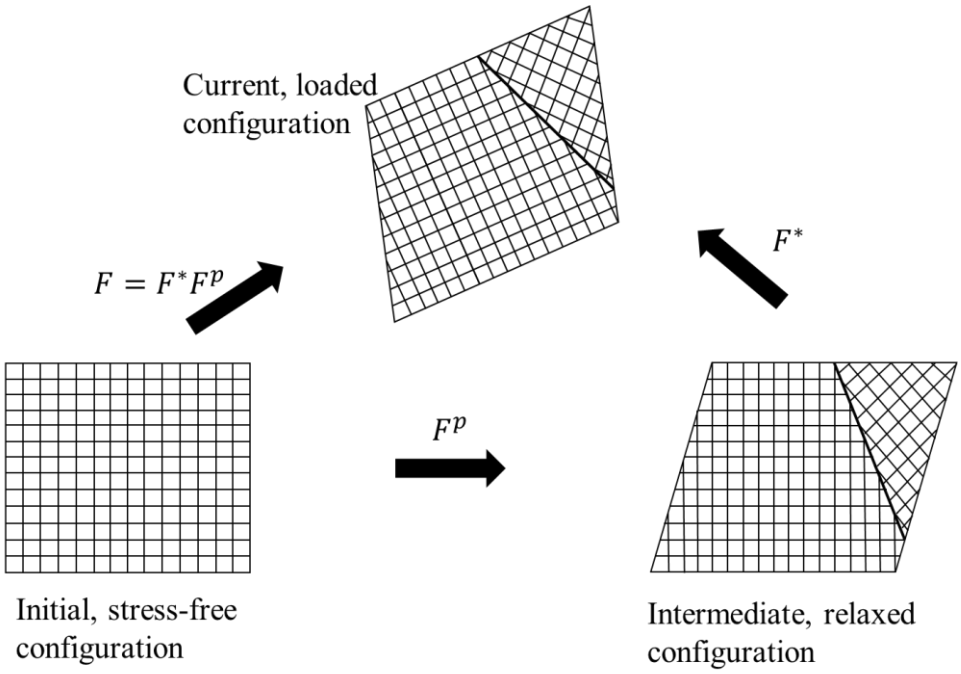

Figure 2. 25 Decomposition of deformation gradient, the kinematic scheme proposed by (Kalidindi, 1998) and (Staroselsky and Anand, 1998).

Therefore, the velocity gradient consists of the contributions from the slip in the untwined region, slip in the twined region, and twinning in the untwined region. Accordingly, the Schmid tensor $\mathbf{m}^s$ of the slip or twinning system s is divided into: $\mathbf{m}^s_{s-untw}$ (slip in the untwined region), $\mathbf{m}^s_{s-tw}$ (slip in the twined region) and $\mathbf{m}^s_{tw-untw}$ (twinning in the untwined region). Therefore, the plastic velocity gradient $\mathbf{L}^p$, which is considering the twinning volume fraction, is given as:

$$\mathbf{L}^p = f\sum_{s}^{Ns-t}\dot{\gamma}^s\mathbf{m}^s_{s-tw} + \left(1-f_{twinning}\right)\sum_{s}^{Ns}\dot{\gamma}^s\mathbf{m}^s_{s-untw} + \sum_{s}^{Ntw}f^s_{twinning}\dot{\gamma}^{tw}\mathbf{m}^s_{tw-untw} \quad \textbf{(2. 24)}$$

Here, f_{tw} is the volume fraction of the twinning region, $f^s_{tw}$is the volume fraction of twinning accumulated by slip system s. $Ns-t$ is the number of slip systems in the

twined region, Ns is the number of slip systems in the untwined region, Ntw is the number of twinning systems in the untwined region, γ^{tw} is the shear strain of the twinning system, which is a constant (Kalidindi, 1998), and $\dot{f}^s\gamma^{tw}$ is the equivalent shear rate on twinning system s. Similarly, the deviatoric Cauchy stress tensor $\boldsymbol{S}$ is split into twined $\boldsymbol{S}^{tw}$ and untwined $\boldsymbol{S}^{untw}$. Therefore, $\boldsymbol{S} = (1 - f_{tw}) \cdot \boldsymbol{S}^{untw} + f_{tw} \cdot \boldsymbol{S}^{tw}$.

During the deformation, there will be more twined regions generated from the untwined region. The description of the transferred volume fraction of twinning is given as:

$$\Delta f_{tw}^s = \frac{\dot{\gamma}_0}{\gamma^{tw}} \left(\frac{\tau^s}{\tau_c^s}\right)^n \Delta t \qquad \textbf{(2. 25)}$$

Notice that, Δf_{tw}^s should be zero when the calculated value of τ^s is negative, since the twinning is only in one direction, which is positive.

Tomé et al. (Tomé et al., 1991) proposed a predominant twin reorientation (PTR) scheme, where the shear strain of each twinning system can be tracked throughout the deformation. The volume fraction of the twinning region is defined on each twinning system of each grain: $V^{t,g} = \gamma^{tw}/\boldsymbol{S}^{tw}$, $\gamma^{t,g}$ is the shear strain from twinning systems, and S^t is the characteristic twin shear. Once the twinning criterion is met, the grain will be completely reoriented along the most active twinning system, and the twinning volume fraction will be approximately controlled by the number of reoriented grains. The criterion is given by the twinning volume fraction as: $V^c = A^{c1} + A^{c2}\frac{V^{eff}}{V^{acc}}$. V^{eff} is an effective twinned fraction, which is already reoriented. V^{acc} is the sum of twinning fraction over all twinning systems and all grains, given as: $V^{acc} = \sum_g \sum_t V^{t,g}$. However, the PTR scheme could overestimate the twinning volume fraction, as only a part of the grain should be reorientated via twinning (Beyerlein et al., 2011; Prakash et al., 2008).

More recently, the geometry relationship between slip systems and the twin layer is addressed to account for the twin barrier effect (McCormack et al., 2018; Proust et al., 2007).

2.6.3.2 Crystal plasticity based dislocation climb model

As introduced in 2.2.3, dislocation climb is the movement of edge dislocations, whose motion is perpendicular to their slip planes to avoid the obstacle. This process is achieved by edge dislocations absorption or emission of vacancy and interstitial atom. Dislocation climb is an important mechanism at high-temperature and low-stress regimes. Moreover, dislocation climb is highly active under irradiation environments, due to which, vacancies and self-interstitials are super-saturated. Hence, quantifying dislocation climb contribution by modelling method is crucial for thermal and irradiation creep study. In Lebensohn et al. (Lebensohn et al., 2010; Lebensohn et al., 2012), a climb model is proposed based on the directional concept of CP theory. The model is built according to the dislocation coordinate system ($\boldsymbol{\chi}^s$, n^s, $\mathbf{t}^s$), under which, the slip coordinate system ($\mathbf{b}^s$, n^s, $\boldsymbol{\xi}^s$) is adopted as the reference frame. In order to represent the mix of edge and screw dislocations, the dislocation coordinate ($\boldsymbol{\chi}^s$, n^s, $\mathbf{t}^s$) is used to describe the virtual dislocation movement. In the dislocation coordinate system ($\boldsymbol{\chi}^s$, n^s, $\mathbf{t}^s$), $\mathbf{t}^s$ represents the direction along the dislocation line of the hybrid, while $\boldsymbol{\chi}^s$ denotes gliding direction. ψ is the angle between the dislocation coordinate system ($\boldsymbol{\chi}^s$, n^s, $\mathbf{t}^s$) and the slip coordinate system ($\mathbf{b}^s$, n^s, $\boldsymbol{\xi}^s$), which is because of the difference between edge and screw dislocations. According to this, while the dislocation glide (Schmid) tensor determined by the tensorial calculation remains the same as equation (2. 11), the dislocation climb tensor is described as:

$$c^s = \mathbf{b}^s \otimes \boldsymbol{\chi}^s \qquad \textbf{(2. 26)}$$

As only edge dislocation can climb, therefore, the tensor for dislocation climb is influenced by the dislocation population. This can be specified through the angle ψ, which is given as $tg(\psi) = \rho_{edge}/\rho_{screw}$, ρ_{edge} and ρ_{screw} are the density of edge dislocation and screw dislocation, respectively. Notice that, when the edge dislocation is the only type of dislocation considered, there is $\mathbf{b}^s = \boldsymbol{\chi}^s$. Therefore, $c^s = \mathbf{b}^s \otimes \mathbf{b}^s$ (Wen et al., 2017a). On the other hand, as there is no dislocation climb when there is no edge dislocation, the climb tensor will be zero.

The climb driving stress can be described in a similar way to slip: $\tau^s_{climb} = Q^s \cdot S$, here Q^s is the symmetric part of c^s. The plastic strain rate can be expressed as:

$$D^P = \sum_s^n \dot{\gamma}^s P^s + \sum_s^n \dot{\beta}^s Q^s \quad \textbf{(2. 27)}$$

where $\dot{\beta}^s$ denotes the climb strain rate. In the work of Lebensohn et al. (Lebensohn et al., 2012), $\dot{\beta}^s$ is described by an empirical power law. Moreover, there are other physics-based laws (Patra and McDowell, 2012; Wen et al., 2020b) are also adopted to describe dislocation climb in the CP modelling framework.

2.7 CP-based modelling for polycrystals

Hypothetically, the CP-based formulation can be adapted into any crystalline material to describe the corresponding plastic deformation. Scientific research and industrial application mainly focus on polycrystalline metals, as CP-based formulation is a quantitative description of the stress-strain response for single crystals. There is a need for the implementation of CP-based formulation into applicable homogenization methods.

In this section, the polycrystal models will be categorized into two groups according to their target length scale: mean-field and full-field models. The former represents the material through a collection of crystal orientations with assigned volume fractions. It usually deals with grain interaction based on certain general assumptions, and the internal stress distribution within each grain is assumed to be homogenous. In this case, some local information, such as the interaction between neighbouring grains, could be missing. On the other hand, this kind of model has the ability to simulate texture evolution and mechanical behaviour with relatively high efficiency compared with full-field models. The full-field models consider the microstructure through the input micrograph with detailed information, where the mechanical behaviour is captured by CP formulation in each voxel. The detailed microstructure input information results in more computational resources. However, the localized effects or characters can be precisely simulated. For some specific scientific research, which desires high accuracy, the full-field is required, such as the quantification of material damage criterion which requires access to intragranular stress (Wang and Wen, 2021)

2.7.1 Damage effect in polycrystals

According to the geometry dimension, there are four damage types in crystalline: vacancy and interstitial atom represented point defects; dislocation represented line defect; grain boundary, twinning represented planar defects; void, crack represented volume defect. The existence of these defects is not always detrimental to the mechanical properties of materials, but can have some positive effects. For example, high dislocation and precipitation volume number density can contribute to higher critical resolved shear stress (CRSS); finer grain structure resulting in a higher amount of grain boundaries can enhance diffusional creep; more dislocations decorated grain boundaries are more thermal-stable etc. However, depending on the size and shape of the void and crack, they can result in high-stress concentration and perform as pre-crack in dynamic loading.

For ductile polycrystalline metals, the nucleation and accumulation of voids on grain boundaries are assumed as the principle of damage development mechanism (Bammann and Aifantis, 1989; Gurson, 1977). Under the continuum damage mechanics framework, the description of damage can be scalar damage variables, vector- or higher-rank tensor-based damage variables (Johnson and Cook, 1985; Menzel and Steinmann, 2003; Murakami, 1983). Apart from limiting the damage on grain boundaries for ductile materials, there are also non-local methods or gradient-based damage methods (Voyiadjis et al., 2004). By formulating the Crystal Plasticity (CP) based constitutive relationship within the framework of continuum damage mechanisms. The internal variables and the response of the material can be expressed by thermodynamics principles (Kumar and Talreja, 2003).

2.7.2 Mean-field models

The rough approximations are normally applied in the early development of polycrystal models, as there are a range of detailed mechanisms were not unveiled. In 1938, the Taylor model was proposed assuming strain is constant, which means each grain is subjected to the same velocity gradient as the bulk (Taylor, 1938). On the contrary, the Sachs model introduced the rule on stress, which supposes the stress for each grain is proportionate to the macroscopic value (Sachs, 1928). For some of the Sachs model applications, the local and bulk stresses are assumed same, which indicates the uniform stress assumption. For the uniform stress rules, the model is the Static model. It is worth

mentioning that Taylor and Static models are also called the upper and lower bound approximations. They represent the two extreme cases in polycrystal homogenization. Normally, the actual solution case for the aggregate should vary between the extremes.

Nevertheless, the Taylor model normally can provide relatively good predictions of texture evolution under plastic deformation, especially for materials with low Stacking Fault Energy, e.g. Copper. On the other hand, the Taylor model exhibits some deviations from the extreme assumption. Particularly the predictions of large plastic deformation, after which the crystals are significantly shaped. For this need, the relaxed-constraints models were proposed. The shear modes are added to relax the full-constraint uniform strain condition. Van Houtte et al. (Van Houtte et al., 2005) summarized these models with a general expression as:

$$\bar{L} = L + \sum_{r=1}^{R} K^r \dot{\gamma}_r^{rlx} \qquad \textbf{(2. 28)}$$

here $\bar{L}$ represents the velocity gradient of the aggregate. R denotes the total number of relaxations, which is according to the deformed grain shape. K^r is the relaxation mode. $\dot{\gamma}_r^{rlx}$ is a free variable determined through the minimization of the plastic work (dissipation) from both slip and relaxation (Van Houtte et al., 2005).

Nonetheless, compared to the original Taylor model, there are no compelling advantages in the classic relaxed-constraints model applications (Van Houtte et al., 2005). This is because the local interactions between neighbouring crystals are not taken into account. Therefore, there is a significant improvement in simulation results by considering the neighbouring grains interactions in multigrain models, e.g. LAMEL (Lee et al., 2002; Van Houtte et al., 2002; Van Houtte et al., 2005) and grain interaction (GIA) (Crumbach et al., 2006; Engler et al., 2005) models. The whole polycrystals are broken down into a range of clusters, each consisting of several crystals, which are chosen arbitrarily from the original input micrograph. The full-constraints Taylor model is applied to every cluster, while the relaxed-constraints model is adapted between each cluster.

LAMEL model is designed for rolling tests, dealing with clusters with two grains, in which the grain interfaces keep parallel to the rolling direction. The relaxation factor

K^r of the neighbouring grains is imposed to be opposite to each other. While GIA model assigns eight grains within one cluster, which contains four two-grain stacks. The grain boundaries and the cluster/matrix interfaces are arranged perpendicularly. Similar to the LAMEL model, the two-grain stacks are relaxed. However, the energy of the boundaries (described by the density of geometrically necessary dislocation, GND) are considered in the total plastic deformation to provide inter-grain compatibility (Engler et al., 2005).

Each grain is assumed as an individual ellipsoidal inclusion by self-consistent type CP models, in which, the inclusion is embedded in the homogeneous effective medium (HEM) with the uniform properties of the bulk. In this way, the interaction between each grain and the HEM is accounted for the original complicated local grain interactions. The interaction laws are employed for this simplification. Notice that, the properties of each grain and HEM are updated at each calculation step. Therefore, iterative convergence algorithms are necessarily adapted to achieve consistency for polycrystal deformation.

The self-consistent models have been developed since the 1960s, and many models are established according to the same principle. However, there is a range of different descriptions for the grain-HEM interaction, e.g. (Ahzi and M'Guil, 2008; Berveiller and Zaoui, 1978; Hill, 1965a; Kröner, 1961). In this section, the prominent visco-plastic self-consistent (VPSC) model will be introduced summarily (Beyerlein and Tomé, 2008; Lebensohn et al., 2007; Lebensohn and Tomé, 1993; Wroński et al., 2022).

In the VPSC model, the stress-strain responses for microscopic single crystal and the macroscopic bulk are given in similar constitutive laws as follows:

$$\begin{aligned} \mathrm{D} &= \mathrm{M}\mathrm{S} + \mathrm{D}_0 \\ \overline{\mathrm{D}} &= \overline{\mathrm{M}}\overline{\mathrm{S}} + \overline{\mathrm{D}}_0 \end{aligned} \qquad \textbf{(2. 29)}$$

where $\overline{\mathrm{S}}$ and $\overline{\mathrm{D}}$ denote the macroscopic deviatoric Cauchy stress and macroscopic plastic strain rate of the aggregate. M and $\overline{\mathrm{M}}$ are the local and macroscopic fourth-order visco-plastic compliance tensors, respectively. D_0 and $\overline{\mathrm{D}}_0$ represent the back-extrapolated terms for the single grain and the bulk. The grain shape is considered through the Eshelby tensor E to describe its influence on the grain interaction. The interaction law is given as:

$$D - \bar{D} = -\widetilde{M}(S - \bar{S}) \quad \textbf{(2. 30)}$$

where the interaction tensor $\widetilde{M}$ is expressed as:

$$\widetilde{M} = n^{eff}(I - S)^{-1} : S : \bar{M}^{secant} \quad \textbf{(2. 31)}$$

here $\bar{M}^{secant}$ denotes the macroscopic visco-plastic compliance tensor for the secant case. The parameter n^{eff} can be varied to obtain different interactions: $n^{eff} = 1$ is the secant case, $n^{eff} = n$ describes a Tangent case and $1 < n^{eff} < n$ represents an intermediate interaction. In the cases of $n^{eff} = 0$ and $n^{eff} \to \infty$, the interaction law will be equivalent to the upper and lower bound approximations, respectively. A detailed description of the VPSC model can be found in Lebensohn et al. (Lebensohn et al., 2007; Wroński et al., 2022). It is worth mentioning that under the hypothesis of self-consistent modelling, the predicted resultant textures are normally marginally 'sharper' than foreseen. This is because of the absence of 'local interaction'. For instance, in reality, grains with analogous orientations can be shaped individually as they have various local conditions. However, in self-consistent models, the grains with the same orientations will be applied with the same interaction law, which leads to the same resultant grain orientation.

Furthermore, texture simulation is normally employed to evaluate the homogenization methods, which aims to eliminate the effects of single-crystal behaviour. One of the typical problems is FCC rolling transition, which has been comprehensively studied. An exhaustive review has been proposed by Leffers and Ray (Leffers and Ray, 2009).

The anisotropy can cause the uncertainty of complex deformation, especially for materials with poor formability. Moreover, in single-crystal, the anisotropy character normally influences the interaction between neighbouring grains, and results in different local mechanical behaviour. Consequently, it is essential to consider the anisotropy (directionality) and its relevant effects. However, it is beyond the ability of mean-field modelling. Moreover, the relationship between the deformation, texture evolution and the resulting mechanical properties is supposed to be clarified. There are a range of deformation mechanisms responsible for the texture evolution during the

deformation, e.g. the evolution of grain orientation, precipitation, work hardening, damage accumulation, grain recrystallization and recovery etc.

2.7.3 Full-field models

In 1982, the CP-FEM simulation was first implemented by Peirce et al. (Peirce et al., 1982), who simulated single-crystal tensile behaviour with simplified slip systems. It was a constitutive framework including localised plastic flow and non-uniform patterns of lattice rotations. With this as the basis, the CP-FEM had also been applied to solve rate-dependent boundary value problems in polycrystals (Asaro and Needleman, 1985). Thenceforth, CP-FEM has been applied to consider more complicated slip configurations and multi-grain structures owing to the increasing computational power (Roters et al., 2010).

As the most efficient numerical solution method for partial differential equations, finite element (FE) has been applied in multiple scenarios in CP models. The applications of CP-FEM include but are not limited to: texture revolution (Delannay et al., 2009; Lee et al., 2007; Mayeur et al., 2008; Raabe et al., 2002; Wang et al., 2019; Zhang et al., 2019), anisotropy (Furstoss et al., 2021a; Furstoss et al., 2021b; Liu et al., 2020; Zhang et al., 2009), damage behaviour (Amelirad and Assempour, 2022; Li et al., 2022a; Li et al., 2021a; Li et al., 2022b; Xiao et al., 2021), creep deformation (Li et al., 2022a; Li et al., 2021a; Xiong et al., 2020; Zhou et al., 2022), twinning (Jin et al., 2019; Liu et al., 2021; Yaghoobi et al., 2021; Zhang et al., 2022), and recrystallization (Ma et al., 2019; McElfresh and Marian, 2022; Sarrazola et al., 2020). Under the CP-FEM framework, the whole structure is mapped by meshes. In addition, each FE integration point is simulated by the CP model separately, which considers their individual stress-strain response and texture revolution. Consequently, addressed by FE homogenisation, the anisotropy of elastic-plastic shear is associated with various lattice defects is mapped.

Based on CP theory, the force-displacement relationship is determined and input to the CP-FEM framework within a given finite volume element. Additionally, FEM offers the flexibility to deal with the problems suffered by complex loading environments, which are also characterised by randomly shaped geometries. Thus, for complex intragranular or intergranular boundary conditions, CP-FEM is relatively practical to

resolve associated crystalline mechanical problems. Compared with continuum-type models, CP-FEM can consider explicitly the virtual microstructure with grain topology. As the input for CP-FEM simulation, the detailed microstructure information can be directly observed from meso-scale characterization or can be arbitrarily generated to represent and summarise specific materials' microstructure characteristics. Crystallographic texture, grain shapes and sizes, dislocation substructures and densities, internal stresses, and surface roughness can all be included to represent certain microstructures.

The CP-FEM simulations are conducted on the entire mapped crystallographic structure with meshes, therefore, both the local and global stress-strain response and damage evolution can be captured. In addition, depending on the practical situations, the defects at the meso-scale, e.g. pores and precipitation can also be embedded in the input microstructures for research needs (Roters et al., 2010). Similar to large-scale FEM, the mesh generation in CP-FEM is also carried out by defining nodes, but sometimes, each grain can be treated as an individual object. Figure 2. 26 presents a typical meshing example of a laboratory-measured grain structure with each grain mapped individually (Zhao et al., 2008). Other advanced meshing techniques are also available to ensure accuracy. For example, automatic re-meshing was achieved by Logé et al. (Logé et al., 2008) using a special periodic smoothing algorithm to enhance the geometrical compatibility during recrystallization. Yadegari et al. (Yadegari et al., 2014) used two-level Voronoi tessellation, which can consider complex grain morphologies with spatial and size features, coping with complex and non-convex grains.

Figure 2. 26 Schematic CP-FEM meshing example with each grain mapped individually (Zhao et al., 2008).

According to the CP-based formulation, CP-FEM is equipped with the ability to reveal the effects of plastic flow and hardening evolution at the elementary shear system level. Through the associated constitutive equations, various plastic deformation features can be captured considering local boundary conditions, e.g. stress-strain behaviour, strain path changes, rate effects, texture evolution and size-effects. Moreover, the anisotropic characters can be presented adequately by CP theory. According to actual needs, technically, CP-FEM simulation can begin with any deformation stages, which can be achieved by the applicable adjustment of grain mapping and the according microstructure parameters. Although only a limited area can be covered in CP-FEM analysis, the whole structure can be simulated by applying the representative grain region and appropriate boundary conditions. Therefore, the complicated polycrystal deformation prediction can be easily achieved.

Precise capture of damage development is one of the CP-FEM advantages since the type III stress distribution can be predicted accurately. The failure occurs due to stress-strain incompatibilities, which results in shear localisation. CP-FEM can consider the stress-strain localisation resultant uneven damage distribution through the grain structures. Needleman et al. (Needleman and Rice, 1978) originally employed CP-FEM to model the microstructure damage development, which was according to the strain energy definition. Thenceforth, a series of CP-FEM modelling have been built up to simulate the local failure status, e.g. Nicolaou and Semiatin (Nicolaou and Semiatin, 2004) adapted a continuum approach to the CP-FEM framework, which can track the local cavitation development, therefore analyze the associated damage behaviour. The failure will only occur when the critical cavitation value is achieved. CP-FEM can also handle the damage nucleation at grain interfaces through the relationship between boundary properties and interfacial structure (Randle, 2004; Watanabe and Tsurekawa, 2004).

An alternative full-field solver of CP-FEM is crystal plasticity fast Fourier transform (CP-FFT). Different from employing FE to solve the convergence and homogenisation, the fast Fourier transformation (FFT) algorithm is utilized, which can significantly accelerate the computational efficiency. The CP-FFT was originally developed by

Lebensohn (Lebensohn, 2001) adopting the FFT method proposed by Moulinec and Suquet (Moulinec and Suquet, 1998) to predict local stress-strain response, crystal morphology and texture evolution of polycrystals (could be 3D). Later, the CP-FFT has been employed in various deformation scenarios, e.g. (Brenner et al., 2009; Eisenlohr et al., 2013; Kanjarla et al., 2012). Essentially, the FFT simplifies the local homogenization work by incorporating the equilibrated stress field with a constitutive potential based on iteratively adjusted compatible formulations. The local tress-strain response can be solved by Fourier transformation with periodic Green functions, and convolution integrals under the periodic unit cell. This aims to reduce the real space convolution integrals into simple products in Fourier space. Through the calculation, the polarization field can be transformed into Fourier space and the mechanical fields can be achieved by Cartesian space transformation. Moreover, since the polarization field is associated with a strain field, which is unknown, the iterative scheme is required in CP-FFT. Notice that the periodic boundary condition is essentially required in CP-FFT (optional in CP-FEM), which means its application is not as broad as CP-FEM.

2.8 Summary

In this chapter, the characteristics of AM techniques and AMed products are reviewed; the main crystal structure features, deformation mechanisms, and strengthening mechanisms of metallic materials are summarised; and the development and applications of CP modelling are reported. After introducing the features of AMed material microstructure and metallic materials' physical mechanisms, the modelling methods which can capture the most of microstructure characters are addressed in detail. In particular, VPSC and CPFEM modelling frameworks are the most discussed. This chapter is a general introduction to the material, modelling method and physics mechanisms employed in this work. The incorporated physics-based laws and formulation adapted in this project will be depicted and discussed in Chapter 3, while the implication of hierarchical multi-scale (HMS) modelling application has then been discussed to provide examples of state-of-the-art in Chapter 1. The detailed computational formulation employed in both the VPSC and CP-FEM frameworks will be introduced in Chapter 3. The certain applications of the HMS modelling method under VPSC and CP-FEM frameworks in this work will be illustrated in Chapters 4,

and 5. The VPSC framework will be adapted for a general CP-based description of mechanical behaviour; while the CP-FEM framework will capture the damage development including more detailed materials microstructure, especially the unique features (e.g. pores) in AMed materials. As precipitation plays a significant role during the high-temperature creep deformation, its nucleation, growth and dissolving will be described and discussed extensively in Chapter 3 associated with the Thermo-Calc simulations.

Chapter 3 A physics-based model to study plasticity under visco-plasticity self-consistent and crystal plasticity finite element frameworks

In this chapter, the implementation of the visco-plasticity self-consistent (VPSC) and crystal plasticity finite element (CPFE) frameworks used in this project are described in detail. The physics-based crystal plasticity (CP) model built to describe the SS316L creep behaviour is introduced afterwards. This microstructure-sensitive physic-based CP model aims to deliver a full describe the deformation mechanisms and strengthening mechanisms mentioned in Chapter 2. The state-on-art of the mechanism-based model is addressed in this chapter as well, which provides a more accurate description of materials' creep behaviour. The relevant applications of the combination of this newly

proposed model with VPSC and CP-FEM characterised by various microstructure features will be illustrated in Chapters 4, 5 and 6.

3.1 Introduction

The microstructure-related materials' mechanical properties are multi-scale based. The scale of grain/sub-grain sizes, precipitations, solid solution, and grain boundary are micro-scale. The deformation mechanisms are meso-scale, e.g. texture evolution, grain interaction, and mechanical hardening. The resultant bulk mechanical behaviour is large-scale, which is normally indicated as stress/strain curves. As a consequence of the complex microstructure, in reality, the mechanics of materials are controlled by a broad spectrum of simultaneously operative deformation mechanisms, which are reviewed in Chapter 2. Furthermore, these physical phenomenon occur and develop under various length and time scales. Therefore, it is crucial to have a detailed understanding of materials' mechanical behaviour at different scales. The establishment of a microstructure-based multiscale constitutive model can link the detailed microstructure characteristics with the corresponding mechanical properties.

Crystal plasticity (CP) is a multi-scale based constitutive theory, which can be applied from atomic movement to bulk mechanical. Normally, dislocation slip is the dominant deformation mechanism of polycrystalline in most circumstances. Apart from dislocation slip, dislocation climb, twinning, and grain boundary sliding can also be considered under the CP method. Their effects on the macroscopic properties can be quantified. Since the distribution of dislocations is discrete, and the displacement is discontinuous, it is hard to capture these phenomena by continuum mechanics. On the one hand, a simple treatment is connecting the mean shear rate (considering the physics processes) of each slip system with the uniaxial strain rate of the aggregate, which is carried out through a texture and lattice structure-dependent Taylor factor. This kind of 1-D model is sufficient enough to capture the general material properties. However, more sophisticated outputs such as anisotropy are needed for some specific applications. On the other hand, the slip is assumed uniform in CP theory. Moreover, the discontinuous dislocation movement is assumed as a continuous plastic deformation statistically. According to this, the inhomogeneous deformation evolution can be described by the CP method. In this way, the micro-scale deformation mechanism and

kinematics are linked to the macro-scale mechanism behaviour (Misra et al., 2021). As stress and strain are described by tensors, CP theory can be described with nonlinear variational formulations (Roters et al., 2010). Therefore, the main task of the CP model is to solve a series of partial differential equations. Plastic shear stress and strain are introduced to capture the dislocation movement on each slip system. Through the integration of the evolution equations for the crystalline orientation and the critical CRSS, the local crystallographic state and hardening state of the material are captured. For each integration point, the stress-strain distribution is calculated by the CP model. Accordingly, plastic deformation and lattice rotation are taken into account.

There is a range of mechanisms active during the thermal creep behaviour. All three different dimension damages (point, line and volume) are associated with either materials hardening phenomenon or the dislocation density revolution process. Therefore, there is a need to describe and quantify these effects on the mechanical response. As shown in Figure 3. 1, this predictive tool is not only expected to cover various length scales, but also needs to track in-time structural evolution.

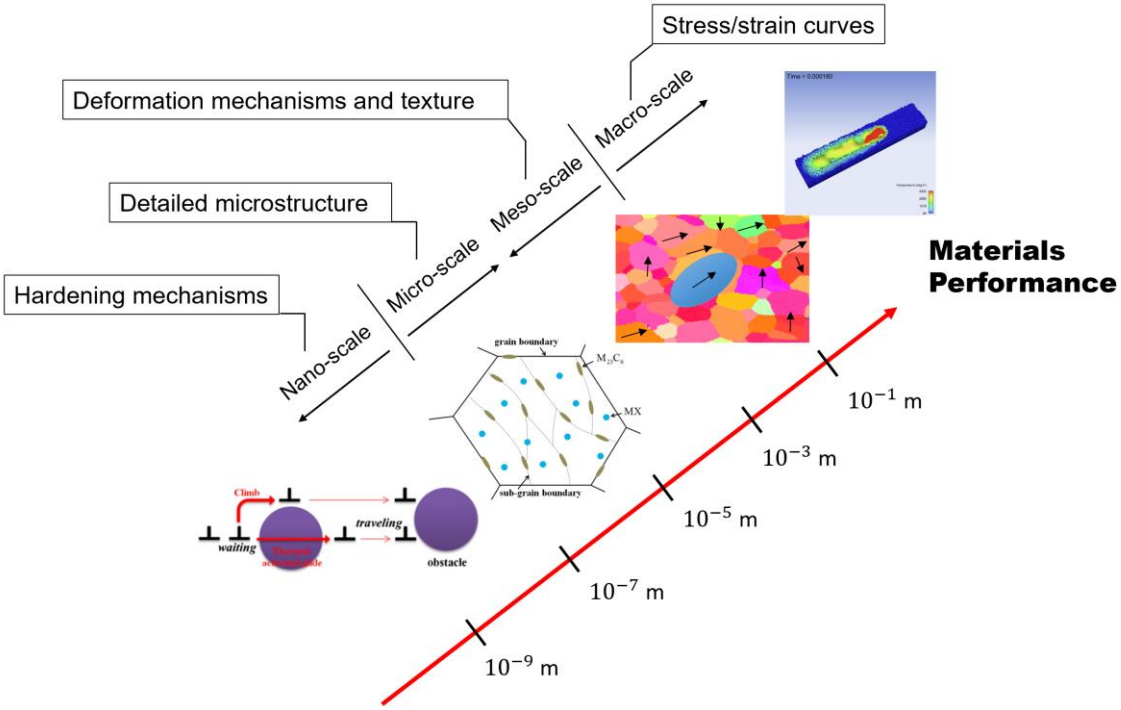

Figure 3. 1 Illustration of hierarchical multi-scale modelling.

The hierarchical multi-scale modelling is capable of conducting simplified implementation with relatively efficient computation since there is no required feedback from the higher scale to the lower scale. It avoids the spurious wave reflections in the connection region caused by the direct coupling of different scales, therefore, there are more numerous uses and strong capabilities (Fang et al., 2022; Ozturk et al., 2019). As introduced in Chapter 2, the strengthening/hardening mechanisms and the plastic deformation response in crystalline materials are the result of the sophisticated interactions between the dislocations, solid solution atoms, vacancies, grain boundaries, precipitates, and other defects (Essmann and Mughrabi, 1979; Kalidindi, 2001; Li et al., 2020; Li et al., 2016; Zhang et al., 2008). Those mechanisms and structural phenomena are associated with different scales, which eventually will account for the bulk behaviour of the material. There are a range of research has been done through experiments and observation to understand the multi-scale relationship between the atomic-scale lattice distortion, nano-scale precipitation evolution, micro-scale dislocation interactions, and macro-scale mechanical response (Ding et al., 2019; Liang et al., 2018; Zhang et al., 2021a). The hierarchical multi-scale modelling can employ the atomic scale simulation results under continuum scales as the constitutive material parameters (Shilkrot et al., 2002). For instance, the information on Burgers vector, lattice fraction, solid solution hardening from various foreign atoms, the strength of Frank-Read dislocation sources and dislocation mobility are taken from molecular dynamics (MD) simulations in nano-scale. The detailed microstructures are captured in micro-scale, such as grain and sub-grain sizes, mobile and im-mobile dislocation densities, precipitation size and number density etc. Moreover, it includes various meso-scale deformation mechanisms, e.g. the phase transition, dislocation glide and climb and deformation twinning (Roters et al., 2019). The texture evolution is also tracked under meso-scale. Eventually, the final bulk stress-strain response is delivered upon all the considered microstructures and mechanisms. The properties are shown on macro-scale, and the performance of material can be evaluated.

The CP theory-based Hierarchical Multi-Scale (HMS) modelling method can greatly benefit modern industries by simulating the mechanical behaviour of metallic materials with high accuracy. As different scale levels are interrelated, the microstructure- and mechanism-dependent deformation response can be tracked precisely. Through the

HMS modelling method, not only the structural safety and economy can be maintained and evaluated, but the materials system can also be redesigned. In addition, by redesigning the alloy, the according processing method can also be improved.

In this chapter, a unified physics-based CP model will be addressed in detail. The multi-scale structural characters and deformation mechanisms during the thermal creep will be covered in this model. By following the description of formulations of the physics-based CP model, the details of the VPSC and CP-FEM framework employed in this work will be introduced. The physics-based CP model will be adapted in both VPSC and CP-FEM frameworks, the according simulation results will be illustrated in Chapters 4 and 5.

3.2 The development of model

In this section, the details of materials and the corresponding experimental information studied in this work will be first introduced, Based on the specific material and the creep conditions, the formulation of the mechanism-based CP model employed in this project is illustrated. The associated hardening mechanisms and deformation behaviour have been reviewed in Chapter 2. In Chapters 4 and 5, this unified CP model will be employed to simulate both the additive manufactured (AMed) stainless steel (SS) 316L and wrought SS316L thermal creep behaviour. Notice that, the thermal creep model introduced in the chapter has only covered the primary stage and secondary stage of materials creep response. The tertiary creep stage, which includes the damage part, will be introduced in Chapter 6.

3.2.1 Thermal creep model

According to Figure 2. 19 and the experimental conditions adopted in this project, the contribution to the total plastic deformation came from both dislocation glide and diffusional creep. When temperature $T < 0.7\,T_m$ (T_m is the absolute melting temperature), Coble creep is usually more dominant than Nabarro-Herring creep in total diffusional creep contribution (Estrin, 1998a; Maruyama, 2008). Normally, for the service conditions of 316L SS in the nuclear industry, the working temperature is lower than two-thirds of the 316L SS melting temperature (McMurtrey et al., 2021).

According to the melting point of 316L SS, which is 1648 K-1673 K, and the creep experiment condition in this work, which is 823 K-923 K with 90-150 MPa loading. Therefore, the diffusional creep mechanism discussed here is only Coble creep, which requires vacancies movement along the grain boundaries.

Since the dislocation glide and Coble creep mechanisms are considered to account for the overall creep behaviour in the proposed model. The corresponding contributions need to be quantified physically and thermodynamically. By considering the loading condition, which includes stress and temperature, and the relevant microstructure features, the entire creep progress can be described precisely.

Therefore, for each grain embedded in the polycrystals, the plastic strain rate is described as (Wen et al., 2018):

$$\dot{\varepsilon}^{p} = \dot{\varepsilon}^{d} + \dot{\varepsilon}^{coble} \tag{3. 1}$$

where $\dot{\varepsilon}^{d}$ and $\dot{\varepsilon}^{coble}$ denote the strain rate contributions from dislocation glide and Coble creep, respectively, which will be introduced in this section later.

3.2.1.1 Dislocation glide

The plastic strain rate on each grain activated by conservative dislocation glide can be described by the sum of the mean shear rates of all slip systems ($\bar{\dot{\gamma}}^{s}$) (Beyerlein and Tomé, 2008; Tome and Lebensohn, 2023):

$$\dot{\varepsilon}_{ij}^{d} = \sum\nolimits_{s} m_{ij}^{s} \bar{\dot{\gamma}}^{s} \tag{3. 2}$$

With $m^{s} = \frac{1}{2}(n^{s} \otimes b^{s})$ (Beyerlein and Tomé, 2008; Tome and Lebensohn, 2023), which is the symmetric part of the Schmid tensor. n^{s} and b^{s} are the normal and Burgers vectors of slip system *s*.

In reality, due to the overlapping of elastic fields around different dislocation segments, the stress/strain distribution inside the grain is inhomogeneous. In order to consider the inhomogeneous deformation response, theoretically, each grain is divided into an infinite number of sub-material points. As such, each sub-material point's local

stress/strain states are taken into the calculation. As proven by line profile analysis, the stress distribution inside each grain is Gaussian (Groma and Bakó, 1998; Groma and Székely, 2000; Kalácska et al., 2017; Wilkens, 1970; Yadegari et al., 2014).

Therefore, the mean shear rate $\bar{\dot{\gamma}}^s$ can be described as follows (Wang et al., 2017a; Wang et al., 2016):

$$\bar{\dot{\gamma}}^s = \int_{-\infty}^{\infty} \dot{\gamma}^s(\tau^s) P(\tau^s - \bar{\tau}^s) d\,\tau^s \tag{3. 3}$$

When it was originally proposed, it was aiming to introduce a better relation between localised micro-mechanisms and bulk mechanical response, which has also been applied later to other creep modelling (Bieberdorf et al., 2021; Wen et al., 2017a). Here, τ^s denotes the sub-material level local resolved shear stress. $\dot{\gamma}^s$ is the corresponding shear rate, which represents the localised stress-strain response including microstructural effects (e.g. grain/sub-grain boundaries, dislocation density, precipitates). *P* represents the Gaussian distribution function incorporating the volume fraction of the sub-material points with specific local stress. In this formulation, the volume fraction is modelled using a normal distribution of shear stresses about the mean value, $\bar{\tau}^s = \boldsymbol{\sigma}:\boldsymbol{m}$ ($\boldsymbol{\sigma}$ is the deviatoric Cauchy stress tensor of one grain), and distribution variance *V* is given as (Wang et al., 2017b; Wang et al., 2016):

$$P(\tau^s - \bar{\tau}^s) = \frac{1}{\sqrt{2\pi}V} \exp\left(-\frac{(\tau^s - \bar{\tau}^s)^2}{2V^2}\right) \tag{3. 4 }$$

The current model assumes the creep strain accumulates from the motion of the dislocation inside the cell, which actually is a range of thermally activated obstacle-bypass processes. Therefore, the conducted plastic slip rate (shear rate) on each slip system *s* can be described by the classic Orowan equation as follows (Orowan, 1940):

$$\dot{\gamma}^s = \rho_{cell}^s \boldsymbol{b} v^s \mathrm{sign}(\tau^s) \tag{3. 5}$$

With dislocation density inside the cell ρ_{cell}^s, Burgers vector $\boldsymbol{b}$, and average velocity of dislocations travelling between obstacles v^s. Notice that, not only the dislocation inside

the cell is considered in the model, but the dislocation density ρ_{cw}^{s} on the cell wall are also accounted for creep behaviour, which will be introduced later.

The average dislocation moving velocity v^s is determined by the mean spacing for dislocations to travel between obstacles (dislocation mean free path λ^s), and the corresponding time, t^s. The latter includes the time travelling within the free spacing, t_t^s, and the average time a dislocation spends waiting at an obstacle before the bypass, t_w^s (Austin and McDowell, 2011; Lloyd et al., 2014; Wang et al., 2016):

$$v^s = \frac{\lambda^s}{t^s} \tag{3. 6}$$

$$t^s = t_w^s + t_t^s \tag{3. 7}$$

The dislocation mean free path is decided by the density of obstacles for dislocations gliding, and there are two different types of obstacles in this work, namely precipitates and the other dislocations inside the cell. Accordingly, λ^s is given as (Bertin et al., 2014b; Patra and McDowell, 2012; Sobie et al., 2015):

$$\lambda^s = \left(\frac{1}{\lambda_{p,cell}^s} + \frac{1}{\lambda_{\rho,cell}^s} \right)^{-1} \tag{3. 8}$$

$$\lambda_{\rho,cell}^s = \frac{1}{\sqrt{\sum_{s'} \alpha^{ss'} \rho_{cell}^{s'}}} \tag{3. 9}$$

$$\lambda_p^s = \frac{1}{h_p \sqrt{N_p^{cell} D_p^{cell}}} \tag{3. 10}$$

Here, $\lambda_{p,cell}^s$ represents the mean free path for dislocation-dislocation interaction, while $\lambda_{\rho,cell}^s$ denotes the mean free path for dislocation-obstacle interaction. $\alpha^{ss'}$ is the effective latent hardening matrix, which represents the intensity level of dislocation-dislocation interaction between slip systems s and s' (Bertin et al., 2014a; Franciosi and Zaoui, 1982). This includes the interaction between dislocations from the same slip system (self-interaction, $s = s'$). h_p is the precipitate trapping coefficient. N_p^{cell} and

D_p^{cell} denote the number density and mean size of the precipitates inside the cell, respectively.

The dislocation travelling time t_t^s is decided by the dislocation mean free path λ^s and the homologous travelling velocity v_t^s. The dislocation travelling velocity is roughly assumed equal to the shear wave velocity $C_s = \sqrt{\mu/\rho_0}$, where μ is the shear modulus, and ρ_0 is the mass density (Austin and McDowell, 2011; Hirth et al., 1983). For 316L SS, with $\rho_0 = 8000\ \mathrm{kg/m^3}$ (Kamath et al., 2014; Xue et al., 2007a; Zhong et al., 2019), and $\mu = 88884.6 - T * 37.7$ (T is the absolute temperature, and μ is expressed in MPa) (Puchi Cabrera, 2001a). As for the dislocation bypass waiting time t_w^s is decided by the corresponding probability for a dislocation to meet different obstacle types. Since the other dislocations and the precipitates are the obstacles considered in the proposed model, therefore, P_ρ and $1 - P_\rho$ represent the probability for a moving dislocation encounter the other dislocations and the precipitates, respectively. Here, $t_{w,\rho}^s$ and $t_{w,p}^s$ are the according waiting time (Wen et al., 2017a):

$$t_w^s = P_\rho t_{w,\rho}^s + (1 - P_\rho) t_{w,p}^s \tag{3. 11}$$

Whereas P_ρ is expressed as (Wen et al., 2017a):

$$P_\rho = \frac{1}{\lambda_{\rho,cell}^s} \Big/ \frac{1}{\lambda^s} \tag{3. 12}$$

Since the dislocation glid is thermally activated, the waiting time to bypass the obstacles can be determined by Kocks-type enthalpy law (Austin and McDowell, 2011; Kocks et al., 1975a; Lloyd et al., 2014), which includes the short-range effects from both dislocation and precipitate are inside the cell:

$$\frac{1}{t_{w,i}^s} = \frac{v_i^s}{\exp\left(\frac{\Delta G_i^s}{kT}\right)} \tag{3. 13}$$

Here ΔG_i^s is the activation energy for the dislocation ($i = \rho$) and precipitate ($i = p$) unpinning process, while k is the Boltzmann constant and v_i^s is the effective attempt frequency to overcome the obstacle. ΔG_i^s is described as follows:

$$\Delta G_i^s = \begin{cases} \Delta G_{0,i}\left(1-\left(\frac{\tau^s}{\tau_{CRSS}^s}\right)^p\right)^q, & if\ \tau^s < \tau_c^s \\ 0 & if\ \tau^s \geq \tau_c^s \end{cases} \quad \textbf{(3. 14)}$$

With $\Delta G_{0,i}$ denotes the thermal activation energy without the external stresses, p and q are the exponent parameters, which decide the shape of the obstacles resistant profile (Kocks et al., 1975c). τ_{CRSS}^s is the critical resolved shear stress (CRSS) determining the resistance for dislocation glide on slip system s.

In order to give a detailed creep deformation description for both the wrought and AM materials in this unified model, it is crucial to build an accurate definition of CRSS. Therefore, there are four kinds of mechanisms are considered to contribute to the total CRSS, which include lattice friction, τ_0, dislocation hardening, τ_ρ^s, precipitation hardening, τ_p, and solid solution hardening τ_{ss}:

$$\tau_{CRSS}^s = \tau_0 + \tau_\rho^s + \tau_p + \tau_{ss} \quad \textbf{(3. 15)}$$

Notice that, τ_0 is temperature-dependent, and the value can be obtained from single-crystal tests or MD simulations.

τ_ρ^s is given by the classic Taylor law (Franciosi and Zaoui, 1982):

$$\tau_\rho^s = \mu b\sqrt{\sum_{s'} \alpha^{ss'}(\rho_{cell}^{s'} + \rho_{cw}^{s'})} \quad \textbf{(3. 16)}$$

where $\rho_{cw}^{s'}$ denotes the density of cell wall dislocations, which contain mainly the dislocations in the cell wall but include also those pinned in the dislocation forest. Notice that equation (3. 16) describes the dislocation-dislocation interaction between slip systems s and s'.

τ_p is expressed using the dispersed barrier hardening (DBH) model (Sobie et al., 2015):

$$\tau_p = h_p \mu b \sqrt{N_p^{cell} D_p^{cell} + N_p^{cw} D_p^{cw}} \quad \textbf{(3. 17)}$$

N_p^{cw} and D_p^{cw} denote the number density and the mean size of the precipitates in the cell walls (sub-grain boundaries) respectively Different from the influence of the dislocations and precipitates inside the cell on the dislocation waiting is short-range, the effect from dislocations and precipitates both inside the cell and on cell walls described here are long-range effects. Therefore, τ_ρ^s and τ_p include the contribution from all dislocations and precipitates.

The details of precipitation hardening associated Thermo-Calc simulation will be introduced in section 3.3.

3.2.1.2 Dislocation density evolution

The dislocation densities are associated with the determination of the value of shear rate on each slip system (equation (3. 5)), the dislocation mean free path (equation (3. 8)) and the CRSS (equation (3. 15))The dislocation densities evolution has essential influence at the primary stage of thermal creep. For the model proposed in this project, the dislocation density evolution of the crystal cell consists of three parts: the generation of dislocation, dislocation annihilation, and the dislocation trapped in the cell wall, which can be described as:

$$\dot{\rho}_{cell}^s = \dot{\rho}_{cell,gen}^s - \dot{\rho}_{cell,ann}^s - \rho_{cell,trap}^s \quad \textbf{(3. 18)}$$

The dislocation generation term is given as follows (Kocks and Mecking, 2003; Mecking and Kocks, 1981):

$$\dot{\rho}_{cell,gen}^s = \frac{k_1}{b\lambda^s} |\bar{\dot{\gamma}}^s| \quad \textbf{(3. 19)}$$

while the dislocation annihilation is based on the encounter of two dislocations with opposite Burgers vectors, which is given below (Beyerlein and Tomé, 2008):

$$\dot{\rho}^s_{cell,ann} = f_{re}\rho^s_{t-1}|\bar{\dot{\gamma}}^s| \quad \textbf{(3. 20)}$$

where f is the dynamic recovery parameter, given as (Estrin, 1998b):

$$f_{re} = k_2\left(\frac{\dot{\varepsilon}^0}{\dot{\varepsilon}}\right)^{1/n_0} \quad \textbf{(3. 21)}$$

$\dot{\varepsilon}^0$ is reference strain rate, n_0 is the strain rate sensitivity parameter. In this work, $\dot{\varepsilon}^0$ is temperature dependent.

$$\rho^s_{cell,trap} = \frac{k_3}{D_{sub}}|\bar{\dot{\gamma}}^s| \quad \textbf{(3. 22)}$$

The cell wall dislocation density update within the wall is not considered in the current model. k_1, k_2, and k_3 are material constants.

3.2.1.3 Coble creep

As mentioned at the beginning of section 3.2.2, under the loading condition in this project, Coble creep is considered the dominant diffusion creep mechanism. This creep law was first proposed by (Coble, 1963), and is written as:

$$\dot{\varepsilon}^{coble}_{ij} = \frac{\alpha_{gb}D_{gb}\delta_{gb}\Omega}{\pi D^3 kT}\sigma_{ij} \quad \textbf{(3. 23)}$$

where α_{gb} is a constant, δ_{gb} is the grain boundary thickness, Ω is the atomic volume; D_{gb} is the grain boundary diffusion coefficient, which is written as:

$$D_{gb} = D_{gb,0}\exp\left(-\frac{Q_{gb}}{kT}\right) \quad \textbf{(3. 24)}$$

Where $D_{gb,0}$ is the pre-exponential factor and Q_{gb} is the effective activation energy for grain boundary diffusion. Q_{gb} consists of two parts: the vacancy formation energy, Q^f_{gb} and the vacancy migration energy, Q^m_{gb}.

The expression of Coble creep can be simplified as follows (Wen et al., 2017a):

$$\dot{\varepsilon}_{ij}^{coble} = \frac{A_{coble}\sigma_{ij}}{D^3 T}\exp\left(-\frac{Q_{gb}}{kT}\right) \quad \textbf{(3. 25)}$$

where $A_{coble} = \frac{\alpha_{gb} D_{gb,0} \delta_{gb} \Omega}{\pi k}$ is a constant assumed to be identical for both wrought and AM materials. The values of A_{coble} and Q_{gb} will be discussed in Chapter 4.

It is worth mentioning that the difference between wrought and AM materials is considered through the grain and sub-grain sizes factor D, which conventionally refers to the grain size. However, the sub-grain size is utilised for AM materials in this work.

3.2.1.4 Dislocation climb

Notice that, dislocation climb is one of the deformation mechanisms for polycrystal materials, which has been widely discussed in SS316L under high-temperature creep (Morris and Harries, 1978; Rieth, 2007; Rieth et al., 2004b). Nonetheless, the concentration of a range of different solute elements in SS316L is too high to consider every case of vacancy/interstitial diffusion for commercial materials. As dislocation climb is also associated with solutes diffusion, it is too complicated to quantify every different case, especially the interaction between dislocations and obstacles during the climb. In addition, such multi-complex diffusional interaction has not been systematically investigated through atomic-scale simulation or experimental methods. Consequently, the contribution of creep from dislocation climb cannot be quantified precisely, and then, it is not considered in the current proposed model. The general dislocation climb model will be introduced in Appendix I.

3.2.1.5 Grain boundary sliding

Similar to dislocation climb, grain boundary sliding (GBS) is also an active deformation mechanism in 316L SS. The creep rate caused by GBS can be quantified through the expression (Langdon, 1970; Yang et al., 2021a):

$$\dot{\varepsilon}_{GBS} = \frac{\beta b^2 \sigma_{ij}^2}{D\mu kT} D_{gb} \quad \textbf{(3. 26)}$$

Here, β is a constant close to unity, T is the absolute temperature. D_{gb} is the grain boundary diffusion coefficient, which has been described in equation (3. 24).

The specific value and contribution of creep rate from grain boundary sliding will be discussed in detail in Chapter 4.

3.3 Precipitation evolution in 316L stainless steel

In this section, the precipitation evolution in 316L stainless steel (SS) is comprehensively discussed. The nucleation, growth and dissolving of various precipitates in 316L SS are introduced. By considering the materials' chemical concentration, microstructure information, and temperature combined duration conditions, the evolution of precipitation is simulated by Thermo-Calc software.

3.3.1 Introduction

A literature review on the precipitation hardening mechanism in metallic materials has been provided in Chapter 2. The existence of precipitates inside the grain cell can interact with mobile dislocations, which results in hindered dislocation movement, thus, the material is hardened. This type of strengthening mechanism is caused by a short-range effect. As a short-range effect, precipitation impedes dislocation mobility by direct interaction. This interaction extent is quantified by precipitate-type of obstacles within the grain cell, $\lambda_{p,cell}^{s}$, which is given in equation (3. 10): $\lambda_p^s = \frac{1}{h_p \sqrt{N_p^{cell} D_p^{cell}}}$. Therefore, the hardening effect of precipitation interior of the grain cell is presented by the dislocation mean free path λ^s in equation (3. 8): $\lambda^s = \left(\frac{1}{\lambda_{p,cell}^s} + \frac{1}{\lambda_{\rho,cell}^s}\right)^{-1}$. As a part of the critical resolved shear stress (CRSS), the precipitation hardening contribution τ_p has been considered through the equation (3. 17) in the proposed physics-based model, which is given as: $\tau_p = h_p \mu b \sqrt{N_p^{cell} D_p^{cell} + N_p^{cw} D_p^{cw}}$ (Sobie et al., 2015). Different from the dislocation

mean free path, τ_p is the long-range precipitation hardening effect. This hardening phenomenon is caused by both of the precipitates interior the grain cell and the precipitates on the cell wall. It can be told that characteristics of precipitation: number density and diameter are required to quantify the precipitation short-range effect and long-range effect.

3.3.2 Determination of precipitation

Precipitation is a time-dependent process, which is affected by chemical composition, ageing temperature and certain defects in the matrix acting as nucleation sites. For 316L SS type material, $M_{23}C_6$ is commonly considered as the dominant precipitate (Lewis and Hattersley, 1965; Padilha et al., 2007; Sahlaoui et al., 2004). This type of precipitate usually forms firstly on grain boundaries. However, they can spread on twins and dislocations as well after a certain ageing time. As a relatively stable carbide, it is rare for $M_{23}C_6$ to transit into M_6C. Such transition usually depends on the chemical composition and ageing condition, which is unlikely for the materials and creep environment involved in this work. While the formation of MX carbides/nitrides requires specific chemical composition proportion and ageing conditions, which is impossible to happen in this work either (Keown and Pickering, 1974).

Although 316L SS is regarded as austenitic steel, there is still a small amount of δ ferrite (<1%), decorated on HAGBs in the wrought materials (Rieth et al., 2004b). Moreover, there is a reasonable amount of δ ferrite and $M_{23}C_6$ inherited from the imperfect heat treatment. The σ phase detected in wrought 316L SS during the creep is firstly and mostly contributed from δ ferrite, which is inevitable (Villanueva et al., 2006). On the other hand, the $\gamma \rightleftharpoons \gamma^* + \sigma$ eutectoid reaction merely occurs after thousands of hours creep test around $600℃$ (Villanueva et al., 2006). In addition, η phase only can be found with a minimum of 1000h ageing between $625℃ - 800℃$ (Sahlaoui et al., 2004). Similarly, the formation of χ phase is mainly recorded above $750℃$ in 316L SS. Apart from aging temperature and time, the formation of precipitation also depends on the chemical composition. For instance, either Nb or Ti is required for the Z and G phases (Sourmail, 2001). Generally according to the chemical compositions of both AM and wrought 316L SS analysed in this work (Rieth et al., 2004b; Williams et al., 2021),

$M_{23}C_6, \sigma, \eta$ and χ precipitates may be formed. However, considering the creep time and temperature ranges, only $M_{23}C_6$ and σ are could be formed in AM materials creep tests (Williams et al., 2021),. Meanwhile, whereas $M_{23}C_6, \sigma$ and η could be formed in wrought materials due to the long creep time (Padilha et al., 2007; Rieth et al., 2004b).

Based on the entire time scale of creep behaviour, in this work, it is only possible and worthy to consider the precipitation of $M_{23}C_6$. Since most σ in the wrought 316L SS is from the residual δ ferrite, which is inherited from heat treatment; while the creep time for AMed 316L SS is not long enough for the reaction of $\gamma \rightleftharpoons \gamma^* + \sigma$ to occur (Padilha et al., 2007; Terada et al., 2008). Compared to $M_{23}C_6$, it is usually assumed three reasons for the late appearance of σ phase. Firstly, the chemical composition of σ decided that it cannot be easily formed unless the matrix is carbon and nitrogen depleted; secondly, the tetragonal crystal structure made σ difficult to nucleate in the parent austenitic matrix; moreover, σ is rich in chromium and molybdenum, which require additional diffusion time (Hall and Algie, 1966; Padilha et al., 2007; Villanueva et al., 2006). In addition, a similar explanation can be applied to η phase. Typically, the generation of a new phase would result in the fading of another. Some people proposed a possible relationship between $M_{23}C_6$ dissolving and σ appearance is rather chemical movement but competition. The formation of σ consumes chromium and molybdenum, forming a depletion area in the adjacent matrix. In addition, there is no carbon in σ. As the low concentration of molybdenum and chromium in austenite leads to higher carbon solubility. Therefore, meanwhile, there is the resolution of $M_{23}C_6$ carbides (Padilha et al., 2007; Weiss and Stickler, 1972). But Asghary et al. (Asghary et al., 2019) reported that in nimonic 105 superalloy, there is no reduction in the percentage of carbides with σ nucleation and growth. The possible explanation is the consumption of the matrix phase leads to σ formation, which is the eutectoid reaction $\gamma \rightleftharpoons \gamma^* + \sigma$ reported after thousands of hours creep.

3.3.3 Thermo-Calc simulation

The characters required in the proposed model to describe the precipitation hardening are presented in 3.31, while the determination of the precipitation type applied in this work is illustrated in 3.3.2. Thermo-Calc is a prominent software package widely

utilized in the field of materials science and engineering. Developed by a team of researchers and experts, Thermo-Calc offers comprehensive computational tools for thermodynamic modeling, phase diagram calculations, and materials property predictions. Thermo-Calc's strength lies in its extensive thermodynamic database, which includes a vast range of elements and compounds. This database enables users to accurately predict phase stability, solidification behavior, and material properties for diverse alloy systems, making it invaluable for materials design and optimization. By adapting Thermo-Calc software (version 2022a) (Andersson et al., 2002), the number density and mean diameter evolution of $M_{23}C_6$ during the isothermal creep in both wrought and AM 316L SS under different temperatures are determined.

The TCFE10: Steels/Fe-alloys database was chosen, from which the thermodynamic data can be obtained for TC-PRISMA calculation. The chemical compositions reported in Rieth et al. 2004 (Rieth et al., 2004b) and Williams et al. 2021 (Williams et al., 2021) are input directly for the simulations of wrought and AM 316L SS, respectively. The cell dislocation densities (act as nucleation sites in the cell) and grain/sub-grain sizes mentioned above are used as input. Since AM 316L SS exhibits a strong sub-grain structure and low angle grain boundaries (LAGBs) can act as preferred nucleation sites as high angle grain boundaries (HAGBs). The sub-grain size is considered in Thermo-Calc simulations to emphasise the significance of sub-grain structure in AM materials (Hong et al., 2021a). The values of interfacial energy for $M_{23}C_6$ forming on grain boundaries and dislocations are chosen to be $0.27\ J/m^2$ and $0.3\ J/m^2$ respectively (Prat et al., 2014; Sanhueza et al., 2017; Xiao et al., 2013), which reflects the fact that the formation of $M_{23}C_6$ is easier on grain boundaries than dislocations due to higher diffusivity (Lewis and Hattersley, 1965; Padilha et al., 2007). Since the specific interfacial energies require molecular dynamics simulations. These values are obtained through back-fitting within the range given in the literature (Sanhueza et al., 2017; Xiao et al., 2013).

Thermo-Calc simulations start from a precipitation-free matrix and can capture the precipitate size and density development over the isothermal ageing heat treatment process. In addition, the Ostwald ripening phenomenon is also considered (Guo and Sha, 2002). Notice that, the strain energy can also influence the precipitation. However, the

according effects cannot be accurately evaluated as a function of the ongoing deformation of precipitation in the Thermo-Calc, similar to the other existing modelling and experimental methods. This is one of the error sources, which results in the deviation of simulation results.

The precipitation hardening effects on the cell wall and interior of the cell are indicated by $N_p D_p$ in Figure 3.2 via Thermo-Calc, (a) and (b) are AM and wrought 316L SS respectively. AM and wrought cases are simulated under the corresponding creep temperature. According to the Thermo-Calc simulation results, the precipitation process in all cases saturates significantly fast (within 1.3% of the total creep time), which can be maintained for a while (> 38% of total creep time) before Ostwald ripening occurs. In the simulation of this project, only the saturation values for the diameter size and number density of $M_{23}C_6$, are considered in the precipitation hardening model, which is listed in

Table 3. 1. The evolution of the precipitation sizes and densities can be neglected in the whole process of the simulation for two main reasons:(1) the influence from Ostwald ripening is negligible during the overall creep stages, since the precipitation exceeded saturation very quickly, and (2) the real precipitation evolution should achieve the saturation status faster than simulated by Thermo-Calc. The reasons for the faster saturation in reality are due to: (1) The wrought 316L SS is supposed to embody a great number of precipitates prior to the creep test, because of the hot-rolling and heat treatment (Rieth et al., 2004b). (2) The precipitation process is around 10 times faster in AMed materials compared to traditionally fabricated 316L SS, as a result of high densities of dislocations and LAGBs (Yin et al., 2021). (3) The consistent loading can also accelerate the formation and growth of precipitation (Härtel et al., 2018; Liu et al., 2022b; Ma et al., 2018), however, cannot be considered in Thermo-Calc simulations. Since the loading factor is not built in the Thermo-Calc.

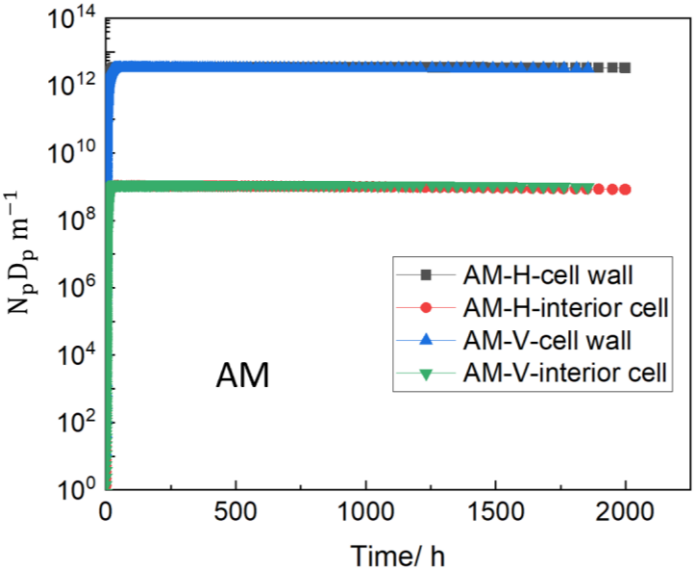

(a)

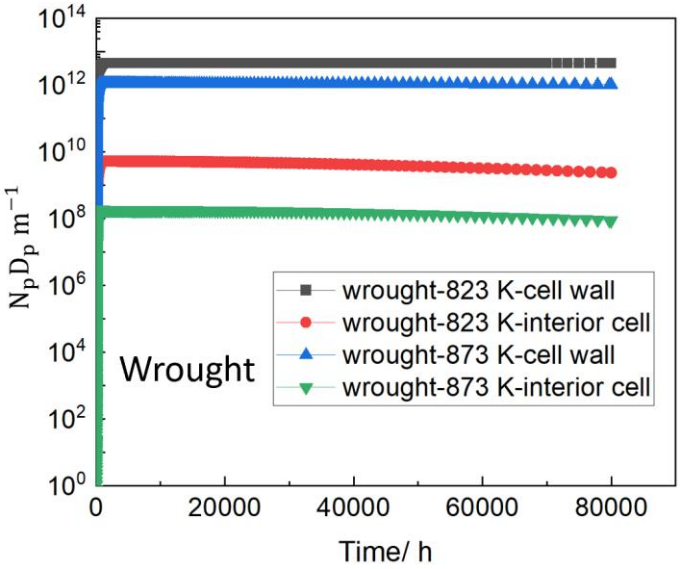

(b)

Figure 3. 2 The evolution of number density, N_p and mean diameter, $D_p$of $M_{23}C_6$ from Thermo-Calc; AM-H (horizontally built), AM-V (vertically built).

Table 3. 1 Thermo-Calc simulation results for $M_{23}C_6$ (The superscript *cell* and *cw* denote the precipitates interior of the cell and on the cell wall, respectively); AM-H (horizontally built), AM-V (vertically built).

Character	AM-H 923 K	AM-V 923 K	Wrought 823 K	Wrought 873 K
$N_p^{cell}\ (m^{-3})$	1.87×10^{16}	$1.98\ \times 10^{16}$	1.37×10^{17}	2.22×10^{15}
$D_p^{cell}\ (nm)$	56	58	38	80
$N_p^{cw}\ (m^{-3})$	6.14×10^{19}	$5.56\ \times 10^{19}$	1.08×10^{20}	1.32×10^{19}
$D_p^{cw}\ (nm)$	57.2	59	42	84

3.4 Visco-plasticity self-consistent framework

The proposed model is implemented under the VPSC framework, considering each grain is embedded in the whole polycrystal structure as a visco-plastic inclusion. The polycrystals around the grain r behave as a homogeneous effective medium (HEM), which is characterized by the properties of the entire aggregate. Local grain orientation decides the interaction between the grain and the medium, which means the local stress/strain response is texture-related.

In this section, the computational framework of visco-plasticity self-consistent (VPSC) formulations adapted in this work is presented. The VPSC framework is employed independently to capture the primary stage and secondary stage of materials' thermal creep behaviour, which is in Chapter 4. The according simulation results will also be compared to the CP-FEM predictions, in which, the same mechanism-based model is employed (Chapter 5).

3.4.1 Mechanisms

The VPSC can simulate the plastic deformation of aggregations from the external loading, which is according to the physical shear mechanisms including dislocation glide, climb and twinning. The grain interactions are also considered, which means that apart from the macro-scale stress-strain behaviour and materials strengthening, crystal

reorientation is also accounted for. Therefore, the hardening and texture evolution associated with deformation can be captured.

3.4.2 Formulations

In this section, the detailed VPSC formulations are described. Notice that, the VPSC formulations are developed on the CP-based constitutive kinematics, which has been introduced in Chapter 2. The CP-based constitutive kinematics expression is a general description, which can be employed in any polycrystal model.

As for self-consistent approximation, it is one of the most common homogenization methods. The self-consistent approximation was first proposed to estimate the mechanical response behaviour of polycrystals by Hershey (Hershey, 1954). And the VPSC model formulation is first proposed by Molinari et al. (1987) as follows:

$$\mathbf{S} - \bar{\mathbf{S}} = (\boldsymbol{\Gamma}^{-1} + \mathbf{A}^{\mathrm{t}}) \cdot (\mathbf{D} - \bar{\mathbf{D}}) \tag{3. 27}$$

Where $\boldsymbol{\Gamma}$ is a fourth-order interaction tensor, while $\mathbf{A}^{\mathrm{t}}$ is also a fourth-order tensor that represents the tangent modulus of the polycrystals. $\mathbf{S}$ is local stress, while $\bar{\mathbf{S}}$ is macroscopic stress; and $\mathbf{D}$ is the local strain rate, while $\bar{\mathbf{D}}$ is applied strain rate.

It was improved by Molinari and Tóth (1994) by introducing a tuning parameter α. Therefore, the enhanced interaction law for VPSC model is given as:

$$\mathbf{S} - \bar{\mathbf{S}} = \alpha\left(\boldsymbol{\Gamma}^{\boldsymbol{s}^{-1}} + \mathbf{A}^{\mathrm{s}}\right) \cdot (\mathbf{D} - \bar{\mathbf{D}}) \tag{3. 28}$$

Where $\boldsymbol{\Gamma}^{\boldsymbol{s}}$ is a fourth-order interaction tensor, and $\mathbf{A}^{\mathrm{s}}$ is a fourth-order tensor of secant modulus, they are given as $\boldsymbol{\Gamma}^{\boldsymbol{s}} = \mathrm{m}\boldsymbol{\Gamma}^{\boldsymbol{t}^{-1}}$ and $\mathbf{A}^{\mathrm{t}} = \mathrm{m}\mathbf{A}^{\mathrm{s}}$ ($\mathrm{m} = \mathrm{n}^{-1}$, n is the power in equation (2. 17). By changing the value of α, the current interaction law can be adjusted into different model types.

The polycrystals are described by weighted orientations, as the different orientations represent grains, while the various weights represent the corresponding fractions. Under the VPSC framework, each grain is treated as an ellipsoidal visco-plastic inclusion

decorated in the visco-plastic medium. Meanwhile, both the inclusion and medium are characterised by anisotropy.

3.4.2.1 Local constitutive behaviour and homogenization

The grain level visco-plastic constitutive behaviour can be described by the non-linear rate-sensitive equation:

$$\dot{\varepsilon}(\bar{x}) = \sum_s P^s \dot{\gamma}^s(\bar{u}) = \dot{\gamma}_0 \sum_s \left(\frac{\sigma(\bar{u}) : m^s(\bar{u})}{\tau_0^s(\bar{u})} \right)^n \text{sign}\big(\sigma(\bar{u}) : m^s(\bar{u})\big) m^s(\bar{u}) \quad \textbf{(3. 29)}$$

Where P^s is the symmetric Schmid tensor given in equation (2. 13) in Chapter 2, $\dot{\gamma}^s(\bar{u})$ is the local shear-rate on slip system *s*, $\dot{\gamma}_0$ is a normalisation factor, $\tau_0^s(\bar{u})$ is the threshold stress and *n* is the rate-sensitivity exponent.

By linearizing equation (3. 29) inside a grain r, it has:

$$\dot{\varepsilon}(\bar{u}) = M^{(r)} : \sigma(\bar{u}) + \dot{\varepsilon}^{0(r)} \quad \textbf{(3. 30)}$$

Here, $M^{(r)}$ is the visco-plastic compliance, and $\dot{\varepsilon}^{0(r)}$ is the back-extrapolated term of grain r. Notice that, (r) denotes the average value of the magnitude for the given grain r. Their values vary according to the different linearization assumptions. Similarly, the average strain rate in grain r is given as:

$$\dot{\varepsilon}^{(r)} = M^{(r)} : \sigma^{(r)} + \dot{\varepsilon}^{0(r)} \quad \textbf{(3. 31)}$$

The medium (polycrystal) level homogenization shows a linear relation as:

$$\dot{E} = \bar{M} : \Sigma + \dot{E}^0 \quad \textbf{(3. 32)}$$

Accordingly, $\bar{M}$ and $\dot{E}^0$ are the macroscopic visco-plastic compliance and back extrapolated term, respectively, while $\dot{E}$ and Σ are macroscopic magnitudes. Mura (1987) introduced the equivalent inclusion to “erase” the inhomogeneity. The local

constitutive response is written with respect to the homogeneous macroscopic moduli as:

$$\dot{\varepsilon}(\bar{u}) = \bar{M}{:}\,\sigma(\bar{u}) + \dot{E}^0 + \dot{\varepsilon}^*(u) \tag{3. 33}$$

Here, $\dot{\varepsilon}^*(\bar{u})$ is a eigen-strain-rate field, which comes by replacing the inhomogeneity using an equivalent inclusion. Therefore, the local stress can be described as:

$$\tilde{\sigma}(\bar{u}) = \bar{L}\left(\tilde{\dot{\varepsilon}}(\bar{u}) - \dot{\varepsilon}^*(\bar{u})\right) \tag{3. 34}$$

Where, $\bar{L} = \bar{M}^{-1}$, and "~" means the local deviation of the corresponding tensor from the macro-level. Combined with the equilibrium conditions, it is given as:

$$\sigma^c_{ij,j}(\bar{u}) = \tilde{\sigma}^c_{ij,j}(\bar{u}) = \tilde{\sigma}_{ij,j}(\bar{u}) + \tilde{\sigma}^m_{,i}(\bar{u}) \tag{3. 35}$$

With $\sigma^c_{ij,j}$ and $\sigma^m_{,i}$ denote the Cauchy stress and mean stress.

The relation between strain rate and velocity gradient vector $\tilde{v}(\bar{u})$ is given as:

$$\tilde{\dot{\varepsilon}}_{ij}(\bar{u}) = \frac{1}{2}\left(\tilde{v}_{i,j}(\bar{u}) + \tilde{v}_{j,i}(\bar{u})\right) \tag{3. 36}$$

Combined with incompressibity condition, there is:

$$\begin{vmatrix} \bar{L}_{ijkl}\tilde{v}_{k,lj}(\bar{u}) + \tilde{\sigma}^m_{,i}(\bar{u}) + \mathrm{f}_i(\bar{u}) \\ \tilde{v}_{k,k}(\bar{x}) = 0 \end{vmatrix} \tag{3. 37}$$

Here, the fictitious volume force $\mathrm{f}_i(\bar{u})$ is given as: $\mathrm{f_i}(\bar{\mathrm{u}}) = -\bar{\mathrm{L}}_{\mathrm{ijkl}}\dot{\varepsilon}^*_{\mathrm{kl,j}}(\bar{\mathrm{u}}) = \sigma^*_{\mathrm{ij,j}}(\bar{\mathrm{u}})$, which is associated with heterogeneity.

3.4.2.2 Grain interaction and localization

By transforming the volume to the grain r, the equation (3. 34) is given as:

$$\tilde{\sigma}^{(\mathrm{r})} = \bar{\mathrm{L}}\left(\tilde{\dot{\varepsilon}}^{(\mathrm{r})} - \dot{\varepsilon}^{*(\mathrm{r})}\right) \tag{3. 38}$$

There is strain-rate deviations in the ellipsoidal domain: $\tilde{\dot{\varepsilon}}^{(r)} = S\dot{\varepsilon}^{*(r)}$. By replacing the eigen strain rate into equation (3. 38), it is:

$$\tilde{\varepsilon}^{(r)} = -\widetilde{M}:\tilde{\sigma}^{(r)} \tag{3. 39}$$

With the interaction tensor $\widetilde{M} = (I - S)^{-1}: S: \overline{M}$.

Replacing the local and effective medium relations into equation (3. 39), the localization equation with some manipulation can be written as:

$$\sigma^{(r)} = B^{(r)}: \Sigma + b^{(r)} \tag{3. 40}$$

The stress concentration tensors are given as:

$$B^{(r)} = \left(M^{(r)} + \widetilde{M}\right)^{-1}: \left(\overline{M} + \widetilde{M}\right) \tag{3. 41}$$

$$b^{(r)} = \left(M^{(r)} + \widetilde{M}\right)^{-1}: (\dot{E}^{o} - \dot{\varepsilon}^{o(r)}) \tag{3. 42}$$

3.4.2.3 Self-consistent formulations

Based on the previous derivation, this section introduces a polycrystal model, regarding the grain as an ellipsoidal inclusion ingrained in the medium. The effective medium represents the polycrystal. According to equation (3. 30) and equation (3. 40), the local constitutive equation can be written as:

$$\dot{\varepsilon}^{(r)} = M^{(r)}: \sigma^{(r)} + \dot{\varepsilon}^{o(r)} = M^{(r)}: B^{(r)}: \Sigma + M^{(r)}: b^{(r)} + \dot{\varepsilon}^{o(r)} \tag{3. 43}$$

When the aggregated weighted average strain rates equal to the macro-level value, e.g.:

$$\dot{E} = \langle \dot{\varepsilon}^{(r)} \rangle \tag{3. 44}$$

With "$\langle \quad \rangle$" represents the average over the grain r, quantified by the according volume fraction. Based on equation (3. 32) and equation (3. 43), the self-consistent formulation for homogeneous compliance is given as (Lebensohn et al., 1996; Lebensohn et al., 2004; Walpole, 1969):

$$\overline{M} = \langle M^{(r)}: B^{(r)} \rangle \tag{3. 45}$$

With back-extrapolated term $\dot{E}^{o} = \langle M^{(r)}: b^{(r)} + \dot{\varepsilon}^{o(r)} \rangle$.

In reality, the morphologies of different grains vary, and have different Eshelby tensors. Therefore, grains are associated with different interaction tensors. The generalized self-consistent the macroscopic visco-plastic compliance and back extrapolated term are given as:

$$\bar{\mathrm{M}} = \langle \mathrm{M}^{(\mathrm{r})} : \mathrm{B}^{(\mathrm{r})} \rangle : \langle \mathrm{B}^{(\mathrm{r})} \rangle^{-1} \tag{3. 46}$$

$$\dot{\mathrm{E}}^{\mathrm{o}} = \langle \mathrm{M}^{(\mathrm{r})} : \mathrm{b}^{(\mathrm{r})} + \dot{\varepsilon}^{\mathrm{o}(\mathrm{r})} \rangle - \langle \mathrm{M}^{(\mathrm{r})} : \mathrm{B}^{(\mathrm{r})} \rangle : \langle \mathrm{B}^{(\mathrm{r})} \rangle^{-1} : \langle \dot{\mathrm{b}}^{(\mathrm{r})} \rangle \tag{3. 47}$$

3.4.2.4 Secant, affine, tangent and intermediate linearization

Based on equation(3. 31), for the different linearization assumptions, the value of $M^{(r)}$ and $\varepsilon^{o(r)}$ are different. There are following the specific self-consistent approximation:

- Secant (Hill, 1965b; Hutchinson, 1976)

$$\mathrm{M}_{\mathrm{sec}}^{(\mathrm{r})} = \dot{\gamma}_{\mathrm{o}} \sum_{\mathrm{s}} \frac{\mathrm{m}^{\mathrm{s}(\mathrm{r})} \otimes \mathrm{m}^{\mathrm{s}(\mathrm{r})}}{\tau_0^{\mathrm{s}(\mathrm{r})}} \left(\frac{\mathrm{m}^{\mathrm{s}(\mathrm{r})} : \sigma^{(\mathrm{r})}}{\tau_0^{\mathrm{s}(\mathrm{r})}} \right)^{\mathrm{n}-1} \tag{3. 48}$$

$$\dot{\varepsilon}_{\mathrm{sec}}^{\mathrm{o}(\mathrm{r})} = 0 \tag{3. 49}$$

- Affine (Lebensohn et al., 2004; Masson et al., 2000)

$$\mathrm{M}_{\mathrm{aff}}^{(\mathrm{r})} = \mathrm{n}\gamma_{\mathrm{o}} \sum_{\mathrm{s}} \frac{\mathrm{m}^{\mathrm{s}(\mathrm{r})} \otimes \mathrm{m}^{\mathrm{s}(\mathrm{r})}}{\tau_0^{\mathrm{s}(\mathrm{r})}} \left(\frac{\mathrm{m}^{\mathrm{s}(\mathrm{r})} : \sigma^{(\mathrm{r})}}{\tau_0^{\mathrm{s}(\mathrm{r})}} \right)^{\mathrm{n}-1} \tag{3. 50}$$

$$\dot{\varepsilon}_{\mathrm{aff}}^{\mathrm{o}(\mathrm{r})} = (1 - \mathrm{n})\dot{\gamma}_{\mathrm{o}} \sum_{\mathrm{s}} \left(\frac{\mathrm{m}^{\mathrm{s}(\mathrm{r})} : \sigma^{(\mathrm{r})}}{\tau_0^{\mathrm{s}(\mathrm{r})}} \right)^{\mathrm{n}} \tag{3. 51}$$

- Tangent

The moduli are the same as the affine case. However, the Secant moduli is used to adjust $\bar{M}$ by Molinari et al. (1987), and combined with the tangent-secant relation ($\bar{M}_{tg} = n\bar{M}_{sec}$) by Hutchinson (1976). Therefore the interaction tensor follows as (Lebensohn and Tomé, 1993):

$$\widetilde{\mathrm{M}} = (\mathrm{I} - \mathrm{S})^{-1} : \mathrm{S} : \overline{\mathrm{M}}_{\mathrm{tg}} = \mathrm{n}(\mathrm{I} - \mathrm{S})^{-1} : \mathrm{S} : \overline{\mathrm{M}}_{\mathrm{sec}} \quad \textbf{(3. 52)}$$

3.4.3 Implementation

The VPSC modelling framework is written in FORTRAN 77 and developed by Tome and Lebensohn (Tome and Lebensohn, 2023), and the self-consistent algorithm is solved inside the subroutine. The deformation is conducted by imposing successive deformation increments. For each deformation step, the boundary conditions are imposed to aggregate. The calculated shear rate is used to perform a forward determination of grain reorientation (crystallographic texture revolution), update the yield stresses for each grain (strengthening), and also update the grain shapes (morphologic texture revolution). The macro-scale bulk stress-strain tensor components are determined by volume averages over the corresponding grain components. The anisotropy of stress-strain behaviour and mechanical properties is determined by this averaging procedure over the distribution of orientations. It is worth noting that the VPSC framework employed in this project has already undergone significant development and is considered mature. The partial novelty of this study lies in the utilization of the VPSC framework for conducting physics-based simulations.

3.4.3.1 Input file

The information covered in the input code includes (Tomé and Lebensohn, 2007):

- Initial materials textures: crystallographic texture, which consists of grain orientation and weight; morphological texture, including grain size and shape.
- Materials properties at the single-crystal level consist of active slip systems, critical resolved shear stress (CRSS), and related materials strengthening parameters.
- Boundary conditions.
- Parameters controlling convergence.

3.4.3.2 Work-flow

All the relevant materials parameters and boundary conditions need to be initialised at the beginning. The VPSC numerical procedure of homogenization applied in this project was originally proposed by (Lebensohn and Tomé, 1993). The algorithm starts with an initial guess for grain stresses by Taylor approximation, and calculates an initial guess for linearized grain visco-plastic properties, $M^{(r)}$ and $\dot{\varepsilon}^{0(r)}$. This process is repeated until convergence (Lebensohn et al., 2007; Zecevic et al., 2021):

1) Calculate visco-plastic effective properties, $\overline{M}$, see equation (3. 46), and$\dot{E}^{o}$, see equation (3. 47):

2) Calculate unknown components of visco-plastic strain rate and deviated stress from the applied components using the relation: $\dot{\varepsilon}^{(r)} = M^{(r)}: \tilde{\sigma}^{(r)} + \dot{\varepsilon}^{o(r)}$, see equation (3. 43).

3) Calculate a new guess for grain deviation by solving the interaction equation for each grain: $\dot{\varepsilon}(\bar{x}) = \sum_s P^s \dot{\gamma}^s(\bar{x}) = \dot{\gamma}_0 \sum_s \left(\frac{\sigma(\bar{x}):m^s(\bar{x})}{\tau_0^s(\bar{x})}\right)^n \text{sign}\left(\sigma(\bar{x}):m^s(\bar{x})\right)m^s(\bar{x}) - \quad \dot{\varepsilon} = -\widetilde{M}: (\tilde{\sigma}^{(r)} - \tilde{\sigma})$, see equation (3. 29).

4) Linearize the grain response and calculate new $M^{(r)}$ and $\dot{\varepsilon}^{0(r)}$.

After achieving convergence, the simulation will proceed to conduct the physics-based model. The resolved shear stresses of each slip system are calculated and updated at each step. Once the slip-system level resolved shear stress achieved the CRSS value, the plasticity flow will start and the hardening law is introduced. Then, the stress-strain information will be calculated at each slip system level and accounted for the individual grain. The bulk mechanical behaviour will be calculated by the SC homogenisation method. During each step, according to different interaction laws, each grain will adjust its orientation and shape differently. The schematic VPSC work-flow is shown in Figure

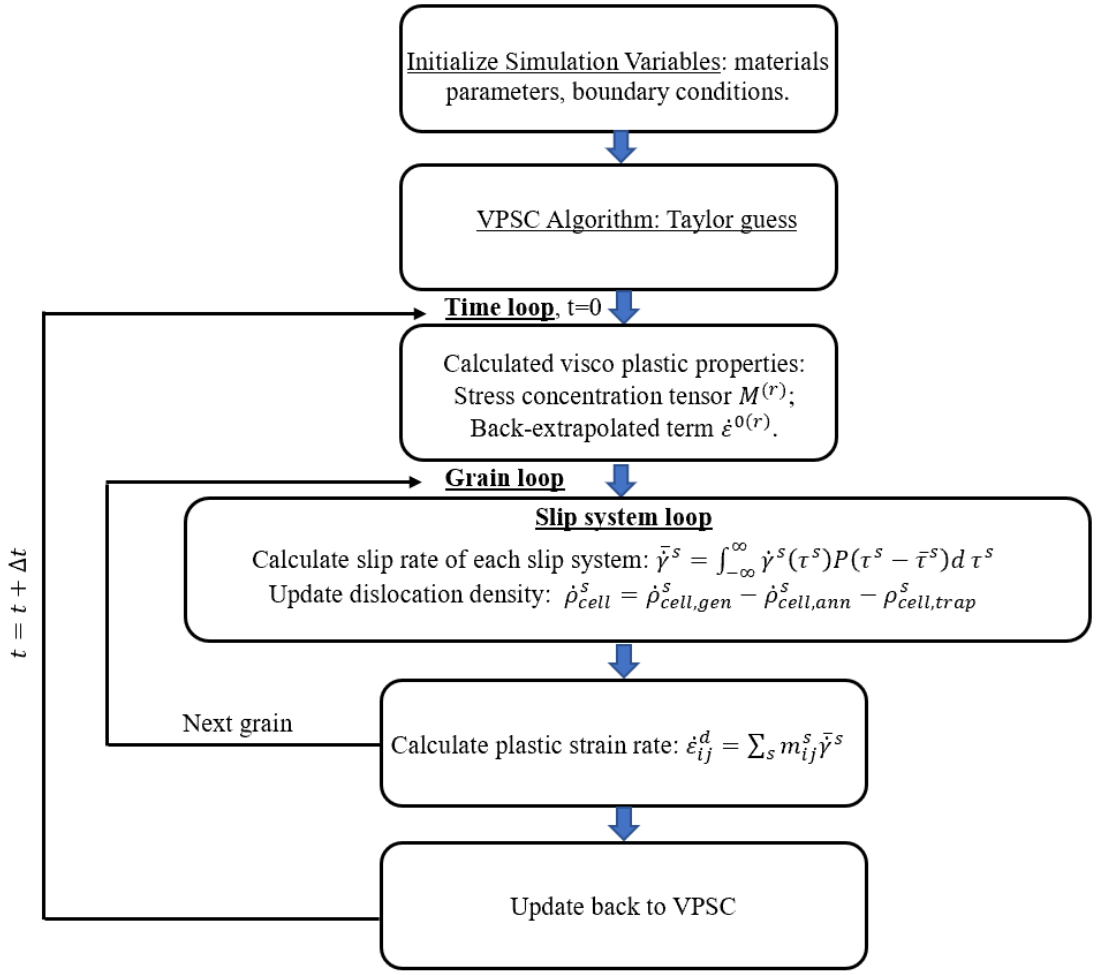

Figure 3. 3 Iterative solve description of VPSC work-flow.

3.5 Crystal plasticity finite element method framework

In this section, the computational framework of the crystal plasticity finite element method (CP-FEM) employed in this work is introduced. The physics-based constitutive CP formulations have been reviewed in Chapter 2. The CP-FEM framework employed in this project is to simulate the primary stage and secondary stage of thermal creep behaviour, which is in Chapter 5. The first two creep stages prediction will be compared to the VPSC simulation based on the same mechanism-based CP model. Furthermore, equipped with Gurson-Tvergaard-Needleman (GTN) formulation, the damage development during the tertiary creep stage will be captured in Chapter 6.

3.5.1 Finite element modelling implementation

The CP constitutive law reviewed in Chapter 2 combined with the unified physics-based CP model introduced in this chapter will be implemented in the finite element framework. The local material point is described and simulated in each dissipative process. The structural information is considered at the material point level, including the crystallographic texture and morphological texture etc.

The CP-FEM framework used in the present work is written in FreeFem++ platform (Hecht, 2012), which is an open-source, partial differential equation solver. It is equipped with enhanced capabilities for solving finite element framework formulations. The parallel calculation can be achieved by FreeFem++ to reduce computation consumption.

3.5.1.1 Mesh configuration and input file

Under the finite element framework, the representative volume element (RVE) of the interested materials is chosen and mapped by meshes. The whole RVE area is mapped evenly, with the revolution of each node being $1\ \mu m \times 1\ \mu m$. Even though the mapped structure is planar-shaped, there are two layers on the thickness dimension. Thus, technically, the meshed area is volume.

It is worth mentioning that different from artificially generated synthetic microstructures, e.g. (Biswas et al., 2019; Pal et al., 2015; Ye et al., 2021), the present project imports the grain mapping (input for CP-FEM) directly from the raw EBSD data from the work of Williams (Williams et al., 2021). Such an attempt aims to capture precisely the effects of a real AM-induced microstructure.

3.5.1.2 Boundary conditions

Eighth-symmetry is a boundary condition used in computational simulations. It is typically applied to reduce the computational domain size and improve computational efficiency while maintaining accurate results. In the context of eighth-symmetry boundary conditions, the physical domain of the problem is divided into eight equal parts, often represented as octants. The simulation is then conducted on only one of these octants, with appropriate boundary conditions applied at the cut boundaries to account for the remaining octants.As shown in Figure 3. 4, eighth-symmetry in the

model is enforced by fixing displacements to zero in the horizontal, vertical, and out-of-plane directions on faces 1, 2, and 5 respectively. For the creep testing, there is positive stress applied normally to face 3 and maintained at a constant magnitude throughout the process to simulate uniaxial tensile creep (Bieberdorf et al., 2021). The formulated enforced boundary condition is given as follows:

$$\text{On face 1: } u_x = 0$$

$$\text{On face 3: } \begin{cases} u_x = u_{disp} \text{ (displacement input)} \\ \int_A \sigma_{ij} n_i dA \text{ (stress input)} \end{cases} \quad \textbf{(3. 53)}$$

$$\text{On face 4: } u_y = 0$$

$$\text{On face 5: } u_z = 0$$

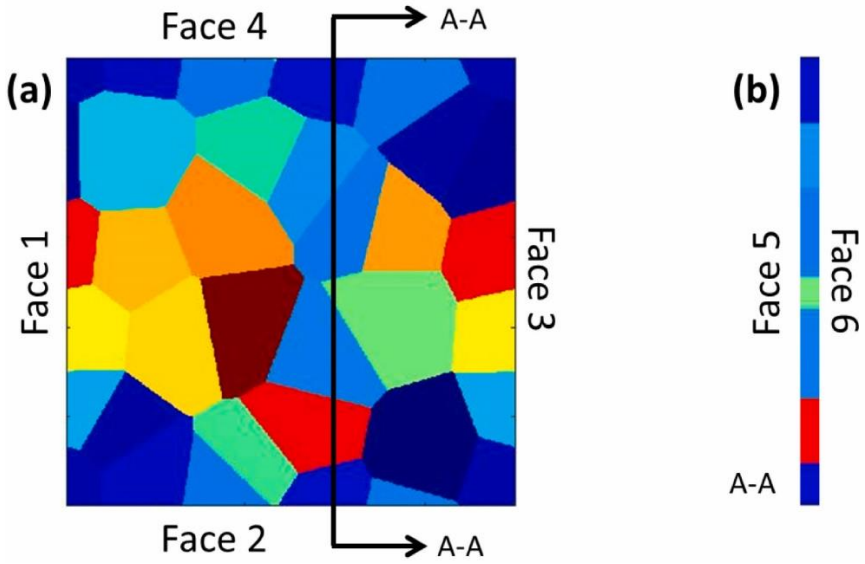

Figure 3. 4 Illustration of input structure boundaries, (a) front view; (b) side view (Bieberdorf et al., 2021).

3.5.1.3 Balance equations

According to Cauchy's first equation of motion, a balance equation can be adapted in the variational form to solve the local displacement in the proposed model. By ignoring the body forces, the body is assumed to be at equilibrium, and the balance equation with plastic strain addition is expressed as:

$$\int_V [\boldsymbol{\varepsilon}(\tilde{u})\boldsymbol{C}\boldsymbol{\varepsilon}(u) + \boldsymbol{\varepsilon}(\tilde{u})\boldsymbol{C}\boldsymbol{\varepsilon}^p(u)]dV = 0 \quad \textbf{(3. 54)}$$

$$\int_V [\boldsymbol{\varepsilon}(\tilde{u})\boldsymbol{C}\boldsymbol{\varepsilon}(u) + \boldsymbol{\varepsilon}(\tilde{u})\boldsymbol{C}\boldsymbol{\varepsilon}^p(u)]dV + \int_A \sigma_{ij} n_i dA = 0 \quad \textbf{(3. 55)}$$

Here, $\boldsymbol{C}$ denotes the stiffness tensor, $\boldsymbol{\varepsilon}$ represents the train tensor, $\boldsymbol{\varepsilon}^p$ is the plastic strain tensor, u and $\tilde{u}$ are the displacement and a virtual displacement, respectively. For the creep case, equation (3. 55) is used to replace equation (3. 54).

The constitutive law is computed and discretised at each time step. For the creep testing case, the balance law (equation (3. 55)) is solved at the beginning of each time step, which employs each mesh mode the local displacement. Therefore, each local strain is given as follows:

$$\varepsilon_{ij} = \frac{\partial u_i}{\partial x_j} \quad \textbf{(3. 56)}$$

As the total strain is the sum of the elastic strain and the plastic strain, thus:

$$\varepsilon_{ij} = \varepsilon_{ij}^e + \varepsilon_{ij}^p \quad \textbf{(3. 57)}$$

Here, ε_{ij}^e and ε_{ij}^p are elastic strain and plastic strain, respectively. The stresses from Hooke's law can be solved, which is given as:

$$\sigma_{ij} = C_{ijkl}\varepsilon_{kl}^e \quad \textbf{(3. 58)}$$

The calculated local stress at each node is adapted to calculate the resolved shear stress for each slip system ($\bar{\tau}^s = \boldsymbol{\sigma}:\mathbf{m}^s$). The rest components in the constitutive law mentioned above can be computed for the final local plastic strain rate, see equation (3. 5) ($\dot{\gamma}^s = \rho_{cell}^s b v^s \cdot \mathrm{sign}(\bar{\tau}^s)$).

3.5.2 Work-flow

The applied boundary conditions and microstructures will be initialised at the start of the simulation. Afterwards, the defined mesh mapping scheme will be applied to the input microstructure. As parallel computation is employed in this framework, the

simulation needs to partition at this stage. After parameters initialisation, structure mapping and simulation compartmentalization, the code will start the physics-based model calculation. Similar to the VPSC framework, the local stress-strain response will be simulated separately, but under CP-FEM, this will be done on each node level. And the homogenization will be done by FEM. Figure 3. 5 illustrates the visualized numerical simulation work-flow.

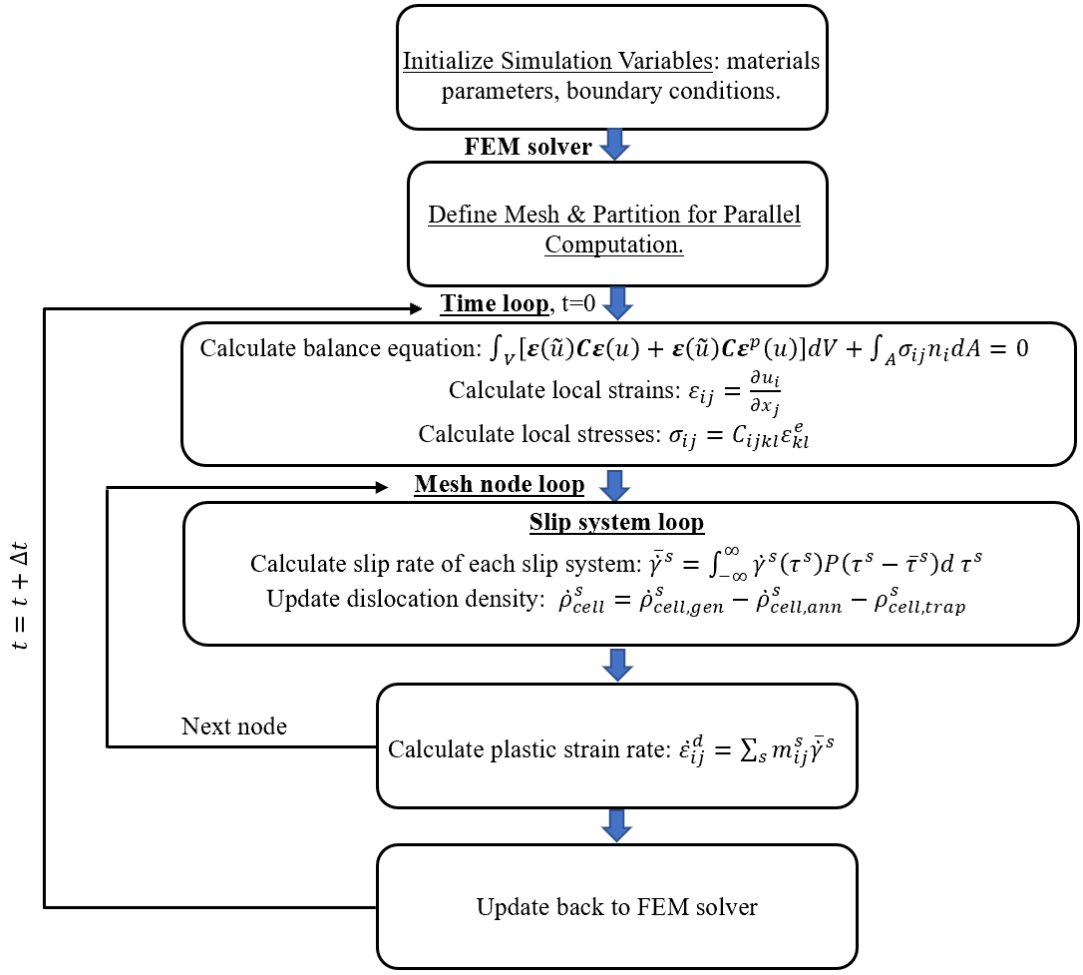

Figure 3. 5 Iterative solve description of CP-FEM work-flow.

3.6 Summary

The significance and unique functionalities of the HMS modelling technique have been introduced at the beginning of this chapter. Based on the multi-scale modelling concept, a unified physics-based CP model has been developed and described in detail. Meanwhile, the targeted materials and creep testing conditions have been introduced.

The VPSC and CP-FEM two types of frameworks, which have been devised and applied to the same physics-based model, are described in detail. Both VPSC and CP-FEM formulations are developed from the CP-based theory, which was reviewed in Chapter 2. The simulation application and calibration in Chapters 4 and 5 are conducted according to the materials information and experimental data introduced at the beginning of this chapter. The primary stage and secondary stage creep will be computed by both VPSC and CP-FEM. The tertiary creep stage, which includes damage evolution, will only be simulated by CP-FEM due to its full-field characters. Moreover, the AM process induced unique defects e.g. various types of pores, will be simulated and evaluated by CP-FEM in Chapter 6.

Chapter 4 Application of physics-based model in comparison of AM and wrought 316L stainless steel high-temperature thermal behaviours

In this chapter, the physics-based model introduced in Chapter 3 will be adapted to capture both the wrought and additive manufactured (AMed) 316L SS creep behaviour under the visco-plasticity self-consistent (VPSC) framework. The detailed microstructural characters are considered in the simulation input, which distinguishes the difference between wrought and additive manufacturing (AM) induced materials features. In addition, the simulation results are compared and indicate the different creep mechanisms' contribution in wrought and AM materials, which can give feedback to materials design. Parametric studies are conducted to investigate the Coble creep contribution evolution during the creep testing, and grain/sub-grain sizes effects on creep response.

4.1 Introduction

A literature review on the characteristics of AM technique and AM-induced unique materials microstructures has been provided in Chapter 2. According to the physics-based crystal plasticity model proposed in Chapter 3, the main characters of AM material are summarised into the dislocation densities interior of the cell, dislocation densities on the cell wall, grain sizes, sub-grain sizes and precipitation to highlight its different structure from wrought material. This highly microstructural-sensitive model is employed under the VPSC framework, aiming to reproduce the creep behaviour reported by Williams et al. (Williams et al., 2021) and Rieth et al. (Rieth et al., 2004a). In this work, the adoption of wrought materials is for the calibration of AM 316L SS. Detailed information on both materials and creep experiments has been mentioned in Section 3.2.

4.2 Simulation condition and parameter calibration

All the parameters used in the proposed physics-based model are discussed in this section.

As mentioned in Section 4.1, the microstructural features of both wrought and AM materials are included and indicated through the proposed model as the simulation input. Firstly, the wrought and AM materials textures are considered to indicate the difference and generate the evolution. The initial textures used as VPSC simulation input are plotted via Mtex toolbox in Matlab (MATLAB, 2022), which is presented in Figure 4. 1. The detailed introduction of the pole figure is available in Appendix II. The initial textures for the AMed materials are extracted from the EBSD data (Williams et al., 2021). A typical FCC rolling texture is employed for the wrought (hot rolled) case. It is worth mentioning that, in the creep testing, the wrought material was loaded perpendicular to the rolling direction (Rieth et al., 2004b).

Notice that, affine linearisation (Lebensohn and Tomé, 1993) in the VPSC framework is chosen in this work to address the grain interaction within the polycrystals.

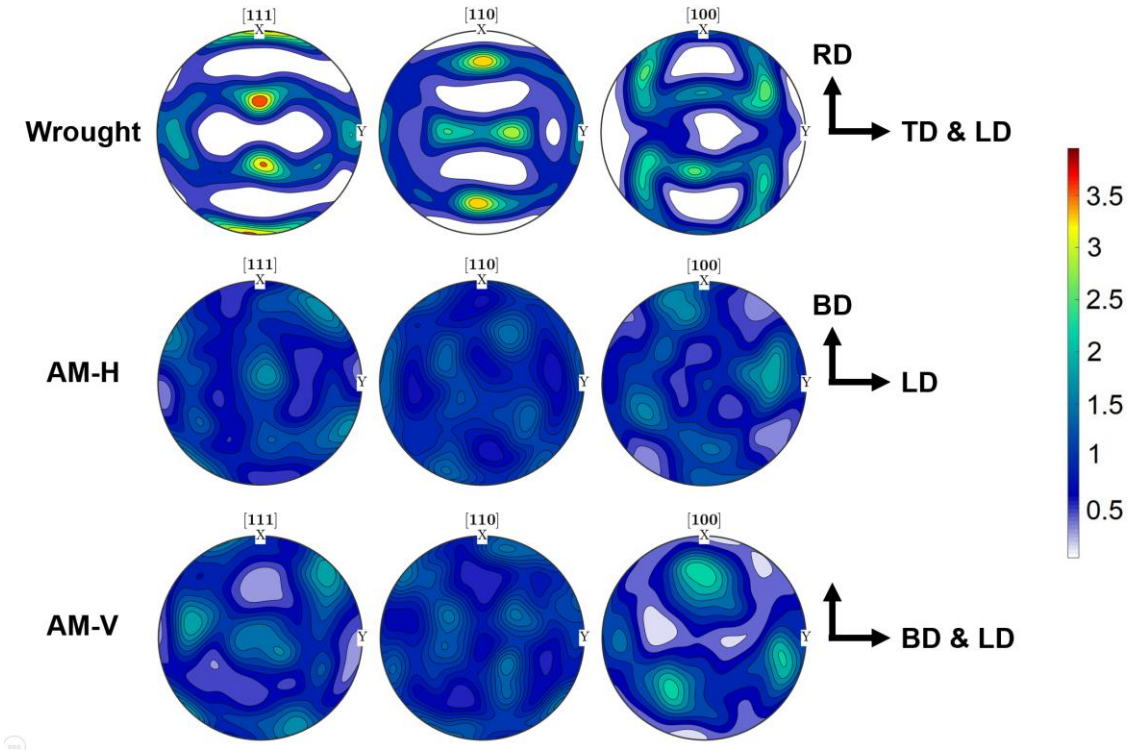

Figure 4. 1 Pole figures of the input textures for wrought, AM-H (AM, horizontally built) and AM-V (AM, vertically built) cases. RD=rolling direction; TD=transverse direction; BD=building direction; LD=loading direction.

According to Rieth et al. (Rieth et al., 2004b), the traditionally fabricated 316L SS shows equiaxed grains with an average grain size of 120 μm. As for AM 316L SS, the microstructural features are extracted from the EBSD data characterised by Williams et al. (Williams et al., 2021). Based on the three Euler-angles-defined microstructure at each pixel in the EBSD raw data, the high angle grain boundaries (HAGBs) and low angle grain boundaries (LAGBs) are determined, which is plotted in Figure 4. 2. Here the HAGBs are defined if the misorientation is greater than 15°, while LAGBs have a misorientation between 2° and 15°. The mean grain sizes, which are defined by HAGBs, are are 37.91 μm and 53.31 μm for horizontally (AM-H) and vertically (AM-V) built samples respectively. The mean grain sizes of AM samples are counted manually according to Figure 4. 2. There is a relation between the grain size and sub-grain size, which is given: (Sabzi et al., 2021)

$$D_{sub} = D \cdot \frac{n_{HAGB}}{n_{LAGB} + n_{HAGB}} \quad \textbf{(4. 1)}$$

Here D is the grain size, while D_{sub} is the sub-grain size. n_{LAGB} and n_{HAGB} refer to the pixel numbers for LAGBs and HAGBs in EBSD data. Therefore, the sub-grain sizes, which are defined by LAGBs, are determined to be 23.14 µm and 26.74 µm for AM-H and AM-V samples, respectively.

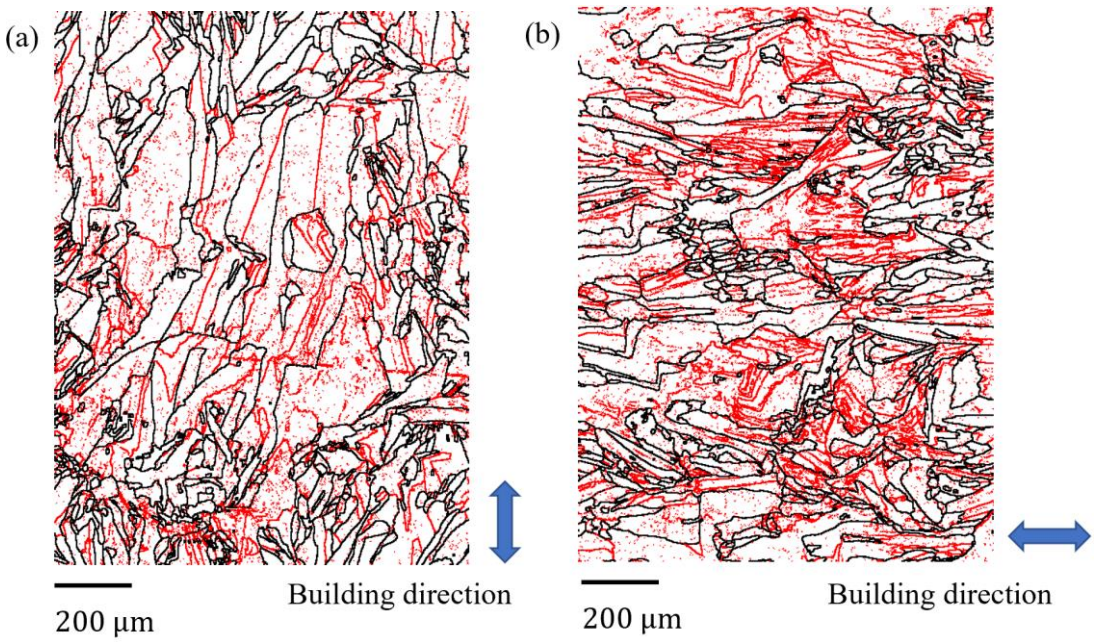

Figure 4. 2 HAGBs (black) and LAGBs (red) in the AM microstructures: (a) AM-H (horizontally built) and (b) AM-V (vertically built).

The values of dislocation density inside the cell and on the cell wall are chosen based on a range of literature sources, e.g. (Ghosh et al., 2019; Hong et al., 2021a; Kocks et al., 1975b; Maric et al., 2018; Pham et al., 2011; Puchi Cabrera, 2001b; Shamsujjoha et al., 2018; Sprouster et al., 2021; Tandon et al., 2018; Weaver et al., 2020; Yin et al., 2019). The initial cell dislocation densities ρ_{cell} adapted in this work for wrought and AM materials are 1.2×10^{13} m^{-2} and 1.2×10^{14} m^{-2}, respectively. There is a relation between the sub-grain size and cell wall dislocation density, which is given as follows (Wen et al., 2017a):

$$D_{sub} \propto \frac{1}{\sqrt{\rho_{cw}}} \quad \textbf{(4. 2)}$$

With the sub-grain sizes determined above, and based on the cell wall dislocation density in AM materials from literature (Hong et al., 2021a; Shamsujjoha et al., 2018; Sprouster et al., 2021; Yin et al., 2019), the initial cell wall dislocation densities ρ_{cw} for AM-V, and AM-H materials, are chosen as 1.85×10^{15} m^{-2} and 2.4×10^{15} m^{-2}, respectively. Since there is no obvious sub-grain structure in wrought 316L SS, therefore, the cell wall dislocation density value of wrought material is chosen as 2.4×10^{14} m^{-2} from the literature (Ghosh et al., 2019; Maric et al., 2018; Pham et al., 2011; Rieth et al., 2004b; Tandon et al., 2018; Weaver et al., 2020). These dislocation densities are of the same magnitude as reported in experiments for hot-rolling wrought (Ghosh et al., 2019; Pham et al., 2011; Weaver et al., 2020) and AMed (Hong et al., 2021a; Shamsujjoha et al., 2018; Sprouster et al., 2021; Yin et al., 2019) 316L SSs. In this project, the initial dislocation densities are assumed to be the same on all slip systems, however, their evolutions are determined individually on each slip system for each grain as described in section 3.2.

The variance V in equation (3. 4) quantifies the intragranular stress fluctuation (responsible for peak broadening) induced by the long-range elastic stress fields around the defects segments in the matrix. The variance theory was proposed based on the line profile analysis which relates to the intragranular stress dispersion with the dislocation density (e.g. (Kalácska et al., 2017; Wang et al., 2017a; Wilkens, 1970; Wilkinson et al., 2014)). However, the high density of precipitates in 316L SS may also affect the intragranular stress distribution which has not been quantified in previous studies. Wang et al. (Wang et al., 2016) have discussed that the intragranular stress dispersion can be assumed to be a function of the cell dislocation density, which is expressed as:

$$V = \eta\sqrt{\rho_{cell}} \quad \textbf{(4. 3)}$$

With $\eta \approx 10^{-7}$ MPa/m, which is a scaling coefficient (Wang et al., 2016). Since the cell dislocation densities should be different in reality interior for each grain on each slip system, the variance is supposed to be various on different slip systems as well. In

addition, the value of variance should vary during the deformation with the dislocation densities evolution (Wen et al., 2017a). However, for the sake of simplicity, the initial dislocation densities interior of the cell and on the cell wall are both set to be the same for every slip system. Therefore, the variance V is also assumed to be equal for all systems, and considered constant throughout the simulations. In this work, the parameter V is back-fitted from the experimental data and assumed to be equal for wrought and AMed materials. $V = 10\sqrt{2}$ MPa is chosen here which is similar to the values used for stainless steels (Kumar and Capolungo, 2022; Wen et al., 2017b; Wen et al., 2020a).

The dislocation density evolution parameters k_1, k_2 and k_3 are all material constants, and calibrated based on the experimental data. According to Was (Was, 2016), the parameter n_0, see equation (3. 21), is related to the strain rate sensitivity. The value of n_0 should be between 3-5 for high temperature cases, and 3.5 is chosen in this work following Wen et al.(Wen et al., 2017b).

The zero-stress activation energies $\Delta G_{0,i}$, see equation (3. 14), for the bypass of dislocation and precipitates, are back-fitted to be 2.0 eV and 4.1 eV respectively. Additionally, since the zero-stress activation energy is the material physics character, it is assumed to be the same for wrought and AMed materials. Theoretically, the value of $\Delta G_{0,p}$ is dependent on the nature of the obstacle, therefore, it can be related to the strength and size of $M_{23}C_6$. However, such a relationship has not been quantified specifically yet. Thus, it is ignored in this project. p $(0 < p < 1)$ and q $(1 < p < 2)$ in equation (3. 14) are the exponent parameters associated with the obstacle resistance profiles (Kocks et al., 1975b), which ae associated with the shape of the obstacle. Their values are obtained by back-fitting the experimental creep data within reasonable ranges.

The attack frequency υ_i^s is related to the mechanism of dislocation to overcome the obstacle (Caillard and Martin, 2003). For the dislocation-precipitate interaction, $\upsilon_p^s = 1.2 \times 10^{10}\ \mathrm{s}^{-1}$ is chosen following Wen et al. (Wen et al., 2017a). It is suggested that the attack frequency for dislocation to bypass dislocation-type obstacles υ_ρ^s, is associated with the average length of the vibrating dislocation segments between two pinning points (Granato et al., 1964; Wen et al., 2018), which is expressed as:

$$v_\rho^s = \chi C_s/\lambda^s \quad \textbf{(4. 4)}$$

χ is an entropy factor (of the order of 1), C_s denotes the shear wave velocity, which is given as:

$$C_s = \sqrt{\mu/\rho_0} \quad \textbf{(4. 5)}$$

The lattice friction τ_0^s is described by the empirical equation $\tau_0^s = 49.225 \times \exp(-0.0008 \times T)$ in MPa, which is derived from the molecular dynamics results from Chu et al. (Chu et al., 2020). The value of lattice friction, apart from the molecular dynamic simulations, can also be obtained experimentally. However, pure Fe, has bcc structure, which is different from the 316L SS fcc structure. Therefore, the fcc structural Fe atom lattice frication in 316L SS can not be obtained from the tensile test of pure ferrite.

The value of solid solution hardening τ_{ss} is back-fitted. More details will be found in section 4.4.

The Coble creep parameters Q_{gb} and A_{coble} are considered to be the same for wrought and AMed materials, since they are materials' own character. According to equations (3. 23), (3. 24), and (3. 25), A_{coble} consists of constant $\alpha_{gb} = 148$ (Coble, 1963), grain boundary thickness $\delta_{gb} \approx 0.7$ nm (Bieberdorf et al., 2021), atomic volume $\Omega \approx b^3$ (Wen et al., 2017a) pre-exponential factor $D_{gb,0} \approx 5 \times 10^{-5}$ $\mathrm{m^2 s^{-1}}$ (Song and Weng, 2005), and the Boltzmann constant k:

$$A_{coble} = \frac{\alpha_{gb} D_{gb,0} \delta_{gb} \Omega}{\pi k} \quad \textbf{(4. 6)}$$

As a result, the calculated value of A_{coble} in this work is 2.052×10^{-12} $\mathrm{K \cdot MPa^{-1} \cdot s^{-1} \cdot m^3}$.

The value of Q_{gb} is determined based on the activation energy in the lattice, Q_l, since there is limited literature mentioned the exact value of Q_{gb}. Gjostein (Gjostein, 1972; Shewmon, 2016) has studied the relationship between the vacancy diffusivities in the

lattice Q_l and in the grain boundaries Q_{gb} in FCC materials. The ratio $R = \frac{Q_{gb}}{Q_l}$ is calculated around $0.4 - 0.5$, since there are more open spaces for atom to jump on grain boundaries (Gjostein, 1972; Shewmon, 2016). Q_l incorporates the sum of the vacancy formation energy Q_l^f, and the vacancy migration energy Q_l^m. Due to the similarity between pure Ni and $\gamma - \mathrm{Fe}$, the value of Q_l of pure Ni, which is 2.64 eV, can be used for $\gamma - \mathrm{Fe}$ (Feng et al., 2019; Foiles et al., 1986; Mansur, 1987; Poletaev et al., 2020; Shang et al., 2016; Song and Weng, 2005). Feng et al. (Feng et al., 2019) calculated $Q_l = 3.49$ eV for $\gamma - \mathrm{Fe}$ using density functional theory. It was reported by Gates and Horton (1977) that Q_l of 316L SS is ~3.70 eV. Overall, according to the literature, the value of Q_l is chose to be 3.43 eV. In this work, the ratio R=0.5. Therefore, Q_{gb} used in this work is determined to be 1.71 eV.

All the parameters used in this chapter are listed in **Table 4. 1**.

Table 4. 1 Parameter used in physics-based crystal plasticity hardening model

Parameter	Value	Source
k (Boltzmann constant)	8.617×10^{-5} eV/K	
b (magnitude of Burgers vector)	2.58×10^{-10} m	(Li et al., 2019b)
V (dislocation distribution variance)	$10\sqrt{2}$ MPa	(Kumar and Capolungo, 2022; Wen et al., 2017b; Wen et al., 2020a)
ρ_0 (mass density)	8000 kg/m^3	(Kamath et al., 2014; Xue et al., 2007b; Zhong et al., 2019)
h_p (trapping coefficient for $M_{23}C_6$ precipitate)	1	(Sobie et al., 2015)

ρ_{cell}^{s} (initial cell dislocation density for each slip system)	1×10^{12} m^{-2} (wrought); 1×10^{13} m^{-2} (AM)	Wrought (Ghosh et al., 2019; Maric et al., 2018; Pham et al., 2011; Tandon et al., 2018; Weaver et al., 2020); AM (Hong et al., 2021a; Shamsujjoha et al., 2018; Sprouster et al., 2021; Yin et al., 2019)*
ρ_{cw}^{s} (initial cell wall dislocation density for each slip system)	2×10^{13} m^{-2} (wrought) 1.54×10^{14} m^{-2} (AM-vertical) 2×10^{14} m^{-2} (AM-horizontal)	Wrought (Ghosh et al., 2019; Maric et al., 2018; Pham et al., 2011; Tandon et al., 2018; Weaver et al., 2020); AM (Hong et al., 2021a; Shamsujjoha et al., 2018; Sprouster et al., 2021; Yin et al., 2019)*
$\alpha^{ss'}$ (latent hardening matrix)	0.7 (collinear); 0.2 (non-collinear)	(Queyreau et al., 2009)*
μ (shear modulus)	$88884.6 - T \times 37.7$	(Puchi Cabrera, 2001b)
$\Delta G_{0,\rho}$ (zero stress activation energy for dislocations)	2 eV	
$\Delta G_{0,p}$ (zero stress activation energy for precipitates)	4.1 eV	
p (exponent parameter)	0.8	(Kocks et al., 1975a)*
q (exponent Parameter)	1.4	(Kocks et al., 1975a)*

T (temperature)	823 K, 873 K (wrought); 923 K (AM)	
τ_0^s (lattice frictional stress)	$49.225 \times \exp(-0.0008 \times T)$	(Chu et al., 2020)
υ_p (attack frequency for precipitation obstacles)	$1.2 \times 10^{10}\ s^{-1}$	(Wen et al., 2017a)
χ (entropy factor)	1	(Wang et al., 2017a)
k_1 (material constant)	0.05	
k_2 (material constant)	40	
n_0 (annihilation strain rate sensitivity)	3.5	(Estrin, 1998a; Poirier, 1985; Weertman, 1968)
D (grain size)	120 μm (wrought); 37.91 μm (AM-horizontal); 53.31 μm (AM-vertical)	(Rieth et al., 2004b) (Sabzi et al., 2021)
D_{sub} (sub-grain size)	23.14 μm (AM-horizontal); 26.74 μm (AM-vertical)	(Sabzi et al., 2021)
A_{Coble} (Coble creep parameter)	$2.052 \times 10^{-12}\ K \cdot MPa^{-1} \cdot s^{-1} \cdot m^3$	
Q_{gb} (activation energy for grain boundary diffusion)	1.71 eV	
τ_{ss} (solid solution hardening)	245 MPa (wrought-823K); 225 MPa (wrought-873K); 210 MPa (AM-923K)	(Cho et al., 2021; Kako et al., 2002; Matijasevic and Almazouzi, 2008; Norström, 1977; Yusuf et al., 2020)*

*Parameter estimated or back-fitted from experimental data within the range given in the listed references.

4.3 Simulation results

Figure 4. 3 and Figure 4. 4 show the simulation results of creep strain and the corresponding creep rate as a function of creep time respectively. It is presented that the experimental creep deformation reported by Williams et al. (Williams et al., 2021) and Rieth et al. (Rieth et al., 2004b) for both AM and wrought 316L SSs can be generally captured by the proposed physics-based CP model. As mentioned in Chapter 3, due to the limitation of VPSC, which is a mean-filed model, the tertiary creep (a fast increment of creep rate at the last stage of deformation as a result of void nucleation, growth and coalescence) is not considered in this chapter. This can lead to some deviations between simulation and experimental results. The creep damage behaviour will be simulated by CP-FEM in Chapter 5.

It is worth mentioning that, from the simulation results, wrought materials exhibit an obvious primary creep stage (fast decreasing of strain rate at the beginning of creep deformation). On the contrary, it is less evident in AM 316L SS. This is because of the associated competition between dislocation-mediated plasticity and diffusion-mediated plasticity. In theory, the dislocation glide-induced creep rate is likely to decrease from the beginning of creep, which is due to the evolution of dislocation densities (Wen et al., 2017b; Wen et al., 2018), whereas the Coble creep rate is supposed to maintain the constant since there is no obvious change of grain or sub-grain sizes at the first stage of creep deformation. As a result, the absence of a significant primary creep stage in the AM 316L SS indicates more deformation contribution from the Coble creep mechanism. The detailed competition between the dislocation glide creep and Coble creep will be discussed in Section 4.4.

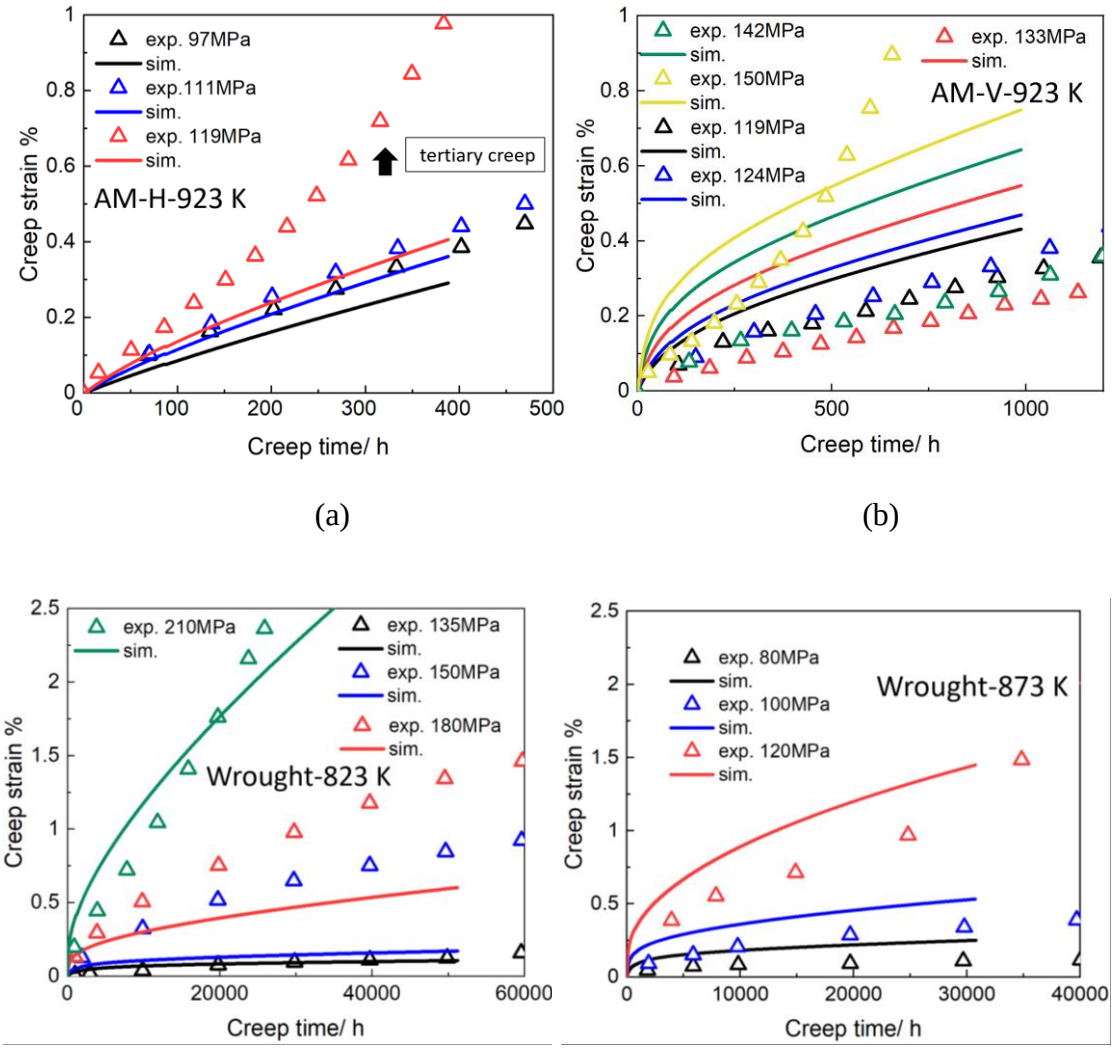

Figure 4. 3 The creep strain comparison between simulation results and experimental data. (a) AM-H (horizontally built); (b) AM-V (vertically built) (both AM cases are performed under 923 K); (c) wrought-823 K; (d) wrought-873 K. Note that tertiary creep is not considered in this work.

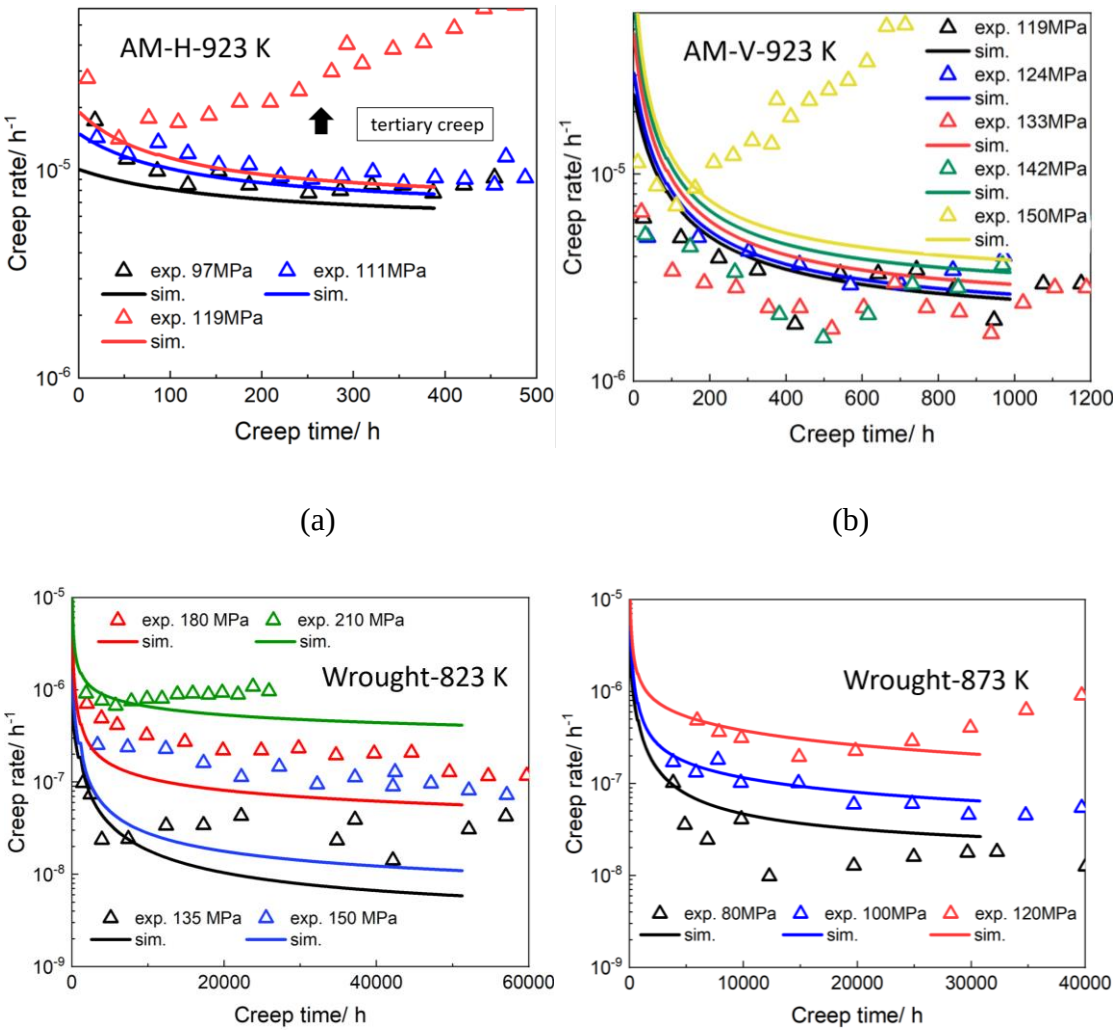

Figure 4. 4 The creep rate comparison between simulation results and experiments. (a) AM-H (horizontally built); (b) AM-V (vertically built) (both AM cases are performed under 923 K); (c) wrought-823 K; (d) wrought-873 K. Note that tertiary creep is not considered in this work.

Figure 4. 5 shows the predicted steady-state creep rates (minimum creep rates) for both AM and wrought 316L SSs, which can generally capture the trend of the original experimental results. The steady-state creep rate is determined by both plasticity and damage (tertiary creep). As the damage is not considered in the VPSC framework, therefore, the theoretical minimum creep rates cannot be achieved in the current predicted results. For this reason, the simulated steady stage creep rates via VPSC computing are chosen at the time that the experimental steady stage creep rates were

reached. As presented in Figure 4. 5, there is a lower strain rate sensitivity in AM materials, which is also reproduced in the simulation results. The lower strain rate sensitivity is because of the relatively high diffusion-mediated creep contribution. In addition, the diffusion-mediated Coble creep value presents a linear relationship between stress and strain rate, which can be found in equation (3. 59).

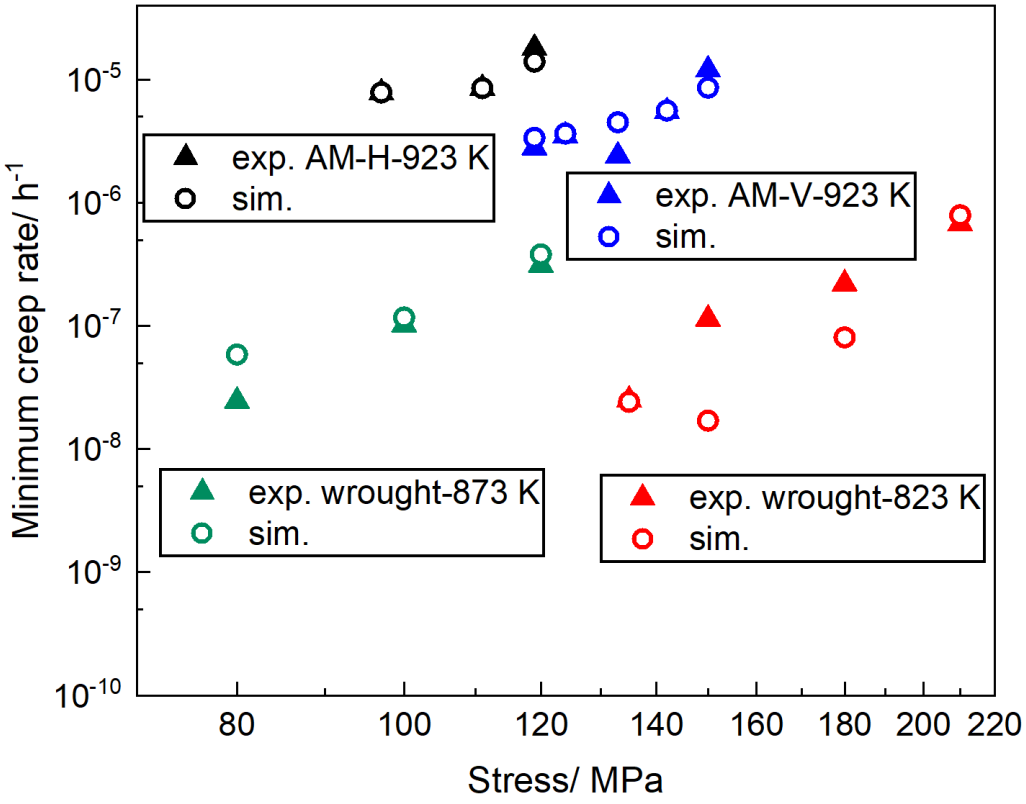

Figure 4. 5 Comparison of minimum creep rate for both AMed and wrought 316L SSs, experimental data from Williams et al. (Williams et al., 2021) and Rieth et al. (Rieth et al., 2004b); AM-H = horizontally built, AM-V = vertically built.

4.4 Discussion

4.4.1 Error sources

As illustrated in Section 4.3, the trend of both AM and wrought 316L SS creep behaviour has been captured. However, there is still some deviation between the experimental data and simulation results. In addition to some inevitable inaccuracies in parameter calibration, based on the current method, the potential error sources could be:

(1) Precipitation evolution at the beginning of creep deformation is not considered as discussed in Section 4.2. (2) Microstructural parameters, such as initial dislocation densities interior of the cell, are set to be the same for AM-H and AM-V cases, which is not true in reality. These kinds of parameters can be determined accurately through systematic experimental and low-scale modelling studies, which can be conducted in the future. (3) The precipitation simulation performed by Thermo-Calc did not include the strain energy effect. (4) AM-induced residual stress is not considered in this work. Since the high-temperature creep environment, which is 923 K in this case, is equivalent to the thermal ageing heat treatment. The high-temperature environment can lead to substantial stress relaxation at the beginning of the creep deformation. As a result, this can affect the creep rates during the beginning several hours of creep and may cause deviations in the results. However, its effects on the long-term creep deformation and the steady-state creep rates should be unnoticeable. (5) The void nucleation and growth, which are generally considered for tertiary creep, may occur at early stages of creep and affect moderately the creep behaviour: this is beyond the scope of the VPSC framework (Bieberdorf et al., 2021). Apart from the inaccuracy in the parameter calibration and experimental results, the error sources can be considered in future work through systematic experimental studies and low-scale simulations.

Notice that the contribution of dislocation climbing in dislocation motion is ignored in this work due to the uncertainty of the interactions between dislocations and solutes or obstacles as mentioned in Section 3.2. However, the effects of climb in the dislocation dynamic recovery process are considered through one of the laws proposed by Estrin (Estrin, 1998a).

4.4.2 Mechanisms and parameters

It is worth mentioning that the structure of the AM-induced material is referred to as non-equilibrium microstructure. The non-equilibrium microstructure is the result of the extremely high cooling rates and cyclic thermal history during the AM processing. Even though the microstructures of AM material and traditionally fabricated material are quite different, their deformation mechanisms (e.g. dislocation-mediated plasticity and diffusion-mediated plasticity) and hardening mechanisms (e.g. grain boundary hardening, dislocation hardening, solid solution hardening and precipitation hardening

etc.) are the same. Therefore, it is reasonable to use the classic formulations (e.g. the Orowan equation and the Kocks-type enthalpy law) to capture the creep deformation of both wrought and AM materials with their own microstructural parameters. Meanwhile, some of the 316L SS its own characteristic parameters, such as A_{coble} and Q_{gb}, are set the same for both od AM and wrought cases. In this way, the proposed model physics-based can effectively simulate and evaluate the effects of different mechanisms, which are described as functions of microstructure. Therefore, the physics-based simulation results can give feedback to future microstructure-tailoring of AM materials. In addition, as a microstructure-sensitive model, the non-equilibrium AM-induced structures are represented via both EBSD data and statistical parameters for AM 316L SS, including structural texture, grain/sub-grain sizes, and dislocation densities. In this work, the microstructural details and creep testing data of wrought 316L SS are performed virtually as a reference for the validation of the universality of the proposed unified model. By describing both the wrought and AM 316L SS, the accuracy of the proposed model can be validated, as well as the microstructure-associated deformation and hardening mechanisms.

4.4.3 Grain boundary sliding

Apart from all the other physical processes considered in the proposed model, grain boundary sliding (GBS) is also one of the important creep principles. Besides the extensive studies in nanocrystalline materials, such as Husain et al. (Husain et al., 2020) and Li et al. (Li et al., 2019a), GBS in 316L SS has been studied extensively as well.

GBS-controlled creep rate, $\dot{\varepsilon}_{\mathrm{GBS}}$, is generally dependent on the grain size, temperature, and loading stress, which is given (Langdon, 1970; Yang et al., 2021a):

$$\dot{\varepsilon}_{GBS} = \frac{\beta b^2 \sigma_{ij}^2}{D\mu kT} D_{gb} \qquad \textbf{(4. 7)}$$

With $\beta = 1$ is the constan. However, for the $\mathrm{M_{23}C_6}$ carbides formed on the grain boundaries of 316L SS can greatly inhibit GBS (Kumar and Capolungo, 2022; Sun and Jonas, 1994; Wu and Koul, 1995). According to the Thermo-Calc simulation results in Section 3.3, the formation of $\mathrm{M_{23}C_6}$ on the grain boundaries are extensive. As a result,

the contribution of the effect of GBS on the total creep behaviour is not considered in this work.

4.4.4 Competition between dislocation motion creep and Coble creep

Usually, the grain boundaries, which are also referred to HAGBs, are decorated with a high dislocation density and associated with Coble creep. Since the medium of Coble creep is the grain boundary, on which occurs vacancy diffusion. As presented in Figure 4. 5, the AM materials show higher minimum creep rates compared to wrought cases. This is attributed to the smaller grain size in AM 316L SS, which results in more grain boundaries and introduces more Coble creep contributions. Similar to the comparison between the AM-H and AM-V cases. Notice that Yoon et al. (Yoon et al., 2020) and Yang et al. (Yang et al., 2021a) also reported a better creep resistance in the vertically built AM materials in comparison to the horizontally built ones, which is matching with the present work. Due to the lower grain size, the Coble creep rates in AM 316L SS are significantly higher compared to the wrought ones. By contrast, the dislocation motion-induced creep is less active in AM materials. This is because of the higher dislocation densities (in the cell and cell wall), which will be discussed later in this section. Figure 4. 6 illustrated the relative activities of diffusion-mediated Coble creep and total creep rates during the whole simulation, which is described by $\dot{\varepsilon}^{coble}/\dot{\varepsilon}^{p}$. It can be straightforward told that Coble creep is the dominant creep mechanism in AM materials. The significance of its role achieves the most at the secondary creep stage. The variations in AM-H and AM-V cases are mainly attributed to the divergence in their grain sizes. As a result, there are higher Coble rates in AM-H cases. As for wrought materials, the contribution of Coble creep is relatively low. In addition, In regions of higher stress, the primary mechanism for dislocation motion prevails, whereas Coble creep exerts a greater influence in regions of lower stress in wrought materials.

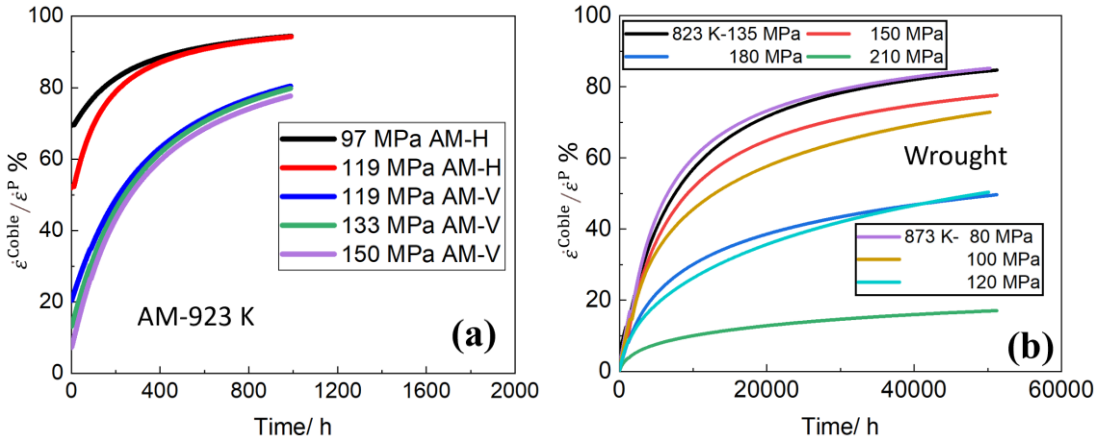

Figure 4. 6 The relative activities of diffusion-mediated Coble creep and total creep rates during the whole simulation, (a) AM 316L SS (AM-H = horizontally built, AM-V = vertically built) and (b) wrought 316L SS.

Normally, the quasi-static tensile test or Vickers hardness test is the most performed to quantify the strength of the material in either engineering application or scientific research, including the AM materials and AM printing strategy design. Therefore, it is a universal understanding that the material (excludes nano material) has a finer crystal structure (higher density of HAGBs and LAGBs) and can exhibit better mechanical properties (e.g. higher yield stress). This conclusion is incorporated with the grain boundary strengthening mentioned in Section 2.2. Nonetheless, many AM materials are designed to withstand creep environments. Hence, the contribution from diffusion-mediated Coble creep cannot be neglected. In addition, a finer sub-grain structure can strengthen the material by impeding the dislocation movement. The sub-grain structure hardening is considered indirectly, via the long-range hardening described by cell wall dislocations, see equation (3. 16). At the same time, the Coble creep contribution is enhanced by the high density of HAGBs. As a result, the contribution from grain size and sub-grain size should be considered and quantified individually during the competition between dislocation-mediated plasticity and diffusion-mediated plasticity and the consequent creep resistance.

4.4.5 Parametric study of grain size and sub-grain size

As mentioned in Section 4.4.4, the role of grain size and sub-grain size should be considered separately in the dislocation motion and Coble creep competition. Therefore, a parametric study is conducted in this section.

Figure 4. 7 is illustrating the results acquired according to the simulations of the AM-V case. The grain sizes are chosen as 60 μm and 40 μm, which can directly determine the Coble creep contribution. Meanwhile, the sub-grain sizes are varying between 30 μm and 20 μm, which aims to indicate the dislocation motion strengthening from the limited sub-grain sizes. As mentioned in Section 4.2.2, the cell wall dislocation density ρ_{cw} is determined based on the relationship: $D_{sub} \propto \frac{1}{\sqrt{\rho_{cw}}}$ (Wen et al., 2017b). Notice that, the precipitate size and number density were also updated via Thermo-Calc simulations accordingly. The corresponding precipitation information is presented in Table 4. 2. Notice that it has been mentioned in Section 3.3.3 that to emphasise the strong sub-grain structure and LAGBs in AM 316L SS can act as preferred nucleation sites as HAGB, the sub-grain size is utilised as input in Thermo-Calc simulations. Therefore, for the cases that have the same sub-grain sizes, the Thermo-Calc precipitation results are the same, since all the other parameters are the same. As shown in Figure 4. 7 (a), at a lower stress regime(100 MPa), diffusion-mediated plasticity is dominant, where the grain sizes show a more significant role in the steady-state creep rate. On the contrary, by loading higher stress (200 MPa, see Figure 4. 7(b)), the dislocation-medicated plasticity is more dominant, while the finer sub-grain sizes tend to enhance the materials' creep resistance. This is consistent with quasi-static tensile test results (Borodachenkova et al., 2015).

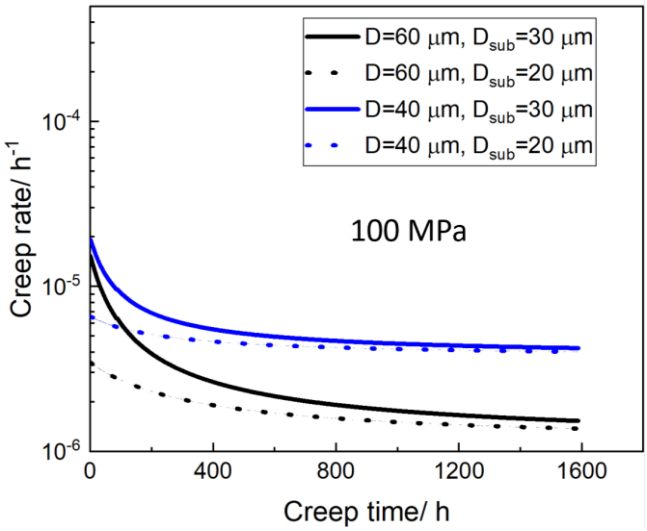

(a)

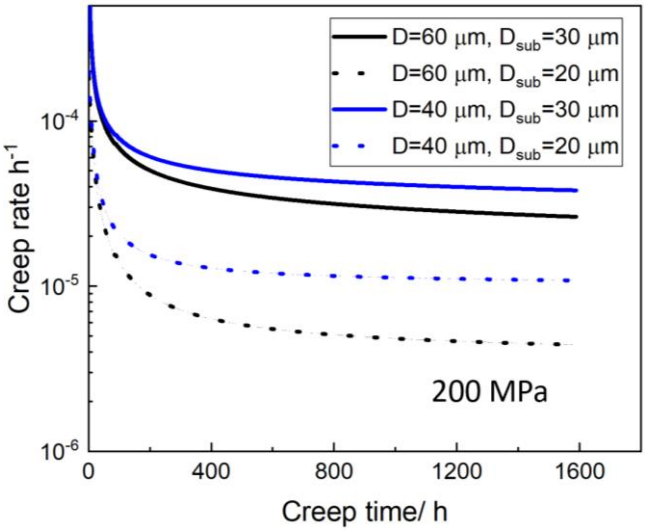

(b)

Figure 4. 7 Comparison of creep rate between using different grain sizes and sub-grain sizes. (a) AM case under 100 MPa loading; (b) AM case under 200 MPa loading. (*D*-grain size, D_{sub}-sub-grain size).

Table 4. 2 Thermo-Calc simulation results for $M_{23}C_6$ in parametric study (The superscript *cell* and *cw* denote the precipitates in the cell interior and on the cell wall, respectively; D-grain size, D_{sub}-sub-grain size)

Character AM-V 923K	$D = 60$ μm $D_{sub} = 30$ μm	$D = 40$ μm $D_{sub} = 30$ μm	$D = 60$ μm $D_{sub} = 20$ μm	$D = 40$ μm $D_{sub} = 20$ μm
N_p^{cell} (m^{-3})	1.56×10^{16}		1.33×10^{17}	
D_p^{cell} (nm)	52		48	
N_p^{cw} (m^{-3})	8.22×10^{19}		1.07×10^{20}	
D_p^{cw} (nm)	52		48	

Although the other corresponding changes inside the microstructures are also supposed to be considered in AM printing strategy design. The parametric study results are demonstrating that the grain and sub-grain microstructures should be devised according to the in-service conditions individually. The direct adaption from quasi-static tensile testing or hardness testing is not sensible and applicable.

4.4.6 Quantification of different strengthening mechanisms

As mentioned in Section 3.2, a unified physics-based CP model is proposed in this work. The microstructure-dependent hardening mechanisms are considered contributions to the CRSS, including lattice friction, dislocation hardening, precipitation hardening, and solid solution strengthening. In order to quantify and study these strengthening mechanisms individually, the values of the terms for each mechanism are listed in Table 4.3. Apparently, the value of CRSS in AM materials is higher than in wrought materials. This is because of significant dislocation hardening in the AM materials, which including the hardening from the cell wall dislocation densities on the sub-grain boundaries.

Notice that the values of the precipitation hardening τ_p^s are relatively low in both AM and wrought cases. This is owing to the τ_p^s calculated here only consists of the long-range precipitation hardening (the hardening results from the long-range stress field around each precipitate). Meanwhile, short-range precipitation hardening is considered via dislocation-precipitate interaction, which is the main part of the precipitation strengthening in the proposed model (Wen et al., 2017b). The case of AM-V (923 K) with 119 MPa loading is taken for instance. It is worth mentioning that the predicted initial creep rates with and without considering the precipitates interior of the cell are 1.5×10^{-5} h^{-1} and 5.5×10^{-2} h^{-1} respectively. There are three orders of magnitude discrepancies, which illustrate the significance of short-range precipitation strengthening.

Table 4. 3 The initial contribution of each strengthening mechanism to the critical resolved shear stress (CRSS). AM-H = AM horizontally built; AM-V = AM vertically built

	AM-H 923 K	AM-V 923 K	Wrought 873 K	Wrought 823 K
Solid solution strengthening/ MPa * τ_{ss}^s	210	210	225	245
Dislocation hardening/ MPa $\tau_\rho^s = \mu b\sqrt{\sum \alpha(\rho_{cell}^s + \rho_{cw}^s)}$	334	295	109	113
Precipitate Hardening/ MPa $\tau_p = h_p \mu b\sqrt{N_p^{cell} D_p^{cell} + N_p^{cw} D_p^{cw}}$	25	24.5	15	31
Lattice friction/ MPa $\tau_0 = 49.225 \times \exp(-0.0008 \times T)$	23.5	23.5	24.5	25.5

Critical resolved shear stress (CRSS)/ MPa				
$\tau_{CRSS} = \tau_0 + \tau_{ss} + \tau_P + \tau_\rho^S$	592.5	553	373.5	414.5

*Parameter estimated or back-fitted from experimental data within the range given in the listed references.

For solid solution strengthening and precipitation strengthening, the key point is the understanding of the relationship between the chemical composition and the mechanical properties of alloys. Compared to the precipitation strengthening can be captured via Thermo-Calc simulations based on the chemical composition and structural information, the solid solution hardening is more complicated. As mentioned in Section 2.3.4, the solid solution hardening value in this project is chosen by the back-fitting method, which is according to the experimental data.

4.5 Summary

In this chapter, the unified physics-based model proposed in Chapter 3 is adapted under the VPSC framework to predict the creep behaviour of both wrought and AM 316L SS. The results indicate that under the VPSC framework, the proposed model is capable to reproduce the experimental data for both wrought and AM 316L SS. Moreover, the diffusion-mediated Coble creep mechanism shows an essential role in the creep behaviour of AM materials. Compared with the wrought materials, the dominant activity of Coble creep (due to the high density of HAGBs) results in less obvious primary stage creep behaviour and lower strain rate sensitivity in the AM materials.

The different roles of the grain size and sub-grain size during creep deformation are analysed separately. It turns out that even the sub-grain size is commonly assumed to have the main hardening contributions, however, a finer grain structure can enhance the diffusion-mediated Coble creep at low-stress and high-temperature conditions, which results in higher creep rate and lower creep resistance. The individual function of grain and sub-grain structure should be considered in materials design, especially when the quasi-static tensile test and hardness test are the main criteria for evaluating the materials' mechanical properties.

In addition, Coble creep is the dominant diffusional creep in this study. Therefore, the uneven distribution of HAGBs in the microstructure can lead to Coble creep localisation, and then stress and strain concentration. According to the different needs in industrial applications, the desired distribution of stress and strain can be achieved by derived microstructure localisation, which can boost the materials' design. By assigning specific physics parameters to each grain, the resultant anisotropic mechanical behaviour can be well captured. For AM technique, the relationship of Process-Structure-Property-Performance is crucial to achieving desired product. Through computation, the AM printing strategies resultant structural characters of the materials can be the input for the physics-based model. Meanwhile, the mechanical properties are predicted, during which, the performance of the materials will be evaluated. In reality, every grain is characterized by various properties, especially AM materials, which exhibit high anisotropy. The simulation of the properties concentration mentioned above is beyond the capability of VPSC, which is a mean-field framework. Therefore, a full-field modelling study is scheduled on this topic. Due to its significant full-field ability, apart from the individual local character, vacancy diffusion-induced damage evolution can also be captured. Thus, the tertiary creep stage can be computed on the grain/sub-grain boundaries (Bieberdorf et al., 2021; Christodoulou et al., 2021; Pokharel et al., 2019). The detailed application of the full-filed CP-FEM framework will be introduced in Chapter 5.

Chapter 5 Microstructurally sensitive creep damage law for polycrystalline material systems

In this chapter, the physics-based model proposed in Chapter 3 will be combined with the classic Gurson-Tvergaard-Needleman (GTN) damage model to capture the whole three stages of creep behaviour. The applicability of the unified model has been verified in Chapter 4 for both AM and wrought 316L SS under the mean-field framework. To capture the localised microstructure features, uneven distribution of stress-strain and damage behaviour during the creep testing, the full-filed framework crystal plasticity finite element method (CP-FEM) is employed to conduct the simulations of AM 316L SS creep behaviour. The grain structure extracted from electron backscatter diffraction (EBSD) data will be directly used as input and mapped by meshes. The local stress-strain response at each node will be calculated individually and implemented via the finite element method (FEM), according to which, to generate the bulk creep behaviour. Apart from the complete reproduced creep curve, the dynamic microstructure evolution is also tracked at each time step. The microstructural changes are visualised by

ParaView software, which turns out the grain boundary orientation plays a key role in the failure of AM materials in high-temperature creep deformation.

5.1 Introduction

The schematic stress-strain curve of creep behaviour has been illustrated in Figure 2.19. There are three stages of creep deformation: primary creep, secondary creep and tertiary creep. The first two stages have been simulated under the visco-plasticity self-consistent (VPSC) framework. However, due to the limitation of the mean-field framework, the tertiary creep stage, which involves localised damage evolution, cannot be reproduced. Therefore, a full-filed framework CP-FEM has been adopted to capture the whole curve of creep behaviour. The detailed formulations and working principles of CP-FEM can be found in Chapter 3. Apart from the physics-based CP model introduced in Chapter 3, a microstructure-sensitive creep damage model for polycrystalline materials will be employed at the same time to describe the damage evolution during the creep. The micro-mechanical damage law is based on the vacancy diffusion inside the matrix, which including three stages: void nucleation, void growth, and void coalescence which eventually will lead to fracture. The effect of the porosity on damage will be calculated as a proper damage term, which will be applied back to the original physics-based CP model. Through FEM computing, the porosity evolution and corresponding damage effect will be simulated locally. The heterogeneous damage distribution and a full-field deformation behaviour will be presented. The AM 316L SS creep response will be as the usage of simulation validation. The detailed materials information and creep test conditions can be found in Section 3.2.1.

Since the different loading directions, which are relative to the building direction, of AM products can result in various mechanical behaviour, a range of studies have been done on this topic (Hamza et al., 2022; Kong et al., 2019; Wang et al., 2018c). As for the loading direction effects on the creep behaviour, due to the long creep testing duration, there are only limited research had been done for the AM 316L SS creep studies. Due to the complicated thermal history of each melting pool formed in the AM process, the different parts of the melting pool boundary can show different creep resistance (Bae et al., 2021; Yoon et al., 2020). Moreover, the grain morphology inside the melting pool can also endue the AM product's anisotropy. To address the effects of

AM-induced anisotropic microstructure, the full-field CP-FEM modelling is adapted to capture the full information of the input microstructure.

5.2 Micro-mechanical damage model

In this section, a micro-mechanical damage model employed in the CP-FEM framework will be introduced in detail. The classic GTN damage model is chosen to describe the void evolution resultant damage behaviour during the creep deformation. The original physics-based CP model proposed in Section 3.2 will be implemented considering the damaging effect.

5.2.1 Plastic micro-damage mechanics

The classic solid mechanic theories, such as elasticity, visco elasticity, plasticity, and visco-plasticity theory of solid mechanics, are the characterizations of non-destructive materials. In reality, damage evolution is always involved during the loading process. Consequently, there is a need for the description of damage mechanics, which can establish a constitutive relationship between the original solid mechanics and the damaged materials. As the further improvement and supplement of the classic solid mechanic's theory, in such manner, the extent of materials damage can be quantified, and the estimated materials service life will be evaluated.

The macro-damage mechanic is the original theory studying the materials' damage evolution, which is also referred to as continuous damage mechanics. The materials are assumed as continuous, which means there is no obvious hydrostatic pressure effect on the yield of the materials. The volume would not change during the deformation (Li and Cui, 2020). The macro-scale damage factor, such as stiffness, cracks and notches, can be characterised by the field theory. However, at the micro-scale, micro-voids are nucleating, growing and aggregating during the deformation (Petch, 1954). In this case, the constant volume principle in the macro-damage mechanic is not applicable anymore. There is a need to describe the ductile fracture considering the micro-mechanisms.

The micro-damage mechanisms include the micro-mechanisms of damage evolution during the deformation. The void nucleation, growth and coalescence are described and accounted for the macro-scale damage behaviour. Therefore, this physics-based damage

mechanic can reproduce the damage evolution inside the materials with a more intuitive geometric representation. The physics of ductile damage and materials fracture are elucidated.

5.2.2 Gurson-Tvergaard-Needleman damage constitutive model

The GTN damage constitutive model is originally developed from the theory proposed by Gurson, which is for the description of a single void growth (Gurson, 1977). The void volume fraction is assumed as the damage variable to quantify the effect of micro-defect damage on the deformation behaviour. Based on this, Tvergaard and Needleman improved the original damage model by introducing void coalescence (Tvergaard and Needleman, 1984). As regards void nucleation, both the strain and stress criteria are considered, and the void nucleation formulation proposed by Chu et al. (Chu and Needleman, 1980) is adapted in this damage model. Originally implemented in the CP-FEM framework by Bieberdorf et al. (Bieberdorf et al., 2021), the GTN damage constitutive model is competent to describe in addition to the void evolution on the grain boundaries (high angle grain boundaries (HAGBs)), but also the tertiary stage creep. For the ductile materials, the GTN formulation is the basis for the increasing local porosity resultant plastic flow.

The final GTN model describes the yield function as the following:

$$\phi = \left(\frac{\sigma_{eq}}{\bar{\sigma}}\right)^2 + 2q_1 f^* \cosh\left(q_2 \frac{\sigma_{kk}}{2\bar{\sigma}}\right) - 1 - (q_1 f^*)^2 \qquad \textbf{(5. 1)}$$

where ϕ denotes the plastic potential, σ_{eq} is the equivalent of stress, $\bar{\sigma}$ is the updated flow stress or yield stress, σ_{kk} is hydrostatic stress. f^* represents the porosity, q_1 and q_2 are constants. The updated yield stress is solved implicitly for when the plastic potential, $\phi = 0$.

A damage factor, $\overline{D}$, is employed to refer to the extent of "damage" existing in the material according to the updated yield stress. The damage factor $\overline{D}$ is described as the ratio of the updated yield stress $\bar{\sigma}$ to the original yield stress σ_{eq}, which is given as:

$$\overline{D} = \frac{\bar{\sigma}}{\sigma_{eq}} \quad \textbf{(5. 2)}$$

It is the damage factor $\overline{D}$ scales the local driving stress for both dislocation motion and Coble creep, the modified formulation will be introduced in Section 5.2.3.

5.2.2.1 Void evolution

As mentioned above, the voids evolve a three-stage process: void nucleation, void growth and void coalescence. Each of them will be described in the section. The microstructural-sensitive damage model is suggested within the framework of the creeping polycrystalline structure.

The cluster dynamics approach is used in the constitutive damage model to track the sub-material point void populations. As such, the newly initiated voids can evolve without interference from previously initiated voids. The voids are discretised at each time step, or iteration i, at which point they implement nucleation. Each population process starts from an initial radius, a_c, and the stress- and strain-dependent void population number density, $\tilde{n}_i$. The voids population's collective void radius, a_i, will be updated at each subsequent time step. The collective void radius of each population grows according to the local stress and strain rate. In addition, the new void populations continue to nucleate at the subsequent time step.

The porosity term, f, at a given material point is calculated by summing each void population's product of volume and number density, which is described as:

$$f = \frac{4}{3}\pi h(\psi) \sum_i \tilde{n}_i a_i^3 \quad \textbf{(5. 3)}$$

here $h(\psi)$ represents a geometry factor for relating void radius to volume, which accounts for the wetting angle, ψ, the detailed formulation will be described later (Needleman and Rice, 1980).

The mean spacing, b, at each material point can be approximated based on porosity, which is given as:

$$b = \left(\frac{3}{4\pi f}\right)^{1/3} \quad \textbf{(5. 4)}$$

Notice that, the number density of voids at each iteration, $\tilde{n}_i$, consist of two parts. The number density of newly nucleated voids, $\tilde{n}_{0\to a_c}$, and the number density of voids has grown, $\tilde{n}_{a_c\to a^*}$. They are expressed as follows:

$$\tilde{n}_{0\to a_c} = \begin{cases} \tilde{n}_0, \text{if } a_c = a_i \\ 0, \text{otherwise} \end{cases} \quad \textbf{(5. 5)}$$

$$\tilde{n}_{a_c\to a^*} = \begin{cases} \tilde{n}_a, \text{if } a + \dot{a}\Delta t = a^* \\ 0, \quad \text{otherwise} \end{cases} \quad \textbf{(5. 6)}$$

a_c is the critical void size, at which value, the void can nucleate, and above which, can start growing. The formulation of a_c will be illustrated in detail.

5.2.2.2 Void nucleation

The void nucleation is attributed to the cohesion of vacancies, which can be either stress or strain-controlled (Chu and Needleman, 1980; Tvergaard and Needleman, 1984). Based on this, the void nucleation criteria of stress and strain are both considered in this work. By following the work of Chu et al. (Chu and Needleman, 1980), at each time step, i, the nucleated number density of voids is weighted to prescribe an effective percentage of stress-controlled and strain-controlled nucleation to the total void number density, $\tilde{n}_i$, which is expressed as:

$$\tilde{n}_{0\to a_c} = \tilde{n}_i^{\varepsilon} + \tilde{n}_i^{\sigma} \quad \textbf{(5. 7)}$$

$$\tilde{n}_i^{\varepsilon} = \begin{cases} F_i - F_{i-1}, \ if\ F_i \geq F_{i-1} \\ 0, \quad if\ F_i < F_{i-1} \end{cases} \quad \textbf{(5. 8)}$$

$$\tilde{n}_i^{\sigma} = \begin{cases} K_i - K_{i-1}, \ if K_i \geq K_{i-1} \\ 0, \quad if\ K_i < K_{i-1} \end{cases} \quad \textbf{(5. 9)}$$

where $\tilde{n}_i^{\varepsilon}$ and $\tilde{n}_i^{\sigma}$ are the number densities of voids nucleated from strain and stress, respectively. While F and K are the cumulative distribution functions, describing the number densities of voids induced by strain and stress, respectively. F is described by

the local plastic strain, ε_d^p, which has been adjusted for porosity. And K is represented by the updated flow stress and hydrostatic stress, $\bar{\sigma}$ and σ_{kk}:

$$F_i(\varepsilon^p) = R_\varepsilon \tilde{n}_{sat} \frac{1}{2}\left[1 + \mathrm{erf}\left(\frac{\varepsilon^p - \varepsilon_c}{\sqrt{2}V_\varepsilon}\right)\right] \quad \textbf{(5. 10)}$$

$$K_i(\bar{\sigma}, \sigma_{kk}) = (1 - R_\varepsilon)\tilde{n}_{sat} \frac{1}{2}\left[1 + \mathrm{erf}\left(\frac{\bar{\sigma} + \frac{1}{3}\sigma_{kk} - \sigma_c}{\sqrt{2}V_\sigma \sigma_y}\right)\right] \quad \textbf{(5. 11)}$$

$\tilde{n}_{sat}$ denoted the total number density of latent nucleation sites, R_ε is the proportion of those nucleations induced by strain, with a value above the mean critical nucleation strain, ε_c. Analogously, σ_c represents the mean critical magnitudes for nucleation stress. V_ε and V_σ are the statistical variance in nucleation strain and stress, respectively. It is worth mentioning that, nucleation controlled by strain and stress are two independent processes, which means they can happen simultaneously.

Notice that, the void nucleation model used in this project only takes into account the voids formed along the grain boundaries. Even there is precipitation interior of the cell, which can be the potential nucleation site for voids. However, both experimental and theoretical observations have shown that voids evolution is strongly preferred to grain boundaries (Basirat et al., 2012). Moreover, due to a lack of information, the current model does not include the pre-existing voids in the as-built AM samples.

5.2.2.3 Void growth

As mentioned in Section 3.2, two main mechanisms are simultaneously active in the present project: dislocation-mediated plasticity and diffusion-mediated plasticity. The creep cavity growth can be attributed to both of them (Needleman and Rice, 1980). Moreover, the coupling effect from these two mechanisms can shorten the vacancy diffusive path length along the grain boundaries, which facilitates the matter's transport through the cavity surfaces. In such a manner, the void growth is stimulated in a quasi-spherical way.

By following the work of Needleman et al. (Needleman and Rice, 1980), the change of void radius, $\dot{a}_i$, is the sum of the visco plasticity induced void growth, $\dot{a}_i^{vp}$, and the diffusion induced void growth, a_i^d:

$$\dot{a}_i(a_i) = \dot{a}_i^{vp}(a_i) + a_i^d(a_i) \tag{5. 12}$$

According to the adjustment based on the original void growth theory, the visco-plasticity-mediated void growth is described as (Chuang, 1982) :

$$\dot{a}_i^{vp}(a_i) = \begin{cases} \frac{1}{2}\dot{\varepsilon}^p a_i \left[\alpha_n \left|\frac{\sigma_{kk}}{3\sigma_{eq}}\right| + \beta_n\right]^n, & if \left|\frac{\sigma_{kk}}{3\sigma_{eq}}\right| > 1 \\ \frac{1}{2}\dot{\varepsilon}^p a_i [\alpha_n + \beta_n]^n \frac{\sigma_{kk}}{3\sigma_{eq}}, & if \left|\frac{\sigma_{kk}}{3\sigma_{eq}}\right| < 1 \end{cases} \tag{5. 13}$$

where, α_n and β_n are creep expansion constants based on the hardening exponent n_h, which are given as follows (Budiansky et al., 1982):

$$\alpha_n = \frac{3}{2n_h} \tag{5. 14}$$

$$\beta_n = \frac{(n_h - 1)(n_h + 0.4319)}{{n_h}^2} \tag{5. 15}$$

The diffusion-induced void growth formulation is following the work of Needleman et al. (Needleman and Rice, 1980), which is expressed as:

$$\dot{a}_i^d(a_i) = \frac{D_d}{a_i^2 h(\psi)} \frac{\sigma_n - (1 - f_{adj})\sigma_s}{ln\frac{1}{f_{adj}} - \frac{1}{2}(3 - f_{adj})(1 - f_{adj})} \tag{5. 16}$$

In the above, σ_n is the local stress resolved in the direction vertical to the grain boundary D_d is the diffusivity term along the grain boundary (Needleman and Rice, 1980):

$$D_d = \frac{D_{gb,0}\delta_B \Omega}{kT} \exp\left(-\frac{Q_{gb}}{kT}\right) \tag{5. 17}$$

Here, δ_B is the thickness of the high-diffusion layer centred along the grain boundary, which is equivalent to the grain boundary thickness. Ω is the atomic factor. Notice that, the principal mechanism of Coble creep is also the vacancy diffusion along the grain boundaries. In Section 3.2, the grain boundary diffusion coefficient, D_{gb}, which is part of the Coble creep formulation and given as: $D_{gb} = D_{gb,0}\exp\left(-\frac{Q_{gb}}{kT}\right)$ (see equation (3. 24)). Theoretically, D_{gb} can describe the diffusion accounts for both the Coble creep

and void growth in the GTN damage model, with $D_{gb,0}$ as grain boundary diffusion pre-factor, and Q_{gb} denotes the grain boundary vacancy self-diffusion activation energy.

The void geometry function $h(\psi)$ is following the work of Chuang et al. (Chuang, 1982), and ψ is the angle of the void surface with respect to the grain boundary at their intersection, namely the wetting angle:

$$h(\psi) = \frac{(1+\cos\psi)^{-1} - \frac{1}{2}\cos\psi}{\sin\psi} \quad \textbf{(5. 18)}$$

Notice that, the typical value for ψ is around 70 degrees, which turns out the value of $h(\psi)$ is about 0.61 (Chuang et al., 1979).

In equation (5. 16), the sintering stress, σ_s, applied on the voids formed an effective surface tension, which is given as follows:

$$\sigma_s(a_i) = \frac{2\gamma_s \sin\psi}{a_i} \quad \textbf{(5. 19)}$$

where γ_s is the free surface energy.

When the surface tension of the void is achieving the value of the normal stress applied to the void, the sintering effect can happen, which means the numerator in equation (5. 16) is less than 0. Thus, the critical void radius, a_c, is related to γ_s, above which, the void will grow, and below which the sintering can happen:

$$a_c = \frac{2\gamma_s \sin\psi}{\sigma_n} \quad \textbf{(5. 20)}$$

In another word, the void can grow at a critical radius, a_c, which balances the applied load and the void surface tension.

In equation (5. 16), f_{adj} is an adjusted porosity term for the regulation of the void growth mediated by diffusional creep (Needleman and Rice, 1980):

$$f_{adj} = \max\left\{\left(\frac{a_i}{b}\right)^2, \left(\frac{a_i}{a_i+1.5L}\right)^2\right\} \quad \textbf{(5. 21)}$$

here L is the characteristic material length scale term, along which vacancies diffuse towards a void and is given as follows:(Needleman and Rice, 1980; Rice, 1981)

$$L = L_0 \exp\left(\mathrm{K}\frac{T_m}{T}\right)\left(\frac{10^{-3}\mu}{\bar{\sigma}}\right)^{(n_L-1)/3} \quad \textbf{(5. 22)}$$

where L_0 and K are constants expressible in terms of the various materials parameters. T_m is the melting temperature of materials, and n_L is the exponent factor.

5.2.2.4 Void coalescence

As the final stage of void evolution, coalescence is the least studied regime. At this stage, the voids are assumed to have grown sufficiently concerning their spacing, and begin to coalesce, which can form micro-cracks and eventually lead to macro-cracking. As the grain boundaries are considered the preferred locations for void nucleation and growth. Therefore, the void coalescence can lead to intergranular cracking, which is more pronounced depending on the polycrystalline layout.

From a physics point of view, the inter-void ligaments will break when reaching the geometry, at which, the critical plastic loading will be achieved. For the simplified assumption, the coalescence will occur once the void radius reaches the void spacing. However, there is no detailed investigation has been done either theoretically or experimentally on the polycrystalline materials' creep behaviour. Therefore, an empirical coalescence criterion is adopted in this project, which is proposed by Tvergaard and Needleman (Tvergaard and Needleman, 1984), based on the modification of Gurson's original damage model:

$$f^* = \begin{cases} f, & if\ f \le f_c \\ f_c + \kappa(f - f_c), & if\ f > f_c \end{cases} \quad \textbf{(5. 23)}$$

where f_c is the critical porosity magnitude, which means the void coalescence can happen when $f > f_c$. κ denotes a coalescence effect factor scaling porosity magnitudes above the critical level. The coalescence effect factor, κ, is described as:

$$\kappa = \frac{1/q_1 - f_c}{f_f - f_c} \tag{5. 24}$$

f_f represents the magnitude of porosity when the material is at failure.

5.2.3 Modified local stress-strain description

As described in the final GTN model yield function, see equation (5. 1). The updated yield stress $\bar{\sigma}$ is solved at each damage time step. Therefore, there will be an updated damage factor, $\overline{D}$, see equation (5. 2). The damage factor, $\overline{D}$, is used to scale the local driving stress for both dislocation motion and Coble creep, in which way, the original constitutive law introduced in Section 3.2 is modified.

By employing $\overline{D}$, the original mean resolved shear stress at each slip system, $\bar{\tau}^s$, is modified as:

$$\bar{\tau}_D^s = \overline{D}\bar{\tau}^s = \overline{D}(\boldsymbol{\sigma}:\boldsymbol{m}) \tag{5. 25}$$

$\bar{\tau}_D^s$ denotes the adjusted resolved shear stress, which includes damage.

There is an assumption in Gurson's derivations, that the loading can be transferred by material volume. Therefore, the cavities cannot bear any loading and need to be eliminated its volume effect. The original plastic strain rate, $\dot{\varepsilon}^p$, see equation (3. 1), is modified as:

$$\dot{\varepsilon}_D^p = (1 - f^*)\dot{\varepsilon}^p \tag{5. 26}$$

$\dot{\varepsilon}_D^p$ is the adjusted plastic strain rate considering the damage effect.

5.2.4 Work-flow

The original iterative numerical simulation of CP-FEM, which only includes the constitutive CP model, has been illustrated in Figure 3. 5. By embedding the GTN damage model, the original work-flow can be adjusted in Figure 5. 1.

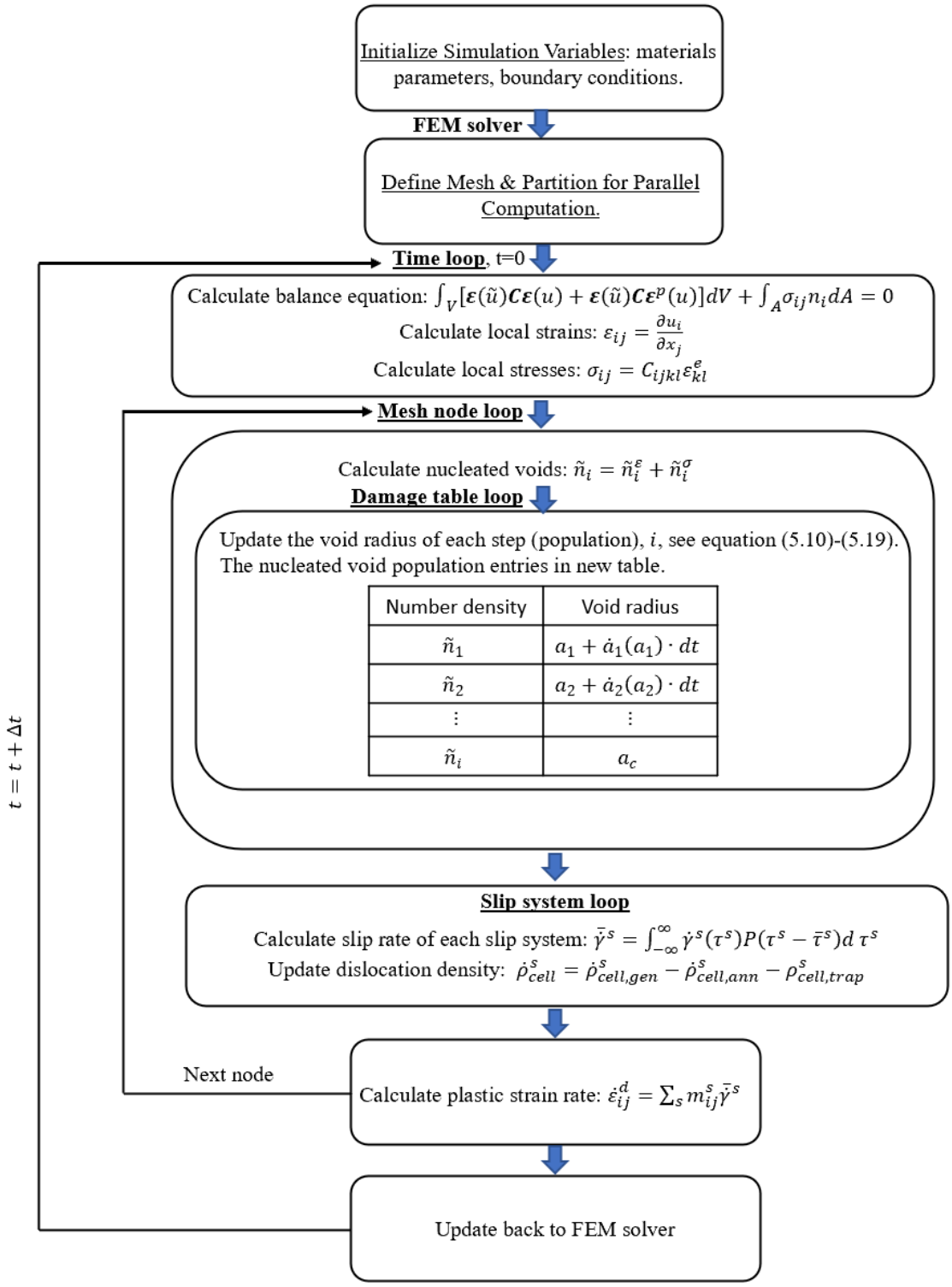

Figure 5. 1 Iterative solve description of numerical work-flow with constitutive damage model.

Notice that, after each time entering the mesh loop, the program will check if this mesh node is grain boundary or not. If this node is identified as grain boundary, then it will enter the damage model part. Otherwise, it will skip the damage part.

5.3 Simulation Conditions

For most of the CP-FEM simulation work, the input microstructures are artificially and randomly generated (Biswas et al., 2019; Pal et al., 2015; Ye et al., 2021). However, in the present project, the computing imports the structural mapping directly extracted from the raw EBSD data. In such a manner, the authentic AM-characterised microstructures are considered by the simulation. In addition, the exact effects of AM-induced unique structure are also introduced.

Williams et al. (Williams et al., 2021) have done a range of creep testing on AM samples. There are two types of AM samples, horizontally (H) built and vertically (V) built samples. The H-built sample means the creep test loading direction is vertical to the building direction, while the V-build sample means the creep loading direction is along the building direction. The homologous EBSD data determined images of as-built AM 316L SS for H and V samples are presented in Figure 5. 2, prior to creep testing. From the grain morphology of the two build orientations, it can be told that the grains are elongated along the building directions in both cases. Since the AM material is known to perform a columnar grain structure (Wang et al., 2018b). In the present project, for each simulation case, each input structure mapping is selected deliberately from three different locations, which are illustrated in Figure 5. 2. In such a manner, the characteristic of AM materials indicated on the microstructure is represented by the EBSD data. Each of the H and V samples has 715x536 pixels in the original EBSD data. The deliberately chosen area for simulation contains 200x200 pixels individually. The size of each pixel is 1 μm^2. Considering the computational efficiency and cost, the original definition for the deliberately chosen areas is reduced to 100x100 pixels via Matlab R2022a. It is worth mentioning that the overall volumetric density of the as-built AM sample is over 99.5% (Williams et al., 2021). However, the as-built pores (mostly lack of fusion) are not considered in the structure mapping.

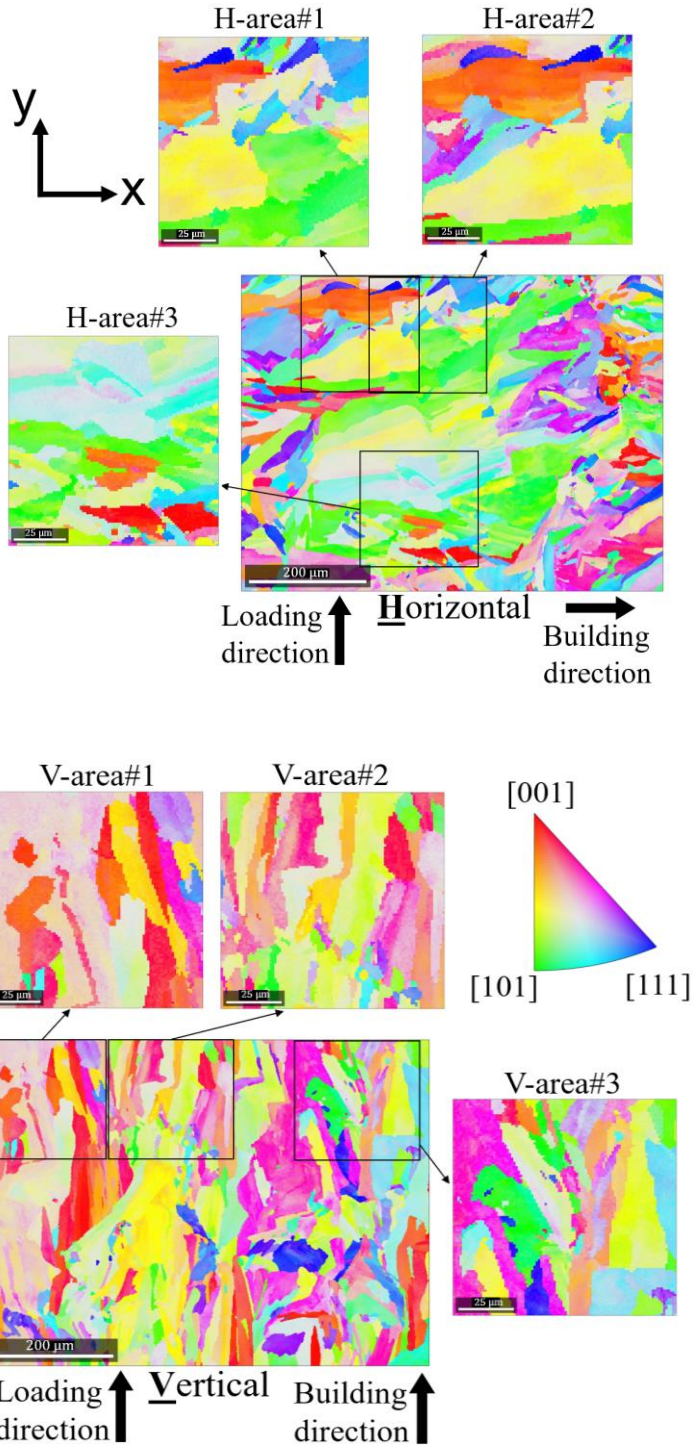

Figure 5. 2 Inverse pole figure structure mapping of the EBSD raw data for H-built and V-built samples (Williams et al., 2021). The deliberately chosen areas are the input for CP-FEM computing.

In the present work, the constitutive damage law proposed in Section 5.2 is only applied on the HAGBs. The precipitation formed during the AM testing, which can also behave

as the damage nucleation site, is not considered in this work. As it is impossible to dynamically track all the precipitation locations interior of the cell during the whole creep testing. Thereby, it is crucial to identify the locations of HAGBs to capture the damage effect. For the pixels, that have a misorientation greater than 15° against the neighbouring pixels are defined as HAGBs. It is worth mentioning that the angles of HAGBs concerning the loading direction are decisive to obtain the loading stress, which is resolved to be normal to the grain boundaries, σ_n. In this project, this grain boundary orientation angle is measured manually, which is also a part of the input added in the CP-FEM simulations to ensure accuracy. This is a time-consuming procedure. However, the HAGBs angles with respect to the loading direction play a significant role in determining the local damage evolution. Additionally, the damage behaviour can strongly influence the creep behaviour of H-built and V-built samples. Furthermore, apart from the HAGBs normal to the loading direction, the effects from the pores accumulated at the conjunctions of HAGBs are also considerable (Meena and Uthaisangsuk, 2021; Sirinakorn et al., 2014). In order to highlight the damage accumulation effect that occurs on HAGBs conjunctions, the HAGB angles are set to be 90° in these areas.

As illustrated in Figure 5. 2, for the input of CP-FEM simulations, the targeted grain microstructural area is converted into a thin plate. Technically, the deliberately selected area is discretised into 100x100x2 tetrahedral elements, which is following the original definition. The quadratic interpolation of displacements is set between each mesh node. The constant loading stress is applied along the y-direction, with a positive value. As presented in Figure 5. 2, in such a manner, the uniaxial tensile creep computation is set for both V-built and H-built samples. The original experimental data reported by Williams et al. (Williams et al., 2021) are collected under 923 K, with loading stresses varying between 97 MPa to 150 MPa. Therefore, the corresponding CP-FEM simulations will be conducted with the corresponding conditions.

5.4 Parameter calibration

In this section, the parameters used under the CP-FEM framework are discussed.

5.4.1 Parameters of plasticity-related modelling

As the simulations performed in this chapter are based on the same AM materials as in Chapter 4. Therefore, all the plasticity-related parameters are inherited from the previous chapter, which is presented in Table 5. 1. The detailed CP hardening model formulations are introduced in Section 3.2.

By following the principle that the dislocation densities are supposed to be identical on each slip system as the initial condition for the computation. The initial interior cell dislocation densities in both cases are set the same, which is 1.2×10^{14} m^{-2}. As for the determination of cell wall dislocation densities, ρ_{cw}. There is a relationship between ρ_{cw} and sub-grain sizes, D_{sub}, which is $D_{sub} \propto \frac{1}{\sqrt{\rho_{cw}}}$ (Wen et al., 2017a). The sub-grain sizes D_{sub} came from the manually counted grain sizes following $d_{sub-G} = d_G \cdot \frac{n_{HAGB}}{n_{LAGB}+n_{HAGB}}$ (Sabzi et al., 2021). Based on the EBSD image reported by Williams et al. (Williams et al., 2021), the number of HAGBs, n_{HAGB}, and the number of LAGBs, n_{LAGB}, are defined through MATLAB. The detailed description of plasticity-related modelling parameters can be found in Section 4.2.

Table 5. 1 Parameters for plasticity-related modelling

Parameter	Value	Reference
k (Boltzmann constant)	8.617×10^{-5} eV/K	
b (magnitude of Burgers vector)	2.58×10^{-10} m	(Li et al., 2019b)
V (dislocation distribution variance)	$10\sqrt{2}$ MPa	(Kumar and Capolungo, 2022; Wen et al., 2017a; Wen et al., 2020a)
ρ_0 (mass density)	8000 $\mathrm{kg/m^3}$	(Kamath et al., 2014; Xue et al., 2007b; Zhong et al., 2019)

h_p (trapping coefficient for $M_{23}C_6$ precipitate)	1	(Sobie et al., 2015)
ρ_{cell}^{s} (initial cell dislocation density for each slip system)	1×10^{13} m^{-2} (AM)	(Hong et al., 2021a; Shamsujjoha et al., 2018; Sprouster et al., 2021; Yin et al., 2019)*
ρ_{cw}^{s} (initial cell wall dislocation density for each slip system)	1.54×10^{14} m^{-2}(AM-vertical) 2×10^{14} m^{-2} (AM-horizontal)	(Hong et al., 2021a; Shamsujjoha et al., 2018; Sprouster et al., 2021; Yin et al., 2019)*
$\alpha^{ss'}$ (latent hardening matrix)	0.7 (collinear); 0.2 (non-collinear)	(Queyreau et al., 2009)*
μ (shear modulus)	$88884.6 - T \times 37.7$	(Puchi Cabrera, 2001b)
$\Delta G_{0,\rho}$ (zero stress activation energy for dislocations)	2 eV	
$\Delta G_{0,p}$ (zero stress activation energy for precipitates)	4.1 eV	
p (exponent parameter)	0.8	(Kocks et al., 1975a)*
q (exponent Parameter)	1.4	(Kocks et al., 1975a)*
T (temperature)	923 K	
τ_0^s (lattice frictional stress)	$49.225 \times \exp(-0.0008 \times T)$	(Chu et al., 2020)

υ_p (attack frequency for precipitation obstacles)	1.2×10^{10} s^{-1}	(Wen et al., 2017a)
χ (entropy factor)	1	(Wang et al., 2017a)
k_1 (material constant)	0.05	
k_2 (material constant)	40	
n_0 (annihilation strain rate sensitivity)	3.5	(Estrin, 1998a; Poirier, 1985; Weertman, 1968)
D (grain size)	37.91 μm (AM-horizontal); 53.31 μm (AM-vertical)	(Rieth et al., 2004b) (Sabzi et al., 2021)
D_{sub} (sub-grain size)	23.14 μm (AM-horizontal); 26.74 μm (AM-vertical)	(Sabzi et al., 2021)
A_{Coble} (Coble creep parameter)	2.052×10^{-12} $K \cdot MPa^{-1} \cdot s^{-1} \cdot m^3$	
Q_{gb} (activation energy for grain boundary diffusion)	1.71 eV	
τ_{ss} (solid solution hardening)	210 MPa (AM-923K)	(Cho et al., 2021; Kako et al., 2002; Matijasevic and Almazouzi, 2008; Norström, 1977; Yusuf et al., 2020)*

*Parameter estimated or back-fitted from experimental data within the range given in the listed references.

The information of precipitation formed during the creep testing under given conditions is simulated by Thermo-Calc. The details can be found in Section 3.3. Table 5. 2 has listed the number densities and sizes of $M_{23}C_6$ used in the hardening model for both horizontally built samples and vertically built samples.

Table 5. 2 The number densities and sizes of $M_{23}C_6$ used in hardening model from Thermo-Calc simulation (*cell*-precipitation interior of the cell, *cw*-precipitation on the cell wall; 923K; H =horizontally built sample, V=vertically built sample).

Character	H	V
	923 K	923 K
N_p^{cell} (m^{-3})	1.87×10^{16}	1.98×10^{16}
D_p^{cell} (nm)	56	58
N_p^{cw} (m^{-3})	6.14×10^{19}	5.56×10^{19}
D_p^{cw} (nm)	57.2	59

5.4.2 Parameters of Gurson-Tvergaard-Needleman damage model

All parameters used in the GTN damage model are shown in Table 5.3.

Most of the damage-related parameters are determined through back-fitting, which is following the work of Bieberdorf et al. (Bieberdorf et al., 2021). The spherical cap tip equilibrium angle, ψ, is chose to be $70°$, which is aiming to maintain the quasi-spherically shape for the voids (Needleman and Rice, 1980).

According to equation (5. 10) and equation (5. 11), there are strain-induced void nucleation and stress-induced void nucleation. In order to balance the two void nucleation sources, the percentage of the voids nucleated from the surpassed strain, R_ε, is selected to be 0.45. A calibration procedure was undertaken utilizing tertiary creep response data obtained from the study of Williams et al. (Williams et al., 2021), which accounted for the determination of several parameters, including both the strain- and

stress-related critical magnitudes for void nucleation ε_c, σ_c, and the corresponding statistical variance V_ε, V_σ. Since the damage evolution in ductile materials proceeds through voids, tend to nucleat and grow from inclusions on HAGBs. Therefore, the potential nucleation sites of voids are highly related to the number density of precipitation on the HAGBs (Daly et al., 2017). However, since the thermokinetics calculation of precipitation for AM materials is based on the sub-grain sizes. Therefore, the value of $\tilde{n}_{sat}$ should be smaller than the actual number density of precipitates on LAGBs. Moreover, according to the number density of pores appeared during creep deformation from literature, the value of $\tilde{n}_{sat}$ is chosen to be 5×10^{15} m^{-3} (Ahmadi et al., 2018; Yadav et al., 2015). The free surface energy, γ_s, is determined as $1\,\mathrm{J/m^2}$ and the grain boundary thickness, δ_B, is chosen as 7×10^{-10} m (Bieberdorf et al., 2021).

In addition, the critical porosity value for the occurrence of void coalescence, f_c, the porosity value at the failure point, f_f, and the constants q_1, q_2 in equation (5. 1) are selected using the back-fitting method based on the data from the work of Gaffard et al. (Gaffard et al., 2005) and Gurson (Gurson, 1977), and Tvergaard and Needleman (Tvergaard and Needleman, 1984) within the reasonable range. Although have been used in the damage model, the values of the grain boundary diffusion pre-exponential factor, $D_{gb,0}$, are discussed in Section 4.2. The values of constants L_0, K, and n_L are based on the data reported in the literature for face-centred cubic (FCC) materials (McMurtrey et al., 2021)

Table 5. 3 Parameters for damage simulation (Bieberdorf et al., 2021)

Parameter	Value	Sources
ψ (angle between the void surface and the grain boundary at their intersection (void geometry factor))	70°	(Needleman and Rice, 1980)

R_ε (proportion of the porosity which nucleats due to a surpassed strain)	0.45*	
$\tilde{n}_{sat}$ (total number of potential nucleation cites)	5 $\times 10^{15}$ m^{-3}	(Ahmadi et al., 2018; Daly et al., 2017; Yadav et al., 2015)
ε_c , σ_c (the mean critical magnitudes for nucleation strain and stress)	0.6, $0.825\sigma_y$	
n_h (hardening exponent)	6.9	
V_ε , V_σ (statistical variance in critical nucleation strain and stress)	0.168, $0.135\sigma_y$	
γ_s (free surface energy)	1 J/m^2	
δ_B (the thickness of the high-diffusion layer centred along the grain boundary)	7×10^{-10} m	
Q_{gb} (activation energy for grain boundary diffusion)	1.71 eV	
f_c (critical porosity above which coalescence begins)	0.10	(Gaffard et al., 2005; Gurson, 1977; Tvergaard and Needleman, 1984)
f_f (porosity of the material at failure)	0.30	(Gaffard et al., 2005; Gurson, 1977; Tvergaard and Needleman, 1984)
q_1, q_2 (constants)	1.5, 1.0	

$D_{gb,0}$ (grain boundary diffusion pre-exponential factor)	5×10^{-5} m^2 $* s^{-1}$	
L_0 (constant)	2.43×10^{-8} m	(Needleman and Rice, 1980)
K (constant)	2.44	(Needleman and Rice, 1980)
T_m (melting temperature)	1660 K	(McMurtrey et al., 2021)
n_L (exponent factor)	4.5	(Needleman and Rice, 1980)
κ (coalescence effect factor)	3.5	

*Parameter estimated or back-fitted from experimental data within the range from references.

5.5 Simulation results and discussion

The simulation results of AM 316L SS creep deformation conducted under the CP-FEM framework are presented and discussed in this section. The primary and secondary stages of creep behaviour simulated by both VPSC and CP-FEM frameworks are compared. By introducing the GTN damage model into the CP-FEM framework, the tertiary stage creep is also captured. Moreover, the simulation results from CP-FEM are visualized by ParaView. The strain, strain and damage distribution are directly indicated on the input microstructures.

5.5.1 Comparison between the VPSC and CP-FEM simulation results

According to the physics-based CP model introduced in Section 3.2, the primary and secondary stages of AM 316L SS creep deformation are well captured under the VPSC framework in Chapter 4. In order to compare the abilities of the mean-field framework and full-field framework. The physics-based CP model is introduced in the CP-FEM, and the corresponding simulation results are compared with those conducted by VPSC presented in Chapter 4. In addition, the primary and secondary creep behaviour simulated by CP-FEM does not include the creep damage effect, which means at this

point, the GTN damage model is not applied yet. As shown in Figure 5. 3, the computed creep rates from both VPSC and CP-FEM simulation results are presented. All three differently selected input areas of both AM-H and AM-V are illustrated and individually compared with the original VPSC results. The relative locations of the selected areas to the whole-grain mapping are illustrated in Figure 5. 2. It can be told that based on the same physics-based CP model, the simulations conducted under CP-FEM have reproduced the original VPSC results. However, since the CP-FEM is full-field with high microstructural sensitivity, there is an obvious diversity in creep responses from different input areas, which is shown in Figure 5. 3 (a), (b), (c), (f), (g), (h). Therefore, it is necessary to use the average simulation results from three different inputs, which are compared with the original VPSC results in Figure 5. 3 (e) and (j). Overall, the averaged CP-FEM results from different input areas can reproduce the VPSC simulations.

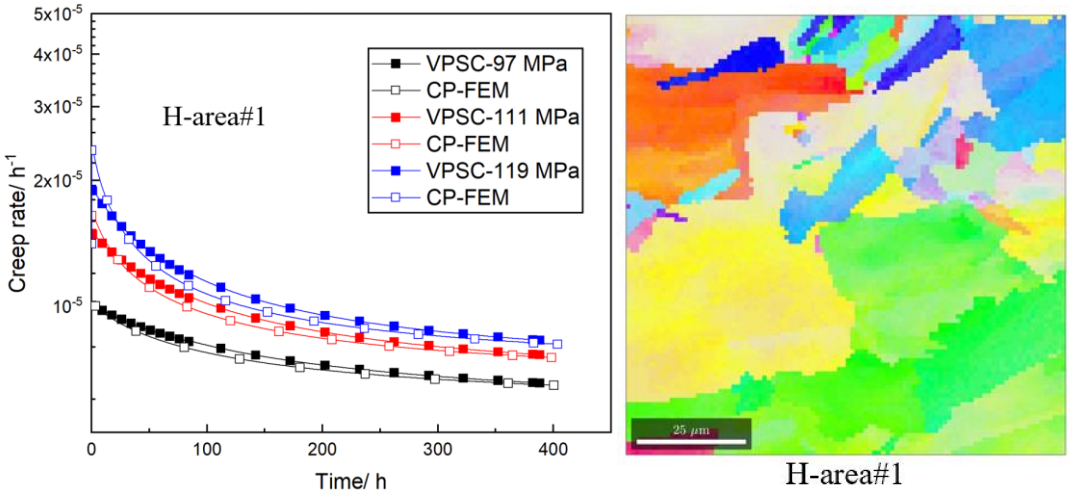

(a)

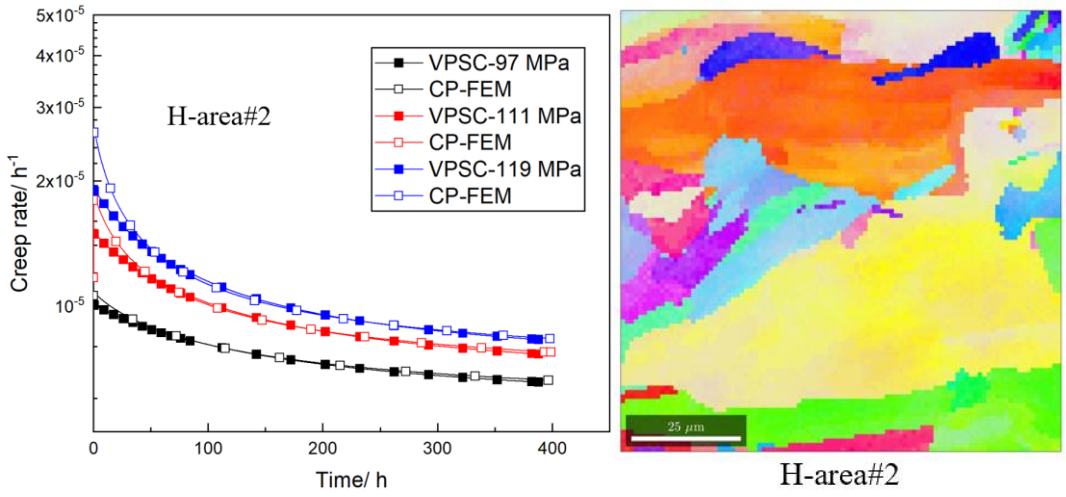
H-area#2
VPSC-97 MPa
CP-FEM
VPSC-111 MPa
CP-FEM
VPSC-119 MPa
CP-FEM
Creep rate/ h-1
Time/ h
25 μm
H-area#2

(b)

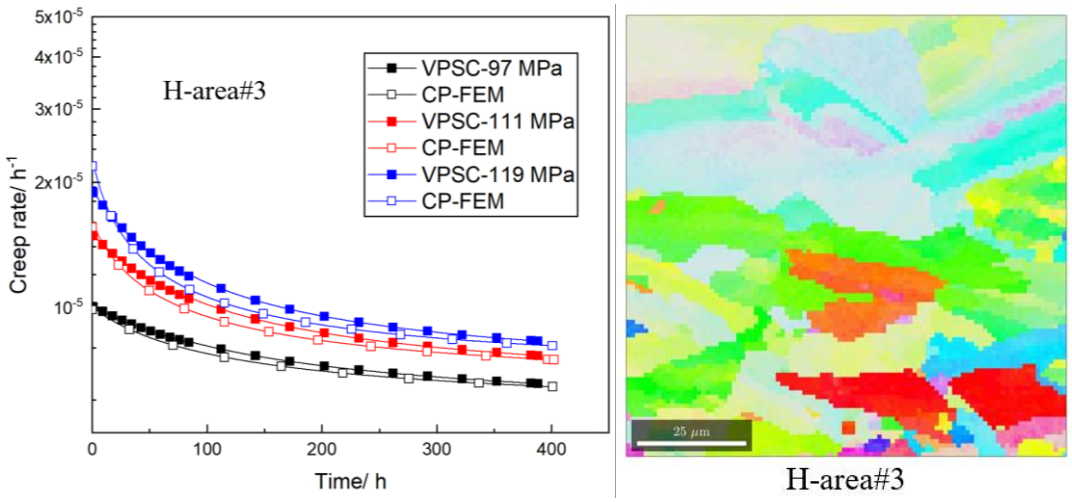
H-area#3
VPSC-97 MPa
CP-FEM
VPSC-111 MPa
CP-FEM
VPSC-119 MPa
CP-FEM
Creep rate/ h-1
Time/ h
25 μm
H-area#3

(c)

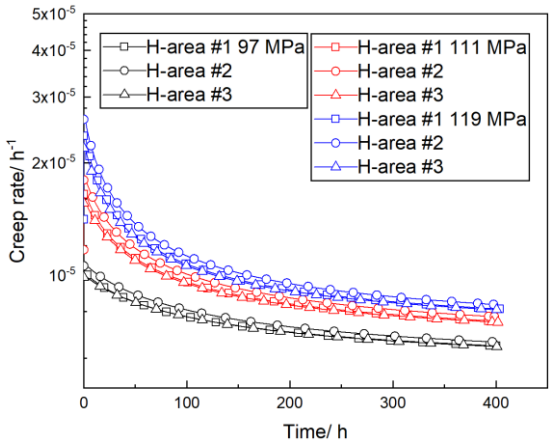
H-area #1 97 MPa
H-area #2
H-area #3
H-area #1 111 MPa
H-area #2
H-area #3
H-area #1 119 MPa
H-area #2
H-area #3
Creep rate/ h-1
Time/ h

(d)

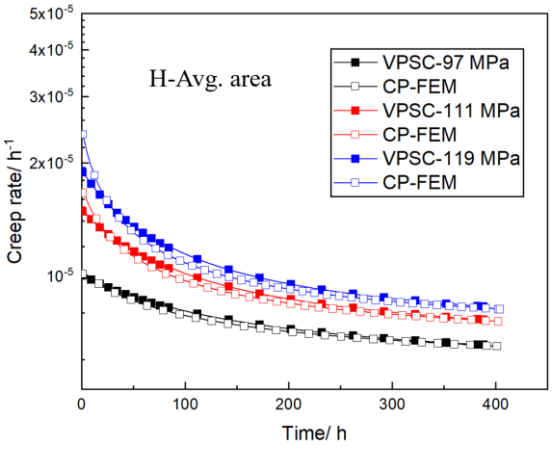
H-Avg. area
VPSC-97 MPa
CP-FEM
VPSC-111 MPa
CP-FEM
VPSC-119 MPa
CP-FEM
Creep rate/ h-1
Time/ h

(e)

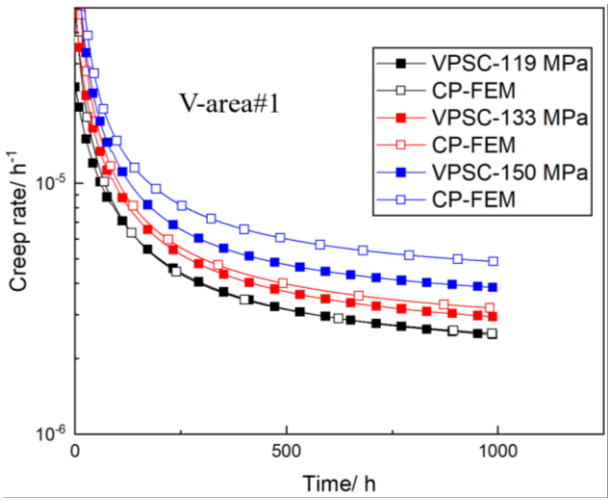

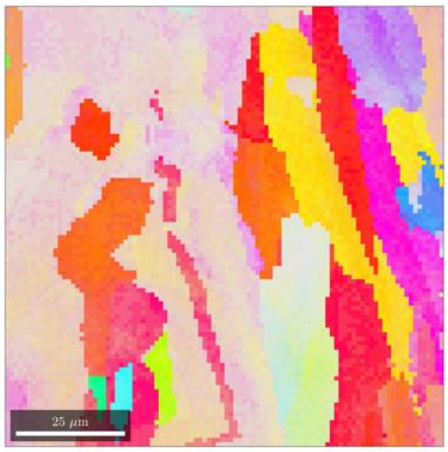

V-area#1

(f)

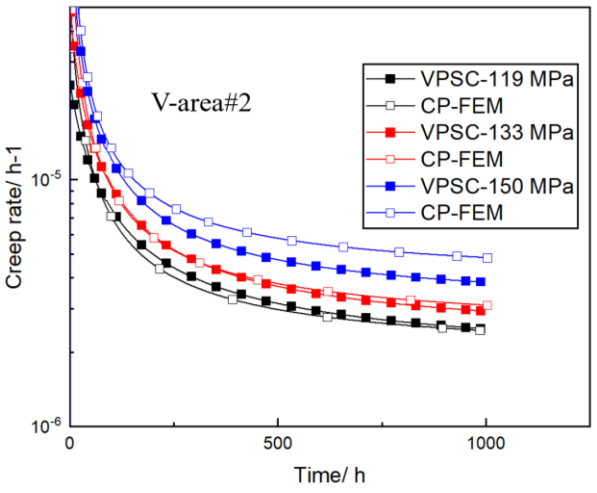

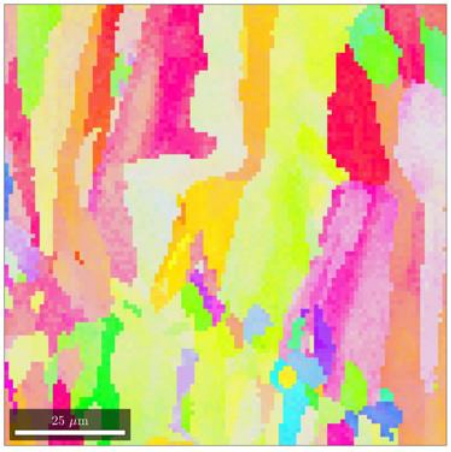

V-area#2

(g)

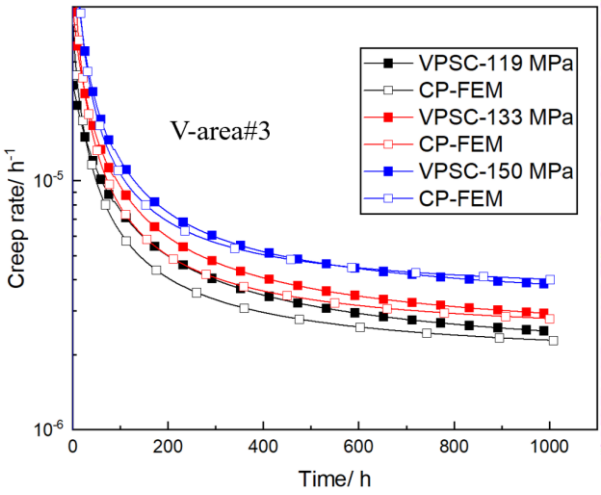

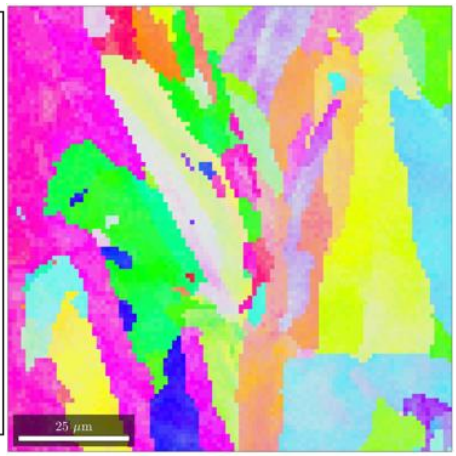

V-area#3

(h)

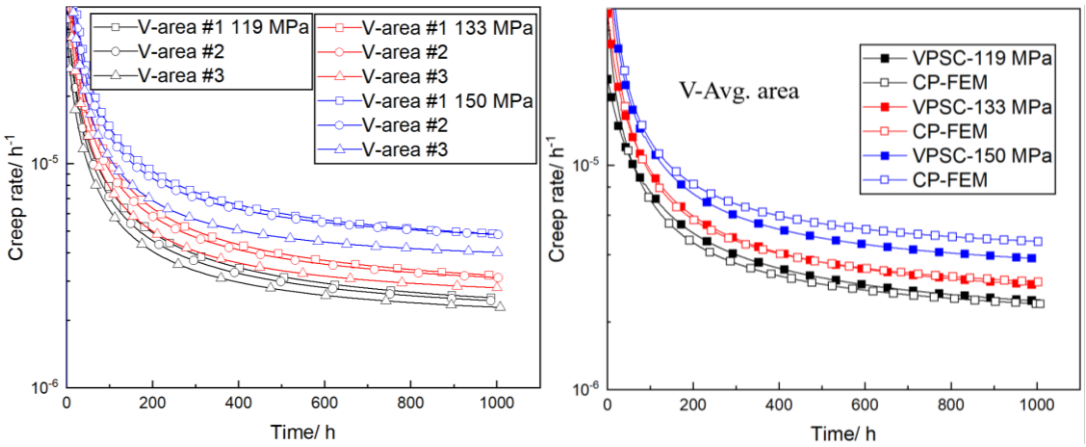

(i) (j)

Figure 5. 3 Primary stage and secondary stage creep rates comparison from VPSC and CP-FEM simulation results. (a) AM-H area#1; (b) AM-H area#2; (c) AM-H area#3; (d) AM-H all three areas comparison; (e) AM-H average results; (f) AM-V area#1; (g) AM-V area#2; (h) AM-Varea#3; (i) AM-V all three areas comparison; (j) AM-V average results.

5.5.2 The full simulation of creep behaviour under the CP-FEM framework

By employing the GTN damage model in the original physics-based CP model, the full creep curve, including the primary stage, secondary, and tertiary stage is captured. The comparison of creep rates between simulation results and experiments for both H and V samples are shown in Figure 5. 4. Notice that the simulation results of the creep rate as a function of creep time are the average results of the three different input areas. The tertiary creep stage is captured in each case.

The behaviour of tertiary creep is highly influenced by the damage factor, $\overline{D}$, see equation (5. 2). The damage factor, $\overline{D}$, scales the local driving stress for both dislocation motion and Coble creep and also determines the stress on the grain boundaries (see equation (5. 25)). In cases where the strain rate is more sensitive to stress, such as the V cases in this study and the simulation mentioned in the work of Bieberdorf et al. (Bieberdorf et al., 2021). There is an obvious increase in strain rate observed due to the

accumulation of damage causing an increase in local stress. On the other hand, for the H cases, diffusional creep is the dominant mechanism, which has been illustrated in Chapter 4. There is a linear relationship between stress and strain for the diffusional creep, see equation (3. 25), which leads to the low strain rate sensitivity in H cases. As a result, the increase in tertiary creep rate in H cases is not as significant as in V cases. This suggests that the damage-related theory used in this study may need improvement to replicate the experimental results.

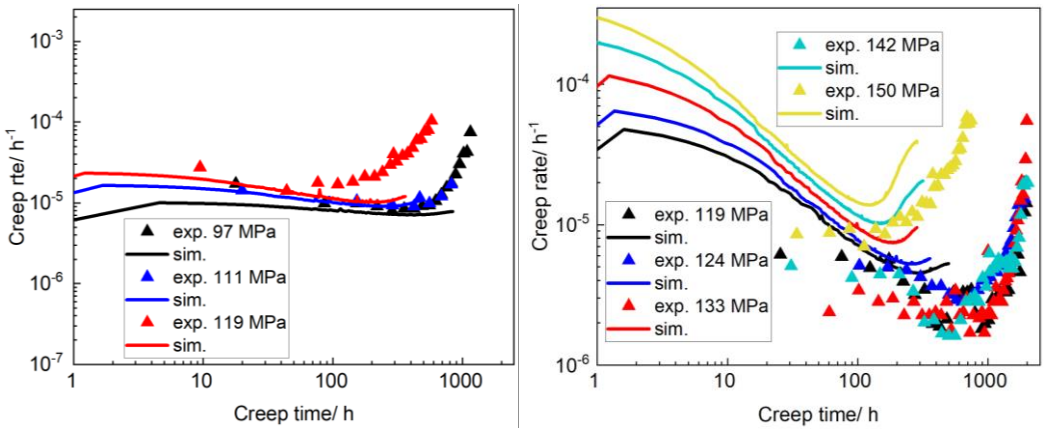

(a) (b)

Figure 5. 4 The full curve creep rates comparison between CP-FEM simulation results and experimental data (Williams et al., 2021) for (a) H (horizontally built) and (b) V (vertically built) samples. Both H and V samples are tested under 923 K.

Furthermore, in both of the H and V cases, there is a noticeable discrepancy between the highest loading stress curve and the other curves in Figure 5. 4. As illustrated in Figure 5. 5, this discrepancy is particularly prominent at the tertiary creep stage, where after the minimum creep rate is observed. The author assumes that a deformation mechanism transition may occur when the applied stresses reach a certain threshold value. The discrepancy is characterized by a transition in the dominant deformation mechanism of the material, where the change in the underlying deformation process results in significant alterations in the material's mechanical properties. A similar transition between moderate and high-stress regimes with different power n has been observed in the other materials as well, e.g. (Charit and Murty, 2008; Nie et al., 2017; Rajaguru and Keralavarma, 2018; Wen et al., 2018). The stress sensitivity described

earlier can partially account for this phenomenon. The creep behaviour in a low-stress regime is primarily governed by diffusional creep mechanisms, while higher stresses follow a power law relationship. Nevertheless, the current CP-FEM framework does not accurately reproduce this "jump" phenomenon. Thus, there is a critical need to advance existing research and potentially elucidate the underlying mechanism responsible for this transition, to facilitate a more accurate and comprehensive understanding of this phenomenon.

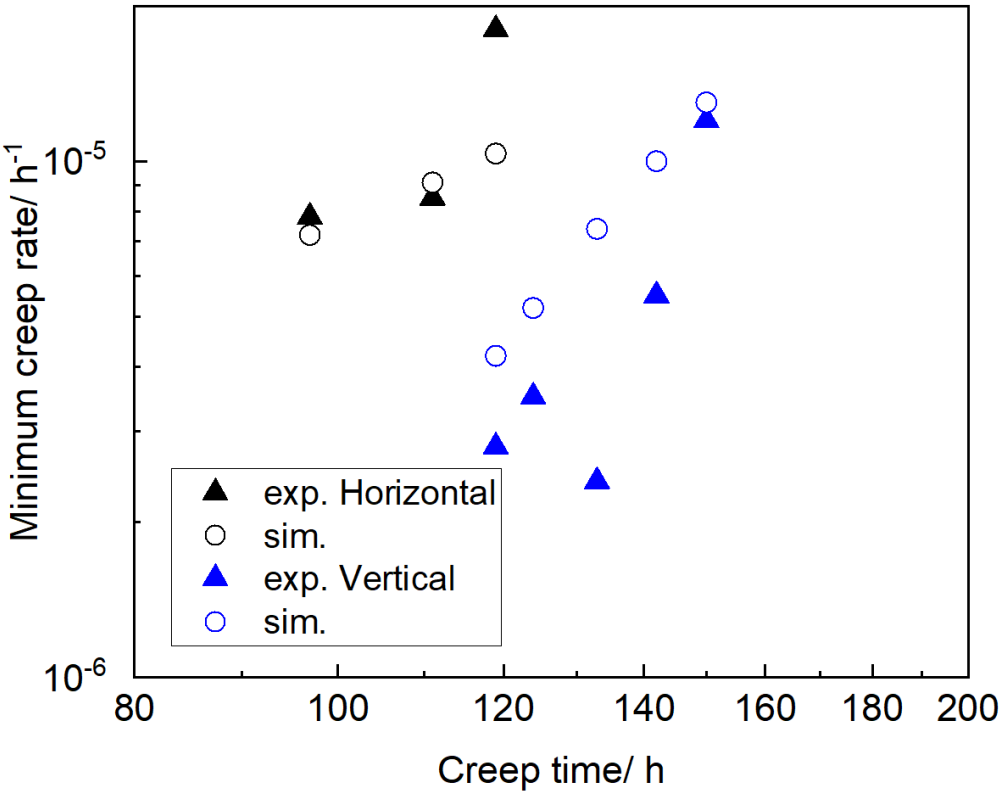

Figure 5. 5 The minimum creep rates comparison between CP-FEM simulation results and experimental data (Williams et al., 2021).

Figure 5. 6 displays the computed creep rate curves for specifically selected areas from the EBSD image. Notably, these curves exhibit distinct creep behaviour even for identical directions in the printed sample. Even though, this variation remains consistent with the overall trend of stress-strain response. These heterogeneous creep rate curves indicate that the creep behaviour is microstructurally sensitive. Therefore, the incorporation of realistic microstructures (e.g., EBSD data) is necessarily required under CP-FEM simulations to investigate the effects of grain structures. In addition,

incorporating the actual grain structure into finite element solvers has enabled the investigation of AM-induced anisotropy under various loading conditions. Nevertheless, for improved accuracy in creep response and mechanical property calculations, utilizing full grain mapping is still essential. Since the full microstructure can include most characters of the material, while the targeted area can represent the bias and specific defect from the whole sample. However, the full microstructure mapping approach entails high computational costs and may lead to numerical instability or convergence issues, which are undesirable for a comprehensive examination of the link between microstructure and property. A feasible alternative is to employ sophisticated microstructure design techniques, such as multilevel Voronoi tessellation, which can construct grain mappings with lower resolutions and still reserve the AM-induced microstructure characteristics . In materials science and microstructure analysis, Voronoi tessellation is employed to characterize and quantify the spatial arrangement of particles, grains, or cells. By representing each particle with a Voronoi cell, important microstructural properties like grain size, shape, and distribution can be analyzed. Voronoi tessellation is particularly useful in understanding material behavior, such as the mechanical properties and permeability of porous materials (El Shawish et al., 2020; Ghorbani Moghaddam et al., 2017; Güvenç et al., 2013).

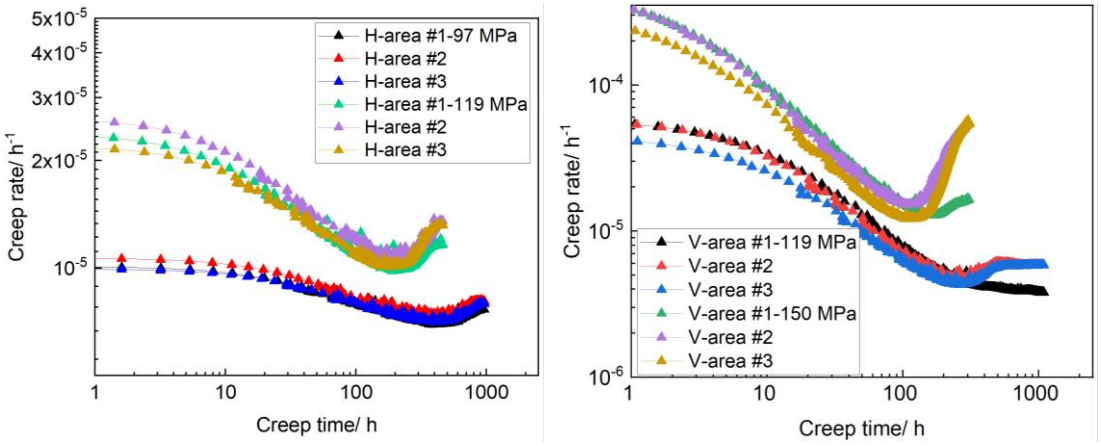

(a) (b)

Figure 5. 6 Simulation results of the different input areas, (a) AM-H (horizontally built); (b) AM-V (vertically built) (both AM cases are conducted under 923 K).

The stress and strain distribution on simulated grain structures under various applied stresses are illustrated in Figure 5. 7, Figure 5. 8, Figure 5. 9, and Figure 5. 10, with the corresponding creep times indicated. The simulated structures are shown in Figure 5. 2, which are deliberately selected from the original EBSD data for both AM-H and AM-V. As the creep time increases, there is a noticeable accumulation of stress and strain within the microstructure. Notably, a conspicuous concentration of strain is observed at the grain boundaries during the later stages of creep deformation, which can be attributed to the localized accumulation of damage within the microstructure. These damage accumulation mechanisms have been elaborated in Section 5.2. The nucleation, growth, and coalescence of voids can weaken the grain boundaries and facilitate deformation localization. Furthermore, the observed strain concentration at the grain boundaries suggests that they play a critical role in accommodating deformation and influencing the overall mechanical response of the material. The insights obtained from these simulations provide valuable information for understanding the microstructural factors that influence the creep behaviour of polycrystalline materials and can guide the design and optimization of new materials with enhanced creep resistance.

σ_{22}	H-area #1	H-area #2	H-area #3
97 MPa	 280 h	 280 h	 280 h
	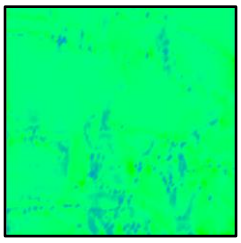 500 h	 500 h	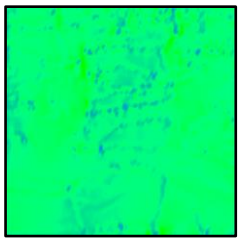 500 h
	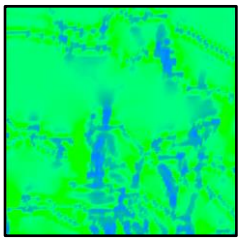 1000 h	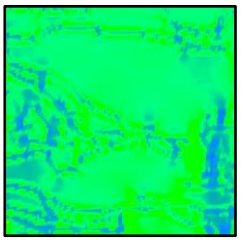 1000 h	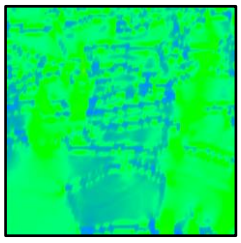 1000 h
119 MPa	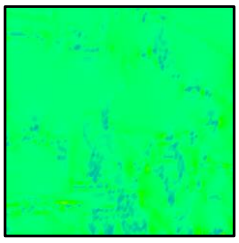 100 h	 100 h	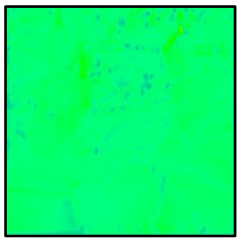 100 h

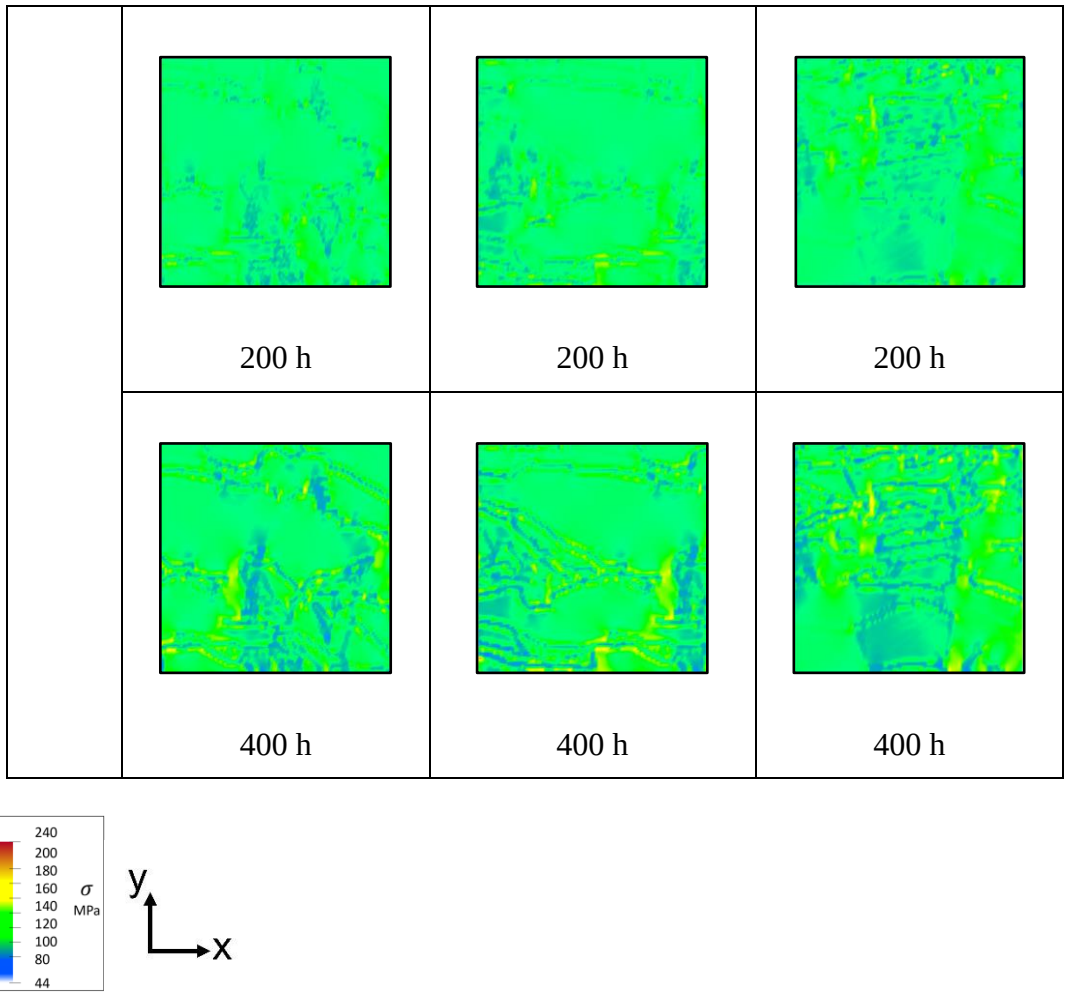

Figure 5. 7 The distribution of tensile stress along the loading direction, σ_{22}, for H samples at selected loading condition and creep time.

ε_{22}	H-area #1	H-area #2	H-area #3
97 MPa	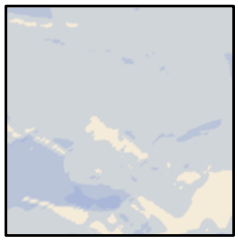 280 h	 280 h	 280 h
	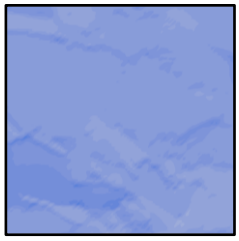 500 h	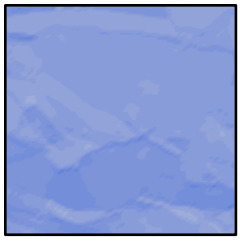 500 h	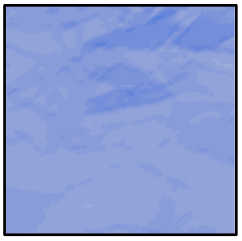 500 h
	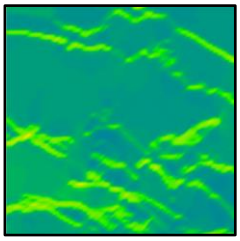 1000 h	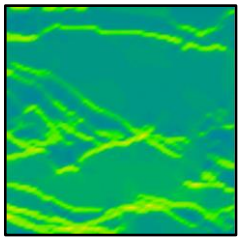 1000 h	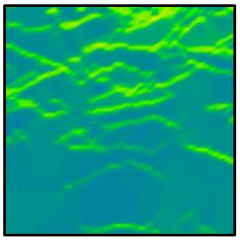 1000 h
119 MPa	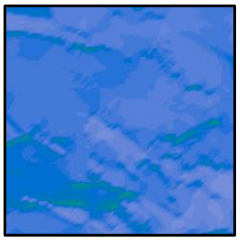 100 h	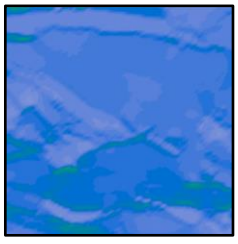 100 h	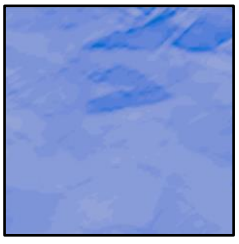 100 h

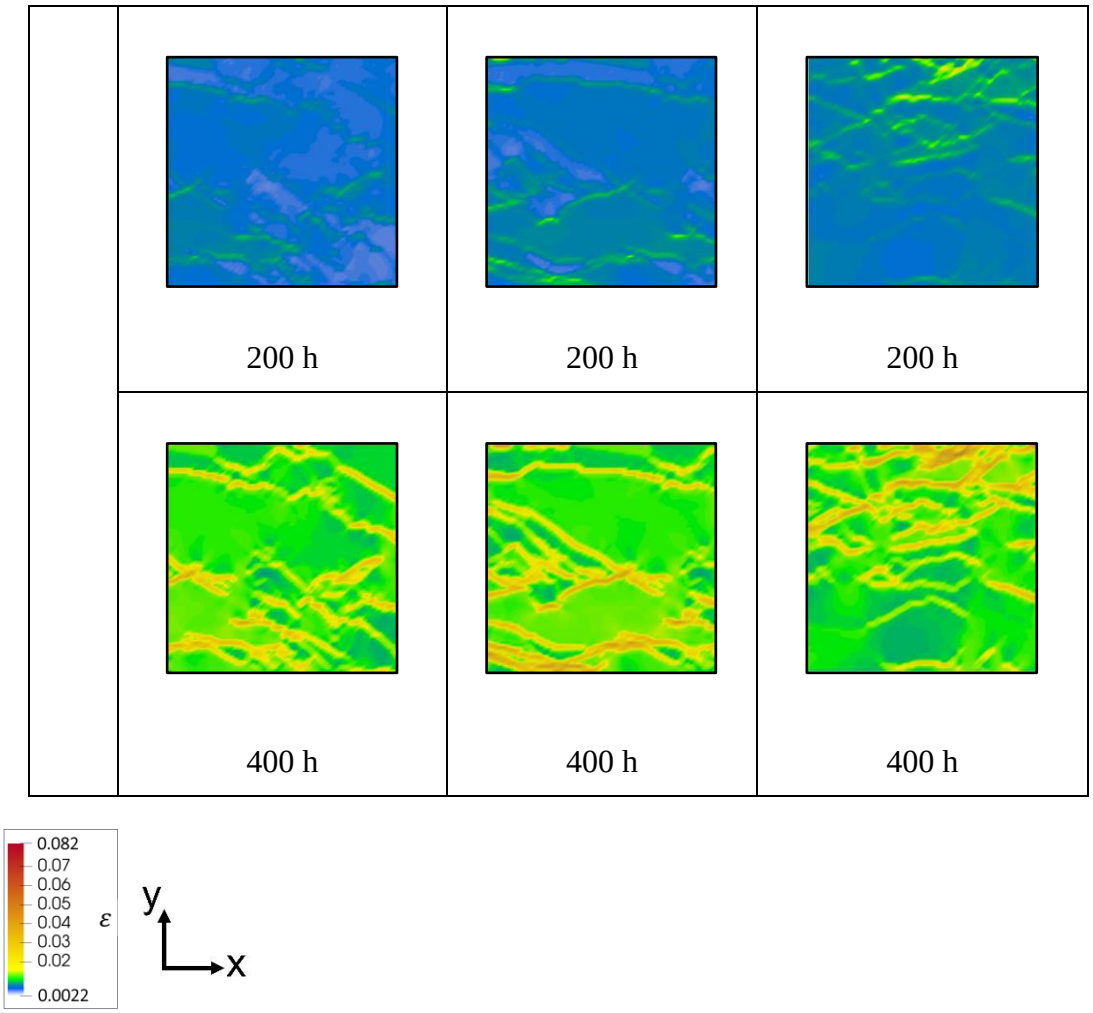

Figure 5. 8 The distribution of normal strain along the loading direction, ε_{22}, for H samples at selected loading condition and creep time.

σ_{22}	V-area #1	V-area #2	V-area #3
119 MPa	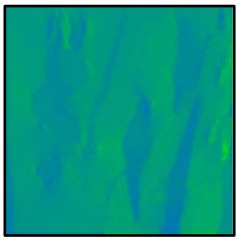 100 h	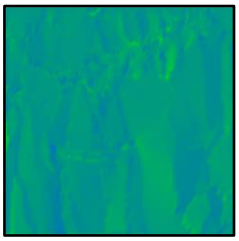 100 h	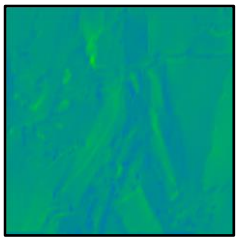 100 h
	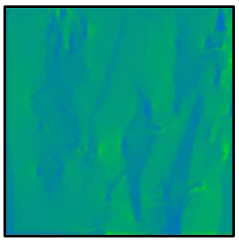 300 h	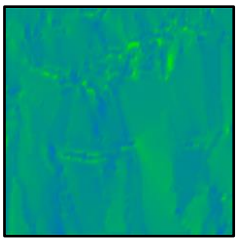 300 h	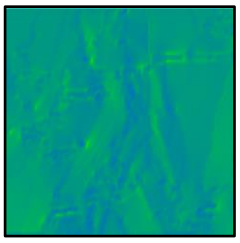 300 h
	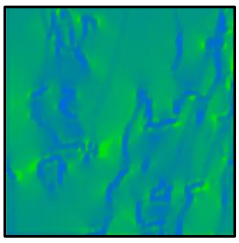 1000 h	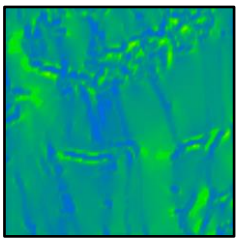 1000 h	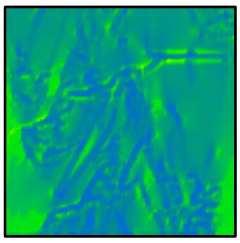 1000 h
150 MPa	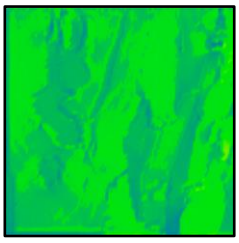 60 h	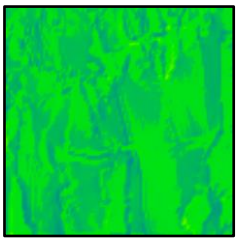 60 h	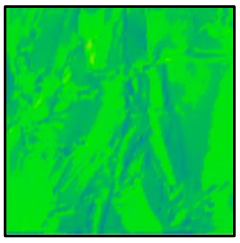 60 h

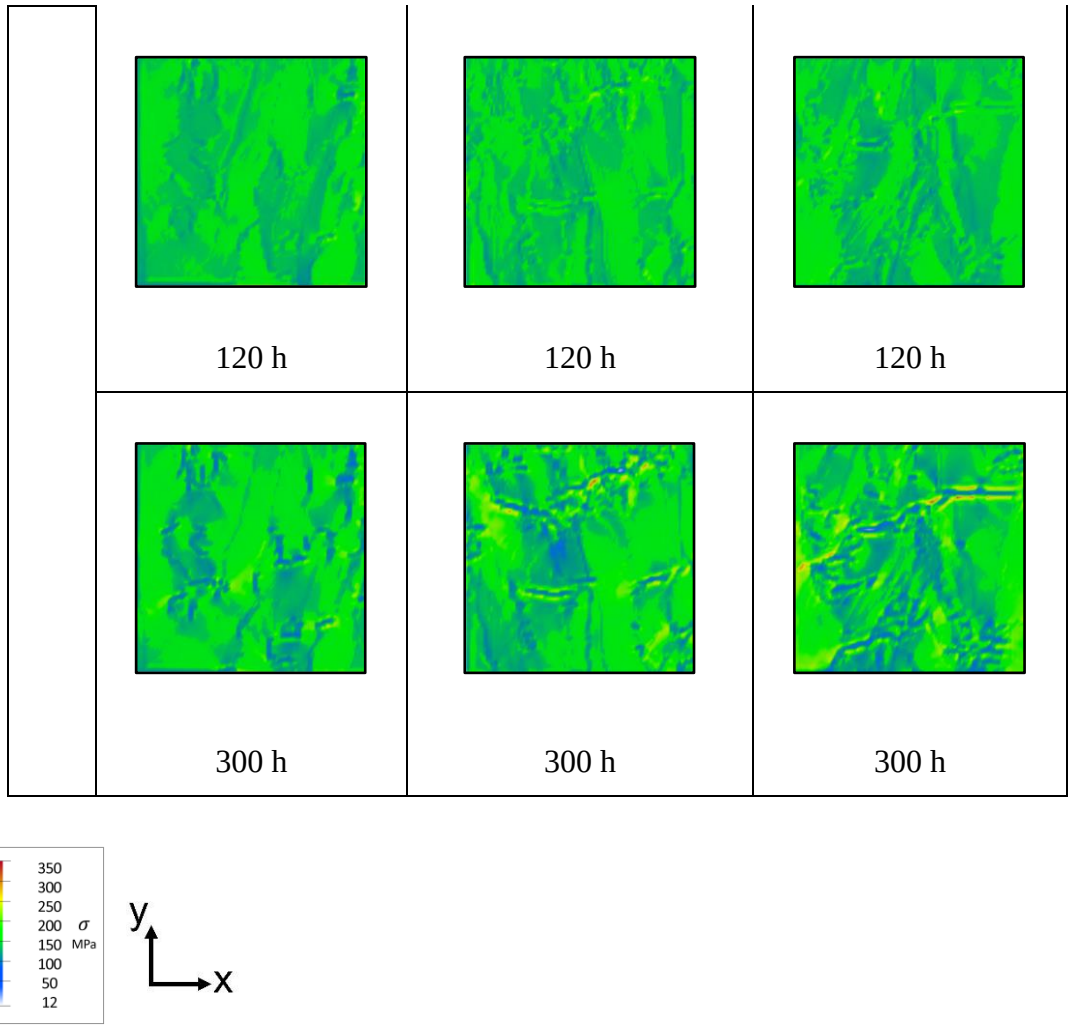

Figure 5. 9 The distribution of tensile stress along the loading direction, σ_{22}, for V samples at selected loading condition and creep time.

ε_{22}	V-area #1	V-area #2	V-area #3
119 MPa	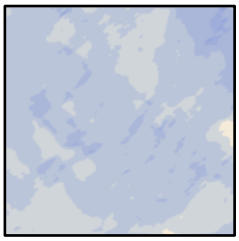 100 h	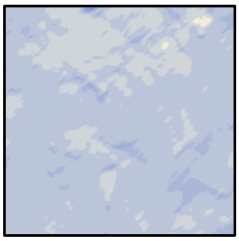 100 h	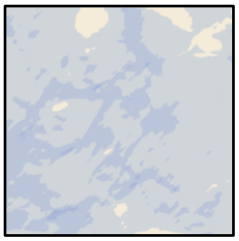 100 h
	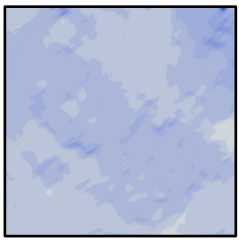 300 h	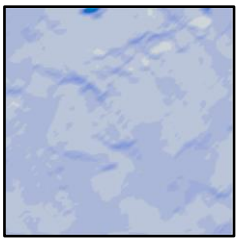 300 h	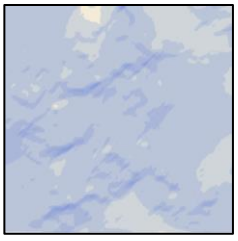 300 h
	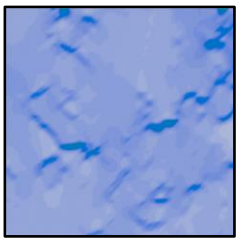 1000 h	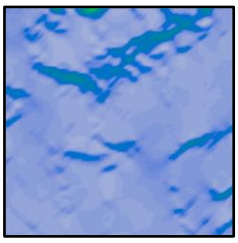 1000 h	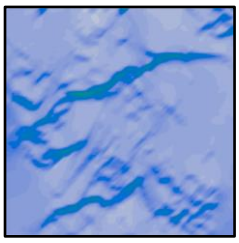 1000 h
150 MPa	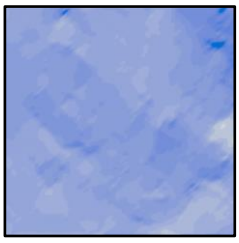 60 h	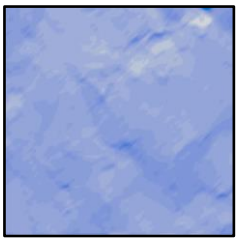 60 h	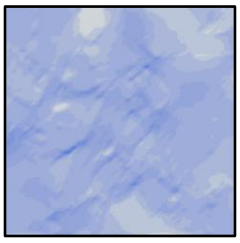 60 h

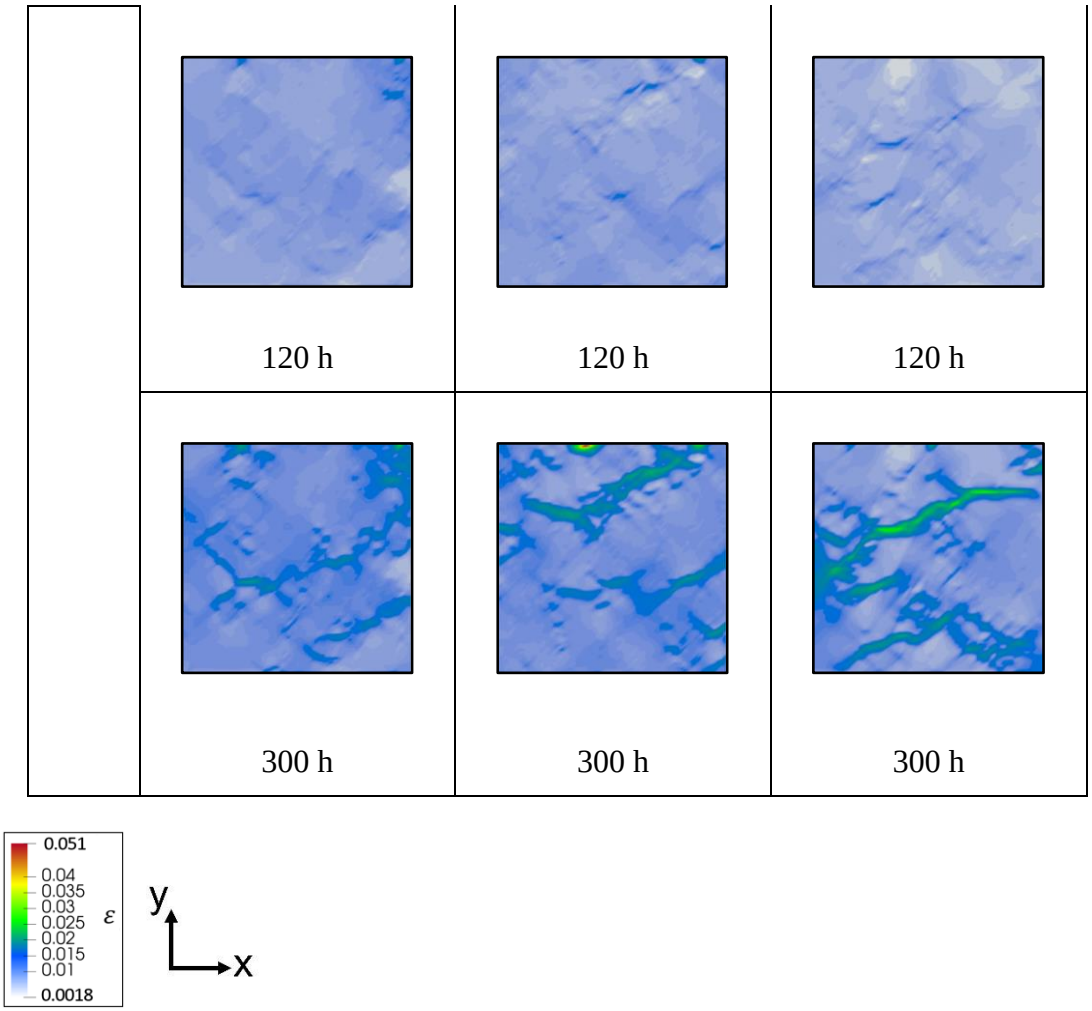

Figure 5. 10 The distribution of normal strain along the loading direction, ε_{22}, for V samples at selected loading conditions and creep time.

At the tertiary stage of creep, the behaviour of a material depends not only on the loading environment but also on its microstructure features. In this study, the H sample exhibits an earlier appearance of tertiary creep. The rate of void growth, which is a key indicator of damage accumulation, strongly depends on the local stress resolved in the direction normal to the grain boundary. This stress can accelerate grain boundary diffusion, leading to the accumulation of vacancies and the formation of damage. Therefore, the orientation of high-angle grain boundaries (HAGBs) relative to the loading direction becomes an important factor to consider.

Figure 5. 11 and Figure 5. 12illustrate the distribution of porosity (i.e., the indicator of damage) on the HAGBs. Comparing the results of the H and V samples, we observe that damage accumulates mainly on the HAGBs that are normal to the loading direction

(y-direction). The microstructure of the H sample is decorated with more HAGBs perpendicular to the loading direction, which may explain why the tertiary creep appears earlier in this sample than in the V sample. These findings highlight the importance of accounting for the angles of HAGBs as part of the input to capture the normal stress applied to the HAGBs.

In AM 316L SSs, the grains tend to be elongated along the building/scan direction, resulting in more grain boundaries parallel to this direction. Therefore, the design of the AM processing should be tailored to specific applications. For example, in pressurized tubes, creep usually accumulates along the hoop direction. Hence, laser scanning along the hoop direction should be preferred to achieve better creep resistance. These insights could help optimize the AM process parameters to achieve desired material properties for different applications.

f^*	H-area #1	H-area #2	H-area #3
97 MPa	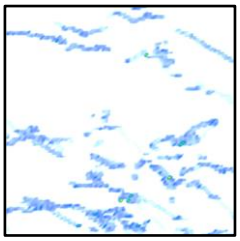 280 h	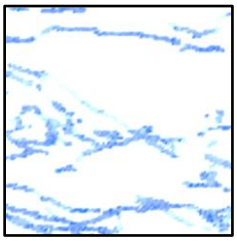 280 h	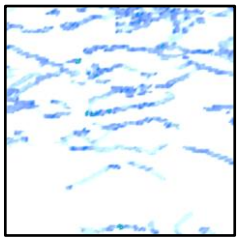 280 h
	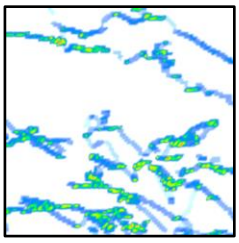 500 h	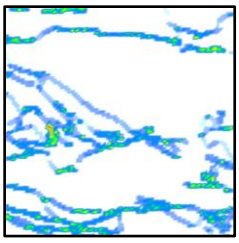 500 h	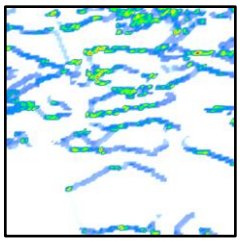 500 h
	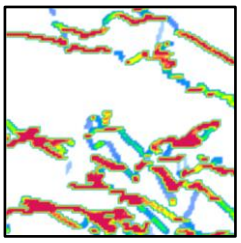 1000 h	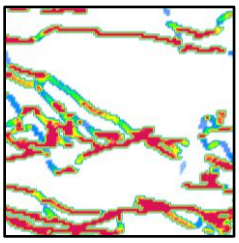 1000 h	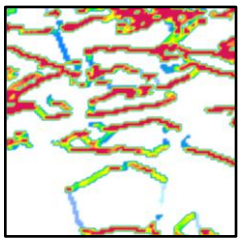 1000 h
119 MPa	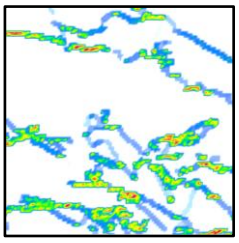 100 h	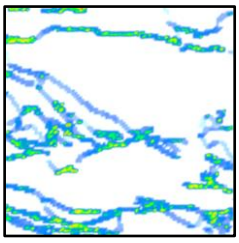 100 h	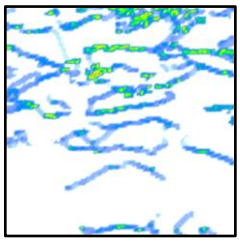 100 h

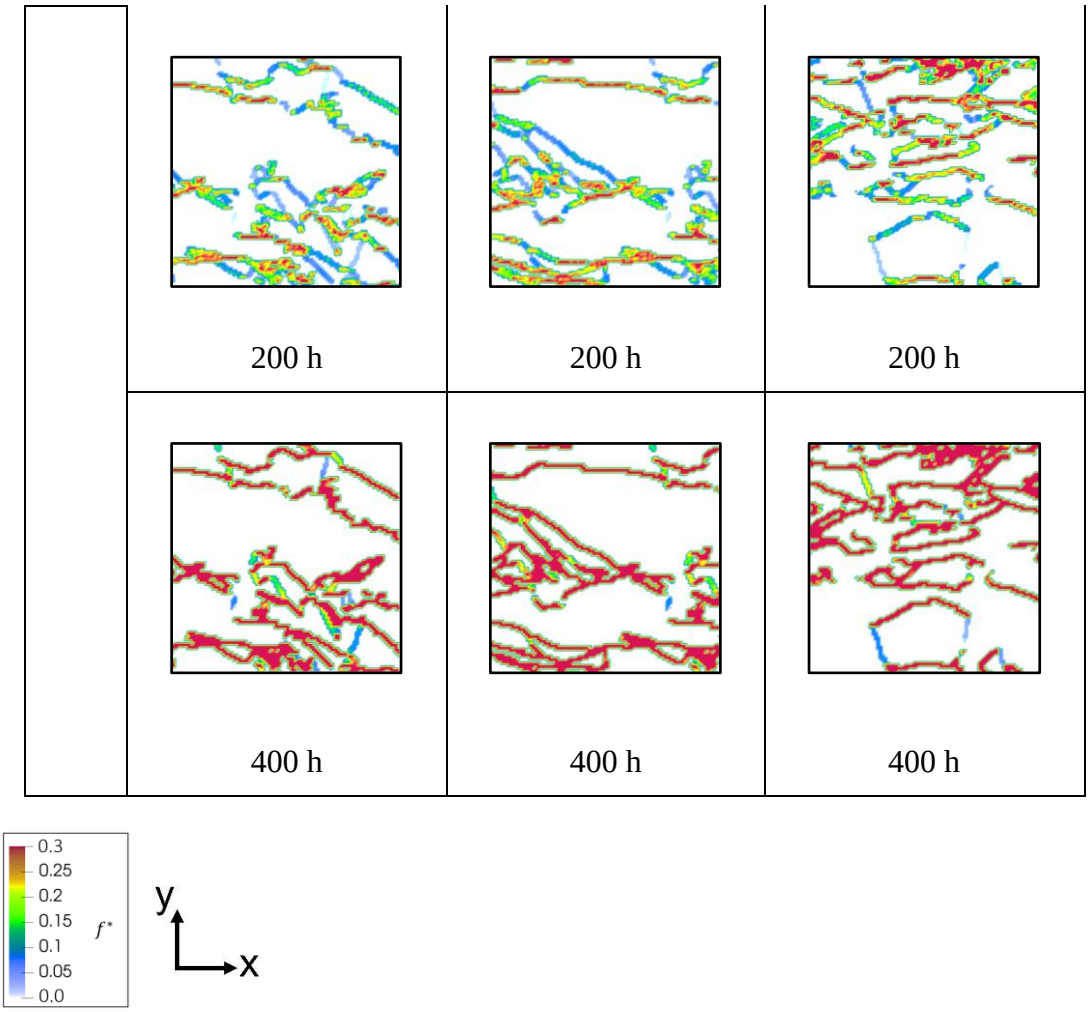

Figure 5. 11 The distribution of porosity, f^*, for H samples at selected loading conditions and creep time.

f^*	V-area #1	V-area #2	V-area #3
119 MPa	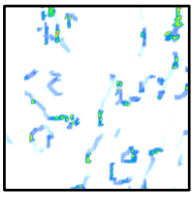 100 h	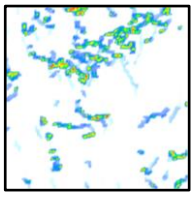 100 h	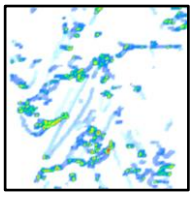 100 h
	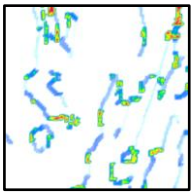 300 h	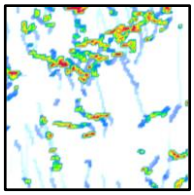 300 h	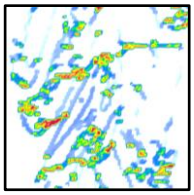 300 h
	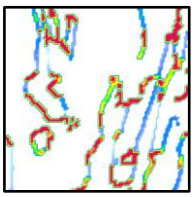 1000 h	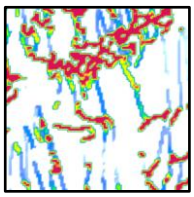 1000 h	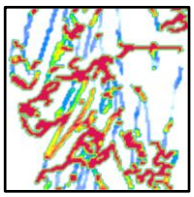 1000 h
150 MPa	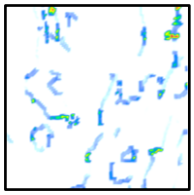 60 h	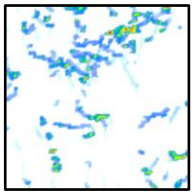 60 h	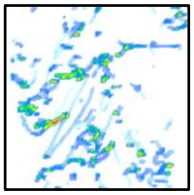 60 h
	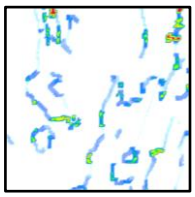	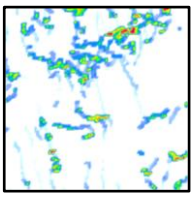	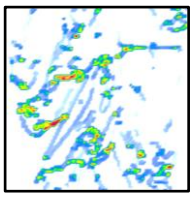

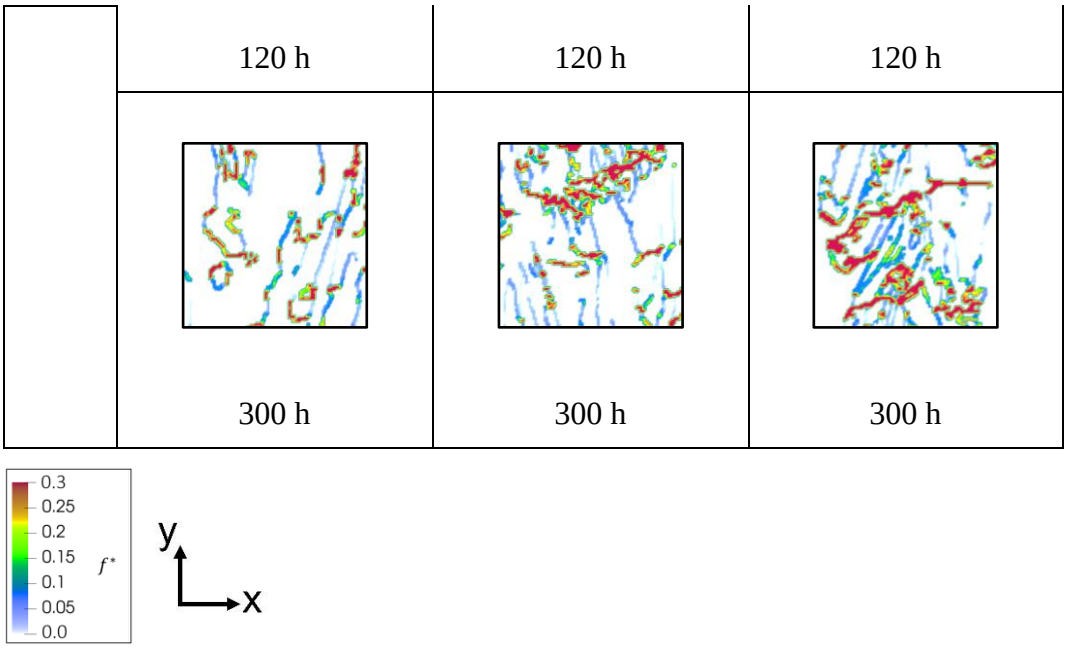

Figure 5. 12 The distribution of porosity, f^*, for V samples at selected loading conditions and creep time.

5.6 Summary

In this chapter, the author performed CP-FEM simulations to investigate the creep behaviour of AM 316L SSs in relation to the building direction with a particular focus on the damage behaviour. To accomplish this, the physics-based CP model proposed in Chapter 3 is inherited and implemented under the CP-FEM framework. Additionally, the GTN damage model is employed to describe the tertiary creep behaviour resulting from void nucleation, growth, and coalescence.

One of the aims of this study was to consider the effects of AM-induced grain structure accurately. Therefore, the EBSD data is directly imported into the CP-FEM framework to simulate the exact microstructure deformation behaviour. The full creep testing curve of each case is reproduced under the CP-FEM framework. The simulation results demonstrated a clear relationship between the orientation of HAGBs concerning the loading direction and damage behaviour. It is observed that the damage tends to accumulate on the HAGBs that are normal to the loading direction.

The discovery of this work has important implications for the design of AM products under specific service conditions. It is evident that the printing strategy should be

tailored according to the service conditions to improve the service life of the materials. For instance, in pressurized tubes, if creep resistance along the hoop direction is desired, laser scanning should be conducted along the same direction to ensure that the grain boundaries are parallel to the hoop direction. Overall, this study contributes to the development of a deeper understanding of the creep behaviour of AM 316L SSs, which has implications for the design and manufacturing of high-performance components.

Chapter 6 Additive manufacturing-characterised microstructure study

This chapter aims to explore the influence of additive manufacturing (AM) on the creep behaviour of materials through the introduction of unique microstructural features, including elongated grain morphology and pores. To achieve the analysis of detailed microstructure behaviour, the full-field framework crystal plasticity finite element method (CP-FEM) framework will be employed in the work.

To avoid any contingency that appeared in the real materials and summarise the average features of AM-characterised grain structures, artificially generated AM-characterised microstructures with elongated grains will be created using the Voronoi diagram principle through MATLAB. The extent of grain elongation will be varied using different biases of two directions on the structure cross-sectional area. To investigate the effects of different types of pores, the specific size and shape of various pores will be incorporated manually into the electron backscatter diffraction (EBSD) data using MATLAB. Subsequently, the creep behaviour of the same material input area with and

without pores will be compared and analysed. To visualise the stress and strain distributions around the pore, ParaView will be utilised. This study aims to enhance the understanding of the relationship between microstructure and creep behaviour, which could provide valuable feedback for materials design.

6.1 Introduction

As shown in Figure 6. 1, the elongated grain shape is one of the representative AM-induced microstructural features. Along the building direction, the as-built AM materials have epitaxial columnar grains due to the elongation by heat removal during solidification (Gorsse et al., 2017; Laleh et al., 2019). The real AM materials grain structures extracted from EBSD data have been simulated in Chapter 5, which contains the elongated grains. Meanwhile, the relationship between the high angle grain boundaries (HAGBs) and the loading directions has been discussed. One of the conclusions from Chapter 5 is that the HAGBs perpendicular to the loading direction prefer to accumulate more damage, therefore, the materials would show an earlier fracture. According to this, the extent of grain elongation can play an important role in materials' mechanical behaviour, especially damage behaviour. In this chapter, the artificially generated grain structures will be employed to investigate the behaviour of the material decorated with differently elongated grains. The elongated grains will be generated by MATLAB code upon the Voronoi diagram principle. In addition, the real AM materials can contain some special situations, which need individual analysis. The grain texture generated through the Voronoi diagram can preserve the AM materials' grain features while eliminating the occasional cases. By introducing a bias, the microstructures with grains elongated to varying degrees can be achieved.

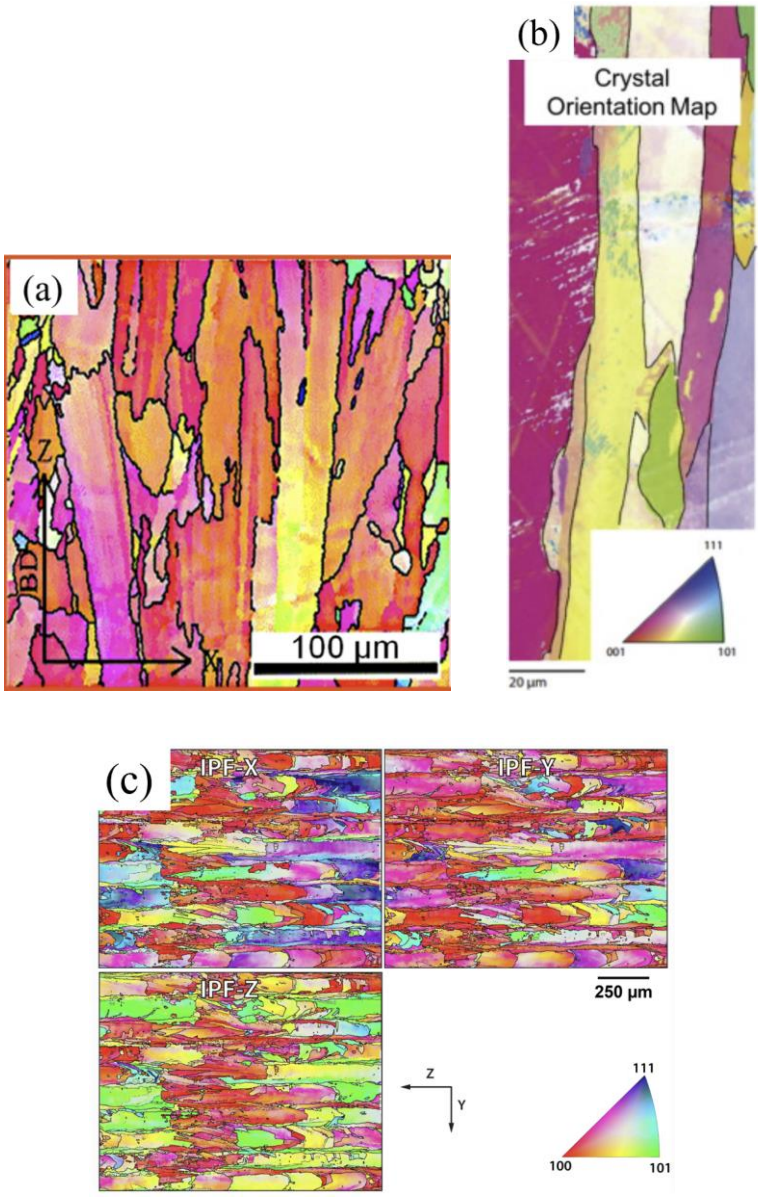

Figure 6. 1 EBSD orientation maps showing grain morphology for the SLM processed materials on cross-section area along the building direction. (a): IN718 (Ni et al., 2017); (b) Co29Cr6Mo alloy (Kok et al., 2018); (c) IN625 (Stoudt et al., 2020).

It is noteworthy to mention that, since the full creep curve simulations based on real AM materials have been done under the CP-FEM framework, therefore, the parameters for simulations in this chapter will be inherited from Chapter 5 apart from the grain size. This is out of the reason the microstructure with differently elongated grains will have different grain sizes.

Apart from the elongated grains, AM-induced pores are also one of the AM materials characteristics. A literature review of different types of pores induced during the AM process has been provided in Section 2.2.1. The scanning strategy can influence the types of pores, shape and size by influencing the properties of the melting pool (Ladani et al., 2017; Mukherjee et al., 2016). The internal pores introduced by the AM process are mainly three kinds, lack of fusion, keyhole, and balling (Johnson et al., 2019; Sabzi et al., 2020c). Since the occurrence of all types of pores is related to heat input, which is related to the laser power, scanning speed and scanning pattern. Therefore, the pores effect study can offer feedback to the AM strategy design, and a better understanding of the processing-structure-property relationship.

Various studies have explored the influence of pores on the mechanical properties of materials under tensile deformation. These studies have shown that the presence of pores can lead to certain drawbacks during tensile deformation (Pham et al., 2017; Wilson-Heid et al., 2019). The nature of these pores is not only limited to AM process-induced pre-existing pores, but also seeded types of pores. However, while the impact of pores on tensile behaviour has been extensively studied, limited research is available on their influence on creep behaviour, which is a critical service environment and can have significant implications for the materials' structural integrity. Therefore, the investigation of the pore effects on the creep deformation of 316L SS is needed. In particular, the study will evaluate how the size, shape, and location of pores affect the creep behaviour of the material. This investigation can provide valuable insights into how pores can impact the long-term performance and durability of materials in high-temperature service environments. The results of this study could have significant implications for the design and engineering of materials for high-temperature applications.

6.2 Investigation of microstructure decorated with elongated grains

In this section, the creep behaviour of materials microstructure with varying extend of elongated grains will be simulated and discussed. The Voronoi diagram will be employed under MATLAB to generate artificial materials microstructures, which are used as input for AM materials creep deformation simulation under the CP-FEM

framework. This Voronoi diagram is a self-developed code with an introduced bias to generate the differently elongated grain structures. The centre of each grain is generated randomly within the area of 100x100 pixels with a given grain number, following the grain allocation with a bias along one of the axis. The texture of AM materials is also randomly generated, which is through the MATLAB MTEX toolbox. Although the study is investigating the microstructure decorated with elongated grains, it is still based on AM-processed materials. Therefore, apart from the grain size, which changes along the grain structures generated with different numbers of grains, all the other parameters are inherited from the real AM materials in Chapters 4 and 5. To have a more comprehensive understanding of the effect of the elongated grain on materials creep behaviour, the two orthogonal loading directions, x-loaded and y-loaded, will be applied on the randomly generated grain structures respectively.

6.2.1 Uniformly elongated grains of varying sizes

As shown in Figure 6. 2, there are two randomly generated microstructures are considered as input files under the CP-FEM framework. These two microstructures are given the same extent of elongated grains, whose elongation ratio is 1:5, within the 100x100 pixels area. Grain structure #1 (GS #1) is assigned 30 grains, with an average grain size of 30 μm; while GS #2 is assigned 20 grains on a 50 μm average. The texture of each grain is randomly selected. Since the simulation is based on the investigation of AM materials. Therefore, apart from the grain sizes, all the other parameters are inherited from Chapters 4 and 5 to preserve the most features of AM-characterised materials. The parameters of the vertically built (AM-V) sample are used in this case and the simulation is conducted under 923 K with 150 MPa external loadings.

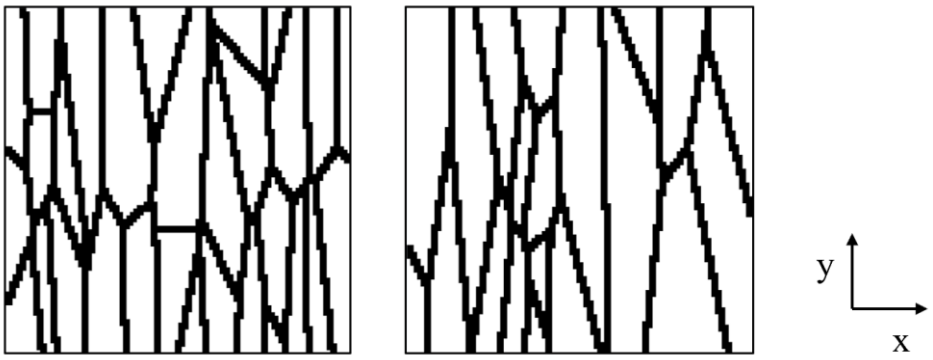

(a) (b)

Figure 6. 2 Randomly generated microstructure input, (a) GS #1; (b) GS #2 (GS-grain structure).

The simulation results are shown in Figure 6. 3, which uses the grain structures from Figure 6. 2(a) and (b) as input. The simulations have been done with loading from both the x-axis and y-axis directions. Apparently, the grain structure input has a finer grain size showing a higher minimum creep rate, which is consistent with the conclusion from Chapter 4. In addition, when the loading direction is perpendicular to most of the HAGBs, there is an obvious increase in creep rates after the materials achieved the minimum creep rate point. This obvious increase is an indication of the damage behaviour. Therefore, the materials with more HAGBs perpendicular to the loading direction will have more obvious damage behaviour. The HAGBs that are vertical to the loading direction are the crucial damage sites. As shown in Figure 6. 4 and Figure 6. 5 at the same loading time, the same microstructure input is loaded differently in directions. When the input structure is x-loaded, with more HAGBs perpendicular to the external loading direction, there are more stress and strain distributed on the HAGBs. This finding is congruent with the conclusion drawn in Chapter 5, indicating a conspicuous correlation between the orientation of the HAGBs concerning the loading direction and the stress and strain localisation observed.

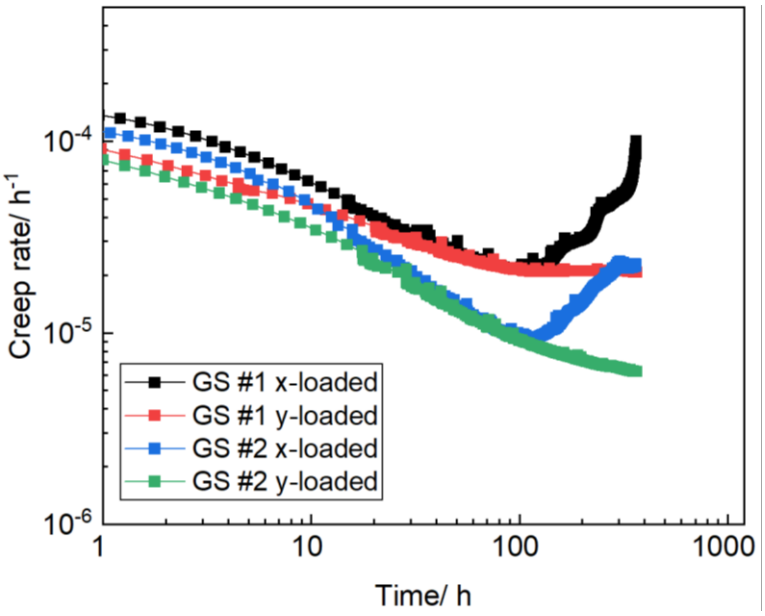

Figure 6. 3 Simulation results of using GS #1 and GS #2 as input with both x-axis and y-axis loading directions (GS-grain structure).

σ_{22}	GS #1	GS #2
x-loaded	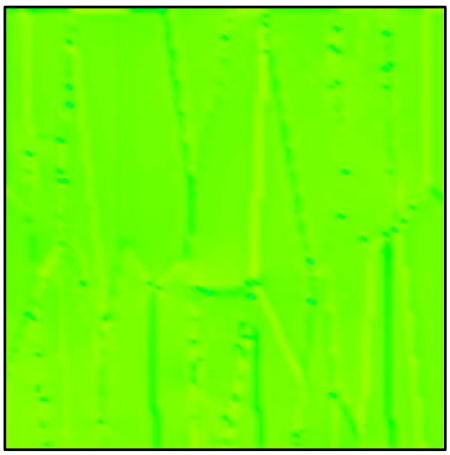 100 h	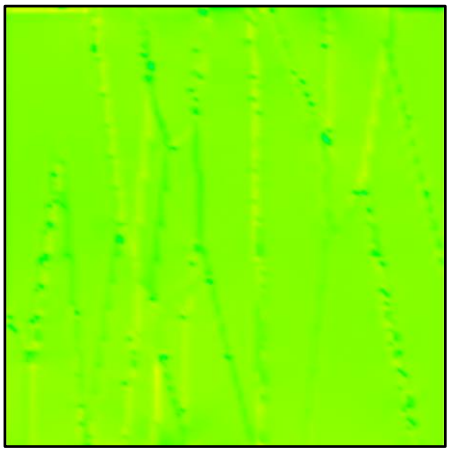 100 h
	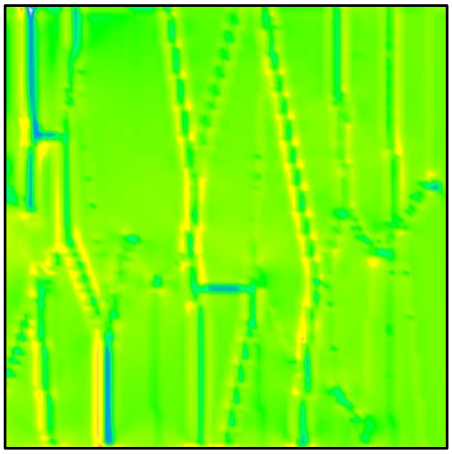 300 h	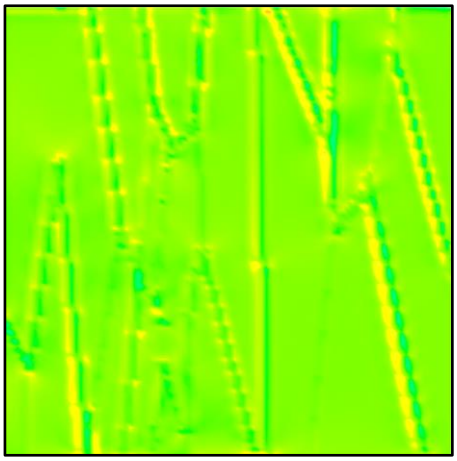 300 h

y-loaded	 100 h	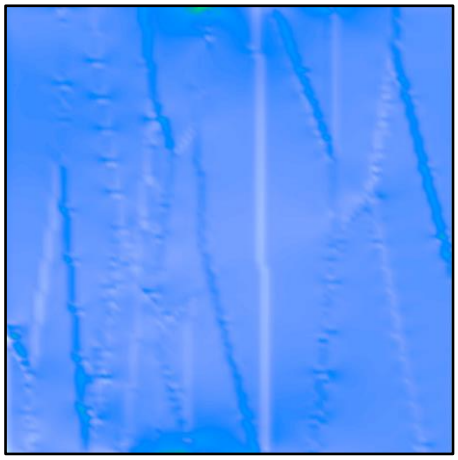 100 h
	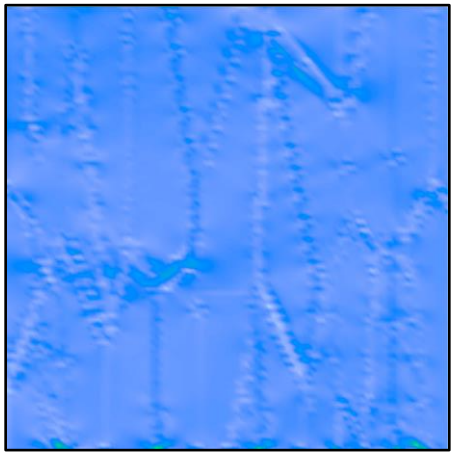 300 h	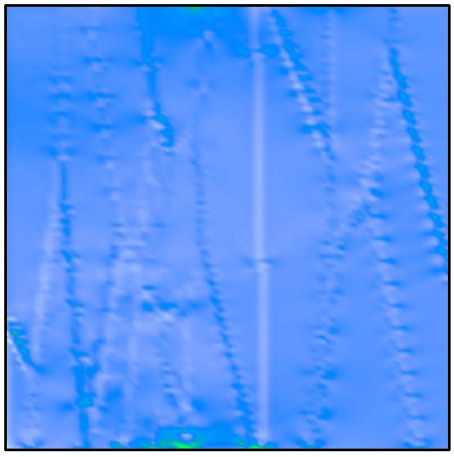 300 h

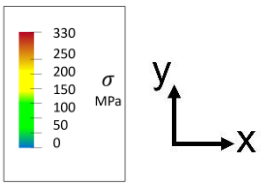

Figure 6. 4 The distribution of tensile stress along the loading direction, σ_{22}, for both GS #1 and GS #2 at selected loading condition and creep time.

ε_{22}	GS #1	GS #2

x-loaded	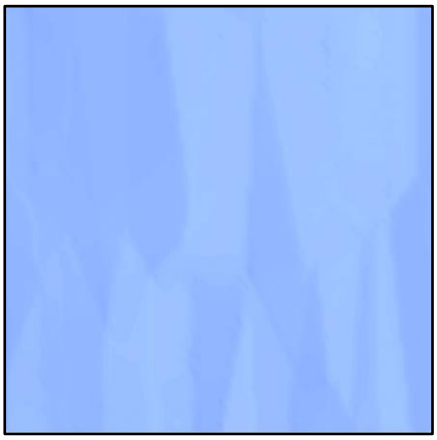 100 h	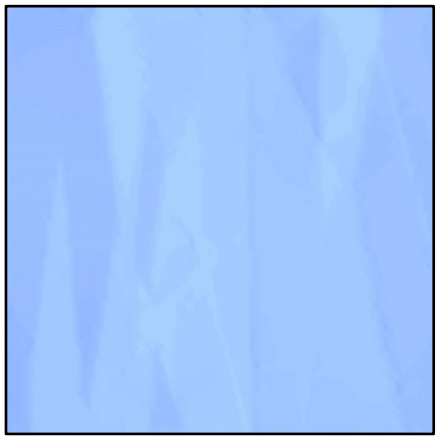 100 h
	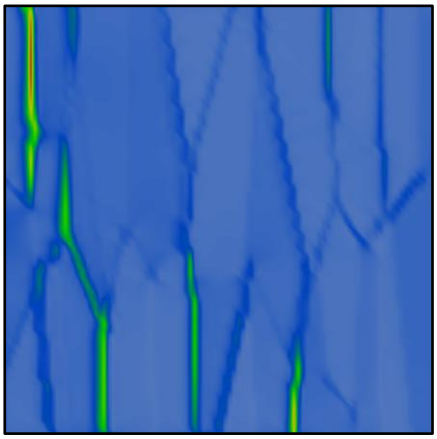 300 h	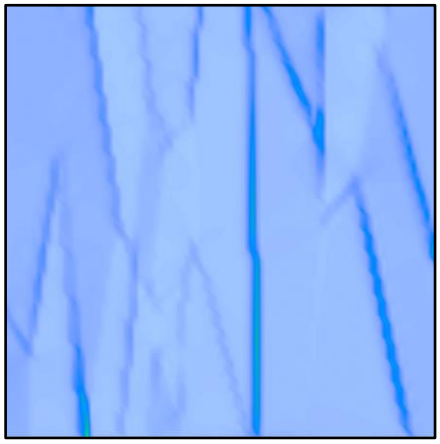 300 h
y-loaded		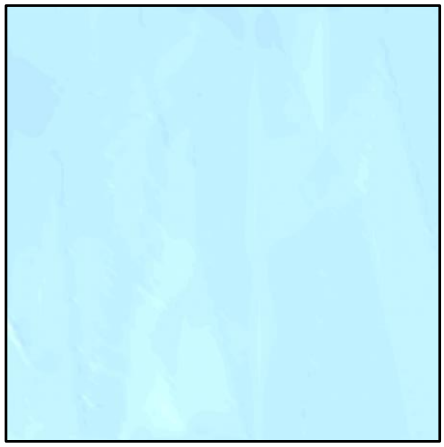

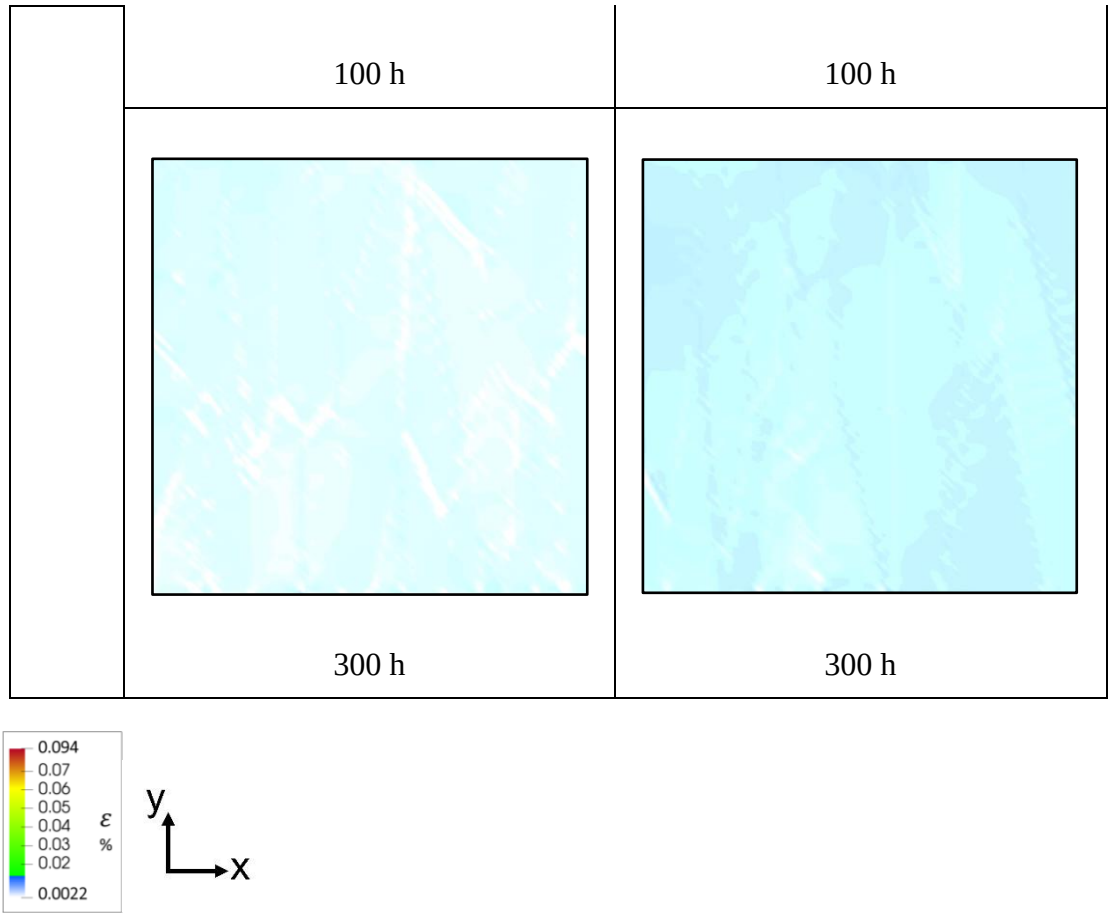

Figure 6. 5 The distribution of normal strain along the loading direction, ε_{22}, for both GS #1 and GS #2.at selected loading condition and creep time.

As shown in Figure 6. 6, it has been observed that the damage accumulation is predominantly observed on HAGBs which are perpendicular to the loading direction. This is consistent with the stress and strain concentration behaviour over the creep time. Hence, for AM purposes, it is recommended to tailor the printing strategy in a manner that aligns with the specific service conditions to enhance the overall service life. In addition, the indication of damage factor, f^*, along the HAGBs is represented in dotting lines. This is due to the limitation of current resolution, and HAGBs are shown in steps like lines in GS input.

f^*	GS #1	GS #2

x-loaded	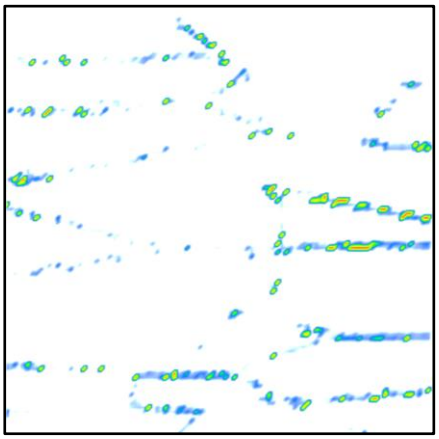 100 h	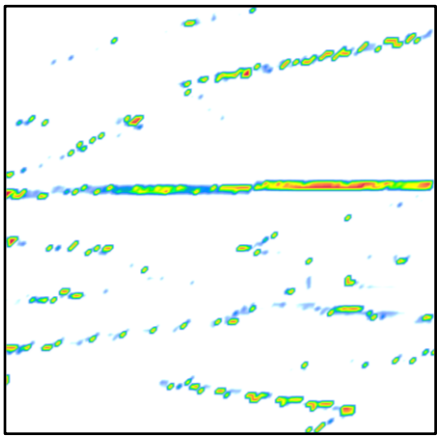 100 h
	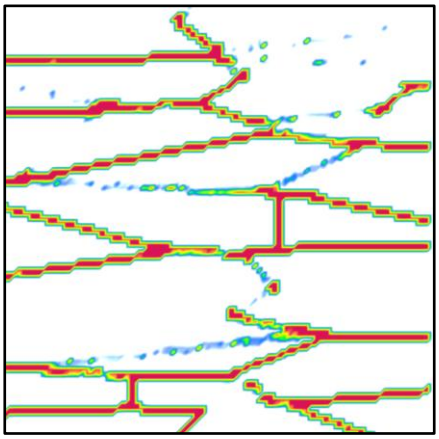 300 h	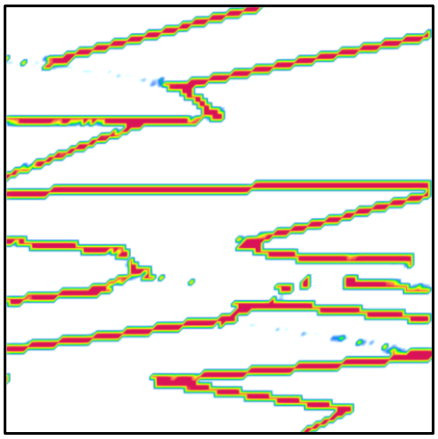 300 h
y-loaded	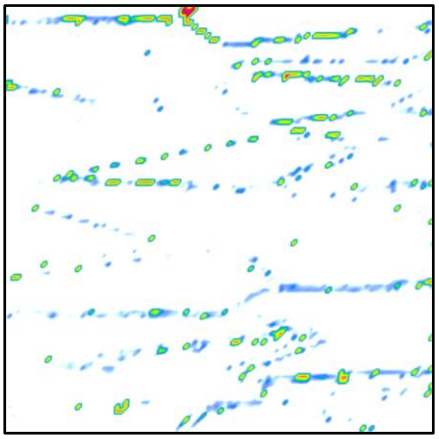 100 h	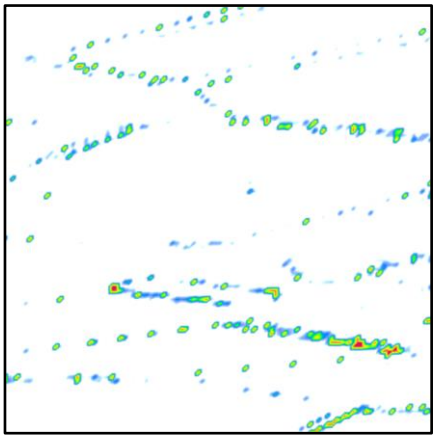 100 h

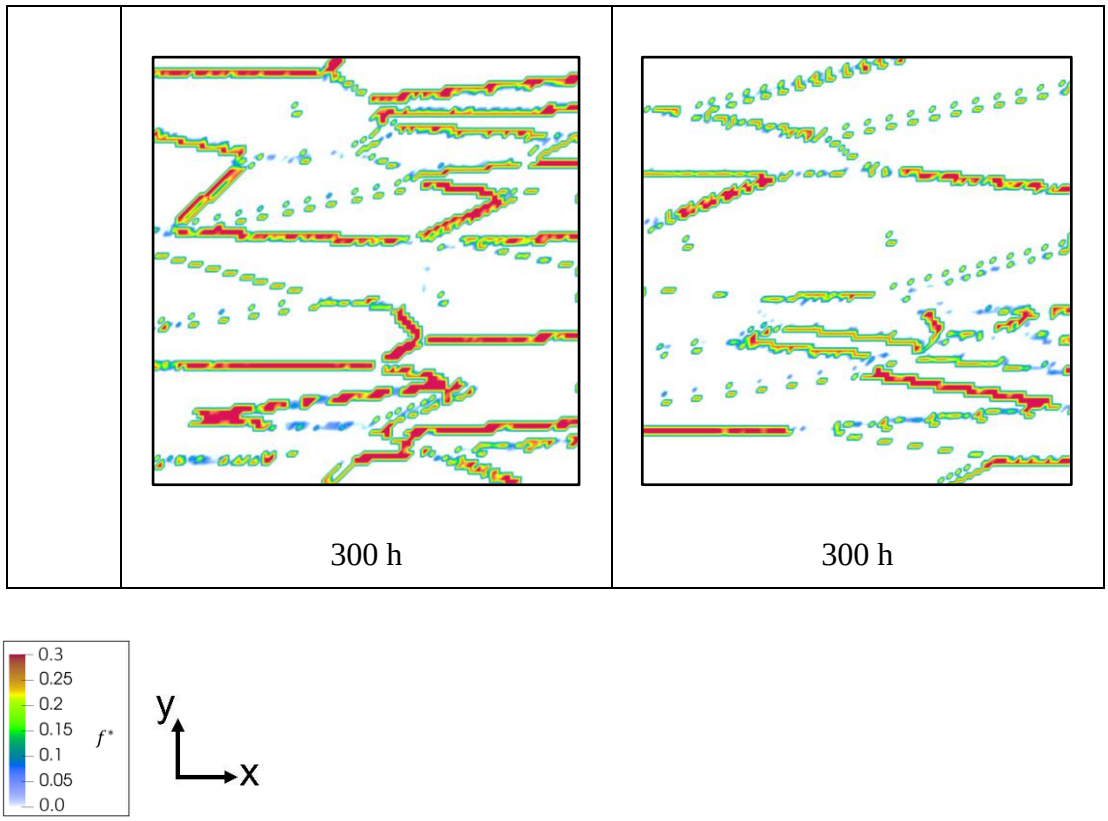

Figure 6. 6 The distribution of porosity, f^*, for both Microstructure #1 and Microstructure #2 at selected loading conditions and creep time.

Apart from the very obviously elongated grain structure, the less stretched grain with a ratio 1:2 is also studied to compare its behaviour with the non-stretched grain structure. Figure 6. 7 shows GS #3 and GS #4. GS #3 is assigned 20 grains on a 50 μm average size in diameter, with a 1:2 ratio elongated long the y direction, while GS #4 is assigned 20 grains in the size of 50 μm without elongation bias. The texture of each grain is randomly selected based on AM materials. All the other parameters are inherited from Chapters 4 and 5 to preserve the features of AM-characterised materials. The parameters of the vertically built (AM-V) sample are used in this case and the simulation is conducted under 923 K with 150 MPa external loading along both x and y directions.

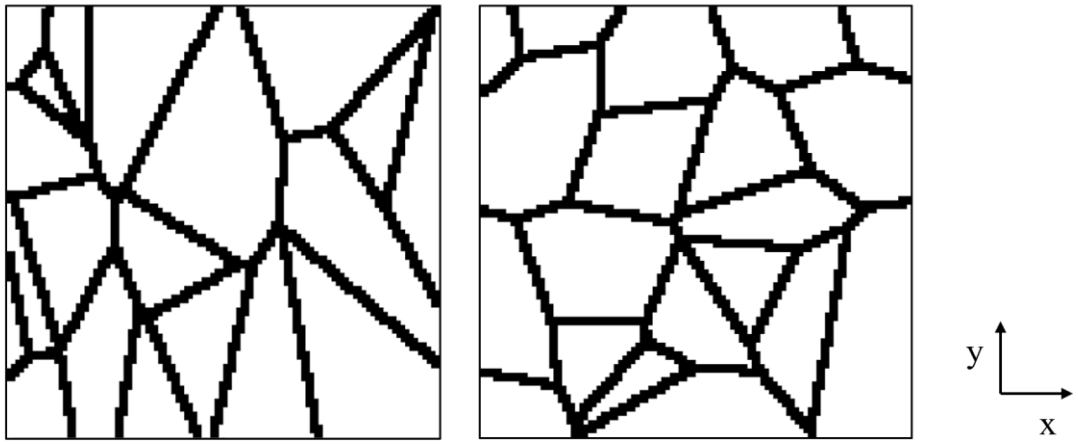

(a) (b)

Figure 6. 7 Randomly generated microstructure input, (a) GS #3; (b) GS #4 (GS-grain structure).

As illustrated in Figure 6. 8, the y-loaded creep behaviour of material shows a delayed damage phenomenon in GS #3. Since the grain elongated ratio in GS #3 is 1:2 along the y direction, while the grain structure ratio in GS #4 is 1:1. Therefore, the loading directions show more obvious effects on GS #3, meanwhile, the mechanical behaviours of GS #4 do not show much difference under different loading directions. The service life and the damage behaviour of the materials are highly related to the HAGBs orientation.

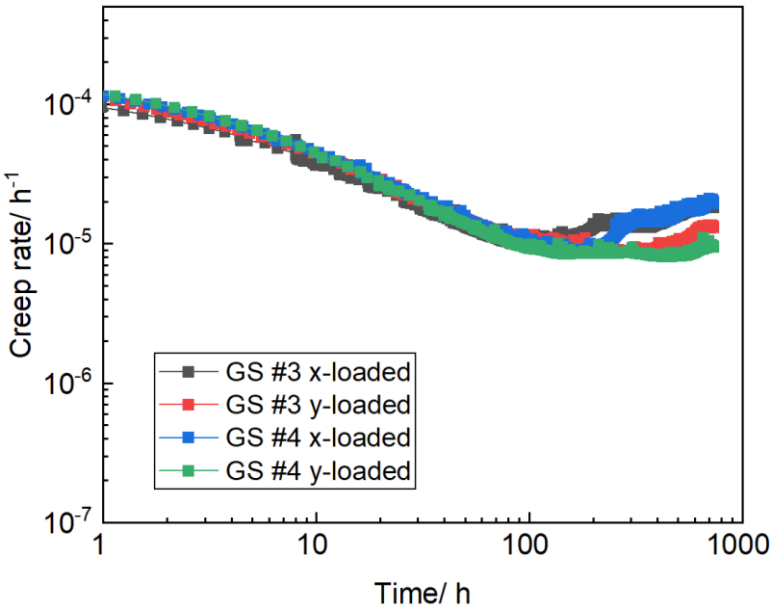

Figure 6. 8 Simulation results of GS #3 and GS #4 with both x- and y- axis as loading directions.

6.3 Investigation of pores

In this section, all the types of pores are introduced manually into the real materials microstructure with the specific size, shape and location. Gas entrapment and lack of fusion types of pores will be studied individually. However, due to the limited computational ability, all the FE simulations in this work are using 100x100 pixels input files. Even after reducing the input resolution, the maximum simulation area is 200x200 pixels. The depth of keyhole-type pores is normally more than 200 μm, which is beyond the current simulation microstructure region. Therefore, the keyhole-type pores are not included in this work.

6.3.1 Gas entrapment

The size of gas entrapment type of pores is normally around 1μm in a more spherical shape. However, the microstructure input file for CP-FEM simulation is made of pixels, which are in 2×2 μm after reducing the resolution. Therefore, the gas entrapment type of pores will be represented by a single pixel in the input microstructure for simplification. Figure 6. 9 shows the input microstructures with manually added gas entrapment-type pores. To investigate effects from pore locations, the pores are put inside the grain and on the HAGBs respectively. Since the HAGBs junctions are the critical location for damage evolution, therefore, the gas entrapment type pore is put on the boundaries junction position to magnify its effect. The original input microstructure was selected from a vertically built AM (AM-V) sample, which is area #3. The creep simulation is conducted under 923 K, with 150 MPa loading. Figure 6. 10 shows the comparison between the original AM-V-area #3-150 MPa without pore and AM-V-area #3-150 MPa with pore simulation results. It can be told that there is no obvious difference between the simulation results that the input microstructure without a pore and the input microstructure has a pore but not on HAGB. This is because gas entrapment-type of pores are in relatively small size, when they are not located in the critical area, the resultant impact is negligible. However, when the gas entrapment pore is located at the HAGBs junction, there is an obvious drop in minimum creep rate, which

is shown in Figure 6. 10 (c). In theory, this is not correct. Since the pore on the HAGB should hinder the resistance of the material to deformation, which means it is supposed to show a higher creep rate.

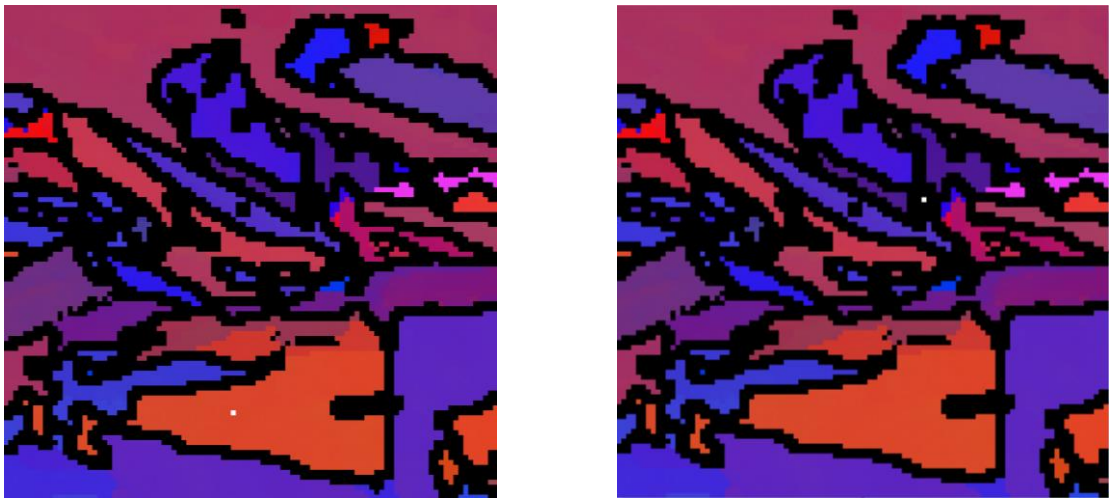

(a) (b)

Figure 6. 9 Input microstructures with gas entrapment type pores from vertically built sample, (a) pore is not on the high angle grain boundary (HAGB); (b) pore is on the HAGBs.

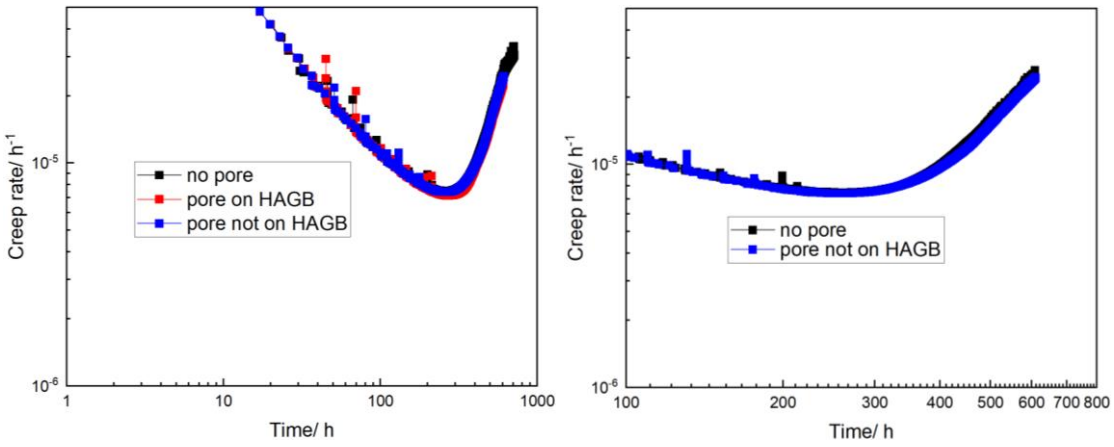

(a) (b)

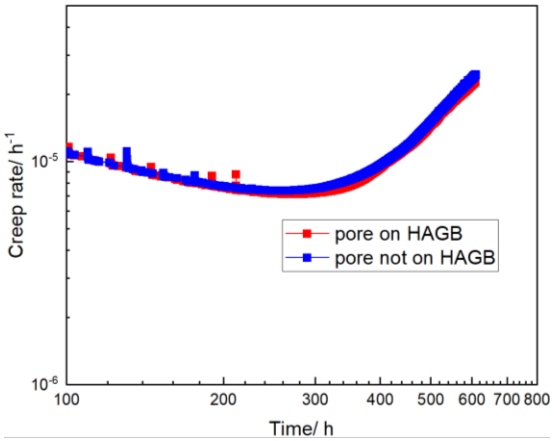

(c)

Figure 6. 10 Simulation results of AM-V-area #3-150 MPa, (a) comparison of the creep behaviour between the microstructure without pore and with pore, which is on and not on the HAGB respectively; (b) magnified comparison of creep behaviour between the microstructure without pore and with pore on HAGB; (c) magnified comparison of creep behaviour between the pore on HAGB and not on HAGB. (AM-V: vertically built additive manufacturing sample)

6.3.2 Lack of fusion

The lack of fusion-type pores can happen both horizontally and vertically spanning between two contiguous layers. The dimensions of lack of fusion-type pores may vary irregularly, typically ranging from 15 to 600 μm. In addition, the irregular dimensions resultant sharp edges can cause great stress concentration, which potentially acts as the pre-cracking point. In this section, a lack of fusion type pore is put in both AM-H-area#3 with loading 119 MPa and AM-V-area#3 with loading 150 MPa to simulate the corresponding materials structure behaviour. The size of inserted pore accounts for 768 μm^2, with a long axis around 58 μm.

Figure 6. 11 and Figure 6. 12 show the comparison of simulation results without pore, with pore not on HAGB and with pore on HAGB, which are based on AM-H 119MPa and AM-V 150 MPa respectively. With a bigger pore size, the simulation results between no pore and with the pore not on HAGB have more difference compared to the gas entrapment-type pore investigation. However, there is also the same phenomenon in this case, that the mechanical behaviour of the materials with pores shows a lower creep rate compared to the materials without pores. The materials with pores on the

HAGB have even lower creep rates compared to the materials with pores that are not on the HAGB. This is not reasonable in the real case. As the existence of pores can weaken the mechanical behaviour of materials, therefore, there will be a higher creep rate which can be even higher if the pore is on the HAGB. The reasons for these abnormal simulation results can be the following: 1) The limitation of the current FE solver, FreeFem++, which is an open-source FE platform cannot deal with certain complicated situations. In this work, the pore as part of the whole material is also mapped with meshes and nodes with much lower stiffness compared to the rest of the material. This is not coherent with reality. 2) The current balance equation in FreeFEM++ code may be adjusted for such a case. 3) Bigger microstructure input area can be adapted to achieve a better prediction under a higher calculation speed. 4) A 3D microstructure is needed for a full understanding of materials' mechanical behaviour.

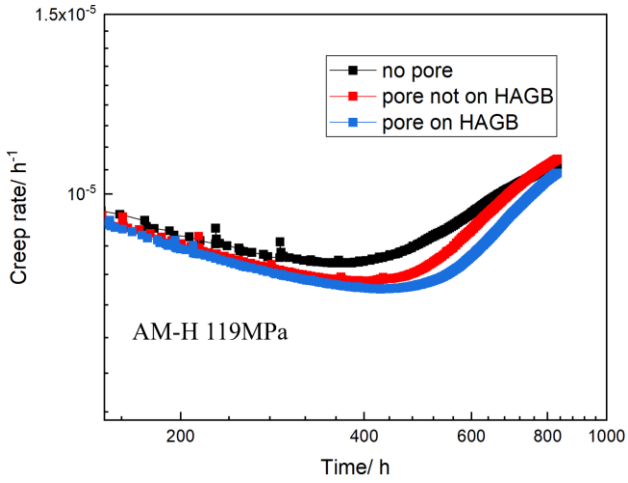

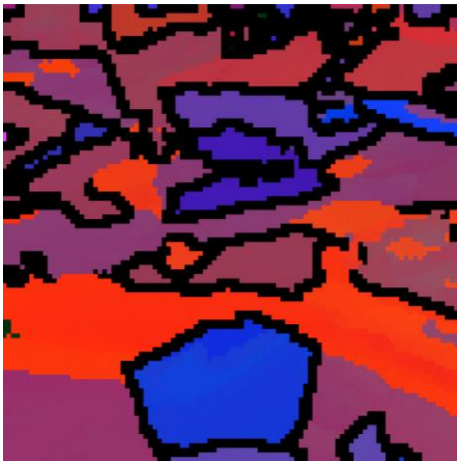

(a) (b)

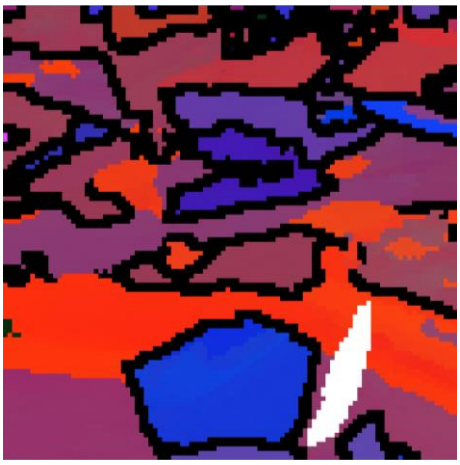

(c) (d)

Figure 6. 11 (a) simulation results of AM-H-area#3 with loading119 MPa comparison; (b) original input microstructure without pore; (c) the input microstructure with pore not on HAGBs; (d) the input microstructure with a pore on HAGBs.

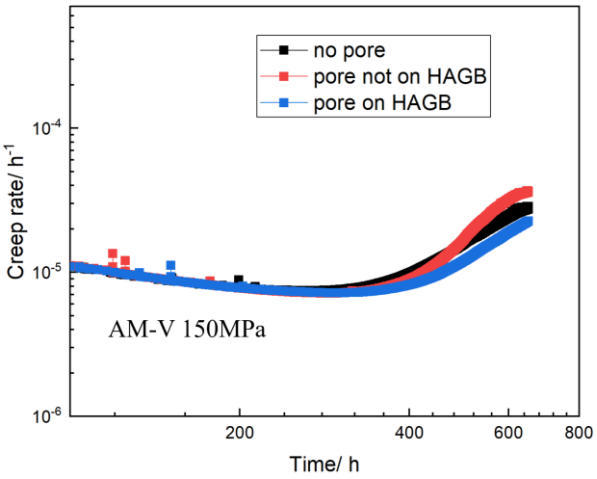

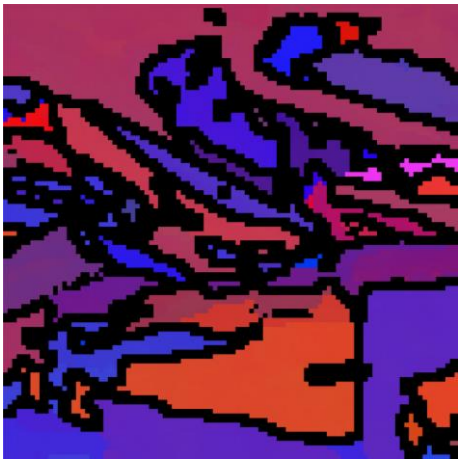

(a) (b)

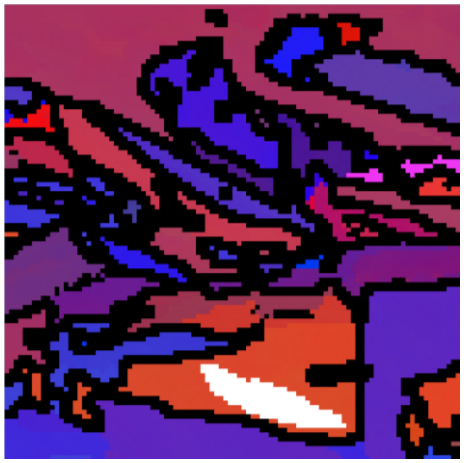

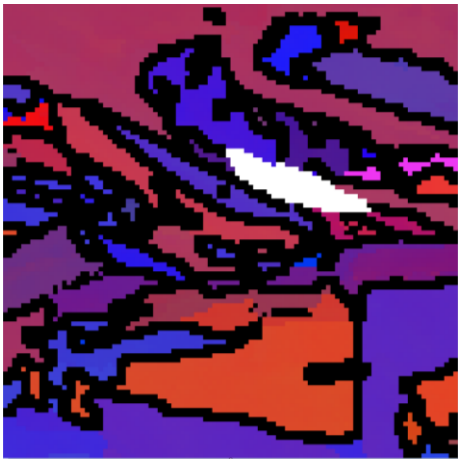

(c) (d)

Figure 6. 12 (a) simulation results of AM-V-area#3 with loading150 MPa comparison; (b) original input microstructure without pore; (c) the input microstructure with pore not on HAGBs; (d) the input microstructure with a pore on HAGBs.

6.4 Summary

The investigation of AM-characterised microstructures has been done in this chapter, including the elongated grains and AM-induced pores. The artificially generated microstructures with random textures are based on the Voronoi diagram principle. The elongated grain shape is achieved by introducing a bias. To study the relation between the orientation of HAGBs and damage behaviour, two orthogonal loading directions are applied to the input microstructures. The microstructures in finer grain sizes show a higher minimum creep rate, which is consistent with the conclusion in Chapter 4. Since there is a competition between the dislocation motion creep and grain boundary diffusional creep-Coble creep, the dislocation motion is getting harder with further creep deformation. Therefore, Coble creep is the dominant deformation mechanism. In addition, the Coble creep rate is related to the grain size, see equation (3. 23), the finer grain size can result in a higher Coble creep rate. In industrial applications, materials with better creep resistance are preferred. Therefore, materials with higher Coble creep rates should be avoided. However, the higher Coble creep rate is from finer grain structures, which are desired features in most scenarios. Hence, this study set a new principle for materials design under thermal creep service conditions, that finner grain structure is not always preferred.

According to the damage behaviour of different microstructure inputs, the relation between the orientation of HAGBs and damage evolution is further revealed, which is consistent with the conclusion from Chapter 5. When the external stress is loaded vertically onto the elongated grains, the material will show an obvious damage phenomenon. On the other hand, when most HAGBs are parallel to the loading direction, there is limited damage evolution can be found on the HAGBs. Therefore, the orientation of HAGBs is crucial in industrial applications which need to be considered.

As one of the AM-characterised defects, the effect of pore depends on its size, shape and relative location to HAGBs. The influence of gas entrapment-type pore, which is not on the HAGBs is negligible. However, due to a range of reasons listed in Section 6.3, the current CP-FEM framework conducted under the FreeFem++ platform has limited ability to process pores effect under FE. Therefore, there is a need for future research to improve the pores analysis strategy. An Abaqus code written in the UMAT

subroutine is currently under development to solve this problem. Ideally, the pore embedded in the whole structure can be processed more precisely. As such, a more comprehensive understanding of pores' effect on the mechanical behaviour of materials can be achieved.

In conclusion, the current CP-FEM simulations provide valuable insights into the creep behaviour of AM materials and highlight the importance of considering the effects of AM-induced grain structure accurately. The results also emphasize the need to design the printing strategy based on specific service conditions to improve the service life of the structure. The meaning of this work is to offer feedback on the materials design and boost the AM process strategy optimisation.

Chapter 7 Conclusion and future work

This chapter serves as the conclusive section of the research project and consists of four distinct segments: Section 7.1 presents a concise summary of this research work and also highlights the principal innovations and contributions of this research project. Section 7.2 expounds on the constraints of the current work presented in this dissertation. Section 7.3 outlines potential avenues to expand this study based on the proposed framework and limitations. Finally, Section 7.4 furnishes the definitive conclusions derived from the research project.

7.1 Concluding remarks

This thesis is focused on the development of a crystal plasticity (CP) based model to capture additive manufacturing (AM) materials' thermal creep performance under various loading conditions. The micro-mechanisms and AM-characterised microstructures are studied in detail via both visco-plasticity self-consistent (VPSC) and crystal plasticity finite element method (CP-FEM) frameworks. The AM 316L SS is used as the targeted material, meanwhile, wrought 316L SS is employed under the unified model for simulation calibration.

The physics-based CP model proposed in this work reproduced the thermal creep behaviour of both wrought and AM materials, during which, the contributions from each micro-mechanisms to the final mechanical behaviour are quantified. The competition between different creep mechanisms is evaluated. The dislocation hardening, precipitation hardening, solid solution hardening, and lattice fraction are considered in this model to account for the critical resolved shear stress (CRSS). The interaction between dislocation and the obstacles is described via mechanism-based formulation with physics meaning. The information on precipitation evolution under the creep environment is simulated through thermokinetic calculations. The corresponding dislocation evolution during the creep deformation is also considered, including dislocation generation and annihilation. This physics-based hardening model is temperature-, stress- and energy-related, which is also dependent on diffusion. Therefore, the classic Gurson-Tvergaard-Needleman (GTN) damage model is employed and embedded in the CP model, which is based on vacancy diffusion. In addition, as a ductile material, the damage evolution of 316L SS is limited on the high angle grain boundaries (HAGBs), which is consistent with the dominant diffusional creep, Coble creep, which occurs during the creep deformation in this work. The dynamic void nucleation, growth and coalescence are fully described considering creep behaviour. Overall, the proposed CP model combined damage model can reproduce the materials' creep deformation with a relatively full physics meaning considering the most micro-mechanisms. The description of the mechanical behaviour of materials is with relatively high fidelity.

The model training was performed under the mean-field VPSC framework, after which, the damage model is adapted under the full-field CP-FEM framework to capture the full creep curves. The detailed microstructural evolution is visualised from CP-FEM simulation results via ParaView. The dynamic stress and strain distribution, and damage localisation are presented directedly on the microstructure input. According to the physical description of AM materials' mechanical behaviour and the corresponding simulation results, the conclusion drawn from this work can offer meaningful feedback to materials design and boost the AM printing strategy optimisations. The main conclusions of this work are as follows:

1. The Coble creep mechanisms have a crucial role to play in the creep behaviour of AM materials. The heightened activity of Coble creep, attributed to the elevated density of HAGBs, results in a relatively insignificant primary creep behaviour and lower strain rate sensitivity in AM materials in comparison to wrought counterparts.

2. The primary disparity between wrought and AM materials regarding the total CRSS is attributed to dislocation hardening. The exceptionally high cooling rate during the AM process engenders localized thermal inhomogeneity, which introduces a substantial quantity of mobile and immobile dislocations.

3. The HAGBs are vertical to the loading direction showing a faster damage evolution and more obvious damage behaviour. Real service conditions necessitate consideration of loading directions relative to the AM building direction since the grain orientation is highly related to the AM building direction.

4. The creep phenomenon manifests a diverse array of material characteristics. The extant model comprehensively delineates the mechanical properties of the material by incorporating a majority of the factors contributing to CRSS. This model provides a foundation for material design, elucidating the aspects that necessitate critical consideration.

7.2 Limitations

Although this study holds significance and novel contributions, the present methodology and author's endeavours entail certain restrictions. This segment elucidates some of the overarching limitations of this research work.

In commercial alloys, such as 316L SS, the presence of a large number of solutes, which can exceed 10 alloying elements, is known to impede vacancy/interstitial diffusion and hinder the dislocation climb mechanism. The mechanism involved in this process is intricate and, to our current understanding, has not been investigated thoroughly via small-scale simulations or experimental techniques. Additionally, the impact of obstacles, including other dislocations and precipitates, on dislocation climb remains unclear. As a result, the precise quantification of the effect of dislocation climb is not feasible, and thus, it has not been considered in this study. However, dislocation climb

is also one of the deformation mechanisms, which accounts for the final mechanical behaviour of materials. Therefore, the absence of dislocation climb in the current model can limit the simulation accuracy.

Since the Thermo-Calc cannot consider the precipitation evolution with loading. Therefore, the effect of strain energy is not included in the thermokinetic calculations of precipitation evolution, which can potentially accelerate the precipitation.

Moreover, although the experimental data used for AM materials simulation validation is obtained from normally produced AM 316L SS with optimised printing parameters. It is not suitable for the extreme conditions, e.g. the AM 316L SS produced using extreme printing strategies. The simulation results obtained for AM materials in this work can only give a general capture of the creep behaviour of AM 316L SS.

The limitation of current computational speed constraints the area of input microstructures. The restricted input size cannot cover all the microstructure features of targeted materials. Therefore, there is a need for higher computational ability, which could be high performance computing (HPC). Moreover, a better FE solver can be employed to achieve a more precise calculation of the mechanical behaviour of materials with pores. The combination of HPC and the advanced FE solver would allow the simulation of 3D materials with more complex geometries. All the simulations in the current work under the CP-FEM framework are based on the 2D materials input, which has two pixels for thickness. The limitation of the materials' geometry consideration can limit the ability to fully evaluate the material performance.

7.4 Future work

Drawing upon the constraints outlined in Section 7.3, this section suggests potential avenues for future research aimed at broadening the scope of this project.

Firstly, since it is complicated to consider the dislocation climb in 316L SS, the designed atomic-scale experiments can help with understanding this complex process. The interaction between solid solution atoms and vacancy can be revealed under specific creep conditions, therefore, a more accurate description of deformation behaviour can be achieved.

Secondly, the limitation of thermokinetic calculations via Thermo-Calc can be overcome by the experimental method as well. The development of models and the corresponding model validation are based on the existing experimental data. The experimental results are crucial for revealing the real phenomenon. Therefore, the real precipitation evolution capture can be achieved through in-situ experiments, considering creep conditions.

Finally, a new Abaqus version of this model is under development, which is written in the UMAT subroutine. This commercial FE platform can allow more advanced FE analysis (FEA) with customised pores. But it is not part of this project. This version of the code can be performed on HPC to achieve a faster calculation speed. Since electron backscatter diffraction (EBSD) data can only present the surface of targeted materials. Therefore, the micro-computerised tomography (Micro-CT) technique is needed to capture information about 3D materials. The detected materials information can be the input for the Abaqus version code to achieve a faster calculation on the understanding of the whole material.

Apart from the potential work based on the discussion of the limitations of this project. There is other future research that can be planned dependent on the existing work.

The model developed in this project is aiming to simulate the thermal creep behaviour of materials. However, 316L SS is also serving as structural materials in nuclear industries. The irradiation effect can be introduced in the current model to achieve the ability to simulate the mechanical behaviour of materials under the nuclear environment. Currently, most mechanical models for industrial structural integrity analysis (SIA) are empirical in nature, based on the interpolation of experimental data obtained within certain stress, irradiation dose and temperature intervals. However, through the micromechanism-dependent modelling framework, the time-dependent microstructure evolution and the resulting material behaviour can be tracked (modelled) precisely. The corresponding deformation mechanisms (dislocation slip, climb and swelling) can be well captured. The dislocation interaction, solid solution effect (irradiation-induced segregation), precipitation, void evolution and self-interstitial atom defects will be considered in the development of the hierarchical multi-scale (HMS) framework. The model development will mainly focus on thermal- and irradiation-resistant alloys but

will account for other first-wall materials (e.g. tungsten and ceramics) in FEA to achieve a comprehensive SIA. Due to the discrepancy in material properties, the thermal expansion and the resulting contact between layers (interfaces) may lead to early failure of the materials, especially at the tungsten tail screwing location (Patra and Tomé, 2017). Therefore, an in-depth understanding of the interfacial behaviour is crucial to predict the service life of the first wall structure and ensure safety. To achieve this purpose, a range of properties will be considered in physics-based models, including magnetism, electrical/thermal conductivity, thermal efficiency, and radiation resistance. Through a systematic analysis of the microstructure-property relationship, the design of new materials systems can be achieved with enhanced properties to withstand the nuclear service conditions.

Since the crystal plasticity theory is applicable under a temperature which is below the material melting temperature. Therefore, apart from the simulation of creep deformation behaviour, a new thermal model can be developed to capture the material's internal stress-strain response once it is solidified from AM process. As such, the residual stress resultant from the AM process can be quantified and the corresponding effects on the mechanical properties of materials can be evaluated.

As for systematic optimisation of AM printing strategies, a database can be established based on various simulations. Based on different AM materials features resulting from different AM printing parameters, the deformation behaviour simulation can be done under various conditions. Therefore, a dataset will be built to link the printing parameters and the corresponding mechanical properties, through which, the targeted materials design in AM can be achieved.

In addition, based on the current Voronoi diagram-generated grain structure input, the grain structure with uneven grain size and shape distribution can be built to reproduce the grain morphology around the melting pool in the as-built AM materials, which is shown in Figure 7. 1. Between each layer of the melting pools, there are relatively finer grains decorating around the elongated grains.

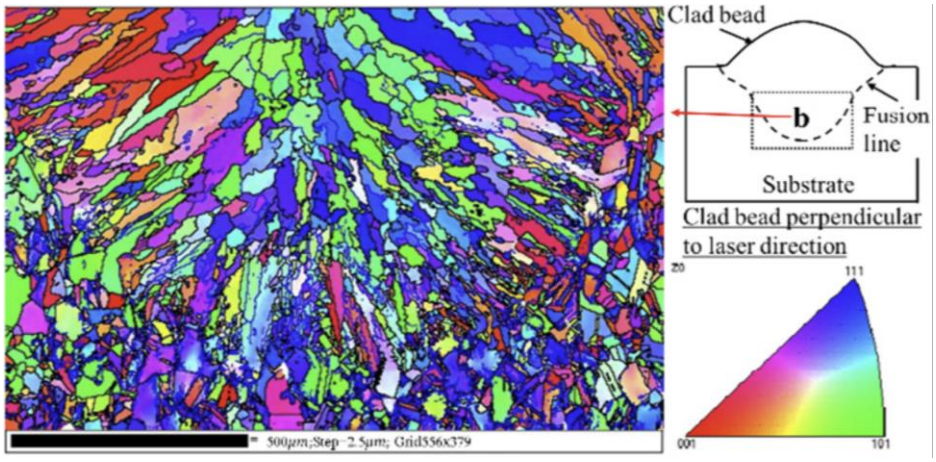

Figure 7. 1 The cross-section along the building direction EBSD figure of as-built AM IN718 (Song et al., 2018).

7.5 Conclusions

Whilst experimental work may unveil authentic phenomena and furnish empirical data, it remains infeasible to quantify the contribution of each micro-mechanism through such means. However, a mechanism-based formulation presents the prospect of quantifying the deformation mechanisms, thereby enhancing the design of the material. In addition, the creep experiments are normally time- and cost-consuming, with design temperature and loading. It is unrealistic to do experiments to cover all the possible creep environments with various materials. The simulation method can not only achieve large time-scale prediction but also can extrapolate the existing experimental results, during which, the potential deformation mechanisms can be revealed.

When materials are under specific loading conditions, there is a range of mico-mechanisms that occur simultaneously, which are highly related to the detailed microstructures of the targeted materials. Both these micro-mechanisms and microstructure features are either on micro-scale or nano-scale and processing-related. Their characteristics can account for the final mechanical behaviour of materials, which can be also called materials performance. HMS modelling is a good connection to bridge the materials features on the micro- or nano-scale with the final bulk-scale materials properties. Through this process, we can have a better understanding of processing-structure-property-performance (PSPP) relationships. The materials modelling requires both high accuracy and efficiency. Based on CP theory, the HMS

modelling framework can offer a precise description of mechanical response considering the real microstructural features with relatively low computational cost. The relative micro-mechanisms and damage behaviour are evaluated through the modelling work, which can give feedback to both material and process designs.

References

Aggarangsi, P., Beuth, J.L., 2006. Localized preheating approaches for reducing residual stress in additive manufacturing, 2006 International Solid Freeform Fabrication Symposium.

Ahmadi, M.R., Sonderegger, B., Yadav, S.D., Poletti, M.C., 2018. Modelling and simulation of diffusion driven pore formation in martensitic steels during creep. Materials Science and Engineering: A 712, 466-477.

Ahzi, S., M'Guil, S., 2008. A new intermediate model for polycrystalline viscoplastic deformation and texture evolution. Acta Materialia 56, 5359-5369.

Alcalá, J., Esqué-de los Ojos, D., Očenášek, J., 2015. Extracting uniaxial responses of single crystals from sharp and spherical hardness measurements. Mechanics of Materials 84, 100-113.

Ali, H., Ma, L., Ghadbeigi, H., Mumtaz, K., 2017. In-situ residual stress reduction, martensitic decomposition and mechanical properties enhancement through high temperature powder bed pre-heating of Selective Laser Melted Ti6Al4V. Materials Science and Engineering: A 695, 211-220.

Amelirad, O., Assempour, A., 2022. Coupled continuum damage mechanics and crystal plasticity model and its application in damage evolution in polycrystalline aggregates. Engineering with Computers 38, 2121-2135.

Anand, L., 2004. Single-crystal elasto-viscoplasticity: application to texture evolution in polycrystalline metals at large strains. Computer methods in applied mechanics and engineering 193, 5359-5383.

Anderson, P.M., Hirth, J.P., Lothe, J., 2017. Theory of dislocations. Cambridge University Press.

Andersson, J.-O., Helander, T., Höglund, L., Shi, P., Sundman, B., 2002. Thermo-Calc & DICTRA, computational tools for materials science. Calphad 26, 273-312.

Armstrong, R., Codd, I., Douthwaite, R., Petch, N., 1962. The plastic deformation of polycrystalline aggregates. The Philosophical Magazine: A Journal of Theoretical Experimental and Applied Physics 7, 45-58.

Asaro, R.J., Needleman, A., 1985. Overview no. 42 texture development and strain hardening in rate dependent polycrystals. Acta metallurgica 33, 923-953.

Asaro, R.J., Rice, J., 1977. Strain localization in ductile single crystals. Journal of the Mechanics and Physics of Solids 25, 309-338.

Asghary, Z., Abbasi, S., Seifollahi, M., Morakabati, M., 2019. Boron effect on phase transformation of σ and M23C6 in nimonic 105 superalloy. Materials Research Express 6, 116529.

Ashby, M.F., 1972. A first report on deformation-mechanism maps. Acta Metallurgica 20, 887-897.

Athul, K.R., Pillai, U.T.S., Srinivasan, A., Pai, B.C., 2016. A review of different creep mechanisms in Mg alloys based on stress exponent and activation energy. Advanced Engineering Materials 18, 770-794.

Austin, R.A., McDowell, D.L., 2011. A dislocation-based constitutive model for viscoplastic deformation of fcc metals at very high strain rates. Int. J. Plast. 27, 1-24.

Ávila Calderón, L.A., Rehmer, B., Schriever, S., Ulbricht, A., Agudo Jácome, L., Sommer, K., Mohr, G., Skrotzki, B., Evans, A., 2022. Creep and creep damage behavior of stainless steel 316L manufactured by laser powder bed fusion. Materials Science and Engineering: A 830, 142223.

Bae, J.H., Yu, J.M., Dao, V.H., Lok, V., Yoon, K.B., 2021. Effects of processing parameters on creep behavior of 316L stainless steel produced using selective laser melting. Journal of Mechanical Science and Technology 35, 3803-3812.

Bakó, B., Clouet, E., Dupuy, L.M., Blétry, M., 2011. Dislocation dynamics simulations with climb: kinetics of dislocation loop coarsening controlled by bulk diffusion. Philosophical Magazine 91, 3173-3191.

Balit, Y., Charkaluk, E., Constantinescu, A., 2020. Digital image correlation for microstructural analysis of deformation pattern in additively manufactured 316L thin walls. Additive Manufacturing 31, 100862.

Bammann, D., Aifantis, E., 1989. A damage model for ductile metals. Nuclear engineering and design 116, 355-362.

Basirat, M., Shrestha, T., Potirniche, G.P., Charit, I., Rink, K., 2012. A study of the creep behavior of modified 9Cr–1Mo steel using continuum-damage modeling. Int. J. Plast. 37, 95-107.

Bejan, A., Kraus, A.D., 2003. Heat transfer handbook. John Wiley & Sons.

Bertin, N., Tomé, C., Beyerlein, I., Barnett, M., Capolungo, L., 2014a. On the strength of dislocation interactions and their effect on latent hardening in pure Magnesium. International Journal of Plasticity 62, 72-92.

Bertin, N., Tomé, C., Beyerlein, I.J., Barnett, M.R., Capolungo, L., 2014b. On the strength of dislocation interactions and their effect on latent hardening in pure Magnesium. Int. J. Plast. 62.

Berveiller, M., Zaoui, A., 1978. An extension of the self-consistent scheme to plastically-flowing polycrystals. Journal of the Mechanics and Physics of Solids 26, 325-344.

Beyerlein, I., Tomé, C., 2008. A dislocation-based constitutive law for pure Zr including temperature effects. International Journal of Plasticity 24, 867-895.

Beyerlein, I.J., Mara, N.A., Bhattacharyya, D., Alexander, D.J., Necker, C.T., 2011. Texture evolution via combined slip and deformation twinning in rolled silver–copper cast eutectic nanocomposite. International journal of plasticity 27, 121-146.

Beyerlein, I.J., Zhang, X., Misra, A., 2014. Growth Twins and Deformation Twins in Metals. Annual Review of Materials Research 44, 329-363.

Bieberdorf, N., Tallman, A., Kumar, M.A., Taupin, V., Lebensohn, R.A., Capolungo, L., 2021. A mechanistic model for creep lifetime of ferritic steels: Application to Grade 91. International Journal of Plasticity 147, 103086.

Biswas, A., Prasad, M.R., Vajragupta, N., ul Hassan, H., Brenne, F., Niendorf, T., Hartmaier, A., 2019. Influence of microstructural features on the strain hardening behavior of additively manufactured metallic components. Advanced Engineering Materials 21, 1900275.

Blum, W., Eisenlohr, P., Breutinger, F., 2002. Understanding creep—a review. Metallurgical and Materials Transactions A 33, 291-303.

Borodachenkova, M., Barlat, F., Wen, W., Bastos, A., Grácio, J.J., 2015. A microstructure-based model for describing the material properties of Al–Zn alloys during high pressure torsion. Int. J. Plast. 68, 150-163.

Böttger, B., Apel, M., Santillana, B., Eskin, D., 2013. Relationship between solidification microstructure and hot cracking susceptibility for continuous casting of low-carbon and high-strength low-alloyed steels: a phase-field study. Metallurgical and Materials Transactions A 44, 3765-3777.

Brenner, R., Lebensohn, R., Castelnau, O., 2009. Elastic anisotropy and yield surface estimates of polycrystals. International Journal of Solids and Structures 46, 3018-3026.

Budiansky, B., Hutchinson, J., Slutsky, S., 1982. Void growth and collapse in viscous solids, Mechanics of solids. Elsevier, pp. 13-45.

Burgers, J., 1939. Internal strains in solids. Proc. Acad. Science 42, 293.

Cabanas, N., Penning, J., Akdut, N., De Cooman, B., 2006. High-temperature deformation properties of austenitic Fe-Mn alloys. Metallurgical and Materials Transactions A 37, 3305-3315.

Cai, W., Nix, W.D., 2016. Imperfections in crystalline solids. Cambridge University Press.

Caillard, D., Martin, J.-L., 2003. Thermally activated mechanisms in crystal plasticity. Elsevier.

Calderón, L.Á., Rehmer, B., Schriever, S., Ulbricht, A., Jácome, L.A., Sommer, K., Mohr, G., Skrotzki, B., Evans, A., 2022. Creep and creep damage behavior of stainless steel 316L manufactured by laser powder bed fusion. Materials Science and Engineering: A 830, 142223.

Carlton, H.D., Haboub, A., Gallegos, G.F., Parkinson, D.Y., MacDowell, A.A., 2016. Damage evolution and failure mechanisms in additively manufactured stainless steel. Materials Science and Engineering: A 651, 406-414.

Carsí, M., Allende, R., Peñalba, F., Jiménez, J., Ruano, O., 2004. Simulation of the forming behaviour of a boron modified P91 ferritic steel. steel research international 75, 26-32.

Cazacu, O., Revil-Baudard, B., Chandola, N., 2019. Plasticity-damage couplings: from single crystal to polycrystalline materials. Springer.

Charit, I., Murty, K.L., 2008. Creep behavior of niobium-modified zirconium alloys. Journal of Nuclear Materials 374, 354-363.

Chen, S.-g., Gao, H.-j., Zhang, Y.-d., Wu, Q., Gao, Z.-h., Zhou, X., 2022. Review on residual stresses in metal additive manufacturing: formation mechanisms, parameter dependencies, prediction and control approaches. Journal of Materials Research and Technology 17, 2950-2974.

Cherry, J., Davies, H., Mehmood, S., Lavery, N., Brown, S., Sienz, J., 2015. Investigation into the effect of process parameters on microstructural and physical properties of 316L stainless steel parts by selective laser melting. The International Journal of Advanced Manufacturing Technology 76, 869-879.

Cho, Y., Gwon, H., Kim, S.-J., 2021. Effects of C and N on high-temperature deformation behavior of 15Cr–15Mn–4Ni austenitic stainless steels. Materials Science and Engineering: A 819, 141463.

Choo, H., Sham, K.-L., Bohling, J., Ngo, A., Xiao, X., Ren, Y., Depond, P.J., Matthews, M.J., Garlea, E., 2019. Effect of laser power on defect, texture, and microstructure of a laser powder bed fusion processed 316L stainless steel. Materials & Design 164, 107534.

Christian, J.W., Mahajan, S., 1995. Deformation twinning. Progress in materials science 39, 1-157.

Christodoulou, P.G., Dancette, S., Lebensohn, R.A., Maire, E., Beyerlein, I.J., 2021. Role of crystallographic orientation on intragranular void growth in polycrystalline FCC materials. Int. J. Plast. 147, 103104.

Chu, C., Needleman, A., 1980. Void nucleation effects in biaxially stretched sheets. ASME. J. Eng. Mater. Technol. July 1980; 102(3): 249–256.

Chu, K., Foster, M.E., Sills, R.B., Zhou, X., Zhu, T., McDowell, D.L., 2020. Temperature and composition dependent screw dislocation mobility in austenitic stainless steels from large-scale molecular dynamics. npj Comput. Mater. 6, 179.

Chuang, T.-J., Kagawa, K.I., Rice, J.R., Sills, L.B., 1979. Overview no. 2: Non-equilibrium models for diffusive cavitation of grain interfaces. Acta Metall. 27, 265-284.

Ciraud, L., 1973. A method and apparatus for making any belongings from any fusible material. German patent application DE 19722263777A1.

Coble, R., 1963. A model for boundary diffusion controlled creep in polycrystalline materials. J. Appl. Phys. 34, 1679-1682.

Cocks, A., 1996. Variational principles, numerical schemes and bounding theorems for deformation by Nabarro-Herring creep. Journal of the Mechanics and Physics of Solids 44, 1429-1452.

Cottrell, A.H., Bilby, B.A., 1949. Dislocation theory of yielding and strain ageing of iron. Proc. Phys. Soc. London, Sect. A 62, 49.

Courtney, T.H., 2005. Mechanical behavior of materials. Waveland Press.

Crumbach, M., Goerdeler, M., Gottstein, G., 2006. Modelling of recrystallisation textures in aluminium alloys: I. Model set-up and integration. Acta Materialia 54, 3275-3289.

Cunningham, R., Narra, S.P., Montgomery, C., Beuth, J., Rollett, A., 2017. Synchrotron-based X-ray microtomography characterization of the effect of processing variables on porosity formation in laser power-bed additive manufacturing of Ti-6Al-4V. Jom 69, 479-484.

Curtin, W.A., Olmsted, D.L., Hector, L.G., 2006. A predictive mechanism for dynamic strain ageing in aluminium–magnesium alloys. Nat. Mater. 5, 875-880.

Daly, M., Burnett, T.L., Pickering, E.J., Tuck, O.C.G., Léonard, F., Kelley, R., Withers, P.J., Sherry, A.H., 2017. A multi-scale correlative investigation of ductile fracture. Acta Materialia 130, 56-68.

Dani Feri, C.t., 2011. File:Point defects in crystal structures DE.svg.

Delannay, L., Melchior, M., Signorelli, J., Remacle, J.-F., Kuwabara, T., 2009. Influence of grain shape on the planar anisotropy of rolled steel sheets–evaluation of three models. Computational materials science 45, 739-743.

Dieter, G.E., Bacon, D., 1976. Mechanical metallurgy. McGraw-hill New York.

Ding, Q., Fu, X., Chen, D., Bei, H., Gludovatz, B., Li, J., Zhang, Z., George, E.P., Yu, Q., Zhu, T., 2019. Real-time nanoscale observation of deformation mechanisms in CrCoNi-based medium-to high-entropy alloys at cryogenic temperatures. Materials Today 25, 21-27.

Dwivedi, S., Rai Dixit, A., Kumar Das, A., 2022. Wetting behavior of selective laser melted (SLM) bio-medical grade stainless steel 316L. Materials Today: Proceedings 56, 46-50.

Eisenlohr, P., Diehl, M., Lebensohn, R.A., Roters, F., 2013. A spectral method solution to crystal elasto-viscoplasticity at finite strains. International Journal of Plasticity 46, 37-53.

El Shawish, S., Vincent, P.-G., Moulinec, H., Cizelj, L., Gélébart, L., 2020. Full-field polycrystal plasticity simulations of neutron-irradiated austenitic stainless steel: a comparison between FE and FFT-based approaches. Journal of Nuclear Materials 529, 151927.

Engler, O., Crumbach, M., Li, S., 2005. Alloy-dependent rolling texture simulation of aluminium alloys with a grain-interaction model. Acta materialia 53, 2241-2257.

Eskandari Sabzi, H., 2022. Alloy and microstructure design for additive manufacturing. Lancaster University.

Eskandari Sabzi, H., Rivera-Díaz-del-Castillo, P.E., 2019. Defect prevention in selective laser melting components: Compositional and process effects. Materials 12, 3791.

Essmann, U., Mughrabi, H., 1979. Annihilation of dislocations during tensile and cyclic deformation and limits of dislocation densities. Philosophical Magazine A 40, 731-756.

Estrin, Y., 1998a. Dislocation theory based constitutive modelling: foundations and applications. J. Mater. Process. Technol. 80-81, 33-39.

Estrin, Y., 1998b. Dislocation theory based constitutive modelling: foundations and applications. Journal of Materials Processing Technology 80, 33-39.

Fang, Q., Lu, W., Chen, Y., Feng, H., Liaw, P.K., Li, J., 2022. Hierarchical multiscale crystal plasticity framework for plasticity and strain hardening of multi-principal element alloys. Journal of the Mechanics and Physics of Solids 169, 105067.

Farhat, H., 2021. Chapter 8 - Lifetime extension: Assessment and considerations, in: Farhat, H. (Ed.), Operation, Maintenance, and Repair of Land-Based Gas Turbines. Elsevier, pp. 175-196.

Feng, Y., Liu, M., Shi, Y., Ma, H., Li, D., Li, Y., Lu, L., Chen, X., 2019. High-throughput modeling of atomic diffusion migration energy barrier of fcc metals. Progress in Natural Science: Materials International 29, 341-348.

Foiles, S., Baskes, M., Daw, M.S., 1986. Embedded-atom-method functions for the fcc metals Cu, Ag, Au, Ni, Pd, Pt, and their alloys. Physical review B 33, 7983.

Franciosi, P., Zaoui, A., 1982. Multislip in f.c.c. crystals a theoretical approach compared with experimental data. Acta Metall. 30, 1627-1637.

Frank, F.C., Read, W.T., 1950. Multiplication Processes for Slow Moving Dislocations. Physical Review 79, 722-723.

Frewin, M., Scott, D., 1999. Finite element model of pulsed laser welding. Welding Journal-New York- 78, 15-s.

Furstoss, J., Petit, C., Ganino, C., Bernacki, M., Pino-Muñoz, D., 2021a. A new finite element approach to model microscale strain localization within olivine aggregates. Solid Earth 12, 2369-2385.

Furstoss, J., Ruiz Sarrazola, D.A., Bernacki, M., Pino Muñoz, D., 2021b. Handling tensors using tensorial Kelvin bases: application to olivine polycrystal deformation modeling using elastically anistropic CPFEM. Computational Mechanics 67, 955-967.

Gaffard, V., Besson, J., Gourgues-Lorenzon, A.-F., 2005. Creep failure model of a tempered martensitic stainless steel integrating multiple deformation and damage mechanisms. Int. J. Fract. 133, 139-166.

Ganeriwala, R., Zohdi, T.I., 2014. Multiphysics modeling and simulation of selective laser sintering manufacturing processes. Procedia Cirp 14, 299-304.

Gasson, P.C., 2008. The Superalloys: Fundamentals and Applications RC Reed Cambridge University Press, The Edinburgh Building, Shaftesbury Road, Cambridge, CB2 2RU, UK, 2006. 372pp. Illustrated.£ 80. ISBN 0-521-85904-2. The Aeronautical Journal 112, 291-291.

Gates, R.S., Horton, C.A.P., 1977. Grain boundary sliding in type 316 austenitic steels, part I the grain size dependence. Materials Science and Engineering 27, 105-114.

Geers, M., Cottura, M., Appolaire, B., Busso, E.P., Forest, S., Villani, A., 2014. Coupled glide-climb diffusion-enhanced crystal plasticity. Journal of the Mechanics and Physics of Solids 70, 136-153.

Ghaoui, S., Ledoux, Y., Vignat, F., Museau, M., Vo, T.H., Villeneuve, F., Ballu, A., 2020. Analysis of geometrical defects in overhang fabrications in electron beam melting based on thermomechanical simulations and experimental validations. Additive Manufacturing 36, 101557.

Ghorbani Moghaddam, M., Achuthan, A., Bednarcyk, B.A., Arnold, S.M., Pineda, E.J., 2017. Grain size-dependent crystal plasticity constitutive model for polycrystal materials. Materials Science and Engineering: A 703, 521-532.

Ghosh, A., Brokmeier, H.-G., Gurao, N.P., 2019. Orientation-dependent deformation micro-mechanism and failure analysis of SS 316 under tensile and cyclic load. Int. J. Fatigue 125, 35-46.

Gjostein, N., 1972. Short circuit diffusion, " Diffusion", Papers Presented at a Seminar of the American Society for Metals, 1972. American Society for Metals.

González-Velázquez, J.L., 2020a. Mechanical behavior and fracture of engineering materials. Springer.

González-Velázquez, J.L., 2020b. Strengthening Mechanisms, in: González-Velázquez, J.L. (Ed.), Mechanical Behavior and Fracture of Engineering Materials. Springer International Publishing, Cham, pp. 103-133.

Gorsse, S., Hutchinson, C., Gouné, M., Banerjee, R.J.S., MaTerialS, T.o.a., 2017. Additive manufacturing of metals: a brief review of the characteristic microstructures and properties of steels, Ti-6Al-4V and high-entropy alloys. Sci Technol Adv Mater. 2017 Aug 25;18(1):584-610.

Granato, A., Lücke, K., Schlipf, J., Teutonico, L., 1964. Entropy factors for thermally activated unpinning of dislocations. Journal of applied physics 35, 2732-2745.

Grilli, N., Cocks, A.C., Tarleton, E., 2020. Crystal plasticity finite element modelling of coarse-grained α-uranium. Computational Materials Science 171, 109276.

Groeber, M., Jackson, M., 2014. DREAM3d: a digital representation environment for the analysis of microstructure in 3d. Integr Mater Manuf Innov 3 (1): 56–72.

Groma, I., Bakó, B., 1998. Probability distribution of internal stresses in parallel straight dislocation systems. Physical Review B 58, 2969-2974.

Groma, I., Székely, F., 2000. Analysis of the asymptotic properties of X-ray line broadening caused by dislocations. J. Appl. Crystallogr. 33, 1329-1334.

Gromov, V., Ivanov, Y.F., Kormyshev, V., Rubannikova, Y.A., Kuznetsov, R., Peregudov, O., 2022. Physical nature of rails strengthening in extremely long-term operation, AIP Conference Proceedings. AIP Publishing LLC, p. 020082.

Gu, D., Shen, Y., 2009. Balling phenomena in direct laser sintering of stainless steel powder: Metallurgical mechanisms and control methods. Materials & Design 30, 2903-2910.

Gu, D.D., Meiners, W., Wissenbach, K., Poprawe, R., 2012. Laser additive manufacturing of metallic components: materials, processes and mechanisms. Int. Mater. Rev. 57, 133-164.

Gu, H., Wei, C., Li, L., Han, Q., Setchi, R., Ryan, M., Li, Q., 2020. Multi-physics modelling of molten pool development and track formation in multi-track, multi-layer and multi-material selective laser melting. International Journal of Heat and Mass Transfer 151, 119458.

Gu, Y., Xiang, Y., Quek, S.S., Srolovitz, D.J., 2015. Three-dimensional formulation of dislocation climb. Journal of the Mechanics and Physics of Solids 83, 319-337.

Guo, Z., Sha, W., 2002. Quantification of precipitation hardening and evolution of precipitates. Mater. Trans. 43, 1273-1282.

Gurson, A.L., 1977. Continuum theory of ductile rupture by void nucleation and growth: Part I—Yield criteria and flow rules for porous ductile media. ASME. J. Eng. Mater. Technol. January 1977; 99(1): 2–15.

Güvenç, O., Henke, T., Laschet, G., Böttger, B., Apel, M., Bambach, M., Hirt, G., 2013. Modeling of static recrystallization kinetics by coupling crystal plasticity FEM and multiphase field calculations. Comput Methods Mater Sci 13, 368-374.

Hadadzadeh, A., Amirkhiz, B.S., Li, J., Mohammadi, M., 2018. Columnar to equiaxed transition during direct metal laser sintering of AlSi10Mg alloy: effect of building direction. Addit. Manuf. 23, 121-131.

Haghdadi, N., Laleh, M., Moyle, M., Primig, S., 2020. Additive manufacturing of steels: a review of achievements and challenges. 1-44.

Hall, E., 1951. The deformation and ageing of mild steel: III discussion of results. Proceedings of the Physical Society. Section B 64, 747.

Hall, E.O., Algie, S.H., 1966. The Sigma Phase. Metallurgical Reviews 11, 61-88.

Hamza, H.M., Deen, K.M., Khaliq, A., Asselin, E., Haider, W., 2021. Microstructural, corrosion and mechanical properties of additively manufactured alloys: a review. Critical Reviews in Solid State and Materials Sciences, 1-53.

Hamza, H.M., Deen, K.M., Khaliq, A., Asselin, E., Haider, W., 2022. Microstructural, corrosion and mechanical properties of additively manufactured alloys: a review. Crit. Rev. Solid State Mater. Sci. 47, 46-98.

Härtel, M., Frint, P., Abstoss, K.G., Wagner, M.F.X., 2018. Effect of Creep and Aging on the Precipitation Kinetics of an Al–Cu Alloy after One Pass of ECAP. Adv. Eng. Mater. 20.

Hassan, W., Farid, M.A., Tosi, A., Rane, K., Strano, M., 2021. The effect of printing parameters on sintered properties of extrusion-based additively manufactured stainless steel 316L parts. The International Journal of Advanced Manufacturing Technology 114, 3057-3067.

Hecht, F., 2012. New development in FreeFem++. Journal of numerical mathematics 20, 251-266.

Herring, C., 1950. Diffusional viscosity of a polycrystalline solid. Journal of applied physics 21, 437-445.

Hershey, A., 1954. The elasticity of an isotropic aggregate of anisotropic cubic crystals. ASME. J. Appl. Mech. September 1954; 21(3): 236–240.

Herzog, D., Seyda, V., Wycisk, E., Emmelmann, C., 2016. Additive manufacturing of metals. Acta Material117, 371-392.

Hidalgo, J., Vittorietti, M., Farahani, H., Vercruysse, F., Petrov, R., Sietsma, J., 2020. Influence of M23C6 carbides on the heterogeneous strain development in annealed 420 stainless steel. Acta Material 200, 74-90.

Hill, R., 1965a. Continuum micro-mechanics of elastoplastic polycrystals. Journal of the Mechanics and Physics of Solids 13, 89-101.

Hill, R., 1965b. A self-consistent mechanics of composite materials. Journal of the Mechanics and Physics of Solids 13, 213-222.

Hirth, J.P., Lothe, J., Mura, T., 1983. Theory of dislocations. J. Appl. Mech. 50, 476.

Hocine, S., Van Swygenhoven, H., Van Petegem, S., Chang, C.S.T., Maimaitiyili, T., Tinti, G., Sanchez, D.F., Grolimund, D., Casati, N., 2020. Operando X-ray diffraction during laser 3D printing. Materials Today 34, 30-40.

Hollenberg, G., Terwilliger, G., Gordon, R.S., 1971. Calculation of stresses and strains in four‐point bending creep tests. Journal of the American Ceramic Society 54, 196-199.

Holt, D.L., 1970. Dislocation cell formation in metals. J. Appl. Phys. 41, 3197-3201.

Hong, Y., Zhou, C., Zheng, Y., Zhang, L., Zheng, J., 2021a. The cellular boundary with high density of dislocations governed the strengthening mechanism in selective laser melted 316L stainless steel. Materials Science and Engineering: A 799, 140279.

Hong, Y., Zhou, C., Zheng, Y., Zhang, L., Zheng, J., 2021b. The Room Temperature Creep of Selective Laser Melted 316L Stainless Steel Investigated by Nanoindentation. J. Mater. Eng. Perform. 30, 6502-6510.

Hosford, W., 2005. Mechanical Behavior of Materials. Cambridge University Press. Cambridge.

Huo, S.H., Qian, M., Schaffer, G.B., Crossin, E., 2011. 21 - Aluminium powder metallurgy, in: Lumley, R. (Ed.), Fundamentals of Aluminium Metallurgy. Woodhead Publishing, pp. 655-701.

Husain, A., La, P., Hongzheng, Y., Jie, S., 2020. Influence of temperature on mechanical properties of nanocrystalline 316L stainless steel investigated via molecular dynamics simulations. Materials 13, 2803.

Hutchinson, J., 1970. Elastic-plastic behaviour of polycrystalline metals and composites. Proceedings of the Royal Society of London. A. Mathematical and Physical Sciences 319, 247-272.

Hutchinson, J.W., 1976. Bounds and self-consistent estimates for creep of polycrystalline materials. Proceedings of the Royal Society of London. A. Mathematical and Physical Sciences 348, 101-127.

Hyer, H., Zhou, L., Mehta, A., Park, S., Huynh, T., Song, S., Bai, Y., Cho, K., McWilliams, B., Sohn, Y., 2021. Composition-dependent solidification cracking of aluminum-silicon alloys during laser powder bed fusion. Acta Materialia 208, 116698.

Jackson, A., 1991. Slip Systems, Handbook of crystallography: for electron microscopists and others. Springer, pp. 83-88.

Jiang, J., Xiong, Y., Zhang, Z., Rosen, D.W., 2022. Machine learning integrated design for additive manufacturing. Journal of Intelligent Manufacturing 33, 1073-1086.

Jin, T., Mourad, H.M., Bronkhorst, C.A., Beyerlein, I.J., 2019. A single crystal plasticity finite element formulation with embedded deformation twins. Journal of the Mechanics and Physics of Solids 133, 103723.

Johnson, G.R., Cook, W.H., 1985. Fracture characteristics of three metals subjected to various strains, strain rates, temperatures and pressures. Engineering fracture mechanics 21, 31-48.

Johnson, L., Mahmoudi, M., Zhang, B., Seede, R., Huang, X., Maier, J.T., Maier, H.J., Karaman, I., Elwany, A., Arróyave, R., 2019. Assessing printability maps in additive manufacturing of metal alloys. Acta Materialia 176, 199-210.

Jones, D.R.H., Ashby, M.F., 2019. Chapter 23 - Mechanisms of Creep, and Creep-Resistant Materials, in: Jones, D.R.H., Ashby, M.F. (Eds.), Engineering Materials 1 (Fifth Edition). Butterworth-Heinemann, pp. 381-394.

Kako, K., Kawakami, E., Ohta, J., Mayuzumi, M., 2002. Effects of Various Alloying Elements on Tensile Properties of High-Purity Fe-18Cr-(14-16)Ni Alloys at Room Temperature. Mater. Trans. 43, 155-162.

Kalácska, S., Groma, I., Borbély, A., Ispánovity, P.D., 2017. Comparison of the dislocation density obtained by HR-EBSD and X-ray profile analysis. Appl. Phys. Lett. 110, 091912.

Kalidindi, S.R., 1998. Incorporation of deformation twinning in crystal plasticity models. Journal of the Mechanics and Physics of Solids 46, 267-290.

Kalidindi, S.R., 2001. Modeling anisotropic strain hardening and deformation textures in low stacking fault energy fcc metals. International Journal of Plasticity 17, 837-860.

Kamath, C., El-Dasher, B., Gallegos, G.F., King, W.E., Sisto, A., 2014. Density of additively-manufactured, 316L SS parts using laser powder-bed fusion at powers up to 400 W. The International Journal of Advanced Manufacturing Technology 74, 65-78.

Kanjarla, A., Lebensohn, R., Balogh, L., Tomé, C., 2012. Study of internal lattice strain distributions in stainless steel using a full-field elasto-viscoplastic formulation based on fast Fourier transforms. Acta Materialia 60, 3094-3106.

Karaman, I., Sehitoglu, H., Maier, H.J., Chumlyakov, Y.I., 2001. Competing mechanisms and modeling of deformation in austenitic stainless steel single crystals with and without nitrogen. Acta Materialia 49, 3919-3933.

Keown, S.R., Pickering, F.B., 1974. Effect of niobium carbide on the creep-rupture properties of austenitic stainless steels. Metals Society, United Kingdom.

Khairallah, S.A., Anderson, A.T., Rubenchik, A., King, W.E., 2016a. Laser powder-bed fusion additive manufacturing: Physics of complex melt flow and formation mechanisms of pores, spatter, and denudation zones. Acta Material 108, 36-45.

Khan, A.S., Huang, S., 1995. Continuum theory of plasticity. John Wiley & Sons.

King, W.E., Barth, H.D., Castillo, V.M., Gallegos, G.F., Gibbs, J.W., Hahn, D.E., Kamath, C., Rubenchik, A.M., 2014. Observation of keyhole-mode laser melting in laser powder-bed fusion additive manufacturing. Journal of Materials Processing Technology 214, 2915-2925.

Klosek, V., 2017. Crystallographic textures. EPJ Web of Conferences 155, 00005.

Kocks, U., Argon, A., Ashby, M., 1975a. Models for macroscopic slip. Prog. Mater. Sci 19, 171-229.

Kocks, U., Mecking, H., 2003. Physics and phenomenology of strain hardening: the FCC case. Progress in materials science 48, 171-273.

Kocks, U.F., AS, A., MF, A., 1975b. Thermodynamics and kinetics of slip.

Kocks, U.F., UF, K., AS, A., MF, A., 1975c. Thermodynamics and kinetics of slip.

Kok, Y., Tan, X.P., Wang, P., Nai, M.L.S., Loh, N.H., Liu, E., Tor, S.B., 2018. Anisotropy and heterogeneity of microstructure and mechanical properties in metal additive manufacturing: A critical review. Mater. Des. 139, 565-586.

Kong, D., Dong, C., Ni, X., Zhang, L., Yao, J., Man, C., Cheng, X., Xiao, K., Li, X., 2019. Mechanical properties and corrosion behavior of selective laser melted 316L stainless steel after different heat treatment processes. Journal of Materials Science & Technology 35, 1499-1507.

Kröner, E., 1958. Kontinuumstheorie der versetzungen und eigenspannungen. Springer.

Kröner, E., 1959. Allgemeine kontinuumstheorie der versetzungen und eigenspannungen. Archive for Rational Mechanics and Analysis 4, 273-334.

Kröner, E., 1961. Zur plastischen verformung des vielkristalls. Acta metallurgica 9, 155-161.

Kröner, E., 1981. Continuum theory of defects. Physics of defects 35, 217-315.

Kruth, J.-P., Froyen, L., Van Vaerenbergh, J., Mercelis, P., Rombouts, M., Lauwers, B., 2004. Selective laser melting of iron-based powder. Journal of materials processing technology 149, 616-622.

Kruth, J.-P., Levy, G., Klocke, F., Childs, T., 2007. Consolidation phenomena in laser and powder-bed based layered manufacturing. CIRP annals 56, 730-759.

Kuhlmann-Wilsdorf, D., 1999. The theory of dislocation-based crystal plasticity. Philosophical Magazine A 79, 955-1008.

Kumar, M.A., Capolungo, L., 2022. Microstructure-sensitive modeling of high temperature creep in grade-91 alloy. Int. J. Plast. 158, 103411.

Kumar, R.S., Talreja, R., 2003. A continuum damage model for linear viscoelastic composite materials. Mechanics of Materials 35, 463-480.

La Fé-Perdomo, I., Ramos-Grez, J.A., Jeria, I., Guerra, C., Barrionuevo, G.O., 2022. Comparative analysis and experimental validation of statistical and machine learning-based regressors for modeling the surface roughness and mechanical properties of 316L stainless steel specimens produced by selective laser melting. Journal of Manufacturing Processes 80, 666-682.

Ladani, L., Romano, J., Brindley, W., Burlatsky, S., 2017. Effective liquid conductivity for improved simulation of thermal transport in laser beam melting powder bed technology. Additive Manufacturing 14, 13-23.

Laleh, M., Hughes, A.E., Xu, W., Haghdadi, N., Wang, K., Cizek, P., Gibson, I., Tan, M.Y., 2019. On the unusual intergranular corrosion resistance of 316L stainless steel additively manufactured by selective laser melting. Corros. Sci. 161, 108189.

Landau, L.D., Lifshi͡ts, E.M., 1960. Mechanics. CUP Archive.

Langdon, T.G., 1970. Grain boundary sliding as a deformation mechanism during creep. The Philosophical Magazine: A Journal of Theoretical Experimental and Applied Physics 22, 689-700.

Lebensohn, R., Solas, D., Canova, G., Brechet, Y., 1996. Modelling damage of Al Zn Mg alloys. Acta materialia 44, 315-325.

Lebensohn, R., Tomé, C., Castaneda, P.P., 2007. Self-consistent modelling of the mechanical behaviour of viscoplastic polycrystals incorporating intragranular field fluctuations. Philos. Mag. 87, 4287-4322.

Lebensohn, R., Tomé, C., Maudlin, P., 2004. A selfconsistent formulation for the prediction of the anisotropic behavior of viscoplastic polycrystals with voids. Journal of the Mechanics and Physics of Solids 52, 249-278.

Lebensohn, R.A., 2001. N-site modeling of a 3D viscoplastic polycrystal using fast Fourier transform. Acta materialia 49, 2723-2737.

Lebensohn, R.A., Hartley, C.S., Tomé, C.N., Castelnau, O., 2010. Modeling the mechanical response of polycrystals deforming by climb and glide. Philosophical Magazine 90, 567-583.

Lebensohn, R.A., Holt, R., Caro, A., Alankar, A., Tomé, C., 2012. Improved constitutive description of single crystal viscoplastic deformation by dislocation climb. Comptes Rendus Mecanique 340, 289-295.

Lebensohn, R.A., Tomé, C., 1993. A self-consistent anisotropic approach for the simulation of plastic deformation and texture development of polycrystals: application to zirconium alloys. Acta Metall. Mater. 41, 2611-2624.

Lee, B., Ahzi, S., Parks, D., 2002. Bicrystal-based modeling of plasticity in FCC metals. J. Eng. Mater. Technol. 124, 27-40.

Lee, B.J., Ahzi, S., Parks, D.M., 2001. Bicrystal-Based Modeling of Plasticity in FCC Metals. Journal of Engineering Materials and Technology 124, 27-40.

Lee, E., Liu, D., 1967. Finite-strain elastic—plastic theory with application to plane-wave analysis. Journal of applied physics 38, 19-27.

Lee, M.-G., Wang, J., Anderson, P.M., 2007. Texture evolution maps for upset deformation of body-centered cubic metals. Materials Science and Engineering: A 463, 263-270.

Leffers, T., Ray, R., 2009. The brass-type texture and its deviation from the copper-type texture. Progress in Materials Science 54, 351-396.

Lewis, M.H., Hattersley, B., 1965. Precipitation of M23C6 in austenitic steels. Acta Metallurgica 13, 1159-1168.

Leyson, G.P.M., Curtin, W.A., 2013. Friedel vs. Labusch: the strong/weak pinning transition in solute strengthened metals. Philos. Mag. 93, 2428-2444.

Leyson, G.P.M., Curtin, W.A., Hector, L.G., Woodward, C.F., 2010. Quantitative prediction of solute strengthening in aluminium alloys. Nat. Mater. 9, 750-755.

Li, G., Cui, S., 2020. A review on theory and application of plastic meso-damage mechanics. Theor. Appl. Fract. Mech. 109, 102686.

Li, J., Chen, H., Fang, Q., Jiang, C., Liu, Y., Liaw, P.K., 2020. Unraveling the dislocation–precipitate interactions in high-entropy alloys. International Journal of Plasticity 133, 102819.

Li, J., Fang, Q., Liu, B., Liu, Y., Liu, Y., 2016. Mechanical behaviors of AlCrFeCuNi high-entropy alloys under uniaxial tension via molecular dynamics simulation. RSC advances 6, 76409-76419.

Li, J., Lu, B., Zhou, H., Tian, C., Xian, Y., Hu, G., Xia, R., 2019a. Molecular dynamics simulation of mechanical properties of nanocrystalline platinum: Grain-size and temperature effects. Phys. Lett. A 383, 1922-1928.

Li, K.-S., Wang, R.-Z., Xu, L., Zhang, C.-C., Xia, X.-X., Tang, M.-J., Zhang, G.-D., Zhang, X.-C., Tu, S.-T., 2022a. Life prediction and damage analysis of creep-fatigue combined with high-low cycle loading by using a crystal plasticity-based approach. International Journal of Fatigue 164, 107154.

Li, K.-S., Wang, R.-Z., Yuan, G.-J., Zhu, S.-P., Zhang, X.-C., Tu, S.-T., Miura, H., 2021a. A crystal plasticity-based approach for creep-fatigue life prediction and damage evaluation in a nickel-based superalloy. International Journal of Fatigue 143, 106031.

Li, L.-T., Lin, Y., Zhou, H.-M., Jiang, Y.-Q., 2013. Modeling the high-temperature creep behaviors of 7075 and 2124 aluminum alloys by continuum damage mechanics model. Computational Materials Science 73, 72-78.

Li, M., Zhang, X., Chen, W.-Y., Byun, T.S., 2021b. Creep behavior of 316 L stainless steel manufactured by laser powder bed fusion. J. Nucl. Mater. 548, 152847.

Li, Y., Gao, P., Zhan, M., Jiang, X., 2022b. Heterogeneous deformation and damage mechanisms in multi-phase TA15 Ti-alloy: Insights from experiments informed damage-crystal plasticity modelling. Materials Science and Engineering: A 848, 143444.

Li, Z., Voisin, T., McKeown, J.T., Ye, J., Braun, T., Kamath, C., King, W.E., Wang, Y.M., 2019b. Tensile properties, strain rate sensitivity, and activation volume of additively manufactured 316L stainless steels. Int. J. Plast. 120, 395-410.

Liang, Y.-J., Wang, L., Wen, Y., Cheng, B., Wu, Q., Cao, T., Xiao, Q., Xue, Y., Sha, G., Wang, Y., 2018. High-content ductile coherent nanoprecipitates achieve ultrastrong high-entropy alloys. Nature communications 9, 1-8.

Lindvall, A., 2020. Modeling and simulation of creep in a thermal energy storage unit.

Liu, C.-J., Gadelmeier, C., Lu, S.-L., Yeh, J.-W., Yen, H.-W., Gorsse, S., Glatzel, U., Yeh, A.-C., 2022a. Tensile creep behavior of HfNbTaTiZr refractory high entropy alloy at elevated temperatures. Acta Materialia 237, 118188.

Liu, G., Mo, H., Wang, J., Shen, Y., 2021. Coupled crystal plasticity finite element-phase field model with kinetics-controlled twinning mechanism for hexagonal metals. Acta Materialia 202, 399-416.

Liu, R., Qiao, Y., Yan, M., Fu, Y., 2012. Mechanical and corrosion resistant properties of martensitic stainless steel plasma nitrocarburized with rare earths addition. Journal of Rare Earths 30, 826-830.

Liu, W., Chen, B.K., Pang, Y., Najafzadeh, A., 2020. A 3D phenomenological yield function with both in and out-of-plane mechanical anisotropy using full-field crystal plasticity spectral method for modelling sheet metal forming of strong textured aluminum alloy. International Journal of Solids and Structures 193, 117-133.

Liu, X., Fan, J., Song, Y., Zhang, P., Chen, F., Yuan, R., Wang, J., Tang, B., Kou, H., Li, J., 2022b. High-temperature tensile and creep behaviour of Inconel 625 superalloy sheet and its associated deformation-failure micromechanisms. Materials Science and Engineering: A 829, 142152.

Liu, Y., Liu, Z., Liu, W., Zhu, Y., 2003. Study of solid solution strengthening of alloying element with phase structure factors. Prog. Nat. Sci. 13, 69-73.

Liu, Y., Zhao, B., Xu, B., Yue, Z., 2007. Experimental and numerical study of the method to determine the creep parameters from the indentation creep testing. Materials Science and Engineering: A 456, 103-108.

Lloyd, J., Clayton, J., Austin, R., McDowell, D., 2014. Plane wave simulation of elastic-viscoplastic single crystals. J. Mech. Phys. Solids 69, 14-32.

Logé, R., Bernacki, M., Resk, H., Delannay, L., Digonnet, H., Chastel, Y., Coupez, T., 2008. Linking plastic deformation to recrystallization in metals using digital microstructures. Philosophical Magazine 88, 3691-3712.

Lu, X., Lin, X., Chiumenti, M., Cervera, M., Li, J., Ma, L., Wei, L., Hu, Y., Huang, W., 2018. Finite element analysis and experimental validation of the thermomechanical behavior in laser solid forming of Ti-6Al-4V. Additive Manufacturing 21, 30-40.

Luo, Z., Zhao, Y., 2018. A survey of finite element analysis of temperature and thermal stress fields in powder bed fusion Additive Manufacturing. Additive Manufacturing 21, 318-332.

Ma, X., Wei, D., Han, Q., Rui, S., Su, D., Yang, W., He, Z., Xiao, J., Wu, Y., Shi, H.-j., 2019. Parametric study of cyclic plasticity behavior in a directionally solidified superalloy with partial recrystallization by crystal plasticity finite element simulation. Journal of Materials Engineering and Performance 28, 3332-3340.

Ma, Z., Zhan, L., Liu, C., Xu, L., Xu, Y., Ma, P., Li, J., 2018. Stress-level-dependency and bimodal precipitation behaviors during creep ageing of Al-Cu alloy: Experiments and modeling. Int. J. Plast. 110, 183-201.

Mansur, L., 1987. Mechanisms and kinetics of radiation effects in metals and alloys. Kinetics of Nohomogeneous Processes. United States: John Wiley and Sons.

Maric, M., Muránsky, O., Karatchevtseva, I., Ungár, T., Hester, J., Studer, A., Scales, N., Ribárik, G., Primig, S., Hill, M.R., 2018. The effect of cold-rolling on the microstructure and corrosion behaviour of 316L alloy in FLiNaK molten salt. Corros. Sci. 142, 133-144.

Martínez-García, V., Pedrini, G., Weidmann, P., Killinger, A., Gadow, R., Osten, W., Schmauder, S., 2019. Non-contact residual stress analysis method with displacement measurements in the nanometric range by laser made material removal and SLM based beam conditioning on ceramic coatings. Surface and Coatings Technology 371, 14-19.

Maruyama, K., 2008. 8 - Fundamental aspects of creep deformation and deformation mechanism map, in: Abe, F., Kern, T.-U., Viswanathan, R. (Eds.), Creep-Resistant Steels. Woodhead Publishing, pp. 265-278.

Masson, R., Bornert, M., Suquet, P., Zaoui, A., 2000. An affine formulation for the prediction of the effective properties of nonlinear composites and polycrystals. Journal of the Mechanics and Physics of Solids 48, 1203-1227.

Matijasevic, M., Almazouzi, A., 2008. Effect of Cr on the mechanical properties and microstructure of Fe–Cr model alloys after n-irradiation. J. Nucl. Mater. 377, 147-154.

MATLAB, 2022. Natick, Massachusetts: The MathWorks Inc. 9.7.0.1190202 (R2019b).

Mayeur, J.R., McDowell, D.L., Neu, R.W., 2008. Crystal plasticity simulations of fretting of Ti-6Al-4V in partial slip regime considering effects of texture. Computational Materials Science 41, 356-365.

McCormack, S.J., Wen, W., Pereloma, E.V., Tomé, C.N., Gazder, A.A., Saleh, A.A., 2018. On the first direct observation of de-twinning in a twinning-induced plasticity steel. Acta Materialia 156, 172-182.

McElfresh, C., Marian, J., 2022. Initial grain orientation controls static recrystallization outcomes in cold-worked iron: Insight from coupled crystal plasticity/vertex dynamics modeling. Acta Materialia, 118631.

McMurtrey, M., Sun, C., Rupp, R., Shiau, C.-H., Hanbury, R., Jerred, N., O'Brien, R., 2021. Investigation of the irradiation effects in additively manufactured 316L steel resulting in decreased irradiation assisted stress corrosion cracking susceptibility. Journal of Nuclear Materials 545, 152739.

Mecking, H., Kocks, U., 1981. Kinetics of flow and strain-hardening. Acta metallurgica 29, 1865-1875.

Meena, C., Uthaisangsuk, V., 2021. Micromechanics Based Modeling of Effect of Sigma Phase on Mechanical and Failure Behavior of Duplex Stainless Steel. Metallurgical and Materials Transactions A 52, 1293-1313.

Megahed, M., Mindt, H.-W., N'Dri, N., Duan, H., Desmaison, O., 2016. Metal additive-manufacturing process and residual stress modeling. Integrating Materials and Manufacturing Innovation 5, 61-93.

Menzel, A., Steinmann, P., 2003. Geometrically non‐linear anisotropic inelasticity based on fictitious configurations: Application to the coupling of continuum damage and multiplicative elasto‐plasticity. International journal for numerical methods in engineering 56, 2233-2266.

Mertens, A., Reginster, S., Paydas, H., Contrepois, Q., Dormal, T., Lemaire, O., Lecomte-Beckers, J., 2014. Mechanical properties of alloy Ti–6Al–4V and of stainless steel 316L processed by selective laser melting: influence of out-of-equilibrium microstructures. Powder Metallurgy 57, 184-189.

Metelkova, J., Kinds, Y., Kempen, K., de Formanoir, C., Witvrouw, A., Van Hooreweder, B., 2018. On the influence of laser defocusing in Selective Laser Melting of 316L. Additive Manufacturing 23, 161-169.

Mirkoohi, E., Tran, H.-C., Lo, Y.-L., Chang, Y.-C., Lin, H.-Y., Liang, S.Y., 2020a. Analytical mechanics modeling of residual stress in laser powder bed considering flow hardening and softening. The International Journal of Advanced Manufacturing Technology 107, 4159-4172.

Mirkoohi, E., Tran, H.-C., Lo, Y.-L., Chang, Y.-C., Lin, H.-Y., Liang, S.Y., 2020b. Analytical mechanics modeling of residual stress in laser powder bed considering flow hardening and softening. 107, 4159-4172.

Mishurova, T., Artzt, K., Rehmer, B., Haubrich, J., Ávila, L., Schoenstein, F., Serrano-Munoz, I., Requena, G., Bruno, G., 2021. Separation of the impact of residual stress and microstructure on the fatigue performance of LPBF Ti-6Al-4V at elevated temperature. International Journal of Fatigue 148, 106239.

Misra, A., Placidi, L., dell'Isola, F., Barchiesi, E., 2021. Identification of a geometrically nonlinear micromorphic continuum via granular micromechanics. Zeitschrift für angewandte Mathematik und Physik 72, 1-21.

Mitchell, T.E., 2001. Yielding in Crystals Containing Atomic-size Obstacles, in: Buschow, K.H.J., Cahn, R.W., Flemings, M.C., Ilschner, B., Kramer, E.J., Mahajan, S., Veyssière, P. (Eds.), Encyclopedia of Materials: Science and Technology. Elsevier, Oxford, pp. 9827-9842.

Molinari, A., Canova, G., Ahzi, S., 1987. A self consistent approach of the large deformation polycrystal viscoplasticity. Acta Metallurgica 35, 2983-2994.

Molinari, A., Tóth, L., 1994. Tuning a self consistent viscoplastic model by finite element results—I. Modeling. Acta Metallurgica et Materialia 42, 2453-2458.

Mordehai, D., Clouet, E., Fivel, M., Verdier, M., 2008. Introducing dislocation climb by bulk diffusion in discrete dislocation dynamics. Philosophical Magazine 88, 899-925.

Morris, D., Harries, D., 1978. Creep and rupture in Type 316 stainless steel at temperatures between 525 and 900 C Part II: Rupture and ductility. Metal science 12, 532-541.

Mott, N.F., Nabarro, F.R.N., 1940. An attempt to estimate the degree of precipitation hardening, with a simple model. Proceedings of the Physical Society 52, 86.

Moulinec, H., Suquet, P., 1998. A numerical method for computing the overall response of nonlinear composites with complex microstructure. Computer methods in applied mechanics and engineering 157, 69-94.

Mukherjee, T., Zuback, J., De, A., DebRoy, T., 2016. Printability of alloys for additive manufacturing. Scientific reports 6, 1-8.

Murakami, S., 1983. Notion of continuum damage mechanics and its application to anisotropic creep damage theory. ASME. J. Eng. Mater. Technol. April 1983; 105(2): 99–105.

Murr, L.E., Gaytan, S.M., Ramirez, D.A., Martinez, E., Hernandez, J., Amato, K.N., Shindo, P.W., Medina, F.R., Wicker, R.B., 2012. Metal fabrication by additive manufacturing using laser and electron beam melting technologies. Journal of Materials Science & Technology 28, 1-14.

Nabarro, F., 1979. Dislocations in seismology. Dislocations in Solids 3.

Nakano, T., 2010. 3 - Mechanical properties of metallic biomaterials, in: Niinomi, M. (Ed.), Metals for Biomedical Devices. Woodhead Publishing, pp. 71-98.

Needleman, A., Rice, J., 1978. Limits to ductility set by plastic flow localization, Mechanics of sheet metal forming. Springer, pp. 237-267.

Needleman, A., Rice, J.R., 1980. Plastic creep flow effects in the diffusive cavitation of grain boundaries. Acta Metallurgica 28, 1315-1332.

Ni, M., Chen, C., Wang, X., Wang, P., Li, R., Zhang, X., Zhou, K., 2017. Anisotropic tensile behavior of in situ precipitation strengthened Inconel 718 fabricated by additive manufacturing. Materials Science and Engineering: A 701, 344-351.

Nicolaou, P., Semiatin, S., 2004. A hybrid micromechanical-macroscopic model for the analysis of the tensile behavior of cavitating materials. Metallurgical and Materials Transactions A 35, 1141-1149.

Nie, K., Wu, W.-P., Zhang, X.-L., Yang, S.-M., 2017. Molecular dynamics study on the grain size, temperature, and stress dependence of creep behavior in nanocrystalline nickel. Journal of Materials Science 52, 2180-2191.

Norström, L.Å., 1977. The influence of nitrogen and grain size on yield strength in Type AISI 316L austenitic stainless steel. Metal Science 11, 208-212.

Ohring, M., 2014. Solutions Manual to Accompany Engineering Materials Science. Academic Press.

Okazaki, K., 1996. Solid-solution hardening and softening in binary iron alloys. Journal of materials science 31, 1087-1099.

Orowan, E., 1934a. Zur kristallplastizität. II. Zeitschrift für Physik 89, 614-633.

Orowan, E., 1934b. Zur kristallplastizität. iii. Zeitschrift für Physik 89, 634-659.

Orowan, E., 1940. Problems of plastic gliding. Proceedings of the Physical Society (1926-1948) 52, 8.

Ozturk, D., Kotha, S., Pilchak, A.L., Ghosh, S., 2019. Two-way multi-scaling for predicting fatigue crack nucleation in titanium alloys using parametrically homogenized constitutive models. Journal of the Mechanics and Physics of Solids 128, 181-207.

Padilha, A., Escriba, D.M., Materna-Morris, E., Rieth, M., Klimenkov, M., 2007. Precipitation in AISI 316L(N) during creep tests at 550 and 600 °C up to 10 years. Journal of Nuclear Materials - J Nucl Mater 362, 132-138.

Pagac, M., Malotova, S., Petru, J., Zlamal, T., 2017. Evaluation of Chosen Parameters of Surface Roughness (microgeometry) on the Samples from Stainless Steel 316L and Manufactured by the Additive Technology SLM. Metal 2017: 26th Anniversary International Conference on Metallurgy and Materials, 2017.

Pal, D., Patil, N., Zeng, K., Teng, C., Stucker, B., 2015. An efficient multi-scale simulation architecture for the prediction of performance metrics of parts fabricated using additive manufacturing. Metallurgical and Materials Transactions A 46, 3852-3863.

Patra, A., McDowell, D.L., 2012. Crystal plasticity-based constitutive modelling of irradiated bcc structures. Philosophical Magazine 92, 861-887.

Patra, A., Tomé, C.N., 2017. Finite element simulation of gap opening between cladding tube and spacer grid in a fuel rod assembly using crystallographic models of irradiation growth and creep. Nuclear Engineering and Design 315, 155-169.

Paul, R., Anand, S., Gerner, F., 2014. Effect of thermal deformation on part errors in metal powder based additive manufacturing processes. ASME. J. Manuf. Sci. Eng. June 2014; 136(3): 031009.

Peirce, D., Asaro, R., Needleman, A., 1982. An analysis of nonuniform and localized deformation in ductile single crystals. Acta metallurgica 30, 1087-1119.

Petch, N., 1953. The cleavage strength of polycrystals. Journal of the Iron and Steel institute 174, 25-28.

Petch, N., 1954. The fracture of metals. Prog. Met. Phys. 5, 1-52.

Pham, M., Dovgyy, B., Hooper, P., 2017. Twinning induced plasticity in austenitic stainless steel 316L made by additive manufacturing. Materials Science and Engineering: A 704, 102-111.

Pham, M.S., Solenthaler, C., Janssens, K.G.F., Holdsworth, S.R., 2011. Dislocation structure evolution and its effects on cyclic deformation response of AISI 316L stainless steel. Materials Science and Engineering: A 528, 3261-3269.

Podgornik, B., Šinko, M., Godec, M., 2021. Dependence of the wear resistance of additive-manufactured maraging steel on the build direction and heat treatment. Addit. Manuf. 46, 102123.

Poirier, J.-P., 1985. Creep of crystals: high-temperature deformation processes in metals, ceramics and minerals. Cambridge University Press.

Pokharel, R., Patra, A., Brown, D.W., Clausen, B., Vogel, S.C., Gray, G.T., 2019. An analysis of phase stresses in additively manufactured 304L stainless steel using neutron diffraction measurements and crystal plasticity finite element simulations. Int. J. Plast. 121, 201-217.

Poletaev, G., Zorya, I., Rakitin, R., Iliina, M., Starostenkov, M., 2020. Interaction of Impurity Atoms of Light Elements with Vacancies and Vacancy Cluster in Fcc Metals. Materials Physics & Mechanics 44.

Pradeep, P.I., Kumar, V.A., Sriranganath, A., Singh, S.K., Sahu, A., Kumar, T.S., Narayanan, P.R., Arumugam, M., Mohan, M., 2020. Characterization and Qualification of LPBF Additively Manufactured AISI-316L Stainless Steel Brackets for Aerospace Application. Transactions of the Indian National Academy of Engineering 5, 603-616.

Prakash, A., Hochrainer, T., Reisacher, E., Riedel, H., 2008. Twinning Models in Self‐Consistent Texture Simulations of TWIP Steels. Steel research international 79, 645-652.

Prat, O., García, J., Rojas, D., Sanhueza, J.P., Camurri, C., 2014. Study of nucleation, growth and coarsening of precipitates in a novel 9%Cr heat resistant steel: Experimental and modeling. Materials Chemistry and Physics 143, 754-764.

Proust, G., Tomé, C., Kaschner, G., 2007. Modeling texture, twinning and hardening evolution during deformation of hexagonal materials. Acta Materialia 55, 2137-2148.

Puchi Cabrera, E., 2001a. High temperature deformation of 316L stainless steel. Materials science and technology 17, 155-161.

Puchi Cabrera, E.S., 2001b. High temperature deformation of 316L stainless steel. Mater. Sci. Technol. 17, 155-161.

Quarrell, A., 1952. The Hardness of Metals. Nature 170, 818-818.

Queyreau, S., Monnet, G., Devincre, B., 2009. Slip systems interactions in α-iron determined by dislocation dynamics simulations. Int. J. Plast. 25, 361-377.

Queyreau, S., Monnet, G., Devincre, B., 2010. Orowan strengthening and forest hardening superposition examined by dislocation dynamics simulations. Acta Materialia 58, 5586-5595.

Raabe, D., Zhao, Z., Mao, W., 2002. On the dependence of in-grain subdivision and deformation texture of aluminum on grain interaction. Acta Materialia 50, 4379-4394.

Rai, R., Elmer, J., Palmer, T., DebRoy, T., 2007. Heat transfer and fluid flow during keyhole mode laser welding of tantalum, Ti–6Al–4V, 304L stainless steel and vanadium. Journal of physics D: Applied physics 40, 5753.

Rajaguru, M., Keralavarma, S., 2018. A discrete dislocation dynamics model of creeping single crystals. Modelling and Simulation in Materials Science and Engineering 26, 035007.

Randle, V., 2004. Twinning-related grain boundary engineering. Acta materialia 52, 4067-4081.

Rice, J.R., 1981. Constraints on the diffusive cavitation of isolated grain boundary facets in creeping polycrystals. Acta Metallurgica 29, 675-681.

Rieth, M., 2007. A comprising steady-state creep model for the austenitic AISI 316 L (N) steel. J. Nucl. Mater. 367, 915-919.

Rieth, M., Falkenstein, A., Graf, P., Heger, S., Jaentsch, U., Klimiankou, M., Materna-Morris, E., Zimmermann, H., 2004a. Creep of the austenitic steel AISI 316 L(N) Experiments and models, p. 80.

Rieth, M., Falkenstein, A., Graf, P., Heger, S., Jäntsch, U., Klimiankou, M., Materna-Morris, E., Zimmermann, H., 2004b. Creep of the austenitic steel AISI 316 L (N). Experiments and models. Forschungszentrum Karlsruhe GmbH Technik und Umwelt (Germany). Inst. fuer ….

Ronneberg, T., Davies, C.M., Hooper, P.A., 2020. Revealing relationships between porosity, microstructure and mechanical properties of laser powder bed fusion 316L stainless steel through heat treatment. Materials & Design 189, 108481.

Roodposhti, P.S., Sarkar, A., Murty, K.L., Brody, H., Scattergood, R., 2016. Grain boundary sliding mechanism during high temperature deformation of AZ31 Magnesium alloy. Materials Science and Engineering: A 669, 171-177.

Rose, M.E., 1995. Elementary theory of angular momentum. Courier Corporation.

Roters, F., Diehl, M., Shanthraj, P., Eisenlohr, P., Reuber, C., Wong, S.L., Maiti, T., Ebrahimi, A., Hochrainer, T., Fabritius, H.-O., 2019. DAMASK–The Düsseldorf Advanced Material Simulation Kit for modeling multi-physics crystal plasticity, thermal, and damage phenomena from the single crystal up to the component scale. Computational Materials Science 158, 420-478.

Roters, F., Eisenlohr, P., Hantcherli, L., Tjahjanto, D.D., Bieler, T.R., Raabe, D., 2010. Overview of constitutive laws, kinematics, homogenization and multiscale methods in crystal plasticity finite-element modeling: Theory, experiments, applications. Acta materialia 58, 1152-1211.

Sabzi, H.E., Aboulkhair, N.T., Liang, X., Li, X.H., Simonelli, M., Fu, H., Rivera-Díaz-del-Castillo, P.E.J., 2020a. Grain refinement in laser powder bed fusion: The influence of dynamic recrystallization and recovery. Materials and Design 196.

Sabzi, H.E., Hernandez-Nava, E., Li, X.-H., Fu, H., San-Martín, D., Rivera-Díaz-del-Castillo, P.E.J., 2021. Strengthening control in laser powder bed fusion of austenitic stainless steels via grain boundary engineering. Materials & Design 212, 110246.

Sabzi, H.E., Maeng, S., Liang, X., Simonelli, M., Aboulkhair, N.T., Rivera-Díaz-del-Castillo, P.E., 2020b. Controlling crack formation and porosity in laser powder bed fusion: Alloy design and process optimisation. Additive Manufacturing 34, 101360.

Sabzi, H.E., Maeng, S., Liang, X., Simonelli, M., Aboulkhair, N.T., Rivera-Díaz-del-Castillo, P.E.J., 2020c. Controlling crack formation and porosity in laser powder bed fusion: Alloy design and process optimisation. Addit. Manuf. 34, 101360.

Sachs, G., 1928. Plasticity problems in metals. Transactions of the Faraday Society 24, 84-92.

Sahlaoui, H., Makhlouf, K., Sidhom, H., Philibert, J., 2004. Effects of ageing conditions on the precipitates evolution, chromium depletion and intergranular corrosion susceptibility of AISI 316L: Experimental and modeling results. Materials Science and Engineering: A 372, 98-108.

Sanaei, N., Fatemi, A., 2021. Defects in additive manufactured metals and their effect on fatigue performance: A state-of-the-art review. Progress in Materials Science 117, 100724.

Sandmann, P., Keller, S., Kashaev, N., Ghouse, S., Hooper, P.A., Klusemann, B., Davies, C.M., 2022. Influence of laser shock peening on the residual stresses in additively manufactured 316L by Laser Powder Bed Fusion: A combined experimental–numerical study. Additive Manufacturing 60, 103204.

Sandström, R., 2023. Primary creep at low stresses in copper. Materials Science and Engineering: A 873, 144950.

Sanhueza, J., Rojas, D., Prat, O., Garcia, J., Espinoza, R., Montalba, C., Melendrez, M., 2017. Precipitation kinetics in a 10.5% Cr heat resistant steel: Experimental results and simulation by TC-PRISMA/DICTRA. Mater. Chem. Phys. 200, 342-353.

Sarrazola, D.R., Muñoz, D.P., Bernacki, M., 2020. A new numerical framework for the full field modeling of dynamic recrystallization in a CPFEM context. Computational Materials Science 179, 109645.

Scheuer, C.J., Cardoso, R.P., Zanetti, F.I., Amaral, T., Brunatto, S.F., 2012. Low-temperature plasma carburizing of AISI 420 martensitic stainless steel: Influence of gas mixture and gas flow rate. Surface and Coatings Technology 206, 5085-5090.

Schmid, E., 1924. Proc. Int. Cong. Appl. Mech. Delft, The Netherlands.

Sealy, M.P., Madireddy, G., Williams, R.E., Rao, P., Toursangsaraki, M., 2018. Hybrid processes in additive manufacturing. Journal of manufacturing Science and Engineering 140.

Seede, R., Shoukr, D., Zhang, B., Whitt, A., Gibbons, S., Flater, P., Elwany, A., Arroyave, R., Karaman, I., 2020. An ultra-high strength martensitic steel fabricated using selective laser melting additive manufacturing: Densification, microstructure, and mechanical properties. Acta Materialia 186, 199-214.

Seifi, M., Salem, A., Beuth, J., Harrysson, O., Lewandowski, J.J., 2016. Overview of materials qualification needs for metal additive manufacturing. Jom 68, 747-764.

Shamsujjoha, M., Agnew, S.R., Fitz-Gerald, J.M., Moore, W.R., Newman, T.A., 2018. High Strength and Ductility of Additively Manufactured 316L Stainless Steel Explained. Metallurgical and Materials Transactions A 49, 3011-3027.

Shang, S.-L., Zhou, B.-C., Wang, W.Y., Ross, A.J., Liu, X.L., Hu, Y.-J., Fang, H.-Z., Wang, Y., Liu, Z.-K., 2016. A comprehensive first-principles study of pure elements: vacancy formation and migration energies and self-diffusion coefficients. Acta Materialia 109, 128-141.

Shen, L.-C., Yang, X.-H., Ho, J.-R., Tung, P.-C., Lin, C.-K., 2020. Effects of Build Direction on the Mechanical Properties of a Martensitic Stainless Steel Fabricated by Selective Laser Melting. Materials 13, 5142.

Shewmon, P., 2016. Diffusion in solids. Springer.

Shilkrot, L., Curtin, W.A., Miller, R.E., 2002. A coupled atomistic/continuum model of defects in solids. Journal of the Mechanics and Physics of Solids 50, 2085-2106.

Shin, D., Yamamoto, Y., Brady, M.P., Lee, S., Haynes, J.A., 2019. Modern data analytics approach to predict creep of high-temperature alloys. Acta Mater. 168, 321-330.

Shiomi, M., Osakada, K., Nakamura, K., Yamashita, T., Abe, F., 2004. Residual Stress within Metallic Model Made by Selective Laser Melting Process. CIRP Annals 53, 195-198.

Singh, R., Gupta, P., Yedla, N., 2019. Single-crystal Al–Cu50Zr50 metallic glass cold welds: tensile and creep behaviour. Molecular Simulation 45, 1549-1562.

Sirinakorn, T., Wongwises, S., Uthaisangsuk, V., 2014. A study of local deformation and damage of dual phase steel. Mater. Des. 64, 729-742.

Sklenička, V., Kuchařová, K., Kvapilová, M., Svoboda, M., Král, P., Dvořák, J., 2017. Creep properties of simulated heat-affected zone of HR3C austenitic steel. Materials Characterization 128, 238-247.

Snow, Z., Nassar, A.R., Reutzel, E.W., 2020. Invited Review Article: Review of the formation and impact of flaws in powder bed fusion additive manufacturing. Additive Manufacturing 36, 101457.

Sobie, C., Bertin, N., Capolungo, L., 2015. Analysis of Obstacle Hardening Models Using Dislocation Dynamics: Application to Irradiation-Induced Defects. Metallurgical and Materials Transactions A 46, 3761-3772.

Soleimani, S.M.Y., Mashreghi, A.R., Ghasemi, S.S., Moshrefifar, M., 2012. The effect of plasma nitriding on the fatigue behavior of DIN 1.2210 cold work tool steel. Materials & Design 35, 87-92.

Song, J., Chew, Y., Bi, G., Yao, X., Zhang, B., Bai, J., Moon, S.K., 2018. Numerical and experimental study of laser aided additive manufacturing for melt-pool profile and grain orientation analysis. Mater. Des. 137, 286-297.

Song, S.H., Weng, L.Q., 2005. Diffusion of vacancy–solute complexes in alloys. Materials Science and Technology 21, 305-310.

Sourmail, T., 2001. Precipitation in creep resistant austenitic stainless steels. Mater. Sci. Technol. 17, 1-14.

Sourmail, T., Bhadeshia, H., MacKay, D.J., 2002. Neural network model of creep strength of austenitic stainless steels. Mater. Sci. Technol. 18, 655-663.

Soutas-Little, R.W., 2012. Elasticity. Courier Corporation.

Sprouster, D.J., Streit Cunningham, W., Halada, G.P., Yan, H., Pattammattel, A., Huang, X., Olds, D., Tilton, M., Chu, Y.S., Dooryhee, E., Manogharan, G.P., Trelewicz, J.R., 2021. Dislocation microstructure and its influence on corrosion behavior in laser additively manufactured 316L stainless steel. Addit. Manuf. 47, 102263.

Standard, A., 2012. Standard terminology for additive manufacturing technologies. ASTM International F2792-12a.

Staroselsky, A., Anand, L., 1998. Inelastic deformation of polycrystalline face centered cubic materials by slip and twinning. Journal of the Mechanics and Physics of Solids 46, 671-696.

Stephens, J.R., Witzke, W.R., 1976. Alloy softening in binary iron solid solutions. Journal of the Less Common Metals 48, 285-308.

Stoudt, M.R., Williams, M.E., Levine, L.E., Creuziger, A., Young, S.A., Heigel, J.C., Lane, B.M., Phan, T.Q., 2020. Location-Specific Microstructure Characterization Within IN625 Additive Manufacturing Benchmark Test Artifacts. Integr. Mater. Manuf. Innovation 9, 54-69.

Su, C., Herbert, E.G., Sohn, S., LaManna, J.A., Oliver, W.C., Pharr, G.M., 2013. Measurement of power-law creep parameters by instrumented indentation methods. Journal of the Mechanics and Physics of Solids 61, 517-536.

Sun, W., Jonas, J., 1994. Influence of dynamic precipitation on grain boundary sliding during high temperature creep. Acta Metall. Mater. 42, 283-292.

Svoboda, J., Lukáš, P., 1997. Modelling of recovery controlled creep in nickel-base superalloy single crystals. Acta Materialia 45, 125-135.

Syed, A.K., Ahmad, B., Guo, H., Machry, T., Eatock, D., Meyer, J., Fitzpatrick, M.E., Zhang, X., 2019. An experimental study of residual stress and direction-dependence of fatigue crack growth behaviour in as-built and stress-relieved selective-laser-melted Ti6Al4V. Materials Science and Engineering: A 755, 246-257.

Tan, J.H.K., Sing, S.L., Yeong, W.Y., 2020. Microstructure modelling for metallic additive manufacturing: a review. Virtual and Physical Prototyping 15, 87-105.

Tandon, V., Patil, A.P., Rathod, R.C., 2018. Correlation of martensite content and dislocation density of cold worked 316L on defect densities of passivating film in acidic environment. Mater. Res. Express 5, 086515.

Tapia, G., Elwany, A., 2014. A review on process monitoring and control in metal-based additive manufacturing. ASME. J. Manuf. Sci. Eng. December 2014; 136(6): 060801. Taylor, G.I., 1938. Plastic strain in metals. J. Inst. Metals 62, 307-324.

tec-science, 2023. Tensile test, p. Cottrell atmosphere.

Tekkaya, A., Lange, K., 2000. An improved relationship between Vickers hardness and yield stress for cold formed materials and its experimental verification. Cirp Annals 49, 205-208.

Terada, M., Escriba, D.M., Costa, I., Materna-Morris, E., Padilha, A.F., 2008. Investigation on the intergranular corrosion resistance of the AISI 316L(N) stainless steel after long time creep testing at 600 °C. Materials Characterization 59, 663-668.

Tilley, R.J., 2004. Understanding solids: the science of materials. John Wiley & Sons.

Tome, C., Lebensohn, R., 2023. Material Modeling with the Visco-Plastic Self-Consistent (VPSC) Approach: Theory and Practical Applications. Elsevier.

Tomé, C., Lebensohn, R., 2007. Visco-plastic self-consistent (vpsc). Los Alamos National Laboratory (USA) and Universidad Nacional de Rosario (Argentina) 6.

Tomé, C.N., Lebensohn, R.A., Kocks, U., 1991. A model for texture development dominated by deformation twinning: application to zirconium alloys. Acta metallurgica et materialia 39, 2667-2680.

Tong, Z., Ren, X., Jiao, J., Zhou, W., Ren, Y., Ye, Y., Larson, E.A., Gu, J., 2019. Laser additive manufacturing of FeCrCoMnNi high-entropy alloy: Effect of heat treatment on

microstructure, residual stress and mechanical property. Journal of alloys and compounds 785, 1144-1159.

Toriumi, M., 1979. Relation between dislocation density and subgrain size of naturally deformed olivine in peridotites. Contributions to Mineralogy and Petrology 68, 181-186.

Trapp, J., Rubenchik, A.M., Guss, G., Matthews, M.J., 2017. In situ absorptivity measurements of metallic powders during laser powder-bed fusion additive manufacturing. Applied Materials Today 9, 341-349.

Tvergaard, V., Needleman, A., 1984. Analysis of the cup-cone fracture in a round tensile bar. Acta metallurgica 32, 157-169.

Van Houtte, P., 1978. Simulation of the rolling and shear texture of brass by the Taylor theory adapted for mechanical twinning. Acta Metallurgica 26, 591-604.

Van Houtte, P., Delannay, L., Kalidindi, S., 2002. Comparison of two grain interaction models for polycrystal plasticity and deformation texture prediction. International Journal of Plasticity 18, 359-377.

Van Houtte, P., Li, S., Seefeldt, M., Delannay, L., 2005. Deformation texture prediction: from the Taylor model to the advanced Lamel model. International journal of plasticity 21, 589-624.

Vastola, G., Zhang, G., Pei, Q., Zhang, Y.-W., 2016. Controlling of residual stress in additive manufacturing of Ti6Al4V by finite element modeling. Additive Manufacturing 12, 231-239.

Villanueva, D.E., Junior, F., Plaut, R., Padilha, A., 2006. Comparative study on sigma phase precipitation of three types of stainless steels: austenitic, superferritic and duplex. Mater. Sci. Technol. 22, 1098-1104.

Voyiadjis, G.Z., Al-Rub, R.K.A., Palazotto, A.N., 2004. Thermodynamic framework for coupling of non-local viscoplasticity and non-local anisotropic viscodamage for dynamic localization problems using gradient theory. International Journal of Plasticity 20, 981-1038.

Vrancken, B., Cain, V., Knutsen, R., Van Humbeeck, J., 2014. Residual stress via the contour method in compact tension specimens produced via selective laser melting. Scripta Materialia 87, 29-32.

Vukkum, V., Gupta, R., 2022. Review on corrosion performance of laser powder-bed fusion printed 316L stainless steel: Effect of processing parameters, manufacturing defects, post-processing, feedstock, and microstructure. Materials & Design, 110874.

Wakeda, M., Tsuru, T., Kohyama, M., Ozaki, T., Sawada, H., Itakura, M., Ogata, S., 2017. Chemical misfit origin of solute strengthening in iron alloys. Acta Mater. 131, 445-456.

Walpole, L., 1969. On the overall elastic moduli of composite materials. Journal of the Mechanics and Physics of Solids 17, 235-251.

Wang, C., Tan, X., Liu, E., Tor, S.B., 2018a. Process parameter optimization and mechanical properties for additively manufactured stainless steel 316L parts by selective electron beam melting. Materials & Design 147, 157-166.

Wang, H., Capolungo, L., Clausen, B., Tomé, C., 2017a. A crystal plasticity model based on transition state theory. International Journal of Plasticity 93, 251-268.

Wang, H., Capolungo, L., Clausen, B., Tomé, C.N., 2017b. A crystal plasticity model based on transition state theory. Int. J. Plast. 93, 251-268.

Wang, H., Clausen, B., Capolungo, L., Beyerlein, I.J., Wang, J., Tome, C.N., 2016. Stress and strain relaxation in magnesium AZ31 rolled plate: In-situ neutron measurement and elastic viscoplastic polycrystal modeling. International Journal of Plasticity 79, 275-292.

Wang, H., Lu, C., Tieu, A.K., Su, L., Deng, G., 2019. Coupled effects of initial orientation scatter and grain-interaction to texture evolution: a crystal plasticity FE study. International Journal of Material Forming 12, 161-171.

Wang, W., Wen, W., 2021. Modeling in Crystal Plasticity: from theory to application. In Encyclopedia of Materials: Metals and Alloys; Caballero, F.G., Ed.; Elsevier: Oxford, UK.

Wang, X., Muniz-Lerma, J.A., Sánchez-Mata, O., Shandiz, M.A., Brochu, M., 2018b. Microstructure and mechanical properties of stainless steel 316L vertical struts manufactured by laser powder bed fusion process. Materials Science and Engineering: A 736, 27-40.

Wang, Y.M., Voisin, T., McKeown, J.T., Ye, J., Calta, N.P., Li, Z., Zeng, Z., Zhang, Y., Chen, W., Roehling, T.T., 2018c. Additively manufactured hierarchical stainless steels with high strength and ductility. Nat. Mater. 17, 63-71.

Was, G.S., 2016. Fundamentals of radiation materials science: metals and alloys. Springer.

Watanabe, T., Tsurekawa, S., 2004. Toughening of brittle materials by grain boundary engineering. Materials Science and Engineering: A 387, 447-455.

Weaver, J.S., Livescu, V., Mara, N.A., 2020. A comparison of adiabatic shear bands in wrought and additively manufactured 316L stainless steel using nanoindentation and electron backscatter diffraction. J. Mater. Sci. 55, 1738-1752.

Webster, G., Wimpory, R., 2001. Non-destructive measurement of residual stress by neutron diffraction. Journal of Materials Processing Technology 117, 395-399.

Weertman, J., 1965. The Peach–Koehler equation for the force on a dislocation modified for hydrostatic pressure. The Philosophical Magazine: A Journal of Theoretical Experimental and Applied Physics 11, 1217-1223.

Weertman, J., 1968. Dislocation climb theory of steady-state creep. Trans. Amer. Soc. Metal. 61, 681-694.

Weertman, J., Weertman, J.R., 1964. Elementary dislocation theory. Macmillan.

Weiss, B., Stickler, R., 1972. Phase instabilities during high temperature exposure of 316 austenitic stainless steel. Metallurgical and Materials Transactions B 3, 851-866.

Wen, W., 2013. Simulation of large deformation response of polycrystals, deforming by slip and twinning, using the viscoplastic Ø-model. Strasbourg.

Wen, W., Capolungo, L., Patra, A., Tomé, C., 2017a. A physics-based crystallographic modeling framework for describing the thermal creep behavior of Fe-Cr alloys. Metallurgical and Materials Transactions A 48, 2603-2617.

Wen, W., Capolungo, L., Patra, A., Tomé, C.J.M., A, M.T., 2017b. A physics-based crystallographic modeling framework for describing the thermal creep behavior of Fe-Cr alloys. 48, 2603-2617.

Wen, W., Capolungo, L., Tomé, C.N., 2018. Mechanism-based modeling of solute strengthening: Application to thermal creep in Zr alloy. Int. J. Plast. 106, 88-106.

Wen, W., Kohnert, A., Arul Kumar, M., Capolungo, L., Tomé, C.N., 2020a. Mechanism-based modeling of thermal and irradiation creep behavior: An application to ferritic/martensitic HT9 steel. Int. J. Plast. 126, 102633.

Wen, W., Kohnert, A., Kumar, M.A., Capolungo, L., Tomé, C.N., 2020b. Mechanism-based modeling of thermal and irradiation creep behavior: An application to ferritic/martensitic HT9 steel. International Journal of Plasticity 126, 102633.

Wert, C.A., Thomson, R.M., Thomson, R.W., 1970. Physics of solids. McGraw-Hill College.

Wiedersich, H., Herschbach, K., 1972. The concept of “chemical stress” caused by arbitrary vacancy and interstitial supersaturations. Scripta Metallurgica 6, 453-457.

Wilkens, M., 1970. The determination of density and distribution of dislocations in deformed single crystals from broadened X-ray diffraction profiles. Physica status solidi (a) 2, 359-370.

Wilkinson, A.J., Tarleton, E., Vilalta-Clemente, A., Jiang, J., Britton, T.B., Collins, D.M., 2014. Measurement of probability distributions for internal stresses in dislocated crystals. Appl. Phys. Lett. 105, 181907.

Williams, R.J., Al-Lami, J., Hooper, P.A., Pham, M.-S., Davies, C.M., 2021. Creep deformation and failure properties of 316 L stainless steel manufactured by laser powder bed fusion under multiaxial loading conditions. Addit. Manuf. 37, 101706.

Williams, R.J., Vecchiato, F., Kelleher, J., Wenman, M.R., Hooper, P.A., Davies, C.M., 2020. Effects of heat treatment on residual stresses in the laser powder bed fusion of 316L stainless steel: Finite element predictions and neutron diffraction measurements. Journal of Manufacturing Processes 57, 641-653.

Wilm, A., 1911. Physikalisch-metallurgische Untersuchungen über magnesiumhaltige Aluminiumlegierungen. Metallurgie: Zeitschrift für de gesamte Hüttenkunde 8, 225-227.

Wilson-Heid, A., Novak, T., Beese, A.M., 2019. Characterization of the effects of internal pores on tensile properties of additively manufactured austenitic stainless steel 316L. Experimental Mechanics 59, 793-804.

Wood, P., Libura, T., Kowalewski, Z.L., Williams, G., Serjouei, A., 2019. Influences of horizontal and vertical build orientations and post-fabrication processes on the fatigue behavior of stainless steel 316L produced by selective laser melting. Materials 12, 4203.

Wroński, M., Kumar, M.A., McCabe, R.J., Wierzbanowski, K., Tome, C.N., 2022. Deformation behavior of CP-titanium under strain path changes: Experiment and crystal plasticity modeling. Int. J. Plast. 148, 103129.

Wu, X., Koul, A., 1995. Grain boundary sliding in the presence of grain boundary precipitates during transient creep. Metallurgical and Materials Transactions A 26, 905-914.

Wu, Z., Gao, Y., Bei, H., 2016. Thermal activation mechanisms and Labusch-type strengthening analysis for a family of high-entropy and equiatomic solid-solution alloys. Acta Mater. 120, 108-119.

Xiao, X., Li, S., Yu, L., 2021. Effect of irradiation damage and indenter radius on pop-in and indentation stress-strain relations: Crystal plasticity finite element simulation. International Journal of Mechanical Sciences 199, 106430.

Xiao, X., Liu, G., Hu, B., Wang, J., Ma, W., 2013. Coarsening behavior for M23C6 carbide in 12% Cr-reduced activation ferrite/martensite steel: experimental study combined with DICTRA simulation. J. Mater. Sci. 48, 5410-5419.

Xiong, Y., Karamched, P., Nguyen, C.-T., Collins, D.M., Magazzeni, C.M., Tarleton, E., Wilkinson, A.J., 2020. Cold creep of titanium: analysis of stress relaxation using synchrotron diffraction and crystal plasticity simulations. Acta Materialia 199, 561-577.

Xue, Q., Cerreta, E., Gray III, G., 2007a. Microstructural characteristics of post-shear localization in cold-rolled 316L stainless steel. Acta Materialia 55, 691-704.

Yadav, S.D., Sonderegger, B., Sartory, B., Sommitsch, C., Poletti, C., 2015. Characterisation and quantification of cavities in 9Cr martensitic steel for power plants. Materials Science and Technology 31, 554-564.

Yadegari, S., Turteltaub, S., Suiker, A., Kok, P., 2014. Analysis of banded microstructures in multiphase steels assisted by transformation-induced plasticity. Computational materials science 84, 339-349.

Yadollahi, A., Shamsaei, N., Thompson, S.M., Seely, D.W., 2015. Effects of process time interval and heat treatment on the mechanical and microstructural properties of direct laser deposited 316L stainless steel. Materials Science and Engineering: A 644, 171-183.

Yaghoobi, M., Chen, Z., Sundararaghavan, V., Daly, S., Allison, J.E., 2021. Crystal Plasticity Finite Element Modeling of Extension Twinning in WE43 Mg Alloys: Calibration and Validation. Integrating Materials and Manufacturing Innovation 10, 488-507.

Yamamoto, Y., Brady, M.P., Ren, Q.-Q., Poplawsky, J.D., Hoelzer, D.T., Lance, M.J., 2022. Creep Behavior and Phase Equilibria in Model Precipitate Strengthened Alumina-Forming Austenitic Alloys. JOM 74, 1453-1468.

Yang, H., Gavras, S., Dieringa, H., 2021a. Creep Characteristics of Metal Matrix Composites.

Yang, X.-q., Liu, Y., Ye, J.-w., Wang, R.-q., Zhou, T.-c., Mao, B.-y., 2019. Enhanced mechanical properties and formability of 316L stainless steel materials 3D-printed using selective laser melting. International Journal of Minerals, Metallurgy and Materials 26, 1396-1404.

Yang, X., Ma, W.-j., Ren, Y.-j., Liu, S.-f., Wang, Y., Wang, W.-l., Tang, H.-p., 2021b. Subgrain microstructures and tensile properties of 316L stainless steel manufactured by selective laser melting. Journal of Iron and Steel Research International 28, 1159-1167.

Ye, W., Akram, J., Mushongera, L.T.J.A.E.M., 2021. Fatigue Behavior of Additively Manufactured IN718 with Columnar Grains. 23, 2001031.

Yin, H., Song, M., Deng, P., Li, L., Prorok, B.C., Lou, X., 2021. Thermal stability and microstructural evolution of additively manufactured 316L stainless steel by laser powder bed fusion at 500–800 ℃. Additive Manufacturing 41, 101981.

Yin, Y.J., Sun, J.Q., Guo, J., Kan, X.F., Yang, D.C., 2019. Mechanism of high yield strength and yield ratio of 316 L stainless steel by additive manufacturing. Materials Science and Engineering: A 744, 773-777.

Yoon, K.B., Dao, V.H., Yu, J.M.J.F., Materials, F.o.E., Structures, 2020. Effects of build direction on tensile and creep properties of 316L stainless steel produced by selective laser melting. 43, 2623-2636.

You, Y., Yan, M.F., 2013. Interactions of foreign interstitial and substitutional atoms in bcc iron from ab initio calculations. Physica B: Condensed Matter 417, 57-69.

Yusuf, S.M., Chen, Y., Yang, S., Gao, N., 2020. Microstructural evolution and strengthening of selective laser melted 316L stainless steel processed by high-pressure torsion. Mater. Charact. 159, 110012.

Zecevic, M., Lebensohn, R.A., Rogers, M., Moore, J., Chiravalle, V., Lieberman, E., Dunning, D., Shipman, G., Knezevic, M., Morgan, N., 2021. Viscoplastic self-consistent formulation as generalized material model for solid mechanics applications. Applications in Engineering Science 6, 100040.

Zhang, B., Li, Y., Bai, Q., 2017. Defect formation mechanisms in selective laser melting: a review. Chinese Journal of Mechanical Engineering 30, 515-527.

Zhang, F., Bower, A., Mishra, R., Boyle, K., 2009. Numerical simulations of necking during tensile deformation of aluminum single crystals. International Journal of Plasticity 25, 49-69.

Zhang, J., Du, S., Ding, S., 2022. Crystal plasticity finite element modeling of twin band formation and evolution together with the macroscale mechanical responses of hexagonal metals. Materials Science and Engineering: A 855, 143856.

Zhang, J., Li, X., Xu, D., Yang, R., 2019. Recent progress in the simulation of microstructure evolution in titanium alloys. Progress in Natural Science: Materials International 29, 295-304.

Zhang, Q., Huang, R., Zhang, X., Cao, T., Xue, Y., Li, X., 2021a. Deformation mechanisms and remarkable strain hardening in single-crystalline high-entropy-alloy micropillars/nanopillars. Nano letters 21, 3671-3679.

Zhang, Y., Zhou, Y.J., Lin, J.P., Chen, G.L., Liaw, P.K., 2008. Solid-solution phase formation rules for multi-component alloys. Advanced engineering materials 10, 534-538.

Zhang, Z., Yuan, X., Zhao, Z., Li, X., Liu, B., Bai, P., 2021b. Electrochemical noise comparative study of pitting corrosion of 316L stainless steel fabricated by selective laser melting and wrought. Journal of Electroanalytical Chemistry 894, 115351.

Zhao, H., Palmiere, E.J., 2018. Effect of austenite grain size on acicular ferrite transformation in a HSLA steel. Materials Characterization 145, 479-489.

Zhao, Z., Ramesh, M., Raabe, D., Cuitino, A., Radovitzky, R., 2008. Investigation of three-dimensional aspects of grain-scale plastic surface deformation of an aluminum oligocrystal. International Journal of Plasticity 24, 2278-2297.

Zheng, B., Zhou, Y., Smugeresky, J., Schoenung, J., Lavernia, E., 2008. Thermal behavior and microstructural evolution during laser deposition with laser-engineered net shaping: Part I. Numerical calculations. Metallurgical and materials transactions A 39, 2228-2236.

Zhong, T., He, K., Li, H., Yang, L., 2019. Mechanical properties of lightweight 316L stainless steel lattice structures fabricated by selective laser melting. Mater. Des. 181, 108076.

Zhou, D., Wang, X., Wang, R., Zhang, T., Yang, X., Jiang, Y., Zhang, X., Gong, J., Tu, S., 2022. An extended crystal plasticity model to simulate the deformation behaviors of hybrid stress–strain controlled creep-fatigue interaction loading. International Journal of Fatigue 156, 106680.

Appendixes

Appendixes I: Dislocation climb model

The dislocation climb can be a reaction-rate-controlled process or a diffusion-controlled process. In irradiated materials, there is a significantly larger current of interstitial atoms or vacancies leaving or entering the dislocation core; while under thermal creep conditions, the dislocation creep is diffusion-controlled. However, in either of them, the dislocation climb is always driven by the interaction between the dislocation and the point defects(interstitial atoms and vacancies), in which condition, the concentration of point defects is non-equilibrium. There is a range of modelling works have been done to describe the dislocation climb, e.g. (Anderson et al., 2017; Bakó et al., 2011; Geers et al., 2014; Gu et al., 2015; Mordehai et al., 2008; Patra and McDowell, 2012; Was, 2016). From a physics perspective, the dislocation climb velocity is not only determined by the flux of interstitial atoms and vacancies around the core of the dislocations, but the climb driving force.

The original dislocation climb velocity v_c^s is given as (Was, 2016):

$$v_c^s = \frac{I_v^s \Omega}{b} \quad \textbf{(I. 1)}$$

where I_v^s is the vacancy current, which is determined by the stress status and vacancy concentration around the dislocation. It is assumed that there is cylindrical control

volume around the dislocation line, and the radius is r. The dislocation core region is where $r \leq r_d$. The Osmotic force, which is also referred as the chemical force, applied on the unit length of the dislocation is given as (Anderson et al., 2017; Wiedersich and Herschbach, 1972):

$$f_{OS}^{s} = -\frac{kTb}{\Omega}\ln\left(\frac{C_v^s(r_d)}{C_v^0}\right) \quad \textbf{(I. 2)}$$

$C_v^s(r_d)$ is the vacancy concentration at r_d, while C_v^0 is the equilibrium vacancy concentration in the bulk, which is temperature-dependent:

$$C_v^0 = \exp\left(S_f^v/k\right)\exp\left(-E_f^v/kT\right) \quad \textbf{(I. 3)}$$

where S_f^v and E_f^v are the vacancy formation entropy and vacancy formation energy, respectively.

Apart from the chemical force, the dislocation climb is also influenced by the climb component of Peach-Koehler force, which is described as: $f_{PK}^s = (\boldsymbol{\sigma} \cdot b^s) \times t^s$ (t^s is the normalized tangent to the dislocation line) (Weertman, 1965; Weertman and Weertman, 1964). The climb component of f_{PK} is given as:

$$f_c^s = f_{PK}^s \cdot n^s = [(\boldsymbol{\sigma} \cdot b^s) \times t^s\,] \cdot n^s = -|b^s|\boldsymbol{\sigma}\colon (b^s \otimes b^s) \quad \textbf{(I. 4)}$$

For the equilibrium state of dislocation, the total force $f^s = f_{OS}^s + f_c^s = 0$, then,

$$C_v^s(r_d) = C_{v,eq}^s = C_v^0\exp\left(\frac{-f_c^s\Omega}{kTb}\right) \quad \textbf{(I. 5)}$$

It is worthy to mention that the matrix vacancy concentration is set to be the same of the equilibrium concentration ($C_v(r \geq r_\infty) = C_v^\infty = C_v^0$, here C_v^∞ is the vacancy concentration at the radius of the outer boundary for the control region, r_∞). Thus, there is a diffusive flow of vacancies along the vacancy concentration gradient. And the dislocation equilibrium status is achieved by absorbing or emitting the vacancy.

The vacancy diffusion flux J is zero at the steady state, and its divergence is null. The Laplace equation around the dislocation core is given as:

$$\nabla^s C_v^s = \frac{1}{r}\frac{\partial}{\partial r} r \frac{\partial C_v^s}{\partial r} = 0 \qquad \textbf{(I. 6)}$$

Therefore, $C_v^s(r) = C_{v,eq}^s + \left(C_v^\infty - C_{v,eq}^s\right)\frac{\ln(r/r_\infty)}{\ln(r_\infty/r_d)}$. And then, the net current per unit length of dislocation absorbing or emitting the vacancies is:

$$I_v^s = 2\pi r \cdot J = 2\pi r \frac{D_v}{\Omega}\frac{\partial C_v^s(r)}{\partial r} = \frac{2\pi D_v\left[C_v^\infty - C_v^0 \exp\left(\frac{-f_c^s \Omega}{kTb}\right)\right]}{\Omega \ln(r_\infty/r_d)} \qquad \textbf{(I. 7)}$$

D_v is the diffusivity of vacancy, hence, the dislocation climb velocity is given as:

$$v_c^s = \frac{I_v^s \Omega}{b} = \frac{2\pi D_v\left[C_v^\infty - C_v^0 \exp\left(\frac{-f_c^s \Omega}{kTb}\right)\right]}{b \ln(r_\infty/r_d)} \qquad \textbf{(I. 8)}$$

Appendixes II: Pole figure

In the fields of crystallography and materials science, pole figures serve as a useful tool for representing the spatial alignment of crystals and the distribution of crystallographic preferred orientations, which is also called texture, of the grains in polycrystalline materials. Technically, the pole figure is the projection of the selected set of crystal plane normal plotted with respect to the sample frame, which is shown in Figure A- 1. The axes of the sample are aligned with the axes of the projection sphere. The pole figures of AM 316L are presented in Figure A- 2, the colour scale bar and the corresponding numbers located at the bottom of each pole figure indicating the texture intensity in units of multiple of a random distribution (m.r.d.) (Choo et al., 2019). For polycrystals, a contour plot is commonly used rather than plotting individual poles. In addition, two pole figures are required for the complete texture analysis, which are not parallel and have different diffraction angles. Since a single pole figure can only represent the crystallographic orientation distribution in one direction, but not the texture in all directions. The pole figures are typically generated using techniques such as X-ray diffraction, electron diffraction, or neutron diffraction, and are analysed using specialized software.

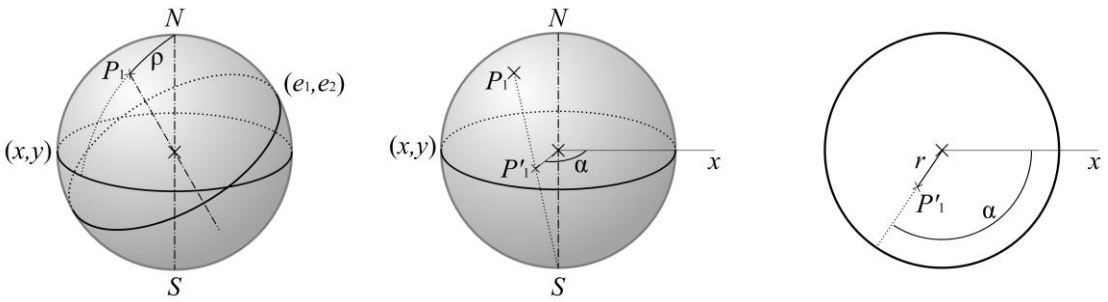

Figure A- 1 Illustration of pole figure.

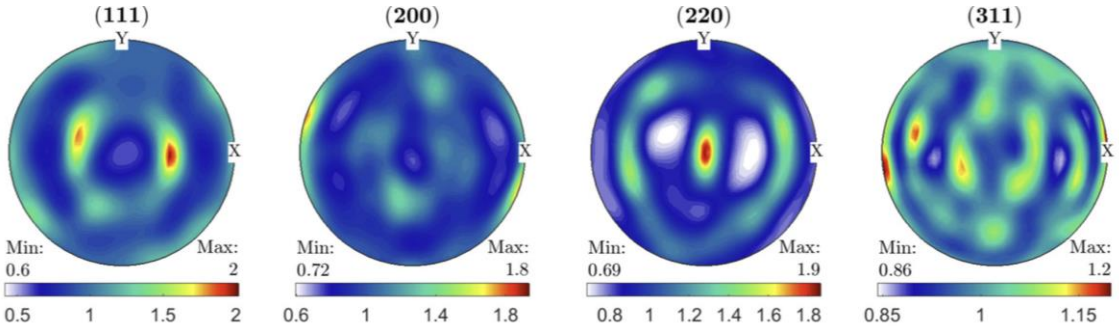

Figure A- 2 Pole figures measured from as-printed L-PBF 316L SS (Choo et al., 2019).